PB 298808

April 1976 UMEE-76R3

A NUMERICAL MODEL FOR LIQUEFACTION IN SAND DEPOSITS

by

Chyr Pyng Liou

The University of Michigan Department of Civil Engineering

50272-101

REPORT DOCUMENTATION PAGE	1. REPORT NO. NSF/RA-761704	2.	3. Recipient's Accession No. PB-258808
4. Title and Subtitle: Numerical Model for Liquefaction in Sand Deposits			5. Report Date: April 1976 6.
7. Author(s): C.P. Liou			8. Performing Organization Rept. No. UMEE-76R3
9. Performing Organization Name and Address: University of Michigan, Civil Engineering Department, Ann Arbor, Michigan 48104			10. Project/Task/Work Unit No. 11. Contract(C) or Grant(G) No. (C) (G) GI34771
12. Sponsoring Organization Name and Address: Engineering and Applied Science (EAS), National Science Foundation, 1800 G Street, N.W., Washington, D.C. 20550			13. Type of Report & Period Covered 14.

15. Supplementary Notes

16. Abstract (Limit: 200 words)

A continuous model for soil liquefaction in a horizontal or nearly horizontal deposit subjected to ground shaking, as in earthquakes, is described. Information from the numerical model is significant because liquefaction may cause soils to lose their shearing strength or undergo extensive lateral displacements resulting in large scale landslides. Liquefaction involves the change of a saturated granular soil to a liquid state due to increased pore water pressure. A liquefaction model was developed comprising two interactive parts, the shear wave submodel and the pressure wave submodel. Shear-strain relationships were formulated for the two-phase soil medium, and the governing equations for pressure wave propagation were then developed. A coupling between shear wave propagation and the vertical motion of soil due to changes in its vertical compressibility was developed. Coupled together, these two submodels constitute the liquefaction model. Application of this liquefaction model to case studies related to the Niigata earthquake of 1964 demonstrated the potential applicability of the model to liquefaction. A literature review, glossary, equations, figures, tables, appendix, and references are included.

17. Document Analysis a. Descriptors

Soils
Soil mechanics
Liquefaction
Secondary waves
Earthquakes
Numerical analysis

b. Identifiers/Open-Ended Terms

Soil liquefaction
Shear wave submodel
Pressure wave submodel
Soil shear strength

c. COSATI Field/Group

18. Availability Statement: NTIS

19. Security Class (This Report)

20. Security Class (This Page)

21. No. of Pages: 221

22. Price: PC A10/MF A01

(See ANSI-Z39.18) See Instructions on Reverse

OPTIONAL FORM 272 (4-77)
(Formerly NTIS-35)
Department of Commerce

CAPITAL SYSTEMS GROUP, INC.
5110 EXECUTIVE BOULEVARD
SUITE 257
ROCKVILLE, MARYLAND 20852

A NUMERICAL MODEL FOR LIQUEFACTION IN SAND DEPOSITS

by
Chyr Pyng Liou

A dissertation submitted in partial fulfillment
of the requirements for the degree of
Doctor of Philosophy
(Civil Engineering)
in The University of Michigan
1976

Doctoral Committee:

Professor Victor L. Streeter, Co-Chairman
Professor E. Benjamin Wylie, Co-Chairman
Professor Ernest F. Brater
Professor Frank E. Richart, Jr.
Professor Alan S. Wineman

Any opinions, findings, conclusions
or recommendations expressed in this
publication are those of the author(s)
and do not necessarily reflect the views
of the National Science Foundation.

To my parents

ACKNOWLEDGEMENTS

The author would like to express his sincerest appreciation to Professor Victor L. Streeter and Professor E. Benjamin Wylie for their guidance, supervision, inspiration and encouragement throughout this study, and to Professor Frank E. Richart, Jr. for providing information and suggestions that were so important to this work. Sincere appreciation is also extended to Professor Ernest F. Brater and Professor Alan S. Wineman for their interest and cooperation.

For assistance in preparing the manuscript, the author is indebted to his friends Mr. Michael G. Ferrick and Mr. William A. Saunders for their help in improving the writing, and to Ms. Lorraine J. Cross for her expert typing.

This study was funded by NSF GI-34771. During earlier stages of his graduate studies the author was supported, in part, by NSF GK-14213. This financial assistance from the National Science Foundation is gratefully acknowledged. The author is also grateful for the teaching assistantships granted by the Civil Engineering Department of The University of Michigan, and for the tuition scholarships provided by the Horace W. King Grant.

TABLE OF CONTENTS

TABLE OF CONTENTS (CON'T)

LIST OF FIGURES

LIST OF FIGURES (CONT'D)

LIST OF FIGURES (CONT'D)

LIST OF FIGURES (CONT'D)

LIST OF FIGURES (CONT'D)

LIST OF TABLES AND CHARTS

LIST OF APPENDICES

NOMENCLATURE

A	elastic coefficient defined in Biot's theory; psf
A	point subscript
AMP	single amplitude of skeleton velocity at a bottom of a uniform elastic deposit undergoing steady oscillatory motion; fps
$\check{A}$	coefficient matrix used in Chapter 6
a_i	constant
B	bulk modulus of the soil skeleton; psf
B	point subscript
$\check{B}$	unit matrix
b_i	constant
C	point subscript
C_b	bulk compressibility of soil skeleton; ft^2/lb
C_c	constrained compressibility of soil skeleton; ft^2/lb
C_w	compressibility of water; ft^2/lb
C_1	parameter in Ramberg-Osgood relationships
c	constant
D	depth of saturated deposit; ft
D	point subscript
$\check{D}$	matrix used in Chapter 6
d	constant
$d_1, d_2, \ldots d_8$	non-zero elements of $\check{D}$
E	point subscript
$\check{E}$	matrix used in Chapter 6
e	void ratio; or the base of natural logarithm
e_{ij}	elements of $\check{E}$

G	tangential shear modulus; psf
G_0	small motion shear modulus, or shear modulus at low strain amplitude; psf
G_s	secant shear modulus; psf
$\overline{G}$	amplitude of $\overline{W}$ when a deposit is in steady, oscillatory motion; fps
g	gravitational acceleration; ft/sec^2
$\overline{H}$	amplitude of W when a deposit is in steady oscillatory motion; fps
i	$\sqrt{-1}$
j	integer subscript
K_0	coefficient of earth pressure at rest
k	permeability of the soil; fps
N	an integer that relates the two time steps Δt and $\overline{\Delta t}$
n	porosity
P	pore water pressure; psf
P^*	excess pore water pressure; psf
$\overline{P}$	$d\overline{H}/dz$
p	point subscript
Q	elastic coefficient defined in Biot's theory; psf
$\overline{Q}$	$d\overline{G}/dz$
R	elastic coefficient defined in Biot's theory; psf
R	parameter in Ramberg-Osgood relationships
R	point subscript
S	point subscript
S	tensile force acting on the portion of the unit area of soil occupied by water; psf

S^*	excess tensile force acting on the portion of the unit area of soil occupied by water; psf
S_0	initial value of S
t	time; seconds
U	velocity of skeleton in x direction; fps
u	displacement field of skeleton in x direction; ft
$\bar{u}$	displacement field of pore water in x direction; ft
V_s	shear wave speed; fps
v	displacement field of skeleton in y direction; ft
$\bar{v}$	displacement field of pore water in y direction; ft
W	velocity of soil skeleton in z direction; fps
WGT	overburden per unit surface area; psf
$\bar{W}$	velocity of pore water relative to the soil skeleton, or the seepage velocity; fps
w	displacement field of skeleton in z direction; ft
$\bar{w}$	displacement of pore water in z direction; ft
x	distance; ft
$\tilde{X}$	a column vector representing the four problem variables σ, S, W and $\bar{W}$
Z	body force per unit mass of water due to the viscous force generated by the flow through pores; ft/sec^2
z	depth; ft
α	parameter in Ramberg-Osgood relationships
α	group of elastic constants; $\alpha = \frac{1}{3}(2G_0 + A)$
α	group of constants

$\alpha_1, \alpha_2, \ldots \alpha_8$	group of constants
β	group of constants
γ	shearing strain
γ_1	shearing strain at strain reversal
$\gamma_{yz}, \gamma_{zx}, \gamma_{xy}$	shearing strain in yz, zx and xy planes
Δt	time step in the pressure wave submodel
$\overline{\Delta t}$	time step in the shear wave submodel
δz	length of elementary volume or control volume; ft
ε	cubic dilatation of soil skeleton
$\overline{\varepsilon}_w$	cubic dilatation of water itself
$\varepsilon_{xx}, \varepsilon_{yy}, \varepsilon_{zz}$	unit volumetric strain of soil skeleton in x, y and z directions
$\overline{\varepsilon}$	cubic dilatation of pore water
$\overline{\varepsilon}_x, \overline{\varepsilon}_y, \overline{\varepsilon}_z$	unit volumetric strain of pore water in x, y, and z directions
η	coefficient used to determine the initial small motion shear modulus
θ	slope of a deposit
$\tilde{\Lambda}$	a diagonal matrix used in Chapter 6
λ	multiplier
$\lambda_1, \lambda_2, \lambda_3, \lambda_4$	the four eigenvalues of $\tilde{A}$ or elements of $\tilde{\Lambda}$, pressure wave speeds; psf
μ	coefficient used to calculate bulk compressibility from small motion shear modulus
ν	Poisson's ratio
ρ	mass density of saturated soil; lb-sec^2/ft
ρ_s	mass density of solid material; lb-sec^2/ft

NOMENCLATURE (CONT'D)

ρ_w	mass density of water; lb-sec^2/ft
σ	total tensile stress in saturated soil; psf
σ_{oct}	octahedral normal tensile stress; psf
$\sigma_{xx}, \sigma_{yy}, \sigma_{zz}$	tensile force acting on the skeleton per unit area of soil in x, y, and z directions respectively; psf
$\bar{\sigma}_0$	effective confining pressure; psf
$\bar{\sigma}_{oct}$	effective octahedral normal tensile stress; psf
$\bar{\sigma}_z$	vertical effective stress; psf
τ	shearing stress; psf
τ_m	shearing strength; psf
τ_1	shearing stress at shearing strain reversal; psf
$\tau_{yz}, \tau_{zx}, \tau_{xy}$	shearing stress in yz, zx and xy plane; psf
ϕ	effective internal angle of friction; degrees or radians
ω	frequency of a steady oscillatory motion of a uniform, linear elastic deposit; radians/sec

CHAPTER 1

INTRODUCTION

When a saturated loose sand is subjected to earthquake vibrations, the pore water pressure increases. One cause of this increase is the compaction of the soil by repeated shearing. The other cause is the dynamic interaction between the pore water and the soil skeleton due to the up-down motion of the bedrock. The increase of the pore water pressure reduces the effective stress in the soil skeleton and hence the shearing strength of the soil is reduced. When the effective stress reduces to zero, the soil has no resistance to shearing and is said to be in a liquid state. The term "liquefaction" refers to the process of changing a saturated granular soil from a solid state to a liquid state as a consequence of increased pore water pressure[77]. Hence liquefaction is regarded as a process instead of a state. Liquefaction is said to be completed at a location when the soil at that location reaches the liquid state.

Liquefaction may cause soils to lose their shearing strength or to undergo excessive lateral displacements, hence liquefaction is hazardous to earth or earth-supported structures. Large scale landslides induced by liquefaction may even result in disasters. Many accounts of distruction have been recorded in the literature[2,19,48,49,63]. These facts necessitate the development of some means to evaluate the susceptibility of saturated soil deposits to liquefaction.

In the past decade, an undrained cyclic load triaxial

or a simple shear test, recommended by Seed, has been used extensively to study the liquefaction potential of saturated sands[61,62,64]. In these tests the soil sample is first consolidated to simulate the static stress condition for a soil element at a certain depth inside a level deposit. At this depth, the time history of the shearing stress induced by earthquake ground motion is converted into an equivalent number of uniform stress cycles. This simulated earthquake loading is then applied to a soil sample around its static equilibrium stress condition to see if it can be liquefied. By repeating the same procedure for various depths the liquefaction potential for the whole deposit can be evaluated.

Although the repeated shearing by an earthquake is very rapid, the soil is not truly in an undrained state. Due to the large bulk modulus of water, a small gradient of the seepage velocity may influence the effective stress to a considerable extent. This is especially true when stratification in permeability exists.

In the triaxial or simple shear test procedure, the time history of the shearing stress induced by earthquake ground motion is obtained without considering the shearing strength reduction by the rise in pore water pressure. Therefore, the interaction between the shearing and the transient effective stress may not be taken into account. It can be said that these test procedures are discrete approaches in that the liquefaction potential is evaluated individually at various depths. The influence of the

the bulk compressibility and the constrained compressibility of the soil.

3. An equation that describes the relationship between time rate of change of the total vertical stress in the soil, the time rate of change of the confined compressional strain in the skeleton, the time rate of pore water pressure change, and the time rate of change of the skeleton's constrained compressibility.

4. An equation describing the pore water pressure variation as a result of pore volume change.

5. The equation of motion of the saturated soil.

6. The equation of motion of the pore water.

7. Relations describing the dependence of the small motion shear modulus and the shear strength upon the effective stress.

The first element describes the propagation of plane shear waves in the deposit. The second element relates the constrained compressibility to the secant shear modulus of the skeleton. Elements 3 to 6 constitute a submodel to describe pressure wave propagation in a saturated deposit in the direction perpendicular to the bedrock. Element 7 provides a means to update the shearing properties of the soil according to the transient effective stress throughout the deposit.

The deposit is divided into a number of equal distance intervals. Within each interval the soil properties are considered to be uniform. Their values are determined by

adjacent soil upon the liquefaction potential at a particular depth is only partially introduced through the determination of the time history of the shearing stress at that depth.

A continuous model for liquefaction in level or nearly horizontal deposits that provides a mutual interaction between shearing deformation and transient pore water pressure will be helpful to increase the understanding of liquefaction and liquefaction induced landslide phenomenon. The concept of compaction due to repeated shearing[69] makes such a model possible.

The liquefaction model, developed in this study, is composed of the following basic elements:

1. A submodel that describes the propagation of plane shear waves in the strain-softening range of a soil when subjected to repeated shearing. A modified Ramberg-Osgood shearing stress-shearing strain relationship is used in this submodel. The small motion shear modulus, i.e., the shear modulus at low shearing strain amplitude, and the shearing strength of the soil are used in the modified Ramberg-Osgood relationship. These two quantities are made to depend upon the effective stress in the soil. The nonlinearity and the damping characteristics of the soil are further described by three more parameters. These parameters are kept constant during shearing.

2. A relationship between the secant shear modulus,

relations designated as element 7 above. When shearing takes place, the shearing stress, shearing strain, and the reduced shear modulus at the end of a time step are computed by the shear wave submodel. The time rate of change of the secant shear modulus and the time varying constrained compressibility of the skeleton over this time step are obtained. These quantites are used via the relationship designated as element 2 above to calculate the transient effective stress, pore water pressure, and the velocities of the skeleton and the pore water. Because the pressure wave velocity is much higher than the shear wave velocity, these computations are performed for several smaller time steps, determined by the first pressure wave speed and the length of the interval. This is necessary in order for the time in the pressure wave submodel to again be compatible with the time in the shear wave submodel. When this is done the small motion shear modulus and the shear strength used in the modified Ramberg-Osgood shearing stress-strain relationship are adjusted according to the current effective stress. This completes one cycle of the computation. The next cycle of computation starts out with the shear wave submodel and updated shearing properties.

When shearing strain reversal takes place in a soil subjected to repeated shearing, there is a sudden increase in the shearing rigidity of the soil. Necessarily, the constrained compressibility of the skeleton decreases instantaneously. Immediately after the shearing strain reversal,

these changes in soil properties are made. Then the computation proceeds according to the sequence described in the previous paragraph until the next shearing strain reversal takes place. The seven basic elements and the coupling described above constitute the model for liquefaction in level or slightly inclined deposits. Detailed development is presented in this report.

The modeling of plane shear wave propagation in soil deposits is reviewed in Chapter 3. The stress-strain relationship of saturated soil, a two phase medium, is formulated in Chapter 4. The governing equations for the propagation of pressure waves are formulated in Chapter 5. An analytical solution for steady oscillatory motions of linear elastic deposits is developed in the same chapter. In Chapter 6, a numerical procedure, based on finite difference and the method of characteristics, is developed. Its accuracy is then checked by employing the analytical solution obtained in Chapter 5. The numerical procedure is used in Chapter 7 to study the motion generated by the weakening of soil skeleton. Chapter 4,5,6 and 7 together present a model for the propagation of pressure waves. The propagation of shear waves and pressure waves are coupled together in Chapter 8 to form the model of liquefaction. The features of the model are demonstrated by examples. The applicability of the model is demonstrated in Chapter 9 by case studies related to the Niigata earthquake of June, 1964.

CHAPTER 2

LITERATURE REVIEW

Early in 1885, Reynolds[53] showed experimentally that sand dilates during shear deformation. Many years later, Casagrande[16] demonstrated the dependence of the soil volume change on the shear deformation and established the fact that when alternating loads are applied to a saturated cohesionless soil under undrained condition, the pore pressure may rise to such a high level that the soil liquefies. Florin and Ivanov[23] subjected deposits of saturated sand twenty centimeters thick to impulsive loadings, and found that loose saturated sand was readily liquefied over the entire depth. For the case of cyclic loading, liquefaction proceeded in layers. The upper layer, with comparatively low confining pressure, liquefied first. Deeper layers liquefied upon further cyclic shearing. The zone of liquefied soil propagated downwards until the whole deposit liquefied. The process of consolidation then took place and moved upwards toward the surface. The initial density and shearing strain in the soil on these tests were presumably relative uniform. However, this trend is correct for non-uniform cases[61].

The disastrous consequences of some recent earthquake induced liquefactions, especially the one caused by the Niigata earthquake of 1964, have drawn the attention of many soil engineers. Seed and Lee[45,46,61] conducted a series

of repeated loading triaxial tests on isotropically consolidated undrained samples. Since then it has been recognized that the susceptibility of a sand to liquefaction is determined by the combined effect of void ratio, confining pressure, cyclic strain amplitude, and the number of stress applications. High void ratio, low confining pressure and large shear strain amplitude are apt to cause liquefaction. Knowing the variation in density with depth and dynamic shearing strain distribution in a deposit, the depth where liquefaction will first occur due to ground vibration can be estimated.

While the triaxial test provides a reasonable approximation to the cyclic stresses in the field, it does not permit a full simulation of the field stress conditions. For many deposits, the soils are subjected to simple shear. By using a simple shear box, Peacock and Seed[51] conducted a series of cyclic loading simple shear tests on saturated sand under undrained conditions. The resistance to liquefaction under simple shear conditions was found to be much less than those under triaxial test conditions. The technique of the simple shear box test was later improved upon by Finn, Pickering and Bransby[22]. In addition to the qualitatively similar results to those of Seed's, Finn et al. indicated the importance of the ratio of the peak cyclic shear stress to the mean initial effective normal stress.

The influence of the initial effective normal stress on liquefaction was also investigated by Seed and Peacock[64]

using both simple shear tests and triaxial tests. They found that in the simple shear tests, the stress required to cause liquefaction increased with the coefficient of earth pressure at rest. In the same study, a correlation between the results obtained by triaxial tests and the simple shear tests was established.

A torsional simple shear device which is able to introduce uniform shear stress and strain throughout the sample has been developed by Ishibashi and Sherif[38]. It was used to examine the effect of the initial coefficient of earth pressure at rest on liquefaction. Their test results indicated that for cyclic loading, if the ratio of maximum change in shear stress to the octahedral normal stress is plotted against the number of stress cycles of liquefaction, the initial value of the coefficient of earth pressure at rest does not influence the liquefaction potential. The authors attributed the difference between their results and those obtained by Seed and Peacock[64] to the fact that the friction stresses along the sides of the simple shear box used by Seed and Peacock increase with increasing horizontal shear stresses. Martin et al.[47] examined the mechanism of progressive pore water pressure increase during undrained cyclic simple shear tests on saturated sands. The volume decrease of the saturated sand was visualized as caused partly by slippage between grain contacts, an irreversible process. They assumed that the volume decrease by slippage in an undrained shearing cycle is the same as that

induced in a drained cycle. By considering the pore pressure increase by the combined effect of volume decrease due to slippage, and volume increase due to unloading of the soil skeleton, a relation between volume reduction during drained cyclic tests and pore water pressure increase in undrained tests was developed. This relation enables one to compute the transient pore water pressure during cyclic loading by use of parameters based on effective stress in the soil. This interesting study has the potential of providing a means for coupling pore water pressure under undrained conditions with the dynamic analysis of a saturated deposit. In the same study, the authors demonstrated the inadequacy of converting a random shearing stress history into an equivalent number of uniform stress cycles for the purpose of computing the transient pore water pressure.

Following Casagrande[31], Castro[17] used the term "liquefaction" for the phenomenon in which loose sand loses its shear strength to such an extent that it flows under a driving force, such as gravitational force in a sloping deposit. He used the term "cyclic mobility" to designate the phenomenon of shearing strain and pore water pressure increase in Seed's consolidated undrained triaxial tests[61]. Castro conducted such tests on isotropically consolidated specimens of dense Ottawa sand and observed the occurence of pore water redistribution. He then concluded that the recorded pore pressures and axial strains during cyclic loading may depend on the development of loosened sand that

forms in a small zone on top of the specimen, hence the ability of a dense sand to sustain cyclic loading may be underestimated. The fact that substantial re-distribution of pore water occurred suggests that under cyclic shearing, the soil may not be in an undrained condition, i.e., pore water may move relative to the soil skeleton.

Based on his previous experimental results, Seed studied the landslides caused by liquefaction during or after earthquakes[63]. The importance of detailed information about the soil properties was emphasized, and a qualitative discussion on the mechanism of landslides was given.

Based on their previous work[62], Seed and Idriss[64] summarized all the factors known to influence liquefaction potential and developed a general method of evaluating this potential. Some comparison of liquefaction potential evaluations with field behavior of soil were also given.

Pyke[52] studied the settlement of a layer of dry soil placed on a shaking table capable of motion in three directions. The results were compared with the settlement or volume change in simple shear test and cyclic triaxial tests. It was shown that the settlement of dry sand under the combined shaking of two horizontal acceleration components are approximately equal to the sum of the settlements caused by the components separately. Vertical accelerations further increase the settlement. Liquefaction characteristics of sands in laboratory tests were evaluated based on the settlement data and a theory suggested by Martin[47]

that accounts for the increase in pore water pressure at constant volume. The effect of shaking in multiple horizontal directions on the shearing stress causing liquefaction in a given number of shearing cycles is to reduce the stress ratio (maximum shearing stress divided by initial effective vertical stress) by 20 percent approximately. Hence, the effect of the second horizontal component on liquefaction is not as great as on the settlement of dry sand. The influence of the vertical acceleration on liquefaction was assumed to be small. No quantitative results however were provided to justify this assumption.

Alba et al.[1] studied the behavior of a range of saturated sands subjected to cyclic loading under undrained conditions by a very large simple shear device. The shear stresses were generated by the inertia of the specimen and a superimposed ballast, as the specimen base was shaken by an actuator. This large simple shear device was designed to obtain a free field zone within the specimen, where the influence of the boundaries would be minimum. Typical pore water pressure transducer records showed that a cyclic pressure variation in addition to that caused by the cyclic stress application was registered at those transducers off the centerline of the specimen. At the centerline of the specimen, this cyclic pore pressure variation was absent. The average specimen shear strains were calculated from the relative displacement between the ballast, the base of the specimen, and the sample height. With regard to the pre-

liquefaction strains, an increase in time rate of strain change was observed when the dynamically induced pore pressure reached a value of about 50 percent of the initial vertical effective stress. Large shear strains that developed after liquefaction was completed were controlled by the dilatant tendency and the relative density of the sand. All test results were plotted in the form of stress ratio (average dynamic shear stress divided by initial vertical effective stress) versus relative density with number of stress cycles to liquefaction as parameter. A favorable comparison between test results and field data was obtained.

Yoshimi and Oh-oka[76] studied the influence of the degree of shear stress reversal on the liquefaction potential of saturated sand. A ring torsion apparatus was fastened to a rotating table. The vertical stress on the specimen was applied by weights. The dynamic shear stress was applied by the inertial torque of the weights when the table was set in torsional vibration. Partially reversed and unreversed tests were performed by imposing shear stress pulses on the initial static shear stress. They found that for partially reversed and unreversed shear tests the shear strain tends to increase in one direction only. For the unreversed test no abrupt change in shear stress is observed even when the pore water pressure reaches a fairly high level. Prior to initial liquefaction, the pore water pressure increment per stress cycle was found to be proportional to the fifth power of the dynamic shear stress. The

proportionality constant depends on the ratio of initial shear stress to initial vertical effective stress.

Due to the difficulties in describing the dynamic soil properties, the analytical and numerical approach to liquefaction lag behind the experimental investigations mentioned above.

One of the earliest investigations devoted to the phenomena of the deformation of saturated soil was by Terzaghi [70]. The soil was assumed to be elastic, and the voids were saturated with water. The settlement of a laterally constrained column of soil under a constant load was investigated. A similar consolidation problem in three dimensions was then studied by Biot[5] from the view point of mathematical physics. In addition to the assumptions that the soil is linearly elastic, homogeneous and isotropic and the strain is small, the existence of a strain energy potential, or the reversibility of soil upon volumetric deformation, was introduced. Apart from the porosity, the number of physical constants necessary to fix the properties of a saturated elastic soil under small strain was shown to be four. The coupling of stresses and strains between the water and the soil skeleton was clearly demonstrated. Biot[6] extended his previous work[5] to the general case of anisotropic material.

After establishing the theory of the deformation of a porous elastic solid containing a compressible fluid, Biot and Willis[8] described the experimental procedures required

to obtain the jacketed compressibility, the unjacketed compressibility, and the coefficient of fluid content. The latter is a measure of the fluid volume entering the pores of a porous sample during an unjacketed compressibility test. These three physical constants together with the shear modulus and the porosity of the medium provide a set of relations so that the four elastic coefficients in the theory of deformation can be determined uniquely. The physical interpretations of these four coefficients in various forms was discussed. A discussion of extending the theory to non-linear media was also included. Fatt[21] used the Biot and Willis' procedure to determine the four elastic coefficients for a sandstone.

In 1956, Biot[7] published a theory for the propagation of stress waves in a porous elastic solid containing a compressible viscous fluid. It was demonstrated that there is one rotational wave and two dilatational waves, denoted as the wave of the first kind and the wave of the second kind. All three waves are transmitted by coupled motions of water and skeleton. For the shear wave, the rotation of the solid is in phase with that of the water. Therefore, a rotation of the solid causes a partial rotational entrainment of the fluid through an inertia coupling. This coupling influences the propagation velocity of the rotational wave. For the dilatational wave of the first kind the inertia coupling between the water and the solid are in phase with each other. While for the wave of the second kind they are out of phase.

The velocity of propagation of the first wave is considerably higher than that of the second wave. The second wave is highly attenuated and the propagation is more like the diffusion process of heat conduction, than that of true waves. Concerning the dissipation of energy due to the viscosity of the fluid, the flow of fluid relative to the solid through the pores was assumed as a Poiseuille flow. The concept of a dissipation function was used and related to the permeability of the soil. The existence of a wave where there is no relative motion between water and solid was conjectured, and a numerical study on the attenuation of all three waves as functions of frequency was presented. Although this work only concerns the steady oscillatory wave propagation in an infinite medium, it is the most important contribution by Biot on this subject.

In 1962, Biot[9] reformulated his theory of the linear mechanics of fluid-saturated porous media in a more systematic manner and the scope was somewhat more general. The generalized Darcy's law was described in detail and the acoustic wave propagation theory was extended to anisotropic media. Viscoelasticity and energy dissipation inside the solid material were discussed. The term viscoelasticity used by Biot encompassed a vast range of possible dissipation processes that could be described by arrangements of dashpots and springs. In a later publication, Biot[10] presented a more refined analysis of the relative motion of the fluid in the pores by introducing the concept of a

viscodynamic operator. Unlike the generalized Darcy's law, the concept of a viscodynamic operator included the dynamic features of the fluid motion in the pores. Various dissipative models which involved intergranular effects, small fluid-filled cracks, relaxation effects due to fluid bulk viscosity were discussed and all these models were translated into specific viscodynamic operators. To the knowledge of the writer, this work is the latest contribution by Biot on the subject of linear acoustic wave propagation in porous dissipative media under zero initial stress conditions.

The influence of initial stress on elastic waves in a continuum was pointed out in 1940 and later emphasized by Biot[4,12]. A theory of deformation of a saturated porous solid under initial stress was presented by Biot[11] in 1963. This theory handles the deformation of a non-linear material by a sequence of incremental deformations. By adding the inertia terms to the equilibrium equations in the theory, the acoustic wave propagation in a saturated porous medium under initial stress can be handled. In 1972, Biot further extended his theory to the finite deformation of porous solids[13].

Other work devoted to the stress-strain relationship, energy dissipation or stress wave propagation of a saturated porous media are summarized in the following few paragraphs.

By assuming the porosity to be constant when both the overall hydrostatic stress and the pore pressure in an

isotropic medium are varied by a same amount, and by using the reciprocal theorem of classical elasticity, Geerstma[24] concluded that only three elastic constants are required for describing pore and rock bulk volume variations if the porosity is explicitly introduced into the theory. A compressibility apparatus was developed which is capable of determining the four elastic coefficients in the Biot's theory. A very similar device was later used by Sawabini[59] to determine the compressibility of unconsolidated oil sands.

Brandt[14] studied the influence of pressure, porosity and liquid saturation on the speed of sound in a porous granular medium. The stress-strain relationship was obtained by using the Hertz theory for the deformation of elastic spheres in contact. The spheres were assumed to be deformable at constant volume. Since the grain shape of sand is not close to a sphere and the number of contacts among grains is hard to estimate, this theory based on spheres in contact may not apply to soil.

Hardin[54] assumed that the shear modulus varied with the one-third power of the effective confining stress and studied the influence of the effective confining stress on the three wave speeds in the Biot's theory. The same theory had also been used by him to study the effects of changes in soil parameters on damping in the saturated soil.

Hall and Richart[34] conducted an experimental study on internal damping of elastic wave energy in granular soils.

Four different materials were used in this investigation and air, water or dilute glycerin were used as a pore fluid. They found that for Ottawa sand, the effect of pore fluid on the internal energy damping depends on the amplitude of vibration. Over the range of amplitudes measured, the water increased the logarithmic decrement by a factor of 1.5 to 4 times that for the dry condition. They observed little difference between the cases where water and dilute glycerin were used as pore fluid.

Hardin and Richart[35] investigated the influence of void ratio and the effective confining pressure on the second pressure wave velocity and the shear wave velocity for round and angular grained sands. They found that both wave velocities for sand varied with approximately 1/4 power of the confining pressure. For a given confining pressure, it was found that the void ratio was the most important variable. The effects of relative density, grain size and gradation entered only through their effects on the void ratio. This work also contained valuable data on the experimentally determined second pressure-wave velocity for different sands, which may be used to estimate the bulk compressibility of the soil under drained conditions; a material property important to the stress wave propagation phenomena.

Ishihara[39] related the four elastic coefficients in the Biot's theory to the compressibilities of the soil bulk, the solid material, and the water. Following Biot's procedures, he derived the frequency equation and studied the

characteristics of the waves. He concluded that the pressure wave of the first kind travels through a saturated medium without causing any change in pore volume, but the pressure wave of the second kind can progress only when change in pore volume takes place. He also concluded that the characteristic frequency of soils is much higher than the frequencies of earthquake vibrations. It is the long wave length associated with the relatively low frequency of shaking that makes the soil deform under undrained condition. This last conclusion is different from the common intutive notion that the undrained condition is caused by very rapid straining.

Based upon the compressibilities of water, solid material, and the skeketon, Ishihara[40] calculated the elastic coefficients in Biot's theory. By examing the magnitudes of these coefficients, the equations that govern the motions of the soil and the water were simplified. He then demonstrated that the simplified equations were of the same form as those developed from elastic theory, and the theory of elasticity could be used to treat "poroelasticity". He then related Young's modulus and Poisson's ratio in the equivalent theory to the material properties of saturated porous medium. Based on the simplified equations he concluded that for earthquakes or artificial vibrations, the soil is loaded under undrained condition. However, the experimental results by Hardin and Richart[35], and by Hall[34], indicated that the apparent mass originating from

the relative motion between the soil skeleton and the water is about 30 to 40 percent of the water mass per unit volume of the soil. It should be noted that these two works by Ishihara only concern wave motions in soils without the presence of boundaries.

Following the same procedure as Biot and Ishihara, Bazant and Krizek[3] expressed the three elastic constants P, Q, and R in Biot's paper in terms of compressibilities of the soil skeleton. Compressibility of solid particles was then demonstrated to be unimportant, and can be neglected for practical problems. An inelastic incremental skeletal strain was incorporated in the stress-strain relationship to describe the nonlinear inelastic behavior of soils. A simple proportionality between the incremental non-elastic skeletal strain and the corresponding pore water pressure rise under undrained conditions was established. The proportional constant was called the densification compliance. Its value was shown to be close to the bulk compressibility of the soil skeleton at the stress level under consideration.

Richart[55] found that based on Ishihara's simplified equations and for low frequency wave propagations, the first pressure-wave velocity is within 1 to 2 percent of the value found from the "Wood Equation" for wave velocity of a mixture of solid particles in water. Therefore, it seems that the stiffness of the soil skeleton is overshadowed by the presence of the pore water. The question of small amounts of air in the pore water upon the wave motion was also

raised.

Ghaboussi[25], Ghaboussi and Wilson[26,27] developed a variational principle by using Biot's theory. This principle incorporated with the finite element method was used to evaluate the pore water pressure and force on soil skeleton in an earthdam-reservoir system. Presently, they have included non-linear material properties in the model in order to evaluate the liquefaction potential[28].

Streeter, Wylie and Richart[68] used the method of characteristics to evaluate the liquefaction potential in a level deposit and in an earth dam. Although the compressional stress-strain in soil skeleton was not considered, the importance of the change in porosity upon liquefaction was indicated. Richart[56] further demonstrated in his Terzaghi lecture that the Ramberg-Osgood shearing stress-strain relationship used in the method of characteristics is realistic.

By using the Biot theory[7], Papadakis[50] studied the plane pressure wave propagation in a horizontal saturated deposit composed of elastic soil. The motion was caused by the vertical movement of the underlying bedrock. He obtained an analytical solution for the steady oscillatory motion of the deposit. Case studies based on this solution lead to the conclusion that "for soils having a very large permeability value, the solid and fluid constituents tend to move together". Since the relative motion between solid and fluid should be larger when the soil is more permeable,

the validity of the analytical solution is doubtful. In the same study, Papadakis neglected the apparent mass terms in the equation of motion for the solid and for the water and hence was able to transform the four governing equations into two pairs of characteristic equations. The motion of saturated deposits subjected to random normal bedrock motions were studied numerically. In his discussion on the pressure wave propagation in relation to liquefaction, he suggested the use of a Ramberg-Osgood type of shearing stress-shearing strain relationship.

The modern theory of mixture was originated by Truesdell and Toupin[72] and later developed by Green and Naghdi[32]. The medium is visualized as if every point in space were occupied by one partical of each constituent of the mixture. According to Ghaboussi[25], this theory is equivalent to Biot's theory when the deformations are infinitely small.

Becker[87] modified the theory of Green and Naghdi[32]. She then used the modified theory to study the behavior of saturated sands in small strain range. Through a nonlinear constitutive equation, normal stress variations due to shear loads was included. In this theory the soil was assumed to be elastic and no compaction or settlement was considered.

By assuming the fluid to be incompressible, Hsieh and Yew[37] employed the concept of the mixture theory to study wave propagation in saturated porous media. The existence of two pressure waves and a shear wave was demonstrated and a numerical study on the frequency equation was given.

CHAPTER 3

SHEAR WAVE TRANSMISSION IN SATURATED SOIL DEPOSITS

The response of dry soil deposits subjected to ground shaking has been studied by the method of characteristics, incorporated with the Ramberg-Osgood shearing stress-strain relationship.[68] The response of saturated soil deposits is different from that of dry deposits in that the effective stress depends on the shearing strain history. However, since the pore water cannot sustain shearing stress and since there is no horizontal relative motion between the pore water and the soil skeleton, the method of characteristics for dry deposits can be applied to the shearing of saturated deposits.

The method of characteristics for shear wave transmission in soil deposits is reviewed in this chapter. This constitutes the shear wave submodel, which is a component of the model for liquefaction.

3-1. Shearing stress-shearing strain relationship

The non-linear shearing stress-strain relationship for soil in the strain softening range can be described by the Ramberg-Osgood relationship defined as follows

for initial loading,

$$\gamma = \frac{\tau}{G_0}\left(1 + \alpha \left| \frac{\tau}{C_1 \tau_m} \right|^{R-1}\right), \tag{3-1}$$

for unloading and reloading,

$$\gamma - \gamma_1 = \frac{\tau - \tau_1}{G_0}\left(1 + \alpha \left| \frac{\tau - \tau_1}{2C_1 \tau_m} \right|^{R-1}\right). \tag{3-2}$$

where G_0 is a small motion shear modulus, γ is shearing strain, τ denotes shearing stress, τ_m is shearing strength, τ_1 and γ_1 represent the coordinate of the most recent strain reversal point on the stress-strain plot. R, α, and C_1 are parameters and their values are constant for a given soil.

The derivative of τ with respect to γ, obtained from Equation (3-1) or Equation (3-2) gives the tangential shear modulus at a given stress level. Letting G be the tangential shear modulus, one can write

$$\Delta\tau = G\ \Delta\gamma$$

in which Δ denotes an incremental change in the quantity under consideration. Dividing both sides by Δt, a time increment, one has

$$\frac{\Delta\tau}{\Delta t} = G\ \frac{\Delta\gamma}{\Delta t}\ .$$

Since the time rate of change in shearing strain is identical with the rate of change of the x-component of the soil speed in the z direction, Figure 3-1, one can write

$$\frac{\partial\tau}{\partial t} = G\ \frac{\partial U}{\partial z} \qquad (3\text{-}3)$$

in which U is the velocity of the soil skeleton in the x direction.

3-2. Equation of motion in x direction for saturated soils

Consider Figure 3-1, the equation of motion can be

written as

$$\frac{\partial \tau}{\partial z} - \rho \frac{\partial U}{\partial t} - \rho g \sin \theta = 0 \qquad (3\text{-}4)$$

in which g is the acceleration of gravitation, θ is the slope of the deposit, and ρ is the mass density of the saturated soil. Knowing the mass density of water ρ_w, the mass density of solid particles ρ_s, and the porosity n, the soil mass density ρ can be calculated as

$$\rho = n \rho_w + (1 - n) \rho_s. \qquad (3\text{-}5)$$

3-3. The characteristic equations

Equation (3-3) and Equation (3-4) form a system of hyperbolic equations and hence can be transformed into the characteristics form that facilitates numerical solutions.

Letting λ be an unknown multiplier, one can combine Equation (3-3) and Equation (3-4) linearly as follows

$$\frac{\partial \tau}{\partial z} - \rho \frac{\partial U}{\partial t} - \rho g \sin \theta + \lambda \left(\frac{\partial \tau}{\partial t} - G \frac{\partial U}{\partial z}\right) = 0,$$

or

$$\lambda \left(\frac{\partial \tau}{\partial t} + \frac{1}{\lambda} \frac{\partial \tau}{\partial z}\right) - \rho \left(\frac{\partial U}{\partial t} + \frac{\lambda G}{\rho} \frac{\partial U}{\partial z}\right) - \rho g \sin \theta = 0. \qquad (3\text{-}6)$$

If one sets

$$\frac{dz}{dt} = \frac{1}{\lambda} = \frac{\lambda G}{\rho} \qquad (3\text{-}7)$$

then all the derivatives in Equation (3-6) are carried out in a common direction designated by $\frac{dz}{dt}$ in the z-t plane.

The values of λ can be obtained from Equation (3-7) as

$$\lambda = \pm\sqrt{\frac{\rho}{G}}$$

whence

$$\frac{dz}{dt} = \pm\sqrt{\frac{G}{\rho}} = \pm V_s \tag{3-8}$$

in which V_s denotes the shear wave speed.

The two characteristic equations, designated as C^+ and C^- equations, are

$$C^+ \begin{cases} \frac{1}{\sqrt{\rho G}} \frac{d\tau}{dt} - \frac{dU}{dt} - g \sin\theta = 0 \\ \frac{dz}{dt} = V_s \ , \end{cases} \tag{3-9}$$

$$C^- \begin{cases} \frac{1}{\sqrt{\rho G}} \frac{d\tau}{dt} + \frac{dU}{dt} + g \sin\theta = 0 \\ \frac{dz}{dt} = -V_s \ . \end{cases} \tag{3-10}$$

3-4. Finite difference approximation

The numerical solution of the C^+ and C^- characteristic equations is visualized on the z-t diagram shown in Figure 3-2. The deposit is divided into a number of equal distance intervals of length Δz. The material properties in each reach are considered to be uniform. A time step common to all intervals is used. The point R is located in such a way that the segment RP represents the C^+ characteristic direction in interval AC at time t. Similarly, point S is located such that the segment SP represents the C^- characteristic

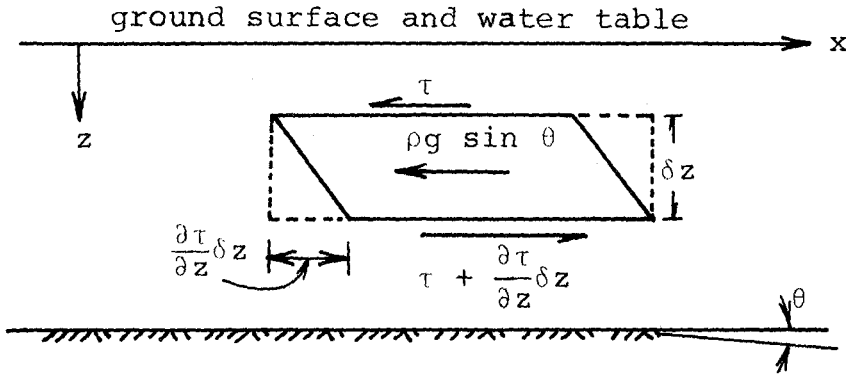

Figure 3-1 Soil element subjected to simple shear

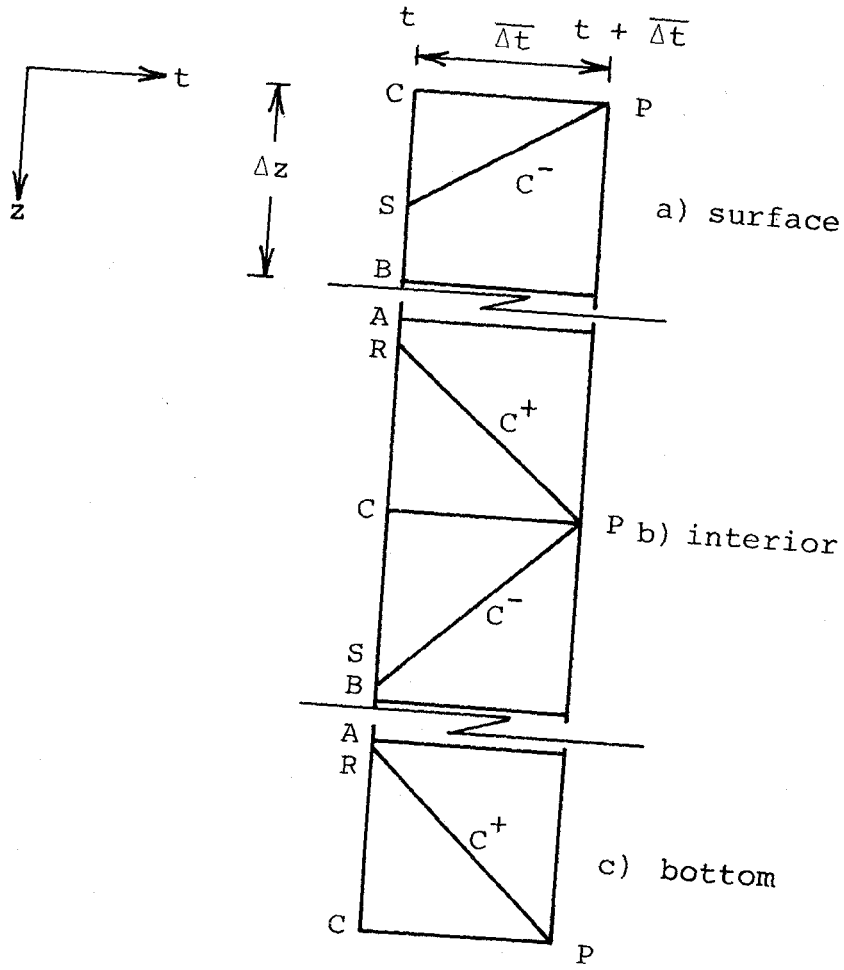

Figure 3-2 x-t diagram for numerical solutions of shear wave propagation

direction in interval CB at the same instant. Conditions at point R and S must be evaluated from known conditions at points A, B and C before the unknowns at point P can be found. Linear interpolation is used for this purpose. At R

$$U_R = U_C - \frac{\overline{\Delta t}}{\Delta z} V_{S_R} (U_C - U_A), \tag{3-11}$$

$$\tau_R = \tau_C - \frac{\overline{\Delta t}}{\Delta z} V_{S_R} (\tau_C - \tau_A), \tag{3-12}$$

and at S

$$U_S = U_C - \frac{\overline{\Delta t}}{\Delta z} V_{S_S} (U_C - U_B), \tag{3-13}$$

$$\tau_S = \tau_C - \frac{\overline{\Delta t}}{\Delta z} V_{S_S} (\tau_C - \tau_B), \tag{3-14}$$

where V_{S_R} and V_{S_S} are the shear wave speeds in interval AC and CB respectively. $\overline{\Delta t}$ is a specified time step. $\overline{\Delta t}$ and Δz are chosen in such a manner that the Courant condition for stability is satisfied.

The C^+ characteristic equation can be approximated as

$$\left(\frac{1}{\sqrt{\rho G}}\right)_R \frac{\tau_p - \tau_R}{\overline{\Delta t}} - \frac{U_p - U_R}{\overline{\Delta t}} - g \sin \theta' = 0, \tag{3-15}$$

and the C^- characteristic equation is approximated as

$$\left(\frac{1}{\sqrt{\rho G}}\right)_S \frac{\tau_p - \tau_S}{\overline{\Delta t}} + \frac{U_p - U_S}{\overline{\Delta t}} + g \sin \theta = 0. \tag{3-16}$$

At every interior point, the two unknowns τ_p and U_p can be solved uniquely from Equation (3-15) and Equation (3-16).

In the context of liquefaction, two types of surface boundary conditions are of importance. The first case is where the water table is at the ground surface. In this case the shearing stress at the surface of the deposit is zero. The surface horizontal velocity can be solved readily from the C^- characteristic equation rising from the interior of the deposit, Figure 3-2a. The boundary condition of the second type is where the water table is below the ground surface. The upper boundary of the deposit is considered at the water table instead of at the ground surface. The layer of dry soil above the water table is approximated by a rigid slab, having the same amount of mass as that of the unsaturated soil. The equation of motion for the slab in the x direction provides one relationship between τ_p and U_p at the water table. Referring to Figure 3-2a, this relation can be expressed as

$$-WGT \sin \theta + .5 (\tau_p + \tau_C) = \frac{WGT}{g} \frac{U_p - U_C}{\overline{\Delta t}} \qquad (3\text{-}17)$$

in which WGT is the weight of the layer of unsaturated soil per unit surface area. The second relationship is the C^- characteristic equation. τ_p and U_p at the water table can be solved using these two relations.

When the distance between the ground surface and the water table is large, the rigid slab approximation is poor and the propagation of the shear wave inside the unsaturated soil should be considered.

At the lower boundary, the velocity U_p is the same as

that of the bedrock, a prescribed quantity. The shear stress τ_p at the bedrock can be solved from the C^+ characteristic equation, as shown in Figure 3-2c.

After τ_p and U_p are solved at every node at the instant $t + \overline{\Delta t}$, a new shear modulus for each distance interval is computed from Equation (3-1) or Equation (3-2) on the basis of the average shear stress in that interval. The same procedure is repeated for obtaining the solution at the next time step.

3-5. Accuracy

Numerical errors associated with the computation procedure can be attributed to two sources, i.e., discretization and interpolation. Error due to discretization can be reduced by reducing the time step and meanwhile keep the Courant condition satisfied. Error due to interpolation for a given space-time grid was investigated numerically by Wylie and Streeter[85]. A 50 foot deposit was used. It was divided into 7 distance intervals for numerical solution. It was shown that when a tangential shear modulus was lowered to 1/6 of its original small motion value, the resulted error was about 5 percent. This estimation of interpolation error was based on the method of characteristics grid, in which interpolations were used only once every 10 time steps.

In the following chapters, except otherwise stated, the amount of discretization and interpolation used fall into the range where the accuracy of the numerical procedure was studied by Wylie and Streeter.

CHAPTER 4

STRESS-STRAIN RELATIONSHIPS FOR SATURATED SANDS

The distribution of stress between the granular soil skeleton and the pore water in a saturated soil plays an important role in liquefaction study. The stress-strain relationship for saturated soil subjected to confined compression is considered. A constrained compressibility of the skeleton appears in the formulation. Its magnitude is related to the bulk compressibility and the secant shear modulus of the soil skeleton through a linear elastic theory suggested by Biot.[7] The use of the formulated relations to portray the irreversible volumetric deformation due to shearing is explained. In this study, the soil grains are assumed to be incompressible.

4-1. Stress-strain relationships for the two phases of a saturated soil subjected to confined compression.

Let n be the porosity of the soil, defined as the ratio of pore volume to total volume of a soil element. When the soil is homogeneous, n equals the ratio of pore area to total area of a cross section. Let w and $\bar{w}$ be the displacement field of the skeleton and of the pore water in z direction. w and $\bar{w}$ are defined in such a way that the volume of solid and water passing through a unit area, fixed in space, are (1 - n) w and $n\bar{w}$ respectively. Both w and $\bar{w}$ are functions of the coordinate z and time t. The initial value of w and $\bar{w}$ are denoted by w_0 and $\bar{w}_0$ respectively.

Consider the elementary volume shown in Figure 4-1. The increase in the volume of solid material above its initial value is

$$-\frac{\partial (1-n)(w-w_0)}{\partial z}\,\delta z =$$

$$\left[-(1-n)\frac{\partial (w-w_0)}{\partial z} + (w-w_0)\frac{\partial n}{\partial z}\right]\delta z,$$

and the increase in the volume of water above its initial value is

$$-\frac{\partial\, n(\bar{w}-\bar{w}_0)}{\partial z}\,\delta z =$$

$$\left[-n\frac{\partial (\bar{w}-\bar{w}_0)}{\partial z} - (\bar{w}-\bar{w}_0)\frac{\partial n}{\partial z}\right]\delta z.$$

The decrease in the volume of water that originally occupied the void space in the elementary volume is the summation of the above two quantities

$$\left\{-\left[(1-n)\frac{\partial (w-w_0)}{\partial z} + n\frac{\partial (\bar{w}-\bar{w}_0)}{\partial z}\right]\right.$$

$$\left.-(\bar{w}-\bar{w}_0 - w + w_0)\frac{\partial n}{\partial z}\right\}\delta z.$$

In the above expression, the last term is a product of two small quantities and can be neglected. By the definition of the compressibility of water, C_w, one can write

$$\frac{1}{C_w} = -\frac{P^*}{\dfrac{(1-n)\dfrac{\partial (w-w_0)}{\partial z} + n\dfrac{\partial (\bar{w}-\bar{w}_0)}{\partial z}}{n}},$$

or

$$\frac{1}{C_w} = \frac{-n\,P^*}{(1-n)\dfrac{\partial(w - w_0)}{\partial z} + n\,\dfrac{\partial(\bar{w} - \bar{w}_0)}{\partial z}} \tag{4-1}$$

in which P* is the excess pore water pressure. The quantity -n P* represents the excess tensile force acting on the portion of the unit area of soil occupied by water. Denote this quantity by S*, then

$$S^* = -n\,P^*. \tag{4-2}$$

In terms of S*, Equation (4-1) can be written as

$$S^* = \frac{(1-n)}{C_w}\,\frac{\partial(w - w_0)}{\partial z} + \frac{n}{C_w}\,\frac{\partial(\bar{w} - \bar{w}_0)}{\partial z} \quad .$$

Let S_0 be the initial hydrostatic value of the tensile force acting on the portion of the unit area of soil occupied by water, and S be the current value of the same quantity, then

$$S = S^* + S_0 \ ,$$

or

$$S = \frac{(1-n)}{C_w}\,\frac{\partial(w - w_0)}{\partial z} + \frac{n}{C_w}\,\frac{\partial(\bar{w} - \bar{w}_0)}{\partial z} + S_0 \ . \tag{4-3}$$

Next, consider the strain in the soil skeleton when in a drained state. No stress in the pore water can be developed although the pores undergo straining. The tensile force acting on the skeleton per unit area of soil is also

the effective tensile stress, $-\bar{\sigma}_z$, while $\bar{\sigma}_z$ denotes the vertical effective stress. Consider a mass of soil with a volume δz before straining, Figure 4-2. After straining, the strain level in the skeleton can be represented by

$$\frac{1}{\delta z}\left[\left(w + \frac{\partial w}{\partial z}\,\delta z\right) - w\right] = \frac{\partial w}{\partial z} .$$

The stress-strain relation for the skeleton is then written as

$$-\bar{\sigma}_z = \frac{1}{C_c}\frac{\partial w}{\partial z} \tag{4-4}$$

in which C_c is the constrained compressibility of the soil skeleton. $\frac{1}{C_c}$ is known as the secant constrained modulus.

The total tensile stress, σ, is the sum of the tensile effective stress and the tensile pore water pressure, i.e.,

$$\sigma = -\bar{\sigma}_z + \frac{S}{n} ,$$

or

$$\sigma = \left(\frac{1}{C_c} + \frac{1}{nC_w}\right)\frac{\partial w}{\partial z} + \frac{1}{C_w}\frac{\partial(\bar{w} - w)}{\partial z}$$

$$- \frac{1}{nC_w}\frac{\partial w_0}{\partial z} - \frac{1}{C_w}\frac{\partial(\bar{w}_0 - w_0)}{\partial z} + \frac{S_0}{n} . \tag{4-5}$$

4-2. The dependence of the constrained modulus of the skeleton upon its secant shear modulus.

As in an elastic solid, constrained compression of a porous material involves both shearing strain and volumetric

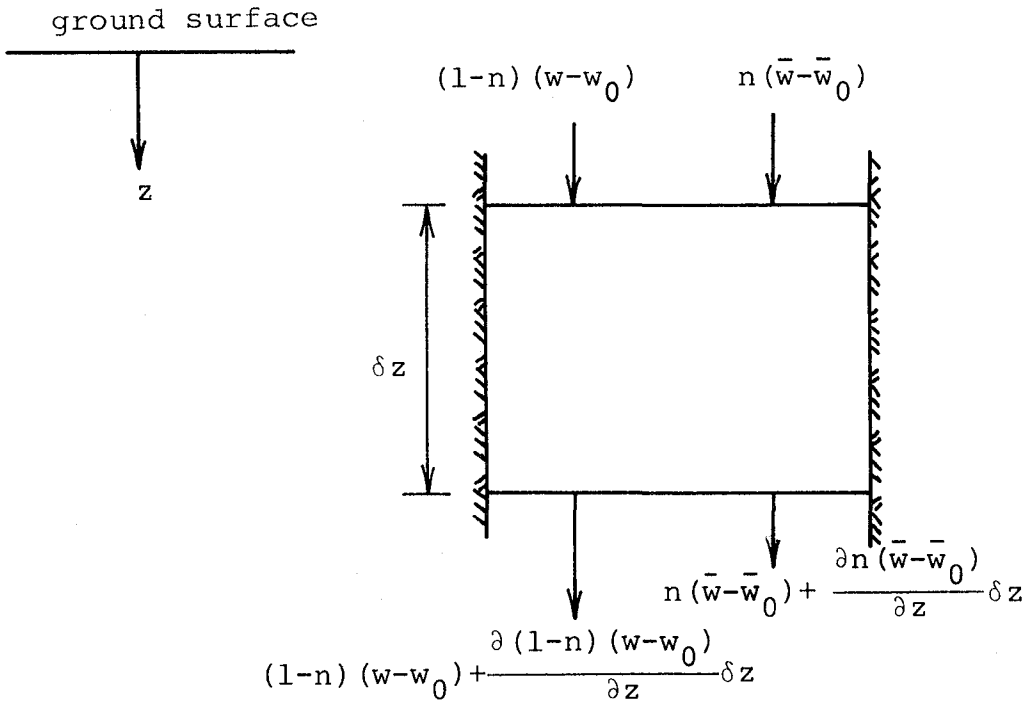

Figure 4-1 Void volume change in a control volume when in confined compression

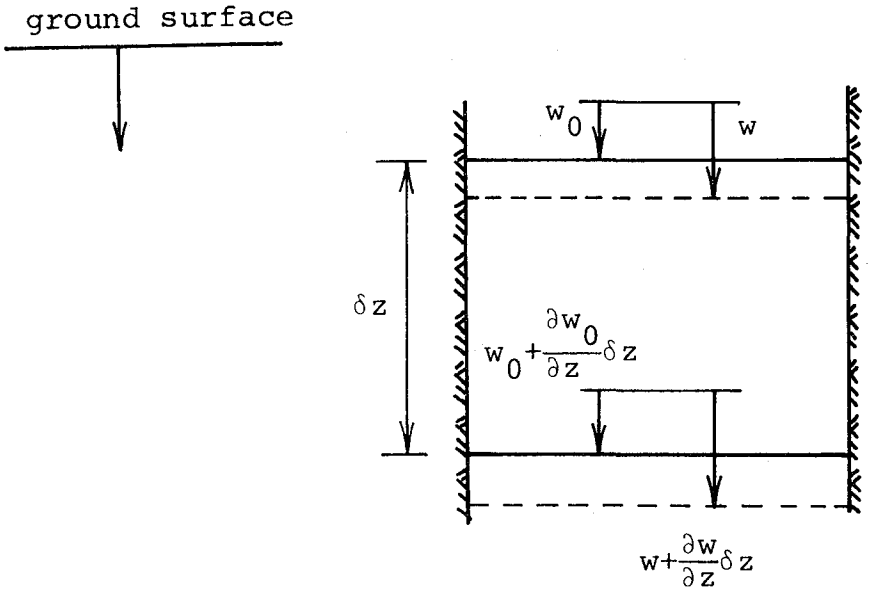

Figure 4-2 Constrained volumetric deformation of an elementary mass of the soil skeleton

strain. So the ability of a porous material to sustain constrained compression under drained conditions depends on its shear modulus. The corresponding behavior of real soil is more complicated. Nevertheless it is reasonable to expect that soil behaves in a similar fashion. In the following, the relation among the constrained compressibility, the bulk compressibility and the secant shear modulus of an isotropic linear elastic porous medium composed of incompressible solid material with zero initial stress is developed. This relation is assumed to hold for soils.

Consider an elementary cube of soil with its sides parallel to the coordinate axes x-y-z. This cube is considered to be large enough compared to the size of the pores so that it can be treated as homogeneous, and at the same time small enough such that it can be regarded as a "point" in a microscopic sense. The average displacement components of the soil skeleton in x, y, and z directions are denoted by u, v, and w, and those of the pore water by $\bar{u}$, $\bar{v}$, and $\bar{w}$. The strain components of the skeleton are

$$\varepsilon_{xx} = \frac{\partial u}{\partial x} , \quad \gamma_{xy} = \frac{\partial u}{\partial y} + \frac{\partial v}{\partial x} \quad \text{etc.},$$

and

$$\bar{\varepsilon}_x = \frac{\partial \bar{u}}{\partial x} , \quad \bar{\varepsilon}_y = \frac{\partial \bar{v}}{\partial y} , \quad \bar{\varepsilon}_z = \frac{\partial \bar{w}}{\partial z} .$$

The cubic dilatation of the soil skeleton, ε, is

$$\varepsilon = \varepsilon_{xx} + \varepsilon_{yy} + \varepsilon_{zz} . \qquad (4\text{-}6)$$

This quantity also represents the cubic dilatation of the soil bulk. The cubic dilatation of pore water, $\bar{\varepsilon}$, is

$$\bar{\varepsilon} = \bar{\varepsilon}_x + \bar{\varepsilon}_y + \bar{\varepsilon}_z \quad .$$

There are two sources that give rise to the dilatation of pore water. The first is the compressibility of water itself. The second is the pore volume change when the skeleton is deformed. This can be made clear by considering a unit cube of soil shown in Figure 4-3. The volume displaced by water and solid in the z direction can be written as

$$- [(1-n)\ \varepsilon_{zz} + n\ \bar{\varepsilon}_z] \ .$$

Similarly, the volumes displaced by water and solid in the other two directions are, respectively,

$$- [(1-n)\ \varepsilon_{xx} + n\ \bar{\varepsilon}_x] \text{ and } - [(1-n)\ \varepsilon_{yy} + n\ \bar{\varepsilon}_y].$$

Thus the total volume decrease due to the displacements is

$$- [(1-n)\ (\varepsilon_{xx} + \varepsilon_{yy} + \varepsilon_{zz}) + n\ (\bar{\varepsilon}_x + \bar{\varepsilon}_y + \bar{\varepsilon}_z)],$$

or

$$- [(1-n)\ \varepsilon + n\ \bar{\varepsilon}].$$

Since no gap between solid and water can be developed, the above quantity must equal the volume decrease caused by the dilation in pore water itself. Hence one can write

$$n\ \bar{\varepsilon}_w = (1-n)\ \varepsilon + n\ \bar{\varepsilon} \qquad (4-7)$$

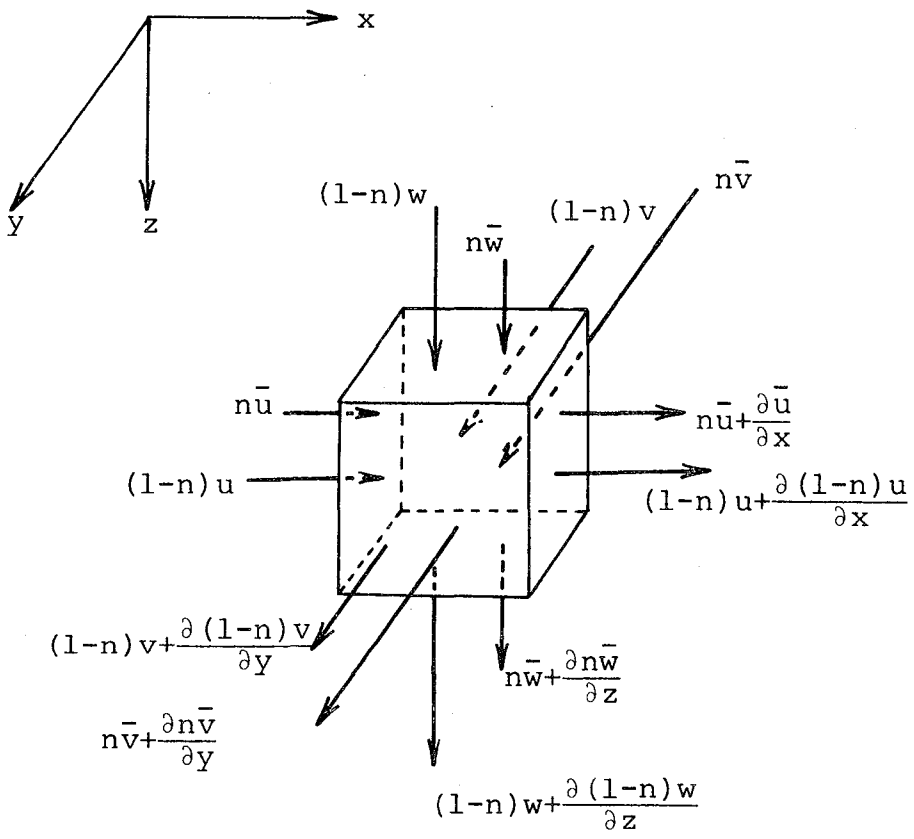

Figure 4-3 Void volume change in a unit cube of a control volume

in which $\bar{\varepsilon}_w$ is the dilation in water. It is related to the change in the mass density of water by

$$\bar{\varepsilon}_w = - \frac{d\rho_w}{\rho_w} \quad .$$

Rearranging Equation (4-7), one obtains,

$$\bar{\varepsilon} = \bar{\varepsilon}_w - \frac{(1-n)}{n} \varepsilon \quad . \tag{4-8}$$

It is seen that $\bar{\varepsilon}$ is composed of two parts, i.e., dilation in water itself and pore volume change.

The general stress-strain relationship for an isotropic, linear elastic porous medium was obtained by Biot.[7] The existence of a strain energy potential was assumed. The result is listed in the following

$$\sigma_{xx} = 2G_0 \varepsilon_{xx} + A \varepsilon + Q \bar{\varepsilon} \tag{4-9}$$

$$\sigma_{yy} = 2G_0 \varepsilon_{yy} + A \varepsilon + Q \bar{\varepsilon} \tag{4-10}$$

$$\sigma_{zz} = 2G_0 \varepsilon_{zz} + A \varepsilon + Q \bar{\varepsilon} \tag{4-11}$$

$$\tau_{yz} = G_0 \gamma_{yz} \tag{4-12}$$

$$\tau_{zx} = G_0 \gamma_{zx} \tag{4-13}$$

$$\tau_{xy} = G_0 \gamma_{xy} \tag{4-14}$$

$$S = Q \varepsilon + R \bar{\varepsilon} \tag{4-15}$$

In the above, σ_{xx} denotes the x component of the tensile force acting on the skeleton per unit area of soil. σ_{yy} and σ_{zz} are similar quantities in the y and z directions. τ_{yz}, τ_{zx}, and τ_{xy} are shear stresses acting on the surfaces of a soil element with normals in the x, y, z directions respectively. γ_{yz}, γ_{zx}, and γ_{xy} denote corresponding shear strains. τ_{xy} and γ_{xy} are synonymous to τ and γ used in Chapter 3. G_0 denotes small motion shear modulus. A, Q, and R are elastic coefficients to be determined by experiment.[8]

The octahedral normal tensile stress, σ_{oct}, is obtained by adding Equations (4-9) through (4-11)

$$\sigma_{oct} = \frac{1}{3} (\sigma_{xx} + \sigma_{yy} + \sigma_{zz})$$

$$= \frac{1}{3} (2G_0 + 3A) \varepsilon + Q \bar{\varepsilon} , \qquad (4\text{-}16)$$

or

$$\sigma_{oct} = \alpha \varepsilon + Q \bar{\varepsilon} \qquad (4\text{-}17)$$

where

$$\alpha = \frac{1}{3} (2G_0 + 3A). \qquad (4\text{-}18)$$

From Equations (4-15) and (4-17) one can write

$$\varepsilon = \frac{R \sigma_{oct} - QS}{R \alpha - Q^2} , \qquad (4\text{-}19)$$

and

$$\bar{\varepsilon} = - \frac{Q \sigma_{oct} - \alpha S}{R \alpha - Q^2} . \qquad (4\text{-}20)$$

Since the volumetric behavior of soil depends on the effective stress, it is desirable to replace σ_{oct} by its effective counterpart, $\bar{\sigma}_{oct}$. By definition

$$\bar{\sigma}_{oct} = (\sigma_{oct} + S) + P$$

in which $\sigma_{oct} + S$ represents the total tensile stress and P is the pore water pressure. S is related to P by an equation similar to Equation (4-2). Hence, one obtains

$$\sigma_{oct} = \bar{\sigma}_{oct} + (n-1)P \ . \qquad (4\text{-}21)$$

Substituting Equation (4-21) into Equations (4-19) and (4-20), one obtains the following

$$\varepsilon = \frac{R\,\bar{\sigma}_{oct} + [R(n-1) + Qn]P}{R\,\alpha - Q^2} \ , \qquad (4\text{-}22)$$

and

$$\bar{\varepsilon} = -\frac{Q\,\bar{\sigma}_{oct} + [Q(n-1) + \alpha\, n]P}{R\,\alpha - Q^2} \qquad (4\text{-}23)$$

Now consider a drained compression test where P is kept zero and hence no dilation in water itself can be developed. Under this condition Equation (4-8) yields

$$\bar{\varepsilon} = -\frac{(1-n)}{n}\,\varepsilon \qquad (4\text{-}24)$$

From Equations (4-22), (4-23), and (4-24), and with the condition that P = 0, one obtains

$$\varepsilon = \frac{R\,\bar{\sigma}_{oct}}{R\,\alpha - Q^2} \ , \qquad (4\text{-}25)$$

and

$$\frac{1-n}{n}\,\varepsilon = \frac{R\,\bar{\sigma}_{oct}}{R\,\alpha - Q^2} \quad , \tag{4-26}$$

whence

$$R = \frac{n}{1-n}\,Q. \tag{4-27}$$

Note that Equation (4-25) indicates that the dilatation of the soil skeleton is proportional to $\bar{\sigma}_{oct}$, the proportionality constant must be the bulk compressibility, C_b. Therefore, by definition, one can write

$$C_b = \frac{R}{R\,\alpha - Q^2} \quad . \tag{4-28}$$

Now, imagine a cube of soil being immersed in water inside a container and then the whole container being pressurized. The water pressure increases in all the pores evenly. Hence no effective stress is generated. Consequently, no strain can be developed in the skeleton. At the same time, the pore water itself is compressed with the pore volume unchanged. Under this condition, Equation (4-8) reduces to

$$\bar{\varepsilon} = \bar{\varepsilon}_w \quad . \tag{4-29}$$

Substituting Equation (4-29) into Equation (4-23) with $\bar{\sigma}_{oct}$ being zero, one obtains

$$\bar{\varepsilon}_w = -\frac{Q\,(n-1) + \alpha\,n}{R\,\alpha - Q^2}\,P \quad . \tag{4-30}$$

Equation (4-30) indicates that the pore water pressure is proportional to the dilatation in water itself. By the definition of the compressibility of water, one can write

$$C_w = \frac{Q\ (n-1) + \alpha\ n}{R\ \alpha - Q^2} \ . \tag{4-31}$$

From Equations (4-27), (4-28) and (4-31) one can solve for Q, R and α. The result is

$$Q = \frac{1-n}{C_w} \ , \tag{4-32}$$

$$R = \frac{n}{C_w} \ , \tag{4-33}$$

$$\alpha = \frac{1}{C_b} + \frac{(1-n)^2}{n\ C_w} \ . \tag{4-34}$$

From Equation (4-18) and Equation (4-34), the elastic coefficient A is obtained as

$$A = -\frac{2}{3} G_0 + \frac{1}{C_b} + \frac{(1-n)^2}{n\ C_w} \ , \tag{4-35}$$

in which C_w is a known property of water, n can be determined by standard procedures, and C_b can be determined by a triaxial test or calculated from known second pressure wave and shear wave speeds in a deposit. Thus the values of A, Q and R can be calculated for a given soil.

For constrained compression in the z direction, no displacement in either the x or y directions can take place. Hence, $\varepsilon = \varepsilon_{zz}$ and $\bar{\varepsilon} = \bar{\varepsilon}_z$, so Equation (4-11) becomes

$$\sigma_{zz} = (2G_0 + A)\ \varepsilon_{zz} + Q\ \bar{\varepsilon}_z \ ,$$

or

$$\sigma_{zz} = [\frac{4}{3} G_0 + \frac{1}{C_b} + \frac{(1-n)^2}{n C_w}] \varepsilon_{zz} + \frac{1-n}{C_w} \bar{\varepsilon}_z . \quad (4-36)$$

Similarly, Equation (4-15) reduces to

$$S = \frac{(1-n)}{C_w} \varepsilon_{zz} + \frac{n}{C_w} \bar{\varepsilon}_z . \quad (4-37)$$

In order to obtain the constrained modulus for the soil skeleton, one needs to consider a drained condition where $S = 0$. Thus, from Equation (4-37),

$$\bar{\varepsilon}_z = \frac{n-1}{n} \varepsilon_{zz} .$$

Substituting this relation into Equation (4-36), and noting that now σ_{zz} is the effective tensile stress, $-\bar{\sigma}_z$. Thus for $S = 0$, one can write

$$-\bar{\sigma}_z = (\frac{4}{3} G_0 + \frac{1}{C_b}) \varepsilon_{zz} . \quad (4-38)$$

From Equation (4-4) and Equation (4-38), one obtains

$$\frac{1}{C_c} = \frac{4}{3} G_0 + \frac{1}{C_b} . \quad (4-39)$$

It is noted that in the linear theory of elasticity of solid materials the same relation among the shear modulus, bulk compressibility and constrained compressibility holds. In a slightly different manner, Ishihara[39] has obtained Equation (4-39) for an isotropic, linear elastic porous medium composed of a compressible solid.

It is assumed that a relation similar to Equation (4-39)

holds for soils when subjected to simple shear, i.e.,

$$\frac{1}{C_c} = \frac{4}{3} G_s + \frac{1}{C_b} \qquad (4\text{-}40)$$

in which G_s is the secant shear modulus of soil. The use of Equation (4-40) is outlined in the following section.

4-3. Compaction and volumetric straining during shearing

When a dry, loose sand is subjected to a monotonic shearing under constant effective confining pressure, its volume and shear modulus decrease until the shearing stress equals its shearing strength. After the shearing strength is reached, deformation continues with no further volume change. The void ratio during constant volume shearing is called the critical void ratio.[16] The mechanism behind this observed behavior was hypothesized by Casagrande to be a continuous rearrangement of sand grains until minimum frictional resistance is reached.[31] A more elaborate mechanism for compaction during repeated shearing is proposed by Youd [78].

Due to the fact that pore water can not be drained readily during a given amount of rapid repeated shearing, the compaction of fully saturated sands is much less than that of dry sands. It is very likely that liquefaction may be completed well before the critical void ratio is reached. The compaction mechanism for saturated sand can be thought as similar to that of dry sands. The amount of compaction, no matter how small, can not be recovered.

In this study, it is hypothesized that as the shearing

strain increases, the shear modulus decreases as does the ability of the skeleton to sustain confined compression. Since the soil is loaded by its own weight, it settles in response to the weakening of the skeleton. During this settlement, both compaction and elastic volumetric straining may take place. The volumetric strain under confined compression, $\frac{\partial w}{\partial z}$, is defined based on the actual displacement. Hence $\frac{\partial w}{\partial z}$ encompasses unit compaction (compaction per unit depth) and elastic volumetric strain.

The time rates of change in $\frac{\partial w}{\partial z}$, $-\bar{\sigma}_z$ and C_c are related by

$$\frac{\partial(-\bar{\sigma}_z)}{\partial t} = -\frac{(-\bar{\sigma}_z)}{C_c}\frac{\partial C_c}{\partial t} + \frac{1}{C_c}\frac{\partial}{\partial t}\left(\frac{\partial w}{\partial z}\right). \qquad (4\text{-}41)$$

This equation is obtained by taking time derivatives on both sides of Equation (4-4). The constrained compressibility is related to the secant shear modulus and the bulk modulus of the skeleton, as shown in Equation (4-40). It is assumed that the bulk compressibility does not change during shearing. Thus, from Equation (4-40), one obtains

$$\Delta C_c = -\frac{4}{3} C_c^2 \Delta G_s \qquad (4\text{-}42)$$

Since the shearing strain softening property of the skeleton is known, $\frac{\partial G_s}{\partial t}$, and thus $\frac{\partial C_c}{\partial t}$, can be considered as known quantities at a given strain level during shearing. Equations (4-41) and (4-42) make it possible to calculate the amount of settlement when a layer of loose sand is sheared.

At the moment of strain reversal in repeated shearing

the soil instantly regains most of its shearing rigidity. As a result, the skeleton recovers much of its confined compressional strength that has been lost during the shearing stroke preceeding the stress reversal. Since this strengthening is instantaneous, Equation (4-41) is not applicable at the instant of shearing strain reversal. Immediately after the strain reversal, the soil, now slightly densified by the compaction that took place during previous strokes, is compacted further as the shearing to the opposite direction proceeds.

CHAPTER 5

PROPAGATION OF PLANE PRESSURE WAVES IN SATURATED DEPOSITS

The governing equations for the pressure wave motions in a saturated deposit are developed in this chapter. The analytical solution for a uniform linear elastic deposit in steady oscillatory motion is developed. The influence of permeability and porosity upon the motion is examined by examples. Wave motions in more realistic deposits can be studied by a numerical procedure, which is considered in Chapter 6.

5-1. Equation of motion of saturated soils

Since a saturated soil is considered as a two phase medium, it is necessary to consider the velocity for each constituent. The velocity of the skeleton, W and the seepage velocity $\overline{W}$ are used to describe the motion of the soil. In terms of the displacement fields defined in Chapter 4, one can write

$$W = \frac{\partial w}{\partial t} , \tag{5-1}$$

and

$$\overline{W} = \frac{\partial}{\partial t} (\overline{w} - w). \tag{5-2}$$

Consider a soil element in Figure 5-1, the equation of motion can be written as

$$(\sigma + \frac{\partial \sigma}{\partial z} \delta z) - \sigma + \rho g \delta z = (\rho \frac{DW}{Dt} + n \rho_w \frac{D\overline{W}}{Dt}) \delta z,$$

or

$$\frac{\partial \sigma}{\partial z} + \rho g = \rho \frac{DW}{Dt} + n \rho_w \frac{D\overline{W}}{Dt} . \qquad (5-3)$$

The presence of the second term on the right hand side is due to the fact that the unbalanced force causes pore water to accelerate relative to the soil skeleton. The convective component in the two accelerations, $W \frac{\partial W}{\partial z}$ and $\overline{W} \frac{\partial \overline{W}}{\partial z}$, are small quantities relative to the remaining terms of the equation and hence can be neglected. Therefore, the equation of motion for soil becomes

$$\frac{\partial \sigma}{\partial z} + \rho g = \rho \frac{\partial W}{\partial t} + n \rho_w \frac{\partial \overline{W}}{\partial t} . \qquad (5-4)$$

5-2. Equation of motion for water in pores

The motion of pore water relative to the soil skeleton is slow and hence is considered as laminar. The resistance force to the flow imparted by the soil skeleton is expressed in terms of Darcy's law. Consider a soil element in Figure 5-2, the equation of relative motion of pore water can be written as

$$(S + \frac{\partial S}{\partial z} \delta z) - S + n \rho_w g \delta z - \delta z \, n \rho_w \frac{\partial W}{\partial t} -$$

$$\delta z \frac{n^2 \rho_w g}{k} \overline{W} = \delta z \, n \rho_w \frac{D\overline{W}}{Dt}$$

in which k is the permeability in z direction. The fourth term on the left side represents the apparent body force due to the acceleration of the skeleton. The fifth term on the left side is due to the viscosity of the pore water.

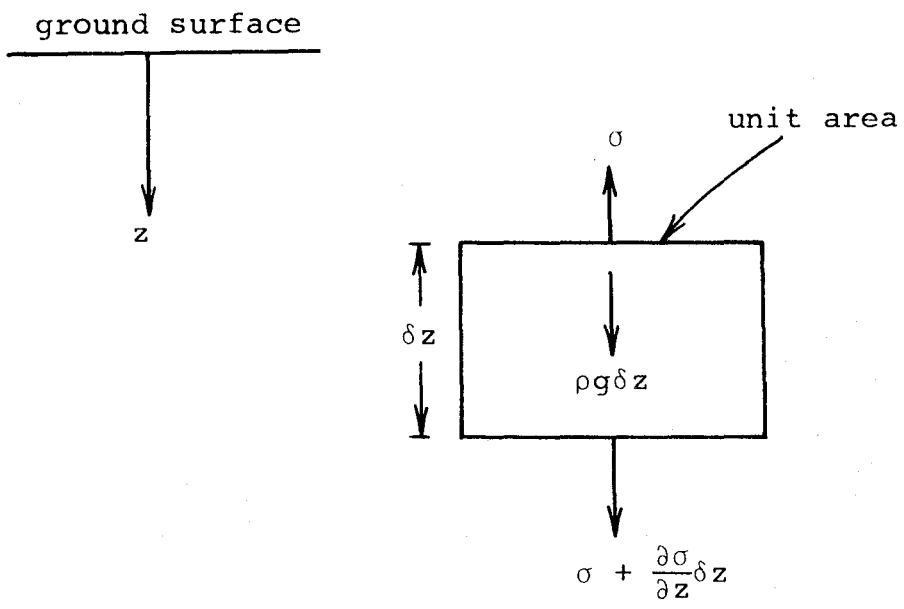

Figure 5-1 Forces on a soil element

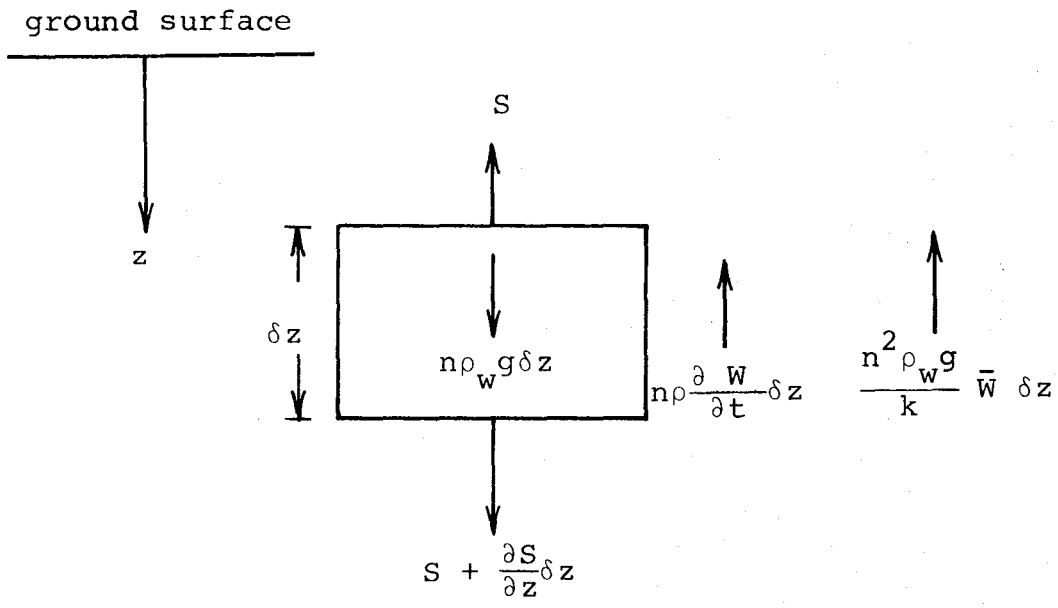

Figure 5-2 Forces on the water portion of a soil element

It is treated as if it were a body force, this detail is given in Appendix 1. After simplifying, the equation of motion for water in pores can be written as

$$\frac{\partial S}{\partial z} + n\,\rho_w\,g - n\,\rho_w\,\frac{\partial W}{\partial t} - \frac{n^2\rho_w g}{k}\,\bar{W} = n\,\rho_w\,\frac{\partial \bar{W}}{\partial t}\,. \qquad (5\text{-}5)$$

5-3. Time derivative of stress strain relations

In the study of pressure wave propagation, it is convenient to work with velocities of the soil constituents rather than their displacements. Take time derivatives on both sides of Equation (4-3), noting that the time derivatives of the quantities with subscript zero vanish, one obtains

$$\frac{\partial S}{\partial t} = \frac{1}{C_w}\,\frac{\partial^2 w}{\partial t \partial z} + \frac{n}{C_w}\,\frac{\partial^2 (\bar{w} - w)}{\partial t \partial z}\,.$$

After interchanging the order of differentiation and employing Equations (5-1) and (5-2), one obtains

$$\frac{\partial S}{\partial t} = \frac{1}{C_w}\,\frac{\partial W}{\partial z} + \frac{n}{C_w}\,\frac{\partial \bar{W}}{\partial z}\,. \qquad (5\text{-}6)$$

Similarly, take time derivatives on both sides of Equation (4-5), one obtains

$$\frac{\partial \sigma}{\partial t} = \left(\frac{1}{C_c} + \frac{1}{n\,C_w}\right)\frac{\partial W}{\partial z} + \frac{1}{C_w}\,\frac{\partial \bar{W}}{\partial z} - \frac{1}{C_c^2}\,\frac{\partial w}{\partial z}\,\frac{\partial C_c}{\partial t}\,.$$

From Equation (4-4) and the definition of effective tensile stress, one can write

$$\frac{1}{C_c^2}\,\frac{\partial w}{\partial z} = \frac{1}{C_c}\left(\sigma - \frac{S}{n}\right)\,,$$

hence

$$\frac{\partial \sigma}{\partial t} = \left(\frac{1}{C_c} + \frac{1}{n\, C_w}\right) \frac{\partial W}{\partial z} + \frac{1}{C_w} \frac{\partial \overline{W}}{\partial z} - \frac{1}{C_c} \left(\sigma - \frac{S}{n}\right) \frac{\partial C_c}{\partial t} \ . \quad (5\text{-}7)$$

Equations (5-4), (5-5), (5-6) and (5-7) together govern the propagation of plane pressure waves.

5-4. Steady oscillatory motion of uniform linear elastic deposit

In this section the soil is considered as linear elastic so the last term in Equation (5-7) vanishes. S and σ can be considered as the dynamic stresses above or below their static value. By dropping the gravity terms in Equations (5-4) and (5-5) and taking time derivatives, one gets

$$\frac{\partial^2 W}{\partial t^2} + \frac{n\, \rho_w}{\rho} \frac{\partial^2 \overline{W}}{\partial t^2} - \frac{1}{\rho} \frac{\partial^2 \sigma}{\partial z \partial t} = 0 \ , \quad (5\text{-}8)$$

and

$$\frac{\partial^2 W}{\partial t^2} + \frac{\partial^2 \overline{W}}{\partial t^2} - \frac{1}{n\, \rho_w} \frac{\partial^2 S}{\partial z \partial t} + \frac{ng}{k} \frac{\partial \overline{W}}{\partial t} = 0 \ . \quad (5\text{-}9)$$

Differentiate Equations (5-6) and (5-7) with respect to z, one obtains

$$\frac{\partial^2 S}{\partial z \partial t} - \frac{1}{C_w} \frac{\partial^2 W}{\partial z^2} - \frac{n}{C_w} \frac{\partial^2 \overline{W}}{\partial z^2} = 0 \ , \quad (5\text{-}10)$$

and

$$\frac{\partial^2 \sigma}{\partial z \partial t} - \left(\frac{1}{C_c} + \frac{1}{n\, C_w}\right) \frac{\partial^2 W}{\partial z^2} - \frac{1}{C_w} \frac{\partial^2 \overline{W}}{\partial z^2} = 0 \ . \quad (5\text{-}11)$$

Eliminating $\frac{\partial^2 \sigma}{\partial z \partial t}$ between Equations (5-8) and (5-11) yields

$$\frac{\partial^2 W}{\partial t^2} + \frac{n \rho_w}{\rho} \frac{\partial^2 \overline{W}}{\partial t^2} - \frac{1}{\rho} \left[\left(\frac{1}{C_c} + \frac{1}{n C_w} \right) \frac{\partial^2 W}{\partial z^2} + \frac{1}{C_w} \frac{\partial^2 \overline{W}}{\partial z^2} \right] = 0. \quad (5\text{-}12)$$

Eliminating $\frac{\partial^2 S}{\partial z \partial t}$ between Equation (5-9) and (5-10) yields

$$\frac{\partial^2 W}{\partial t^2} + \frac{\partial^2 \overline{W}}{\partial t^2} - \frac{1}{n \rho_w} \left(\frac{1}{C_w} \frac{\partial^2 W}{\partial z^2} + \frac{n}{C_w} \frac{\partial^2 \overline{W}}{\partial z^2} \right) + \frac{ng}{k} \frac{\partial \overline{W}}{\partial t} = 0. \quad (5\text{-}13)$$

The simple harmonic motion of the soil deposit is known after $W(z, t)$ and $\overline{W}(z, t)$ are solved simultaneously from Equations (5-12) and (5-13).

Let the solution to Equations (5-12) and (5-13) assume the following form

$$W(z, t) = \overline{H}(z)\, e^{i(\omega t - \frac{\pi}{2})} \quad (5\text{-}14)$$

$$\overline{W}(z, t) = \overline{G}(z)\, e^{i(\omega t - \frac{\pi}{2})} \quad (5\text{-}15)$$

where ω is the specified angular frequency of the motion and $i = \sqrt{-1}$. $\overline{H}(z)$ is the amplitude of the skeleton velocity fluctuation at depth z, and $\overline{G}(z)$ is the amplitude of the seepage velocity fluctuation at depth z. The particular form of $\overline{H}(z)$ and $\overline{G}(z)$ depend on boundary conditions.

Substitute Equations (5-14) and (5-15) into Equations (5-12) and (5-13) and simplifying, one obtains

$$\alpha_1 \frac{d^2 \overline{H}}{dz^2} + \alpha_2 \frac{d^2 \overline{G}}{dz^2} + \alpha_3 \overline{H} + \alpha_4 \overline{G} = 0 , \quad (5\text{-}16)$$

and

$$\alpha_5 \frac{d^2\bar{H}}{dz^2} + \alpha_6 \frac{d^2\bar{G}}{dz^2} + \alpha_7 \bar{H} + \alpha_8 \bar{G} = 0 \qquad (5\text{-}17)$$

in which

$$\alpha_1 = \frac{1}{\rho}\left(\frac{1}{C_c} + \frac{1}{n\,C_w}\right); \quad \alpha_2 = \frac{1}{\rho\,C_w}; \quad \alpha_3 = \omega^2;$$

$$\alpha_4 = \frac{n\,\rho_w\,\omega^2}{\rho}; \quad \alpha_5 = \frac{1}{n\,\rho_w\,C_w}; \quad \alpha_6 = \frac{1}{\rho_w\,C_w};$$

$$\alpha_7 = \omega^2; \quad \alpha_8 = \omega^2 - i\omega\,\frac{ng}{k}\ .$$

For convenience, let

$$\frac{d\bar{H}}{dz} = \bar{P}(z) \text{ and } \frac{d\bar{G}}{dz} = \bar{Q}(z)\ ,$$

then

$$\frac{d^2\bar{H}}{dz^2} = \frac{d\bar{P}}{dz} \text{ and } \frac{d^2\bar{G}}{dz^2} = \frac{d\bar{Q}}{dz}\ .$$

With $\bar{P}(z)$ and $\bar{Q}(z)$, Equations (5-16) and (5-17) can be re-written as a homogeneous system of four first order ordinary differential equations

$$\begin{cases} \alpha_1 \dfrac{d\bar{P}}{dz} + \alpha_2 \dfrac{d\bar{Q}}{dz} + \alpha_3 \bar{H} + \alpha_4 \bar{G} = 0\ , \\ \alpha_5 \dfrac{d\bar{P}}{dz} + \alpha_6 \dfrac{d\bar{Q}}{dz} + \alpha_7 \bar{H} + \alpha_8 \bar{G} = 0\ , \\ \bar{P} - \dfrac{d\bar{H}}{dz} = 0\ , \\ \bar{Q} - \dfrac{d\bar{G}}{dz} = 0\ . \end{cases} \qquad (5\text{-}18)$$

Let $\bar{P}(z) = ae^{\lambda z}$; $\bar{Q}(z) = be^{\lambda z}$; $\bar{H} = ce^{\lambda z}$; and $\bar{G} = de^{\lambda z}$ be a particular solution to the above system, where a, b, c, and d are four constants. Substitute this particular solution into the system, one obtains

$$\begin{cases} \alpha_1 a\lambda + \alpha_2 b\lambda + \alpha_3 c + \alpha_4 d = 0 \\ \alpha_5 a\lambda + \alpha_6 b\lambda + \alpha_7 c + \alpha_8 d = 0 \\ a - c\lambda = 0 \\ b - \lambda d = 0 \ . \end{cases} \tag{5-19}$$

Nontrivial solution for a, b, c, and d exists if and only if the following equation holds

$$\det \begin{vmatrix} \alpha_1\lambda & \alpha_2\lambda & \alpha_3 & \alpha_4 \\ \alpha_5\lambda & \alpha_6\lambda & \alpha_7 & \alpha_8 \\ 1 & 0 & -\lambda & 0 \\ 0 & 1 & 0 & -\lambda \end{vmatrix} = 0. \tag{5-20}$$

The solution to Equation (5-20) is

$$\lambda = \pm\sqrt{\frac{1}{2\gamma_1}\left(-\gamma_2 \pm \sqrt{\gamma_2^2 - 4\gamma_1\gamma_3}\right)} = \begin{matrix} \lambda_1 \\ \lambda_2 \\ \lambda_3 \\ \lambda_4 \end{matrix}$$

in which $\gamma_1 = \alpha_1\alpha_6 - \alpha_2\alpha_5$, $\gamma_2 = \alpha_1\alpha_8 - \alpha_4\alpha_5 - \alpha_2\alpha_7 + \alpha_3\alpha_6$, $\gamma_3 = \alpha_3\alpha_8 - \alpha_4\alpha_7$, and $\lambda_1 > \lambda_2 > \lambda_3 > \lambda_4$.

For λ_j, $j = 1, 2, 3, 4$, one can solve a_j, b_j, c_j and d_j from Equation (5-19). It is noted that since λ is obtained from Equation (5-20), only three equations in System

(5-19) are independent from one another. Consequently, one can always assign unity to d_j, j = 1, 2, 3, 4, and then solve for a_j, b_j, and c_j. Such a solution is written as follows

$$a_j = -\lambda_j \left(\frac{\alpha_2 \lambda_j^2 + \alpha_4}{\alpha_1 \lambda_j^2 + \alpha_3}\right) ,$$

$$b_j = \lambda_j ,$$

$$c_j = -\frac{\alpha_6 \lambda_j^2 + \alpha_8}{\alpha_5 \lambda_j^2 + \alpha_7} ,$$

$$d_j = 1 ,$$

for j = 1, 2, 3, 4. The four particular solutions

$$\begin{aligned} \bar{P}_j(z) &= a_j e^{\lambda_j z} \\ \bar{Q}_j(z) &= b_j e^{\lambda_j z} \\ \bar{H}_j(z) &= c_j e^{\lambda_j z} \\ \bar{G}_j(z) &= e^{\lambda_j z} \end{aligned} \qquad j = 1, 2, 3, 4$$

for the system (5-18) are thus obtained. The general solution to the system can be written as a linear combination of these four particular solutions, as shown in the following

$$\bar{P}(z) = s_1 a_1 e^{\lambda_1 z} + s_2 a_2 e^{\lambda_2 z} + s_3 a_3 e^{\lambda_3 z} + s_4 a_4 e^{\lambda_4 z}$$

$$\bar{Q}(z) = s_1 b_1 e^{\lambda_1 z} + s_2 b_2 e^{\lambda_2 z} + s_3 b_3 e^{\lambda_3 z} + s_4 b_4 e^{\lambda_4 z}$$

$$\bar{H}(z) = s_1 c_1 e^{\lambda_1 z} + s_2 c_2 e^{\lambda_2 z} + s_3 c_3 e^{\lambda_3 z} + s_4 c_4 e^{\lambda_4 z}$$

$$\bar{G}(z) = s_1 e^{\lambda_1 z} + s_2 e^{\lambda_2 z} + s_3 e^{\lambda_3 z} + s_4 e^{\lambda_4 z}$$

in which s_1, s_2, s_3 and s_4 are four constants to be determined from given boundary conditions.

Consider a deposit of soil resting on an impermeable bedrock, the depth of the deposit being D. The boundary condition imposed at the bedrock is

$$W(D, t) = AMP\, e^{i(\omega t - \frac{\pi}{2})},$$

and

$$\bar{W}(D, t) = 0$$

in which AMP is a real number representing the single amplitude of the skeleton velocity at the bottom. At the surface, the condition of constant stresses is imposed, hence

$$\frac{\partial S}{\partial t}\Big|_{z=0} = 0 ,$$

and

$$\frac{\partial \sigma}{\partial t}\Big|_{z=0} = 0 .$$

In terms of $\bar{P}(z)$, $\bar{Q}(z)$, $\bar{H}(z)$ and $\bar{G}(z)$, these boundary conditions can be written as

$$\begin{cases} \overline{H}(D) = AMP , \\ \overline{G}(D) = 0 , \\ \overline{P}(0) = 0 , \\ \overline{Q}(0) = 0 . \end{cases} \tag{5-21}$$

These four equations yield the following four independent equations to determine s_1, s_2, s_3 and s_4 uniquely,

$$\overline{H}(D) = c_1 e^{\lambda_1 D} s_1 + c_2 e^{\lambda_2 D} s_2 + c_3 e^{\lambda_3 D} s_3 + c_4 e^{\lambda_4 D} s_4 = AMP,$$

$$\overline{G}(D) = e^{\lambda_1 D} s_1 + e^{\lambda_2 D} s_2 + e^{\lambda_3 D} s_3 + e^{\lambda_4 D} s_4 = 0 ,$$

$$\overline{P}(0) = a_1 s_1 + a_2 s_2 + a_3 s_3 + a_4 s_4 = 0,$$

$$\overline{Q}(0) = b_1 s_1 + b_2 s_2 + b_3 s_3 + b_4 s_4 = 0 .$$

After solving s_1, s_2, s_3 and s_4 from the above four equations, the solution to System (5-18), subjected to condition (5-21) is obtained. This solution, in terms of W, $\overline{W}$, S and σ is expressed as follows

$$W(z, t) = \overline{H}(z)\, e^{i(\omega t - \frac{\pi}{2})}$$

$$\overline{W}(z, t) = \overline{G}(z)\, e^{i(\omega t - \frac{\pi}{2})}$$

$$S(z, t) = \frac{1}{i\omega C_w} [\overline{P}(z) + n\, \overline{Q}(z)]\, e^{i(\omega t - \frac{\pi}{2})}$$

$$\sigma(z, t) = \frac{1}{i\omega} [(\frac{1}{C_c} + \frac{1}{n C_w})\, \overline{P}(z) + \frac{1}{C_w} \overline{Q}(z)]\, e^{i(\omega t - \frac{\pi}{2})}$$

The computer program used to generate numerical results of this lengthy solution is included in Appendix 2.

5-5. Examples

A level saturated deposit 50 feet deep was used in the following examples to demonstrate the role of various parameters in steady oscillatory motion. For all the examples the mass density of water was taken as 1.94 lb-sec^2/ft, and the imposed skeletal velocity at the impervious surface of the bedrock was 0.2 sin ($2\pi t$) fps. W, $\bar{W}$ and the dynamic stresses S and σ (above or below their static value) were obtained from the program listed in Appendix 2.

Example 5-1. The motion of loose, medium and dense saturated sands

Representative values for the parameters associated with typical loose and dense sand were given by Ishihara,[39] and were used in this chapter. Parameters associated with the medium sand were estimated. All the data are listed in Table 5-1.

TABLE 5-1
PROPERTIES OF SANDS USED IN CHAPTER 5

	Loose Sand	Medium Sand	Dense Sand
n	0.5	0.4	0.3
ρ_s, lb-sec^2/ft	5.13	5.13	5.13
C_c, ft^2/lb	3.4×10^{-7}	2.4×10^{-7}	1.3×10^{-7}
C_w, ft^2/lb	2.3×10^{-8}	2.3×10^{-8}	2.3×10^{-8}
k, fps	0.003	0.001	0.0003

The amplitudes and phase angles of the oscillation throughout the deposit are plotted in Figure 5-3 and Figure 5-4. The phase angle of any quantity under consideration is defined as the phase difference between the quantity and the skeletal velocity at the bottom of the deposit. These plots show that except near the impermeable bedrock, $\overline{W}$, S and σ were in phase with one another, and each individual quantity as 90 degrees out of phase with respect to W. Oscillations in W and $\overline{W}$ in a loose deposit were slightly larger than those in a dense deposit. However, the difference in the amplitudes of dynamic stresses were quite different. These differences might be attributed to the difference in porosity, as shown later in Example 5-3.

Example 5-2. The effect of permeability

In order to see how the motion was influenced by permeability alone, the medium sand was used in conjunction with the permeability of loose and dense sands in Example 5-1. Results are shown in Figures 5-5 and 5-6. It is seen that permeability greatly influenced the relative motion between the skeleton and pore water. The influence of the permeability on the skeletal velocity and the dynamic stress S was small, while it had negligible influence upon the dynamic total stress σ.

Example 5-3. The effect of porosity

The influence of porosity was then examined by using the medium sand in conjunction with the porosity of loose

and dense sands in Example 5-1. Results are shown in Figures 5-7 and 5-8. Except for the seepage velocity, the oscillations of W, S, and σ were close to those shown in Example 5-1. Hence, in general, the effect of porosity overrides that of permeability, and the soil skeleton and pore water tend to move together when the permeability is small.

Computations for Examples 5-1, 5-2, and 5-3 were repeated with a bedrock velocity frequency of 10 Hertz. Results were similar to those described above.

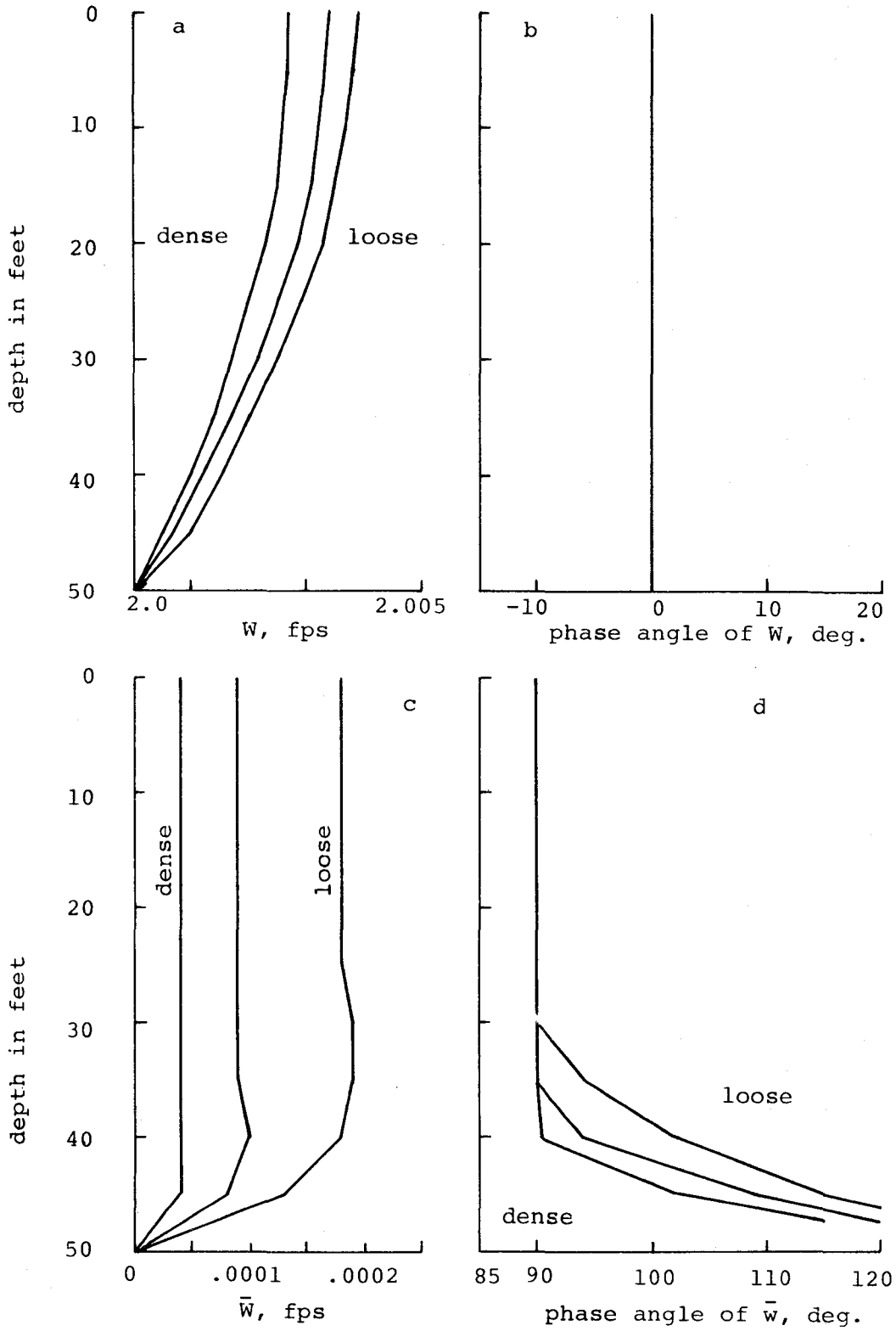

Figure 5-3 Amplitudes and phase angles of W and $\bar{W}$ in loose medium and dense deposits

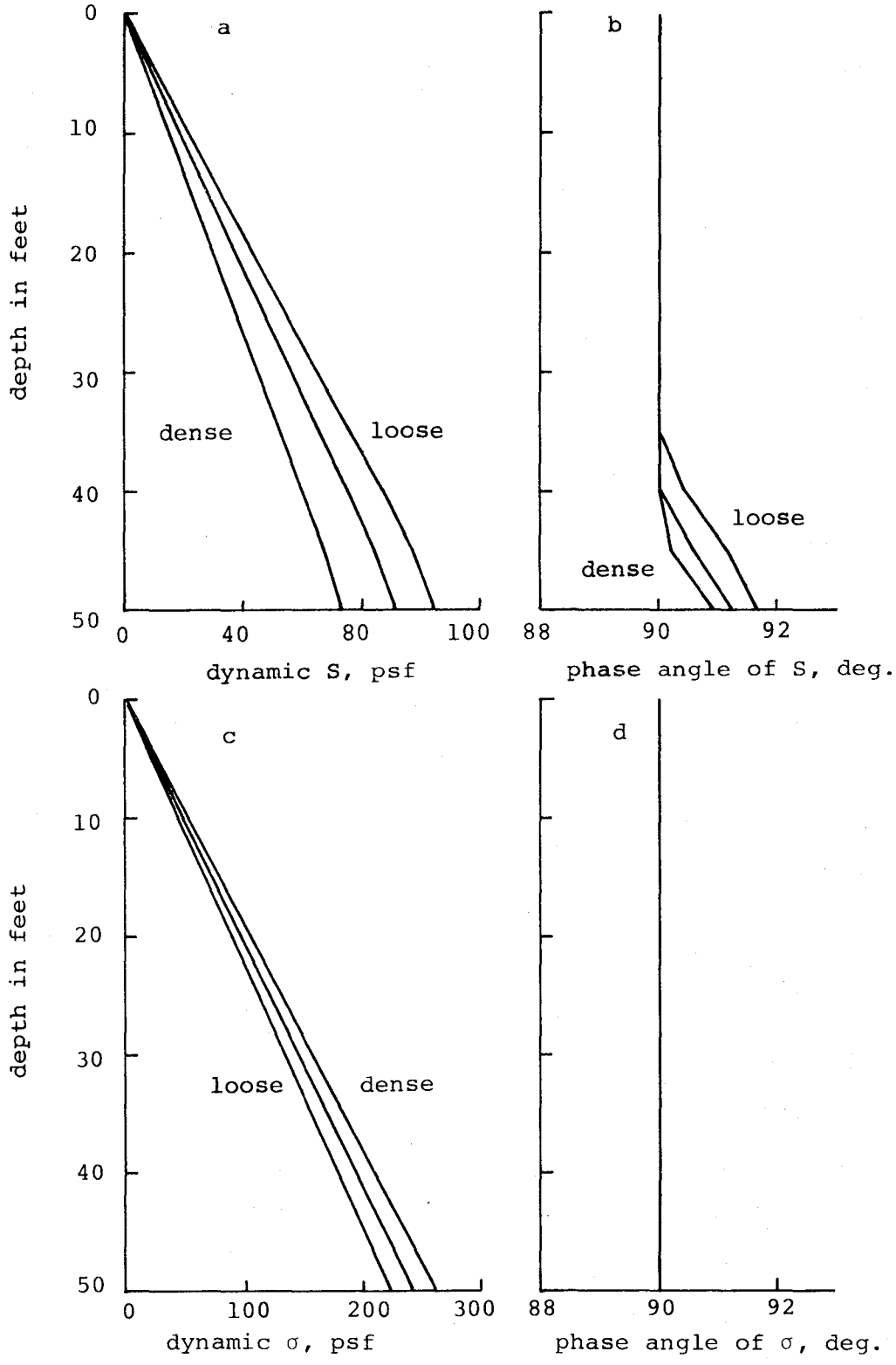

Figure 5-4 Amplitudes and phase angles of dynamic s and σ in loose, medium, and dense deposits

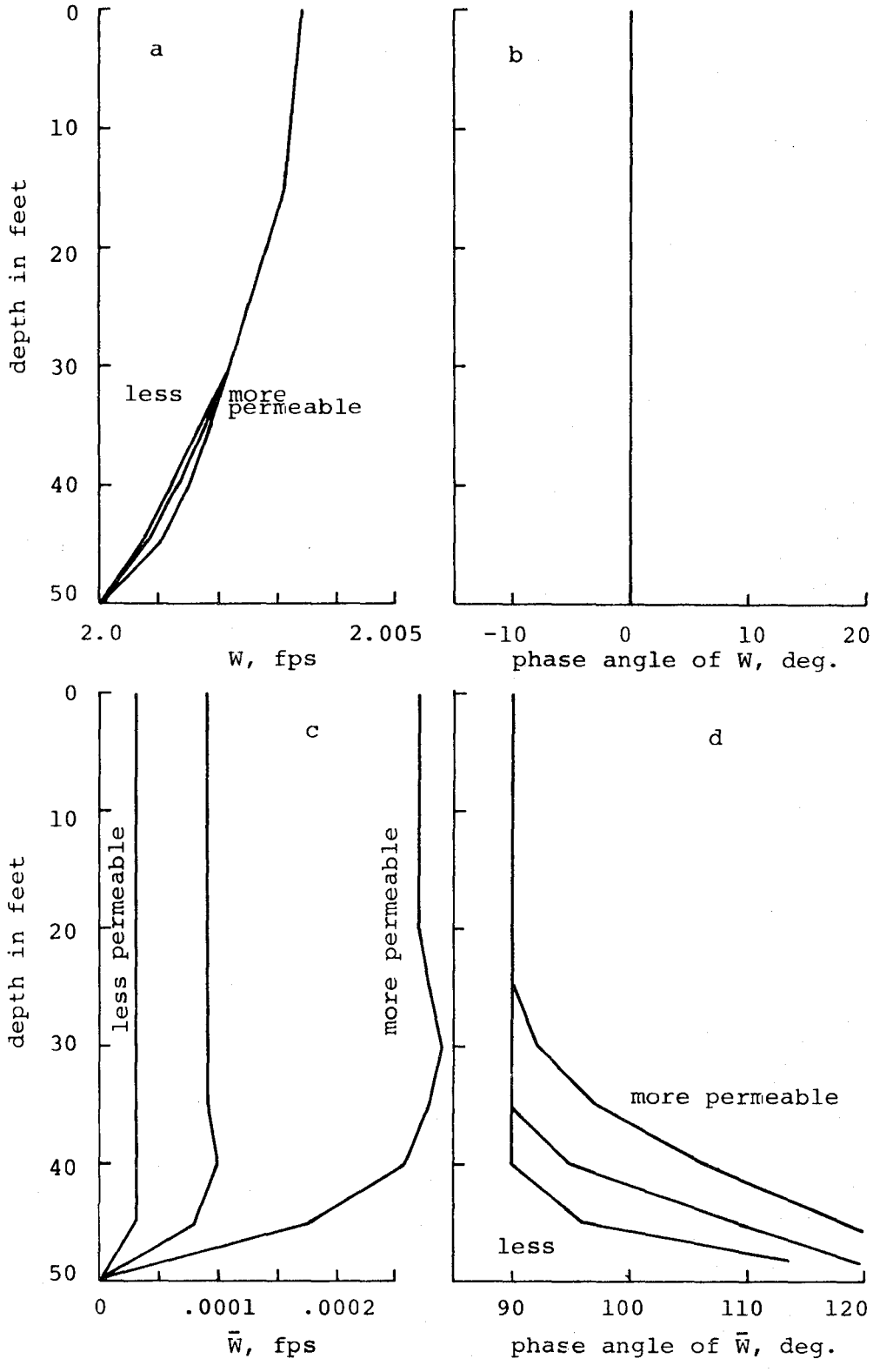

Figure 5-5 Amplitudes and phase angles of W and $\bar{W}$ of a medium sand with low, medium, and high permeability

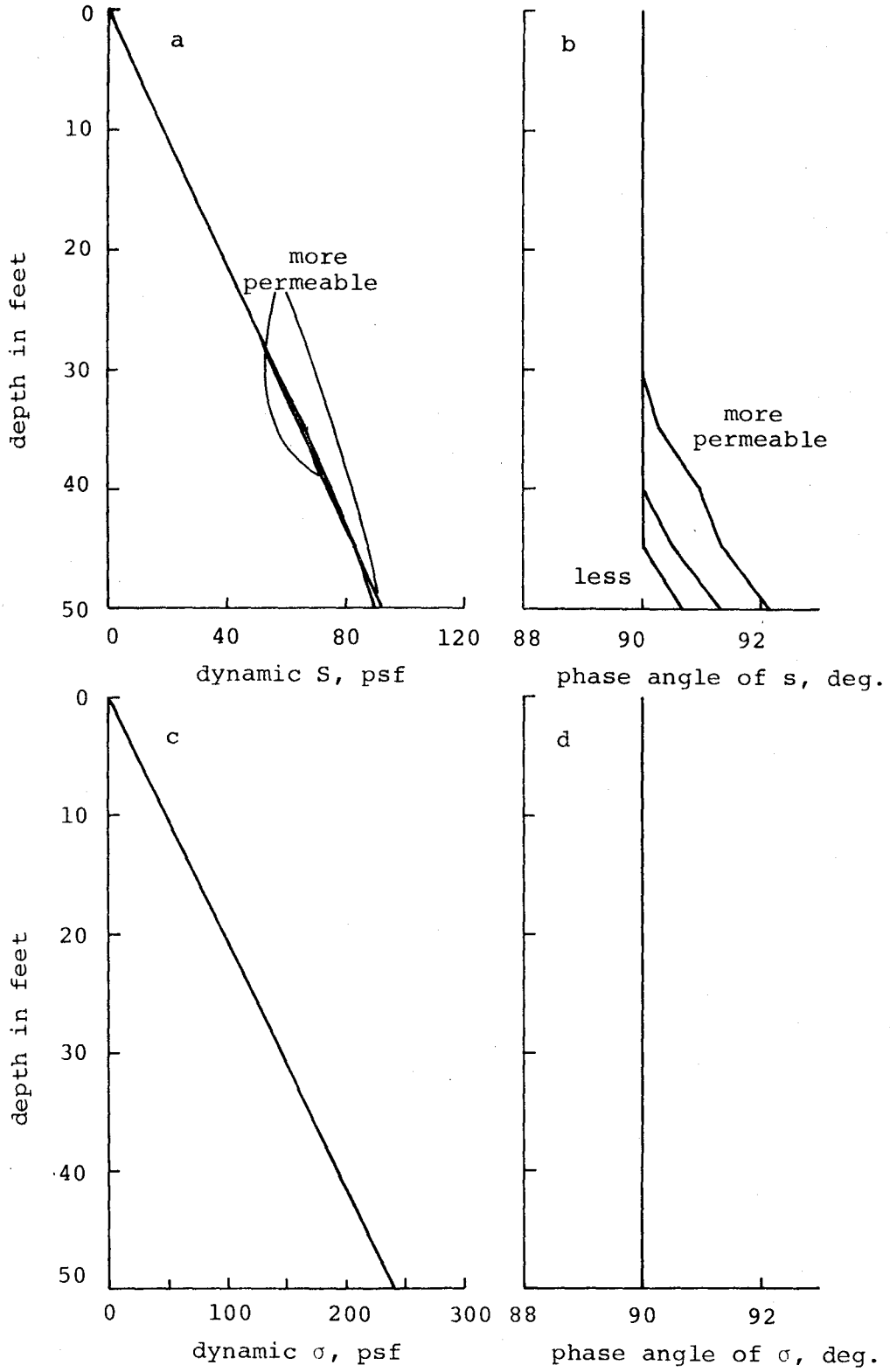

Figure 5-6 Amplitudes and phase angles of dynamic S and σ of a medium sand with low, medium, and high permeability

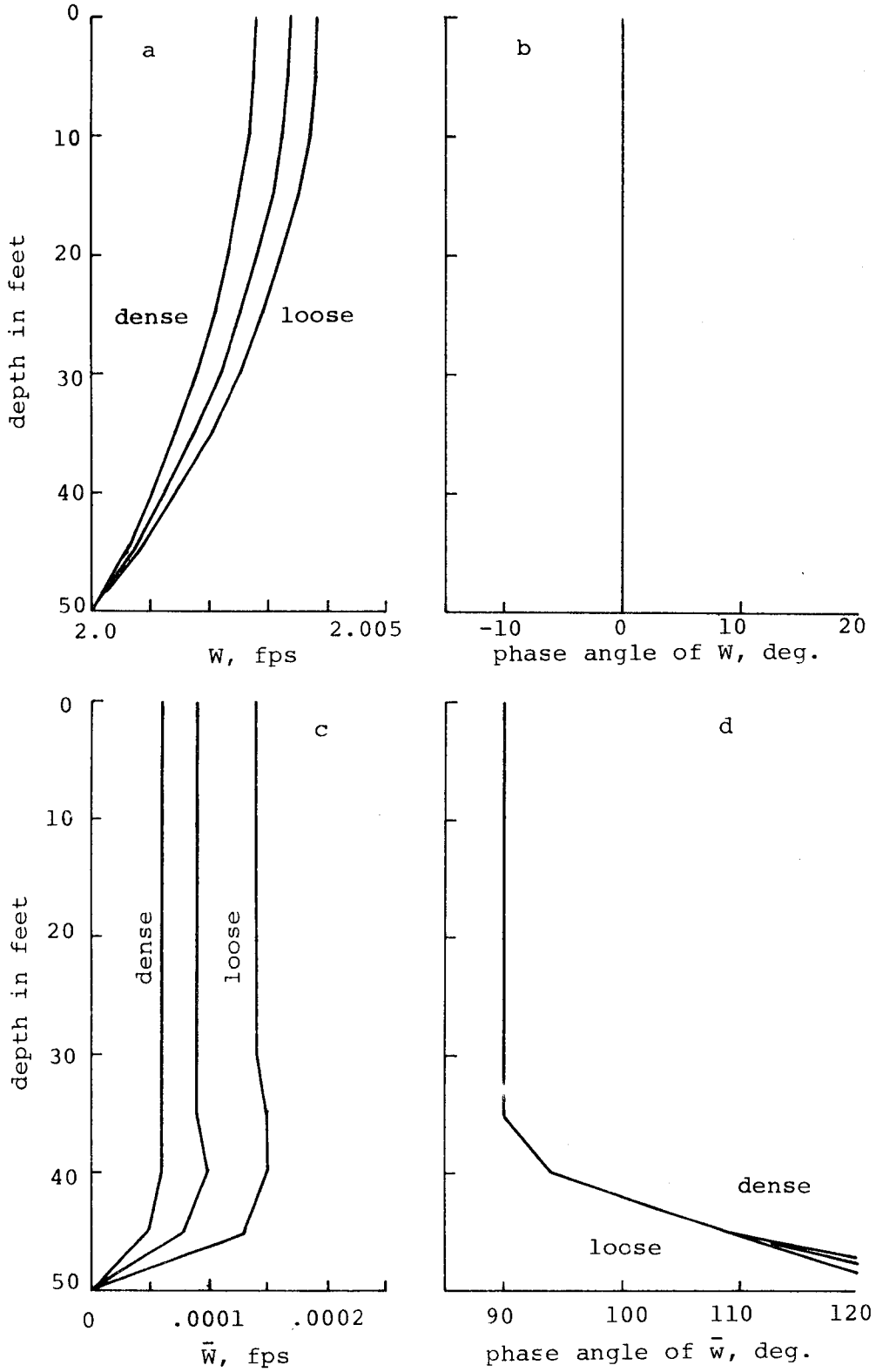

Figure 5-7 Amplitudes and phase angles of W and $\bar{W}$ of loose, medium and dense sand with medium permeability

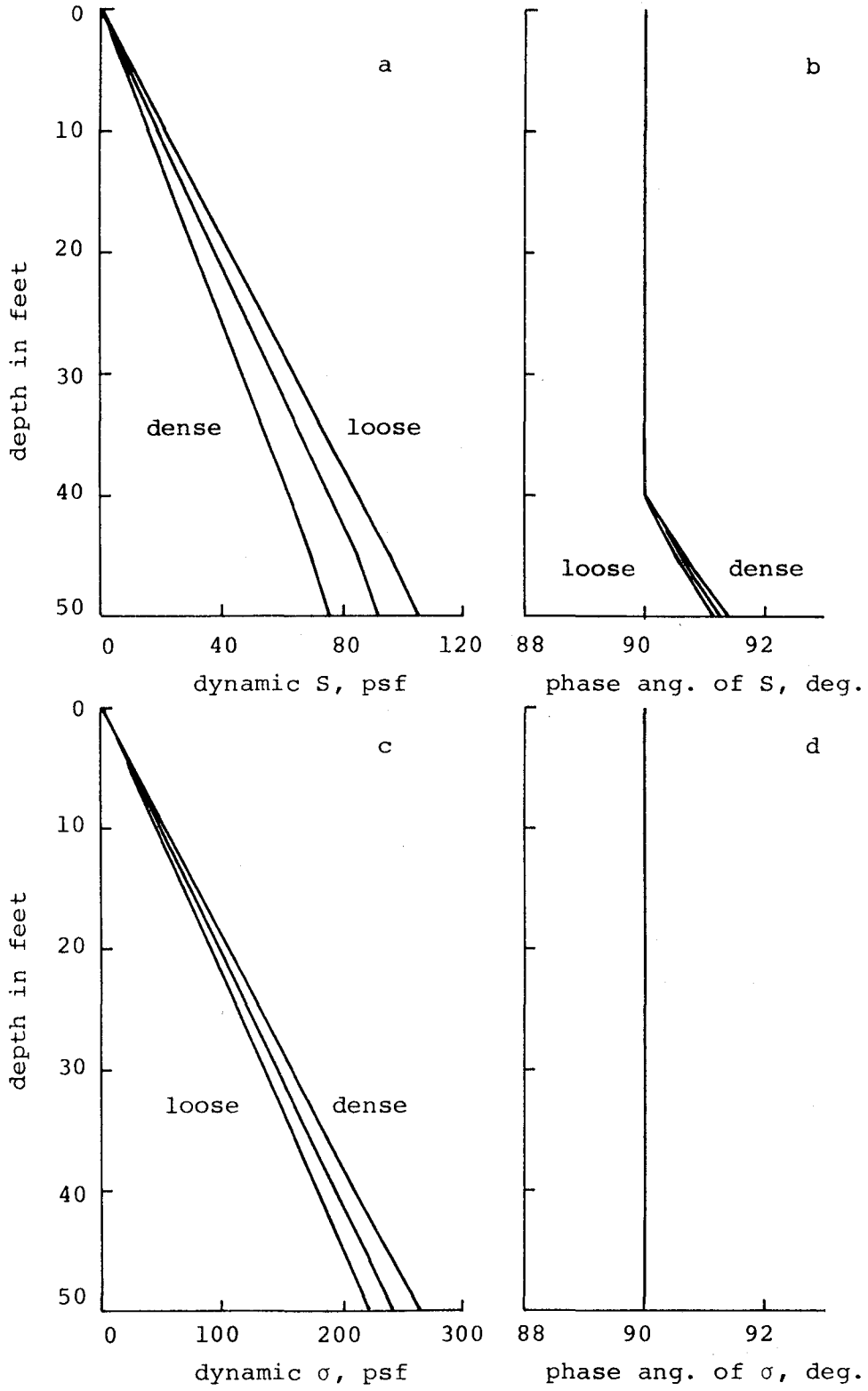

Figure 5-8 Amplitudes and phase angles of S and σ of loose, medium, and dense sands with medium permeability

CHAPTER 6

NUMERICAL SOLUTION BY THE METHOD OF CHARACTERISTICS

In this chapter the set of governing equations is shown to be hyperbolic for most saturated sands. Four characteristic equations are obtained after the governing equations are transformed into the normal form. These characteristic equations are then approximated by finite differences to obtain numerical solutions. The accuracy of the numerical procedure is checked by using the analytical solution obtained in Chapter 5. The numerical procedure developed in this chapter is used in the subsequent chapters to study the motions in deposits with time varying, inelastic material properties.

6-1. The hyperbolicity of the governing equations.

By linear combinations of Equations (5-4) and (5-5), one obtains

$$\frac{\partial W}{\partial t} - \frac{1}{n\rho_w - \rho}\frac{\partial S}{\partial z} + \frac{1}{n\rho_w - \rho}\frac{\partial \sigma}{\partial z} + \frac{n^2\rho_w g}{k(n\rho_w - \rho)}\bar{W} - g = 0 \ , \quad (6\text{-}1)$$

and

$$\frac{\partial W}{\partial t} + \frac{\rho}{n\rho_w(n\rho_w - \rho)}\frac{\partial S}{\partial z} - \frac{1}{n\rho_w - \rho}\frac{\partial \sigma}{\partial z} - \frac{\rho n g}{k(n\rho_w - \rho)}\bar{W} = 0 \ . \quad (6\text{-}2)$$

Write Equations (6-1), (6-2), (5-6) and (5-7) in matrix

form

$$\begin{pmatrix} 1 & 0 & 0 & 0 \\ 0 & 1 & 0 & 0 \\ 0 & 0 & 1 & 0 \\ 0 & 0 & 0 & 1 \end{pmatrix} \begin{pmatrix} W \\ \overline{W} \\ S \\ \sigma \end{pmatrix}_t + \begin{pmatrix} 0 & 0 & \frac{-1}{n\rho_w - \rho} & \frac{1}{n\rho_w - \rho} \\ 0 & 0 & \frac{\rho}{n\rho_w(n\rho_w - \rho)} & \frac{-1}{n\rho_w - \rho} \\ \frac{-1}{C_w} & \frac{-n}{C_w} & 0 & 0 \\ -(\frac{1}{C_c} + \frac{1}{nC_w}) & \frac{-1}{C_w} & 0 & 0 \end{pmatrix} \begin{pmatrix} W \\ \overline{W} \\ S \\ \sigma \end{pmatrix}_z$$

$$+ \begin{pmatrix} \frac{n^2 \rho_w g}{k(n\rho_w - \rho)} \overline{W} - g \\ \frac{-\rho n g}{k(n\rho_w - \rho)} \overline{W} \\ 0 \\ \frac{1}{C_c}(\sigma - \frac{S}{n}) \frac{\partial C_c}{\partial t} \end{pmatrix} = 0 \qquad (6\text{-}3)$$

in which the subscripts t and z at the lower right corner of the brackets represent partial differentiation. Define matrices $\tilde{A}$, $\tilde{B}$, $\tilde{D}$ and $\tilde{X}$ as follows

$$\tilde{A} = \begin{pmatrix} 0 & 0 & \frac{-1}{n\rho_w - \rho} & \frac{1}{n\rho_w - \rho} \\ 0 & 0 & \frac{\rho}{n\rho_w(n\rho_w - \rho)} & \frac{-1}{n\rho_w - \rho} \\ \frac{-1}{C_w} & \frac{-n}{C_w} & 0 & 0 \\ -(\frac{1}{C_c} + \frac{1}{nC_w}) & \frac{-1}{C_w} & 0 & 0 \end{pmatrix} = \begin{pmatrix} 0 & 0 & d_1 & d_2 \\ 0 & 0 & d_3 & d_4 \\ d_5 & d_6 & 0 & 0 \\ d_7 & d_8 & 0 & 0 \end{pmatrix},$$

$$\tilde{B} = \begin{pmatrix} 1 & 0 & 0 & 0 \\ 0 & 1 & 0 & 0 \\ 0 & 0 & 1 & 0 \\ 0 & 0 & 0 & 1 \end{pmatrix}, \qquad \tilde{D} = \begin{pmatrix} \frac{n^2 \rho_w g}{k(n\rho_w - \rho)} \bar{W} - g \\ \frac{-n\rho g}{k(n\rho_w - \rho)} \bar{W} \\ 0 \\ \frac{1}{C_c} (\sigma - \frac{S}{n}) \frac{\partial C_c}{\partial t} \end{pmatrix}, \qquad \tilde{X} = \begin{pmatrix} W \\ \bar{W} \\ S \\ \sigma \end{pmatrix},$$

then Equation (6-3) can be written in the following short form

$$\tilde{B}\, \tilde{X}_t + \tilde{A}\, \tilde{X}_z + \tilde{D} = 0 \ . \tag{6-4}$$

For computational advantages, it is desirable to transform Equation (6-4) into a normal form in which every component equation involves derivatives in only one direction on the z-t plane. Assume such a transformation exists. Denote this transformation by $\tilde{E}$ and let e_{ij}, i, j = 1, 2, 3, 4 be the elements of $\tilde{E}$. Pre-multiplying Equation (6-4) by $\tilde{E}$ yields

$$\tilde{E}\, \tilde{B}\, \tilde{X}_t + \tilde{E}\, \tilde{A}\, \tilde{X}_z + \tilde{E}\, \tilde{D} = 0 \ . \tag{6-5}$$

In order to obtain the normal form, the following condition is imposed on $\tilde{E}$

$$\tilde{E}\, \tilde{A} = \tilde{\Lambda}\, \tilde{E}\, \tilde{B} \tag{6-6}$$

in which $\tilde{\Lambda}$ is a real diagonal matrix with elements $\lambda_1 > \lambda_2 > \lambda_3 > \lambda_4$. Substituting Equation (6-6) into Equation (6-5)

$$\tilde{E}\, \tilde{B}\, \tilde{X}_t + \tilde{\Lambda}\, \tilde{E}\, \tilde{B}\, \tilde{X}_z + \tilde{E}\, \tilde{D} = 0 \ . \tag{6-7}$$

It is seen that in the ith equation of system (6-7), all derivatives take place along the direction $\frac{\partial z}{\partial t} = \lambda_i$ on the z-t plane.

Each row in system (6-6) represents four homogeneous equations in the four unknowns e_{ij}, j = 1, 2, 3, 4. For a non-trivial solution to exist, one must have

$$\det|\tilde{A} - \lambda_i \tilde{B}| = 0 \ . \tag{6-8}$$

Since λ_i represents the direction of differentiation on the z-t plane, all four λ_i's must be real and distinct. This is the sufficient condition for the existence of the transformation $\tilde{E}$, which is taken as the definition for hyperbolicity.

In Equation (6-8), since $\tilde{B}$ is a unit matrix, one can simply solve for the eigenvalues of the matrix $\tilde{A}$ for Λ. Let

$$\alpha = d_1d_5 + d_2d_7 + d_3d_6 + d_4d_8$$

and

$$\beta = d_1d_4d_5d_8 + d_2d_3d_6d_7 - d_1d_4d_6d_7 - d_2d_3d_5d_8 \ ,$$

then Equation (6-8) becomes

$$\lambda_i^4 - \alpha \lambda_i^2 + \beta = 0 \ ,$$

whence

$$\lambda_i = \pm\sqrt{\frac{1}{2}(\alpha \pm \sqrt{\alpha^2 - 4\beta})} \ . \tag{6-9}$$

In order that the four λ_i's be real, it is necessary

that the soil must have properties such that $\beta > 0$ and $\alpha^2 > 4\beta$. One can visualize λ_i as the speed of propagation of disturbances on the z-t plane. Hereafter, the absolute value of λ_1 or λ_4 is called the first p-wave speed and that of λ_2 or λ_3 is called the second p-wave speed.

For the purpose of demonstrating the hyperbolicity of Equation (6-3) for most saturated sands, Equation (6-9) was employed to compute the two wave speeds for two types of sand over a range of void ratio and effective confining pressure. These two sands were the round-grained sand and the angular-grained sand of Hardin and Richart.[35] The small motion shear modulus of these sands were related to the void ratio, e, and the effective confining pressure, $\bar{\sigma}_0$, by:

for round grained sand

$$G_{0\,(psf)} = \frac{31560\ (2.17 - e)^2}{1 + e}\ \bar{\sigma}_{0\,(psf)}^{0.5}\ , \qquad (6\text{-}10)$$

and for angular grained sand

$$G_{0\,(psf)} = \frac{14760\ (2.97 - e)^2}{1 + e}\ \bar{\sigma}_{0\,(psf)}^{0.5}\ . \qquad (6\text{-}11)$$

The effective confining pressure was calculated from the following equation

$$\bar{\sigma}_0 = \frac{1 + 2K_0}{3}\ \bar{\sigma}_z \qquad (6\text{-}12)$$

in which K_0 is the coefficient of earth pressure at rest and $\bar{\sigma}_z$ denotes vertical effective stress.

Based on Ishihara's data[39], the bulk compressibility of the skeleton, C_b, at a particular porosity was calculated

from the following interpolation formula

$$C_b = [4.403 + 0.176\ (n - 0.5)] \times 10^{-6}\ ft^2/lb.$$

This formula is based on the bulk compressibilities given by Ishihara at n = 0.3 and n = 0.5. The constrained compressibility of the skeleton, C_c, was calculated from G_0 and C_b from Equation (4-39). Other data used in the computation were: ρ_w = 1.94 lb-sec^2/ft, $C_w = 2.348 \times 10^{-8}$ ft^2/lb, ρ_s = 5.15 lb-sec^2/ft and K_0 = 1. Results are shown in Figures 6-1 and 6-2. The wave speed for incompressible soil grains suspended in water could be computed from the Wood equation[54] and was also shown in Figure 6-2 for comparison.

From Figures 6-1 and 6-2 it is seen that 4 real and distinct eigenvalues of matrix $\tilde{A}$ were obtained for a wide range of soils. Hence Equation (6-3) is hyperbolic within the range of void ratio and the range of effective confining pressure tested. These ranges are wide enough to cover situations in which possible liquefaction need be investigated.

6-2. The characteristic equations.

After the wave speeds are obtained, one can solve for the transformation $\tilde{E}$. Noting that $\tilde{B}$ is a unit matrix, one can write Equation (6-6) as

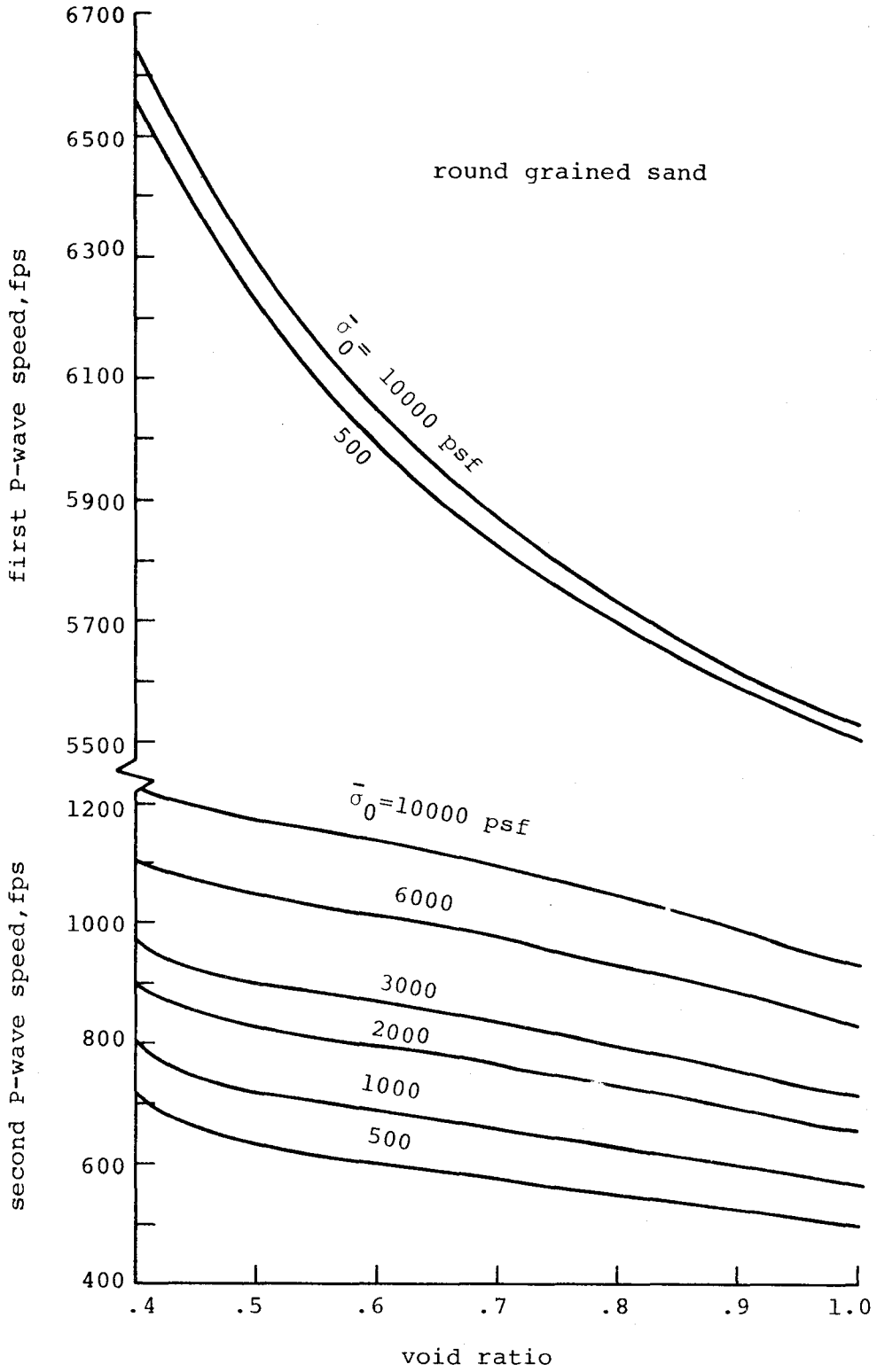

Figure 6-1 Variation of pressure wave speeds with respect to void ratio and effective confining pressure; round grained sand

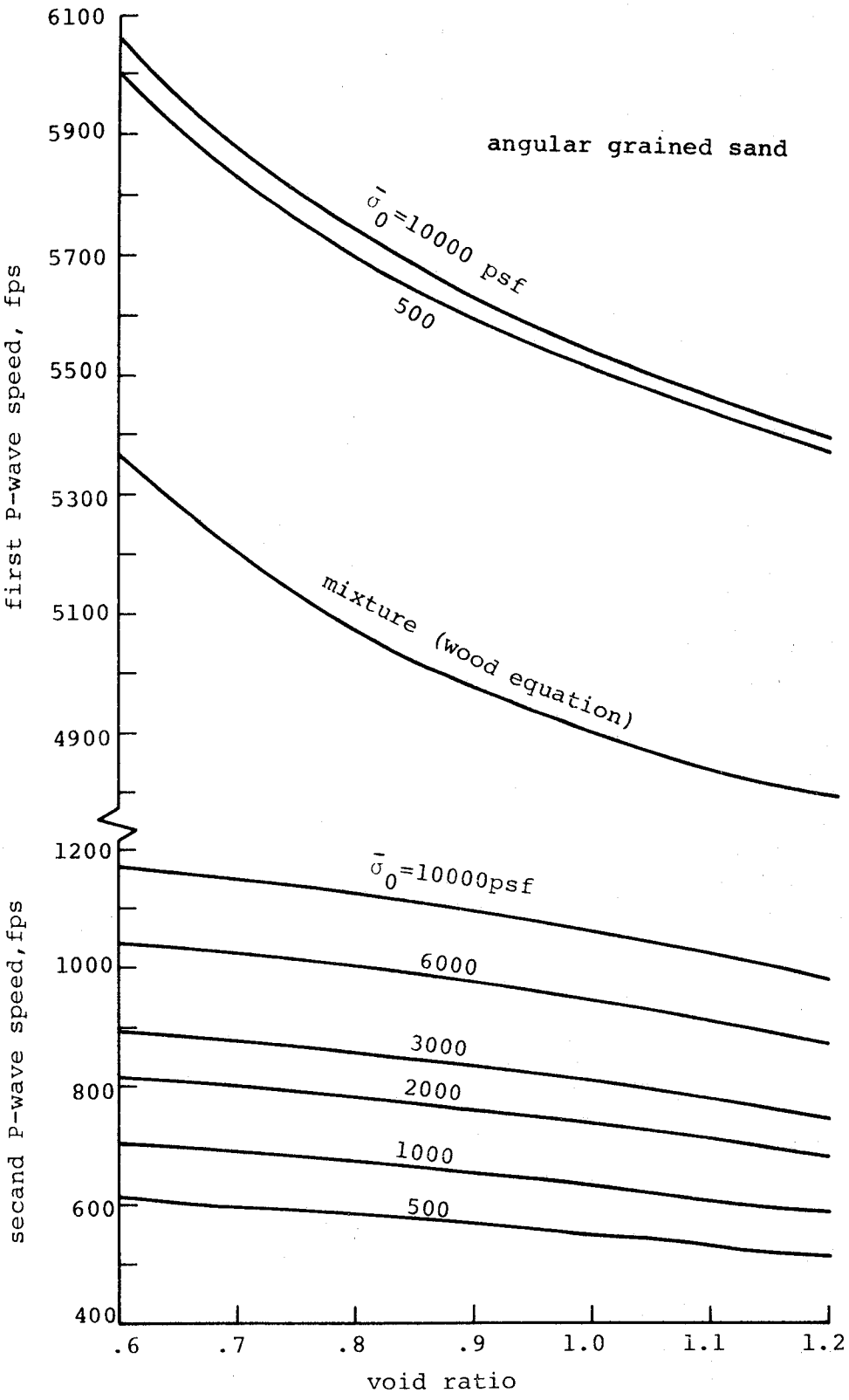

Figure 6-2 Variation of pressure wave speeds with respect to void ratio and effective confining pressure; angular grained sand

$$\begin{pmatrix} e_{11} & e_{12} & e_{13} & e_{14} \\ e_{21} & e_{22} & e_{23} & e_{24} \\ e_{31} & e_{32} & e_{33} & e_{34} \\ e_{41} & e_{42} & e_{43} & e_{44} \end{pmatrix} \begin{pmatrix} 0 & 0 & d_1 & d_2 \\ 0 & 0 & d_3 & d_4 \\ d_5 & d_6 & 0 & 0 \\ d_7 & d_8 & 0 & 0 \end{pmatrix} = \begin{pmatrix} \lambda_1 & 0 & 0 & 0 \\ 0 & \lambda_2 & 0 & 0 \\ 0 & 0 & \lambda_3 & 0 \\ 0 & 0 & 0 & \lambda_4 \end{pmatrix} \begin{pmatrix} e_{11} & e_{12} & e_{13} & e_{14} \\ e_{21} & e_{22} & e_{23} & e_{24} \\ e_{31} & e_{32} & e_{33} & e_{34} \\ e_{41} & e_{42} & e_{43} & e_{44} \end{pmatrix}$$

After the multiplication, one can equate the ith row on both sides and obtain the following

$$\begin{cases} e_{i3}\, d_5 + e_{i4}\, d_7 = \lambda_i\, e_{i1} \\ e_{i3}\, d_6 + e_{i4}\, d_7 = \lambda_i\, e_{i2} \\ e_{i1}\, d_1 + e_{i2}\, d_3 = \lambda_i\, e_{i3} \\ e_{i1}\, d_2 + e_{i2}\, d_4 = \lambda_i\, e_{i4} \end{cases} \qquad (6\text{-}13)$$

for i = 1, 2, 3, 4.

System (6-13) is a homogeneous system for e_{ij}, j = 1, 2, 3, 4. Since λ_i satisfies Equation (6-8), non-trivial solutions exist. Because of this condition, only three equations in system (6-10) are independent. One can set $e_{i4} = 1$ and solve for e_{i1}, e_{i2} and e_{i3} accordingly. The results are

$$\begin{cases} e_{i1} = \dfrac{\lambda_i^{\,2}\, d_5 + d_4\, d_6\, d_7 - d_4\, d_5\, d_8}{\lambda_i (d_4\, d_6 + d_2\, d_5)}\,, \\ e_{i2} = \dfrac{\lambda_i - e_{i1}\, d_2}{d_4}\,, \\ e_{i3} = \dfrac{\lambda_i\, e_{i2} - d_8}{d_6}\,, \\ e_{i4} = 1 \end{cases} \qquad (6\text{-}14)$$

for i = 1, 2, 3, 4. This completes the solution for $\tilde{E}$.

The ith row of Equation (6-5) can be written out in long hand as

$$e_{i1}\frac{\partial W}{\partial t} + e_{i2}\frac{\partial \overline{W}}{\partial t} + e_{i3}\frac{\partial S}{\partial t} + \frac{\partial \sigma}{\partial t} + \lambda_i e_{i1}\frac{\partial W}{\partial z} + \lambda_i e_{i2}\frac{\partial \overline{W}}{\partial z}$$

$$+ \lambda_i e_{i3}\frac{\partial S}{\partial t} + \lambda_i \frac{\partial \sigma}{\partial t} + e_{i1}\left(\frac{n^2\rho_w g}{k(n\rho_w-\rho)}\overline{W} - g\right)$$

$$- e_{i2}\frac{n\rho g}{k(n\rho_w-\rho)}\overline{W} + \frac{1}{C_c}\left(\sigma - \frac{S}{n}\right)\frac{\partial C_c}{\partial t} = 0 ,$$

or

$$e_{i1}\left(\frac{\partial W}{\partial t} + \lambda_i \frac{\partial W}{\partial z}\right) + e_{i2}\left(\frac{\partial \overline{W}}{\partial t} + \lambda_i \frac{\partial \overline{W}}{\partial z}\right) + e_{i3}\left(\frac{\partial S}{\partial t} + \lambda_i \frac{\partial S}{\partial t}\right)$$

$$+ \left(\frac{\partial \sigma}{\partial t} + \lambda_i \frac{\partial \sigma}{\partial z}\right) + e_{i1}\left(\frac{n^2\rho_w g}{k(n\rho_w-\rho)}\overline{W} - g\right) - e_{i2}\frac{n\rho g}{k(n\rho_w-\rho)}\overline{W}$$

$$+ \frac{1}{C_c}\left(\sigma - \frac{S}{n}\right)\frac{\partial C_c}{\partial t} = 0 .$$

In terms of characteristics, one can write

$$C^i \begin{cases} e_{i1}\frac{dW}{dt} + e_{i2}\frac{d\overline{W}}{dt} + e_{i3}\frac{dS}{dt} + \frac{d\sigma}{dt} + e_{i1}\left(\frac{n^2\rho_w g}{k(n\rho_w-\rho)}\overline{W} - g\right) - \\ e_{i2}\frac{n\rho g}{k(n\rho_w-\rho)}\overline{W} + \frac{1}{C_c}\left(\sigma - \frac{S}{n}\right)\frac{\partial C_c}{\partial t} = 0 \\ \frac{dz}{dt} = \lambda_i \end{cases} \qquad (6\text{-}15)$$

for i = 1, 2, 3, 4. The first equation in system (6-15) is called the C^i characteristics equation, and it is valid only if the second equation is satisfied.

System (6-15) is equivalent to System (6-3) in the sense that every solution of the one is a solution of the other. However, in contrast to System (6-3), every characteristics equation in System (6-15) contains derivatives in a common direction on the z-t plane. This fact not only enables one to approximate System (6-15) conveniently by finite differences, it also simplifies the treatment of boundary conditions.

6-3. Finite difference approximation.

The numerical procedure is best visualized on a z-t diagram shown in Figure 6-3. The method of specified time intervals[41] is used to establish the z-t grid. After discretization, the material properties in each distance interval are considered to be uniform. Since the wave speeds vary with time, conditions at points 1, 2, 3, and 4 must be evaluated from known conditions at points A, B and C before the conditions at point p can be found. The following interpolation formulas, in terms of the skeletal velocity W, are used for interior points

at point 1

$$W_1 = W_C + \frac{\lambda_1 \Delta t}{\Delta z} (W_A - W_C) \ , \qquad (6\text{-}16)$$

at point 2

$$W_2 = \frac{1}{2\ \Delta z^2} [\lambda_2 \Delta t(\lambda_2 \Delta t + \Delta z)\ W_A + 2(\lambda_2{}^2 \Delta t^2 - \Delta z^2)\ W_C$$

$$+ \lambda_2 \Delta t\ (\lambda_2 \Delta t - \Delta z)\ W_B] \ , \qquad (6\text{-}17)$$

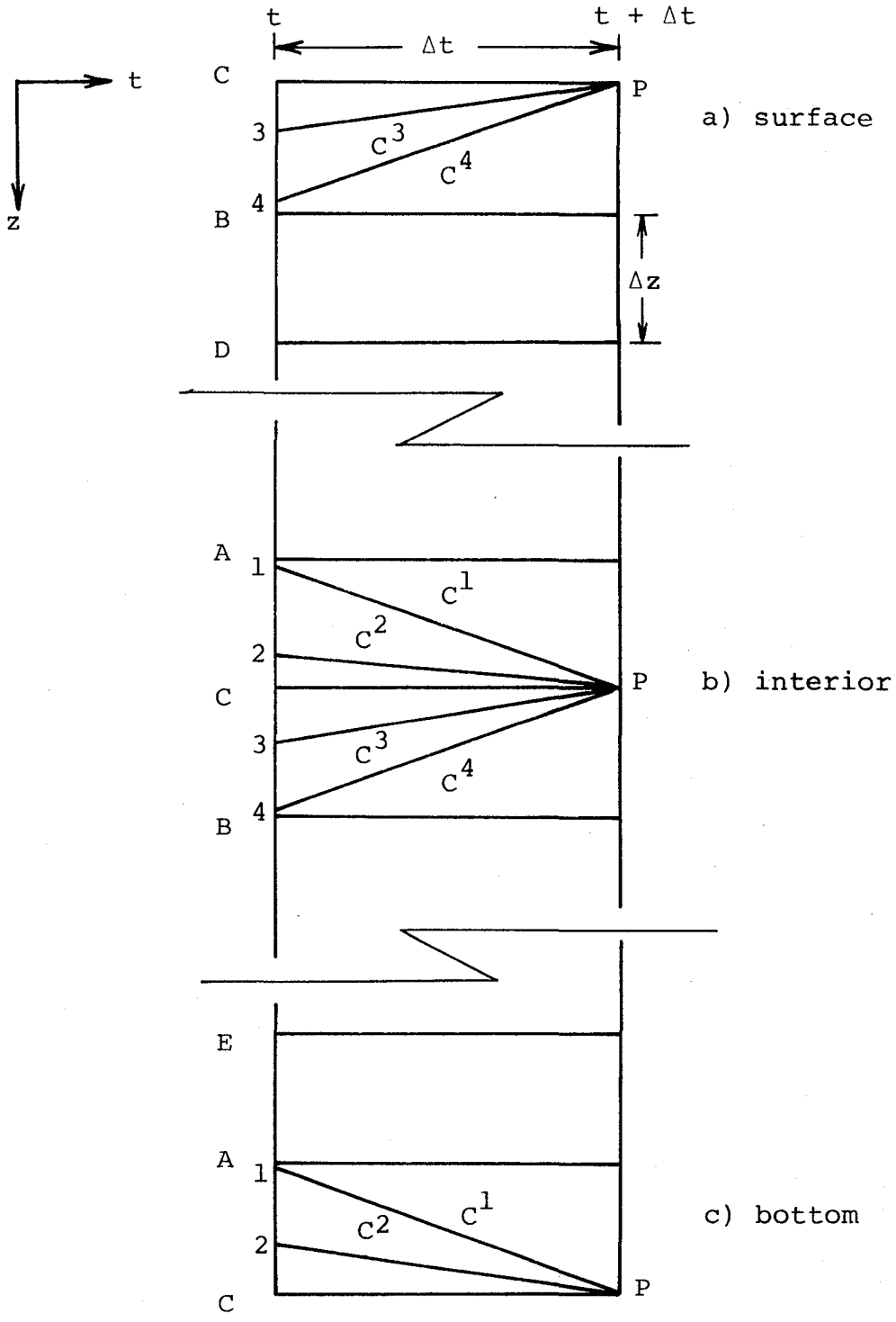

Figure 6-3 z-t diagram for numerical solution of pressure wave propagation in saturated deposits.

at point 3

$$W_3 = \frac{1}{2\ \Delta z^2}\ [\lambda_3\Delta t\ (\lambda_3\Delta t + \Delta z)\ W_A + 2(\lambda_3{}^2\Delta t^2 - \Delta z^2)\ W_C + \lambda_3\Delta t\ (\lambda_3\Delta t - \Delta z)\ W_B]\ , \qquad (6\text{-}18)$$

at point 4

$$W_4 = W_C - \frac{\lambda_4\Delta t}{\Delta z}\ (W_B - W_C)\ . \qquad (6\text{-}19)$$

Similar interpolation formulas are used to obtain $\bar{W}_i$, S_i, and σ_i for i = 1, 2, 3, 4.

The C^i characteristics equation is integrated in its characteristic direction as

$$\begin{aligned} &e_{i1}\ (W_P - W_i) + e_{i2}\ (\bar{W}_P - \bar{W}_i) + e_{i3}\ (S_P - S_i) \\ &+ (\sigma_P - \sigma_i) = \frac{\Delta t}{2}\ [e_{i2}\ \frac{n\rho g}{k(n\rho_w - \rho)}\ (\bar{W}_P + \bar{W}_i) \\ &- e_{i1}\ \frac{n^2\rho_w g}{k(n\rho_w - \rho)}\ (\bar{W}_P + \bar{W}_i)] + \Delta t\ e_{i1}\ g \\ &- \frac{\Delta t}{2}\ [C_{c_t}(\sigma_i - \frac{S_i}{n})\frac{\partial C_c}{\partial t}\Big|_t + C_{c_{t+\Delta t}}(\sigma_P - \frac{S_P}{n})\frac{\partial C_c}{\partial t}\Big|_{t+\Delta t}] \end{aligned} \qquad (6\text{-}20)$$

for i = 1, 2, 3 and 4. e_{i1}, e_{i2} and e_{i3} are evaluated at time t. The subscripts t and t + Δt represent the time at which the quantities under consideration are evaluated. It is adequate to use first order approximations for the coefficients of the first three terms of the characteristic equations of System (6-15), while second order approximations are necessary for the last three terms in the same equation.

For a given initial condition, for example, the static

condition, W_i, $\bar{W}_i$, S_i and σ_i, i = 1, 2, 3, 4, can be computed from the interpolation formulas. One can then solve for W, $\bar{W}$, S, and σ at every interior node from the four equations represented by Equation (6-20).

At the surface of the deposit, two characteristics can be drawn from the interior to the upper boundary. Referring to Figure 6-3a, the interpolation formula for obtaining the conditions at points 3 and 4, in terms of W, are

$$W_3 = \frac{1}{2\ \Delta z^2}\ [(2\Delta z + \lambda_3\Delta t)(\Delta z + \lambda_3\Delta t)\ W_C$$

$$+ 2\lambda_3\Delta t(2\Delta z + \lambda_3\Delta t)\ W_B + \lambda_3\Delta t(\Delta z + \lambda_3\Delta t)\ W_D], \qquad (6\text{-}21)$$

$$W_4 = W_C - \frac{\lambda_4\Delta t}{\Delta z}\ (W_B - W_C)\ . \qquad (6\text{-}22)$$

The boundary conditions, discussed in the next section, together with the integrated C^3 and C^4 characteristic equations in Equation (6-20) constitute a system of four equations which enables one to solve the four variables at the surface.

At the bottom of the deposit, two characteristics can be drawn from the interior to the lower boundary. Referring to Figure 6-3c, the interpolation formula for obtaining the conditions at points 1 and 2, in terms of W, are

$$W_1 = W_C + \frac{\lambda_1\Delta t}{\Delta z}\ (W_A - W_C)\ , \qquad (6\text{-}23)$$

$$W_2 = \frac{1}{2\ \Delta z^2}\ [\lambda_1 \Delta t(\lambda_1 \Delta t - \Delta z)W_E + 2\lambda_1 \Delta t(\lambda_1 \Delta t - 2\Delta z)\ W_A$$

$$+\ (\lambda_1 \Delta t - \Delta z)(\lambda_1 \Delta t - 2\Delta z)W_C]. \quad (6\text{-}24)$$

Two boundary conditions together with the C^1 and C^2 characteristic equations in Equation (6-20) yield a unique solution for the four unknowns at the lower boundary.

After the solution is obtained at $t + \Delta t$, one can obtain the solution at $t + 2\Delta t$ by the same procedure.

6-4. Boundary conditions.

A few boundary conditions are considered in this section.

(a) Free surface.

At the free surface, there is no stress in the soil skeleton, and the pore water pressure is zero, therefore

$$S(0,\ t) = 0\ , \quad (6\text{-}25)$$

and

$$\sigma(0,\ t) = 0\ . \quad (6\text{-}26)$$

W and $\overline{W}$ can then be solved from the integrated C^3 and C^4 characteristic equations.

(b) Unsaturated soil layer above the water table.

The upper boundary of the deposit is always considered to be at the water table. During transients, the vertical acceleration of the soil mass between the ground surface and the upper boundary is negligible when compared with that in the horizontal direction. Therefore, the effective stress at the upper boundary can be considered to be equal

to the weight of the unsaturated soil per unit surface area. The elevation of the water table is treated as fixed during ground shaking. Hence the boundary conditions are

$$S(0, t) = 0 , \tag{6-27}$$

and

$$\sigma(0, t) = WGT . \tag{6-28}$$

(c) Impermeable bedrock at the base of the deposit.

No relative motion between the soil skeleton and pore water can take place at the impermeable base, therefore

$$\overline{W}(D, t) = 0. \tag{6-29}$$

The vertical component of the skeletal velocity at the base is identical to that of the bedrock, hence

$$W(D, t) = \text{vertical component of the bedrock motion} \tag{6-30}$$

Other boundary conditions, such as permeable bedrock, may be incorporated into the numerical procedure. These more complicated boundary conditions are not included in the present study.

6-5. Accuracy.

The accuracy of the numerical procedure is checked by using the steady oscillatory motion treated in Chapter 5. From the analytical solution, the velocities and dynamic stresses at a particular instant can be computed. Then by adding the static stresses to the dynamic stresses, one can obtain the actual level of stresses in the deposit. Using these velocities and stress levels as the initial conditions

and treating the boundary conditions appropriately, the steady oscillatory motion should be closely approximated by the numerical procedure.

Consider a horizontal saturated deposit 50 feet deep with the following material properties: $n = 0.4$, $\rho_s = 5.13$ lb-sec^2/ft, $C_c = 2.4 \times 10^{-7}$ ft^2/lb, $\rho_w = 1.94$ lb-sec^2/ft, $C_w = 2.3 \times 10^{-8}$ ft^2/lb and $k = 0.001$ fps. This deposit was set in steady oscillatory motion with a frequency of 5 Hertz. The skeletal velocity at the impervious bedrock was $0.2 \sin(10\pi t)$ fps.

For the numerical solution, the deposit was divided into 5 equal distant intervals. The solution at a depth of 20 feet was obtained from both the analytical solution and the numerical procedure. Results are plotted in Figures 6-4 and 6-5. In the numerical solution the computation had been carried out for seven cycles, and the motion stayed steady oscillatory throughout these seven cycles. It is seen that the agreement between these solutions was excellent.

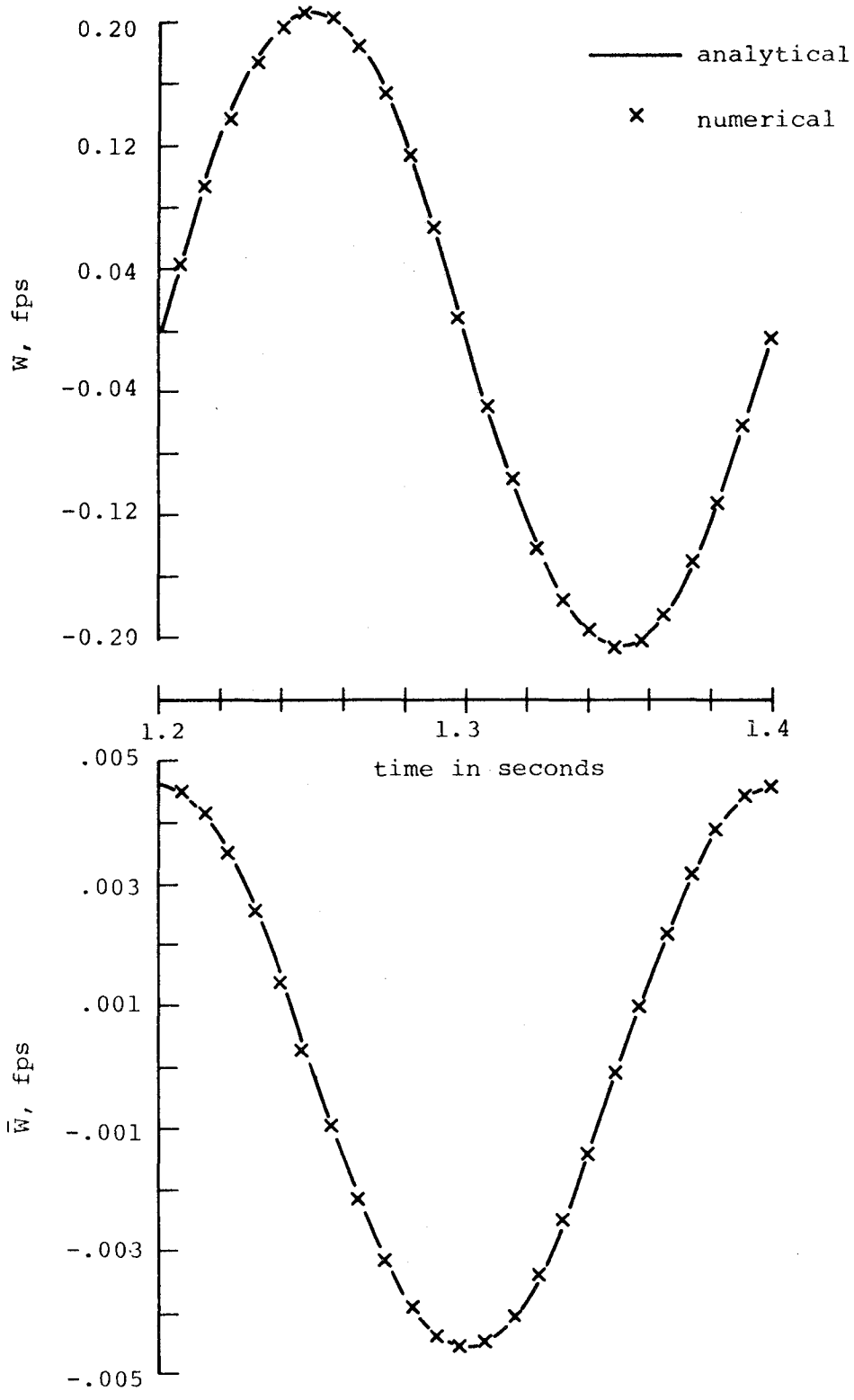

Figure 6-4 Comparison of the analytical solution and the numerical solution, W and $\bar{W}$ 20 feet below the ground surface

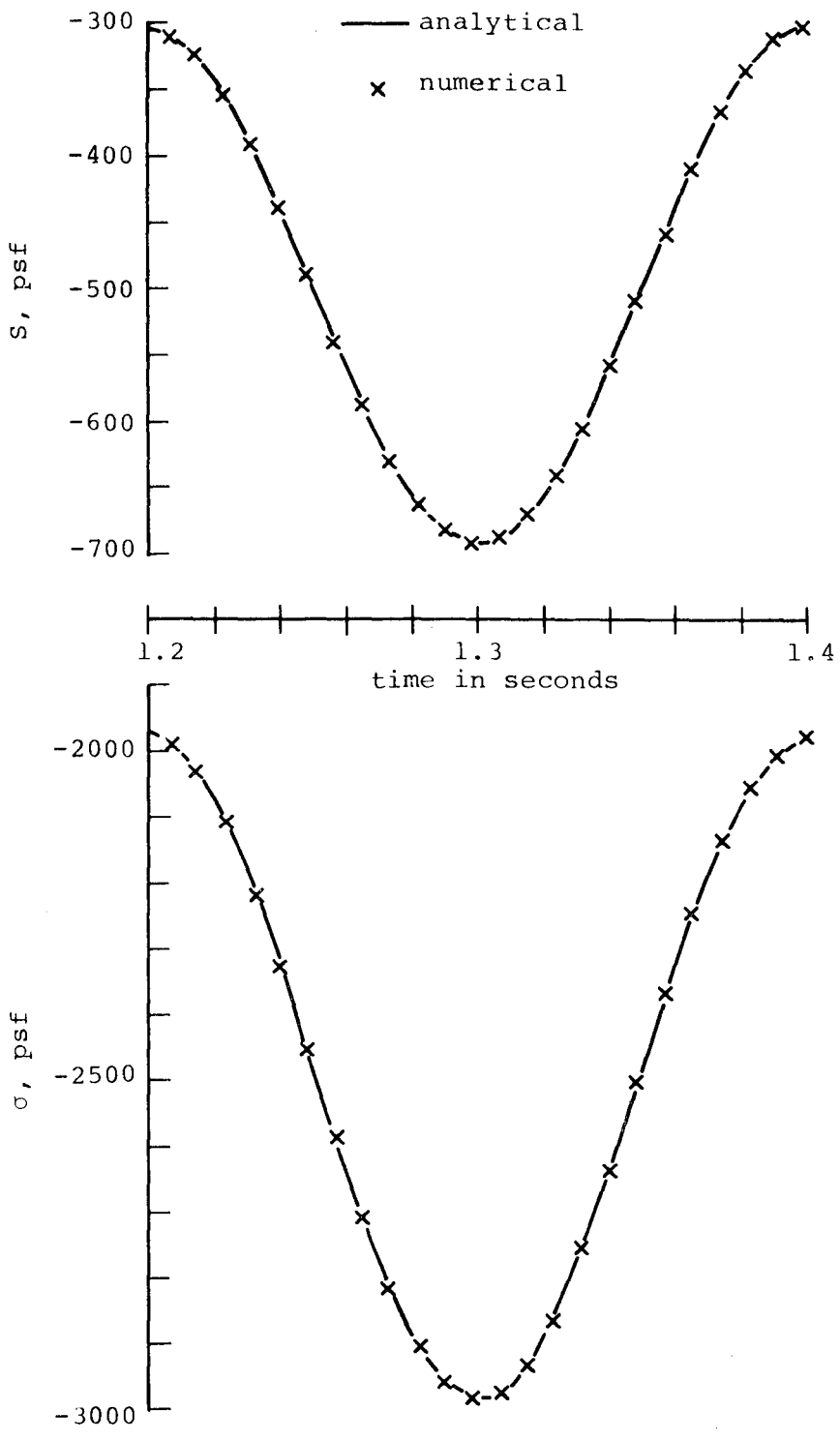

Figure 6-5 Comparison of the analytical solution and the numerical solution; S and σ 20 feet below the ground surface

CHAPTER 7

VERTICAL MOTIONS OF SOILS WITH SPECIFIED TIME HISTORY OF SHEAR MODULI

This chapter concerns the calculation of transient pore water pressure and effective stress in a saturated soil deposit when the constrained compressibility of the soil is rapidly changed. The constrained compressibility at a given depth in the deposit is visualized as a time-varying function resulting from dynamic shearing. In this chapter prespecified time histories of the secant shear modulus are used to simulate changes in the constrained compressibility. Examples are employed to demonstrate the resulting vertical motions and the accompanying changes in effective stress and pore water pressure in a horizontal deposit.

It is to be noted that the shear modulus of the skeleton depends upon the shearing strain amplitude and the effective stress, hence it should not be specified independently. However, the examples with specified shear modulus changes does provide an aid in the description of the pressure wave submodel when changes in constrained compressibility are present. More realistic cases are presented in the next chapter.

7-1. Monotonic weakening of skeleton

Consider a level deposit 53.33 feet deep with following properties: $n = 0.4$, $\rho_s = 5.13$ lb-sec^2/ft, $C_b = 4.8 \times 10^{-7}$ ft^2/lb, $K_0 = 1.0$, $\rho_w = 1.94$ lb-sec^2/ft, $C_w = 2.3 \times 10^{-8}$ ft^2/lb and $k = 0.001$ fps. The water table was 3.33 ft below the

ground surface. The small motion shear modulus, G_0, throughout the deposit was calculated from Equation (6-10). The time history of secant shear modulus at depth z, G_s (z, t), was specified as

$$G_s\ (z,\ t) = \begin{cases} G_0(z)\ \cos\ (2.09\ t),\ t \leq 0.7 \\ \\ G_s(z,\ 0.7) \qquad\qquad ,\ t > 0.7 \end{cases} \tag{7-1}$$

The deposit under the water table was divided into 8 equal distance intervals. The shear modulus in each interval was considered to be the average value of the shear moduli at the ends of the interval. The constrained compressibility of each interval was computed from Equation (4-40). Its time rate of change was computed from

$$\frac{\partial C_c}{\partial t} = -\frac{4}{3}\ C_c^{\,2}\ \frac{\partial G_s}{\partial t} \tag{7-2}$$

This equation can be obtained directly from Equation (4-42).

The response of the deposit to the G_s changes are shown in Figures 7-1 and 7-2. It can be seen that during the course of shear modulus reduction, the pore water pressure increased, and at the same time, the effective stress decreased such that the total stress at a section stayed approximately constant. Accompanying the pore water pressure buildup, there was an upward flow of water. Downward displacement of the skeleton took place throughout the deposit. After the shear modulus in the bottom interval reached the low value at 0.7 seconds, as shown in Figure 7-1, the effective stress at the bottom started to recover, and the excess

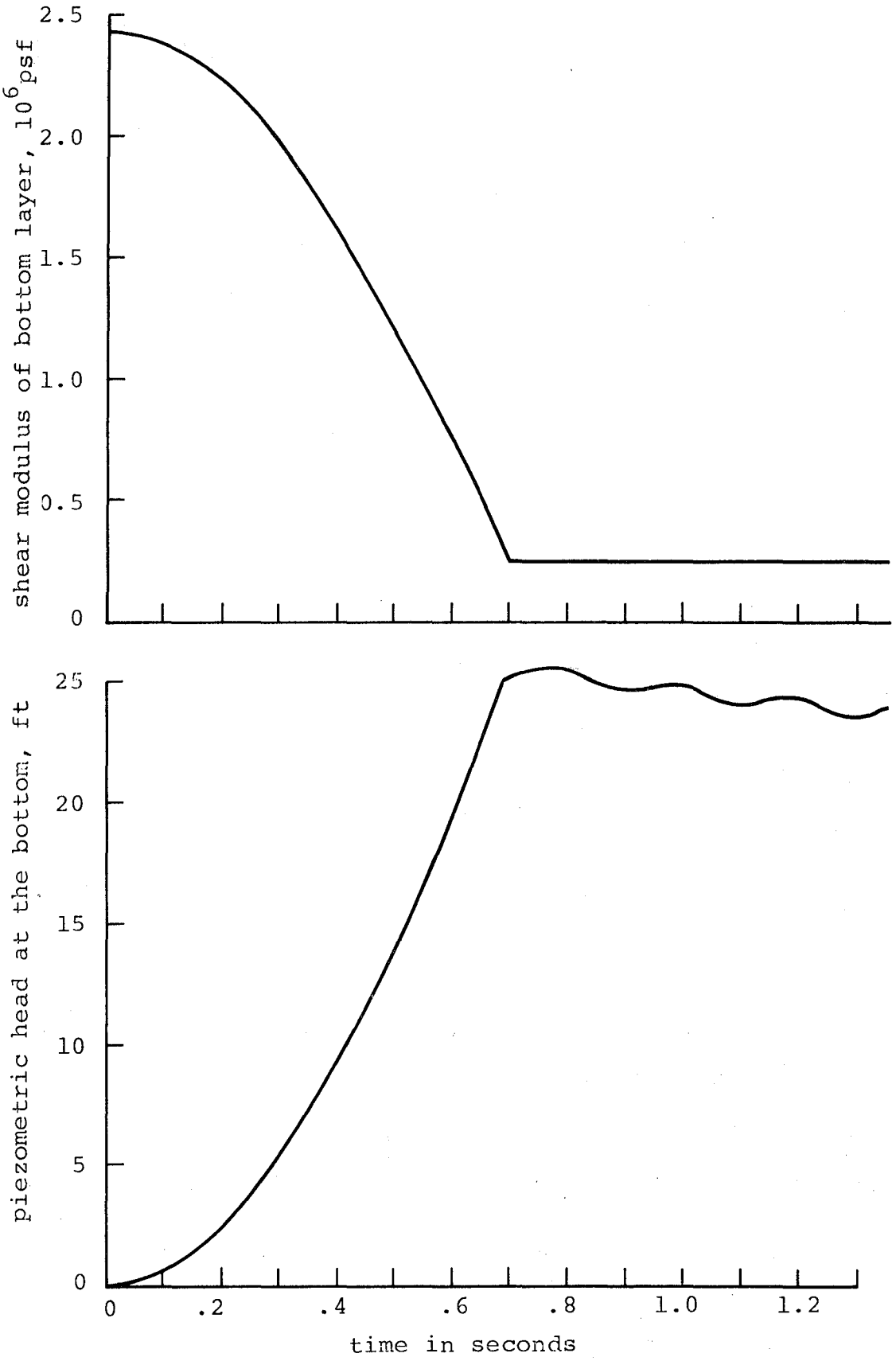

Figure 7-1 Shear modulus reduction and excess pore water pressure change

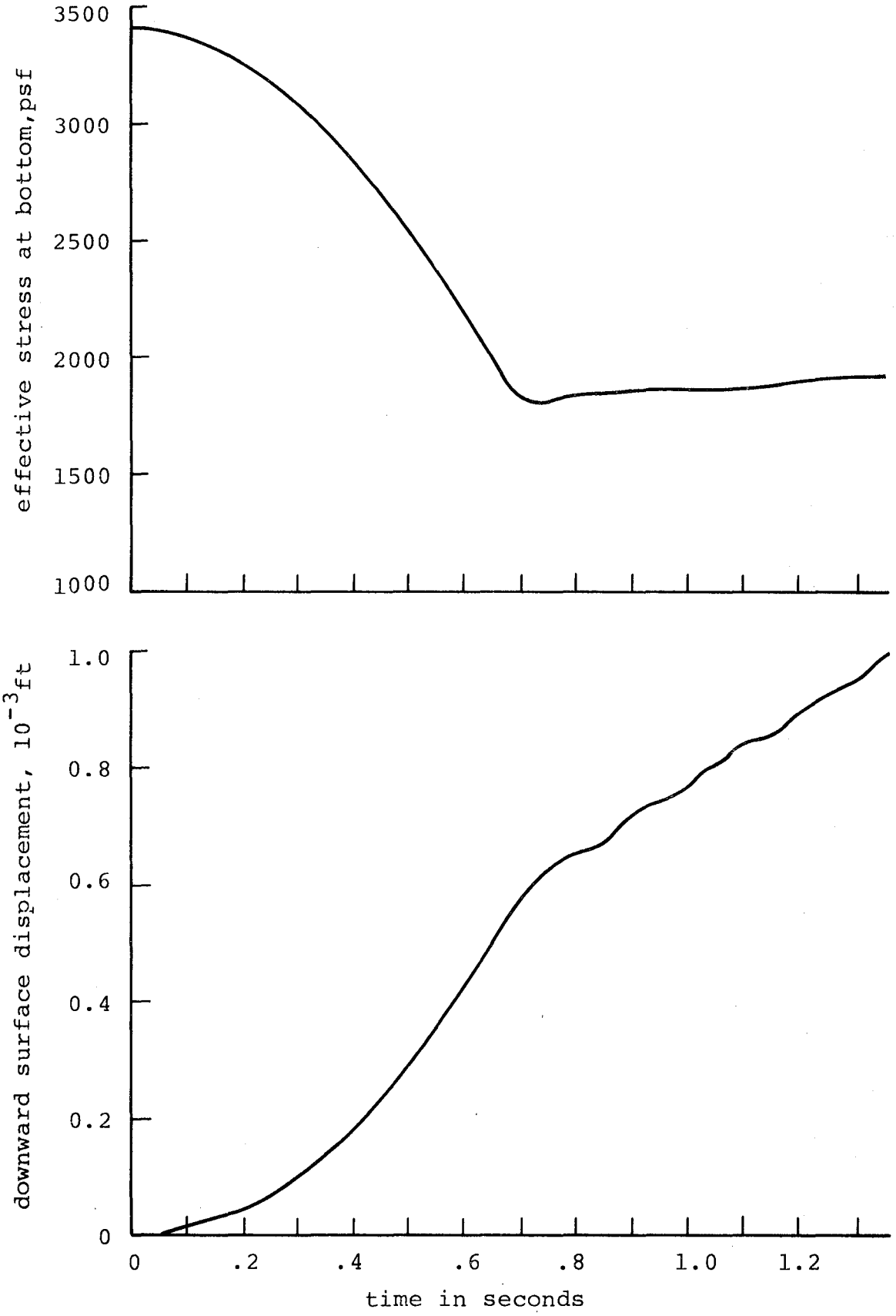

Figure 7-2 Effective stress and downward surface settlement as functions of time

pore water pressure was dissipated gradually. Upward flow of the pore water and the downward movement of the skeleton continued. The tendency toward a new static equilibrium with a smaller porosity was evident.

7-2. Cyclic weakening of the skeleton

When a sand is subjected to cyclic shearing in the strain softening range, its shearing stress-shearing strain relation can be represented schematically by Figure 7-3. Associated with each stroke, for example, from a to b, there is a monotonic decrease in the secant shear modulus. Upon the shearing strain reversal at b, the soil regains most of its shearing rigidity. A monotonic decrease in shear modulus takes place again for stroke bc. The corresponding variation of the secant shear modulus with time is shown schematically in Figure 7-4. Similar shear moduli changes were used in the following example.

Consider a horizontal saturated deposit 50 feet deep with the following properties: $n = 0.5$, $\rho_s = 5.13$ lb-sec^2/ft, $C_b = 2.2 \times 10^{-6}$ ft^2/lb, $K_0 = 1.0$, $\rho_w = 1.94$ lb-sec^2/ft, $C_w = 2.35 \times 10^{-8}$ ft^2/lb, and $k = 0.00328$ fps. The water table was at the ground surface. The small motion shear modulus throughout the deposit was a function of effective stress, as described by Equation (6-10).

The deposit was divided into 8 equal distance intervals. The time history of the specified shear modulus of each interval was shown in Figure 7-5. Associated with each of the jumps at b, c, and d, there was an abrupt decrease in the

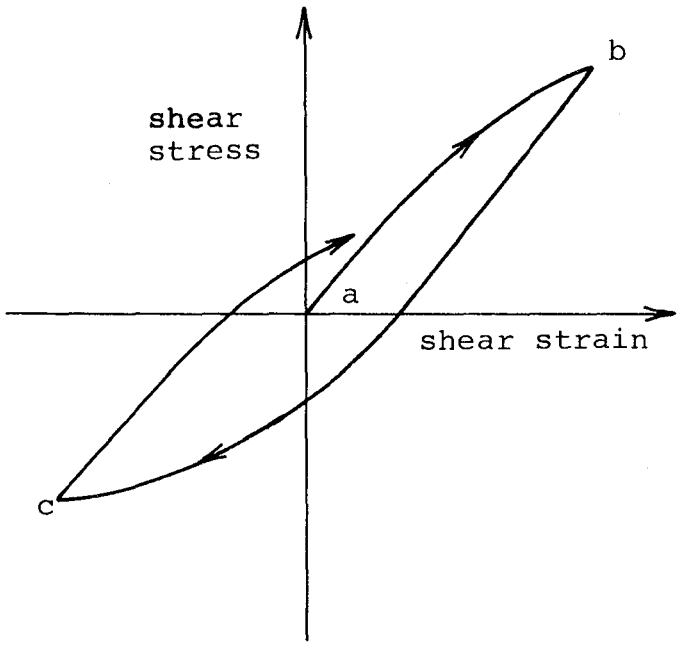

Figure 7-3 Schematic shearing stress-strain relationship

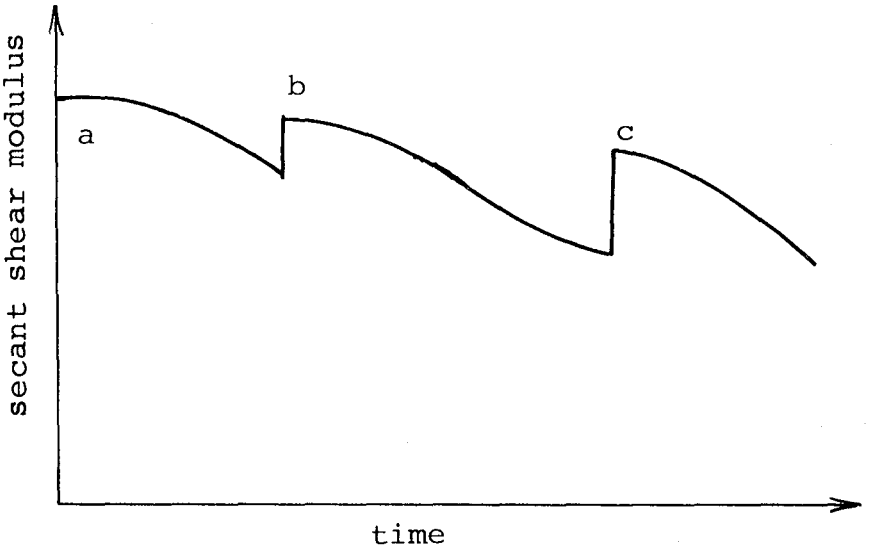

Figure 7-4 Schematic shear modulus change due to shearing

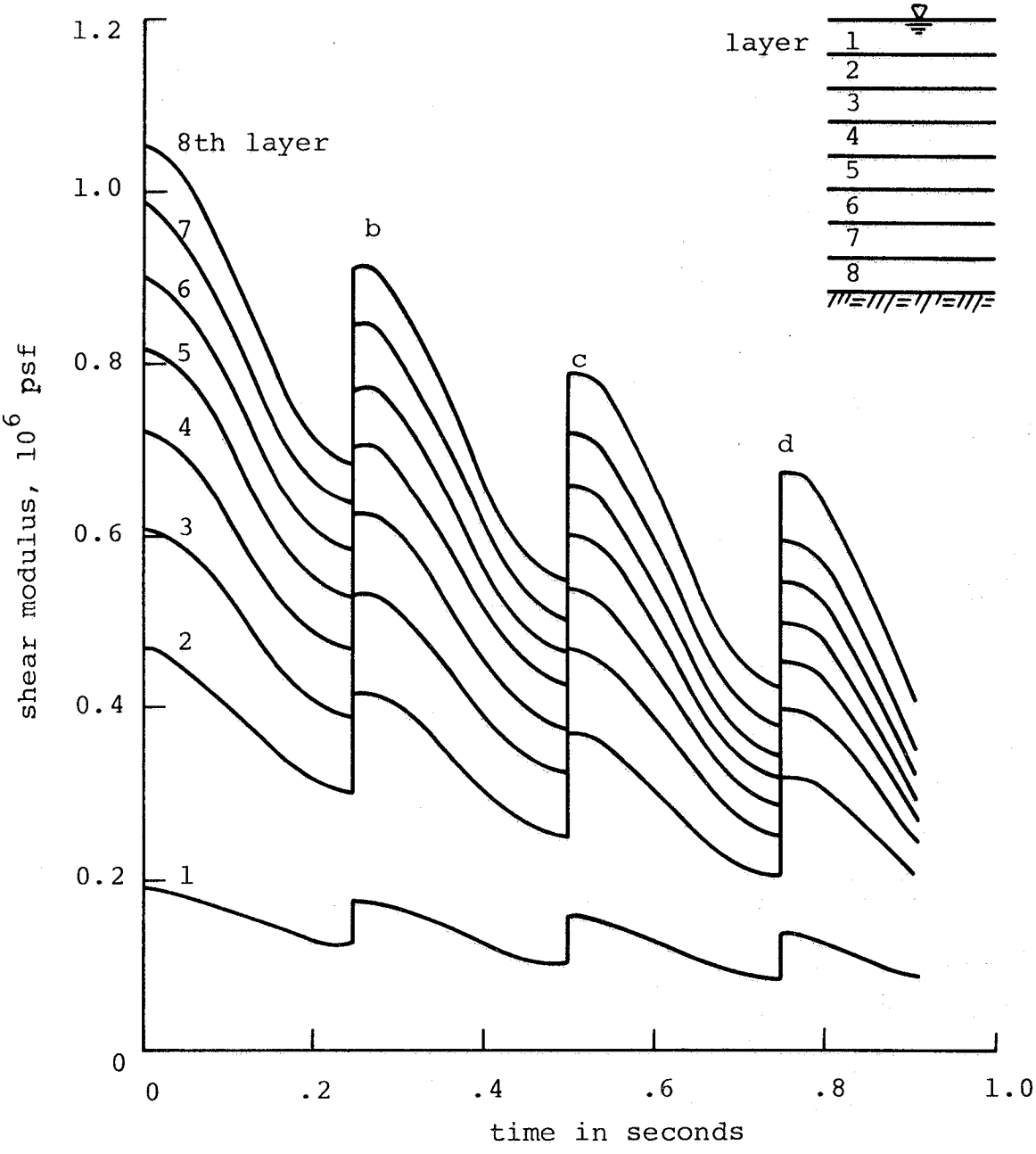

Figure 7-5 Time variations of shear moduli throughout the deposit

constrained compressibility of the skeleton. The time rate of change of the constrained compressibility immediately after the sudden stiffening was considered to be zero. The stresses and velocities immediately before the stiffening were used as the initial condition for the subsequent computations. By this procedure, the sudden stiffening of the skeleton did not interfere with the trend of the soil to move toward a denser state as shearing progresses.

Figure 7-6 illustrates the transfer of stress at the base of the deposit from skeleton to pore water. The pulses in these two traces corresponded to the shear modulus variations. At the beginning and the end of each stroke, the time rate of change of the shear modulus was smaller than that at the middle of the stroke. As a result, the pore water pressure rise at the ends of a shearing stroke was less rapid than that at the middle of the stroke. When the excess pore water pressure became high and, at the same time, the rate of shear modulus decrease was small, the soil might gain some effective stress. This situation occurred briefly at about 0.77 seconds, as indicated in Figure 7-6.

Figure 7-7 shows the profile of the excess pore water pressure, in terms of piezometric head, at various moments. Due to the presence of the impermeable bedrock, there was no pore water pressure gradient at the base of the deposit. In the interior and at the surface of the deposit the gradient of the excess pore water pressure was negative. Accordingly, pore water moved up towards the ground surface and eventually

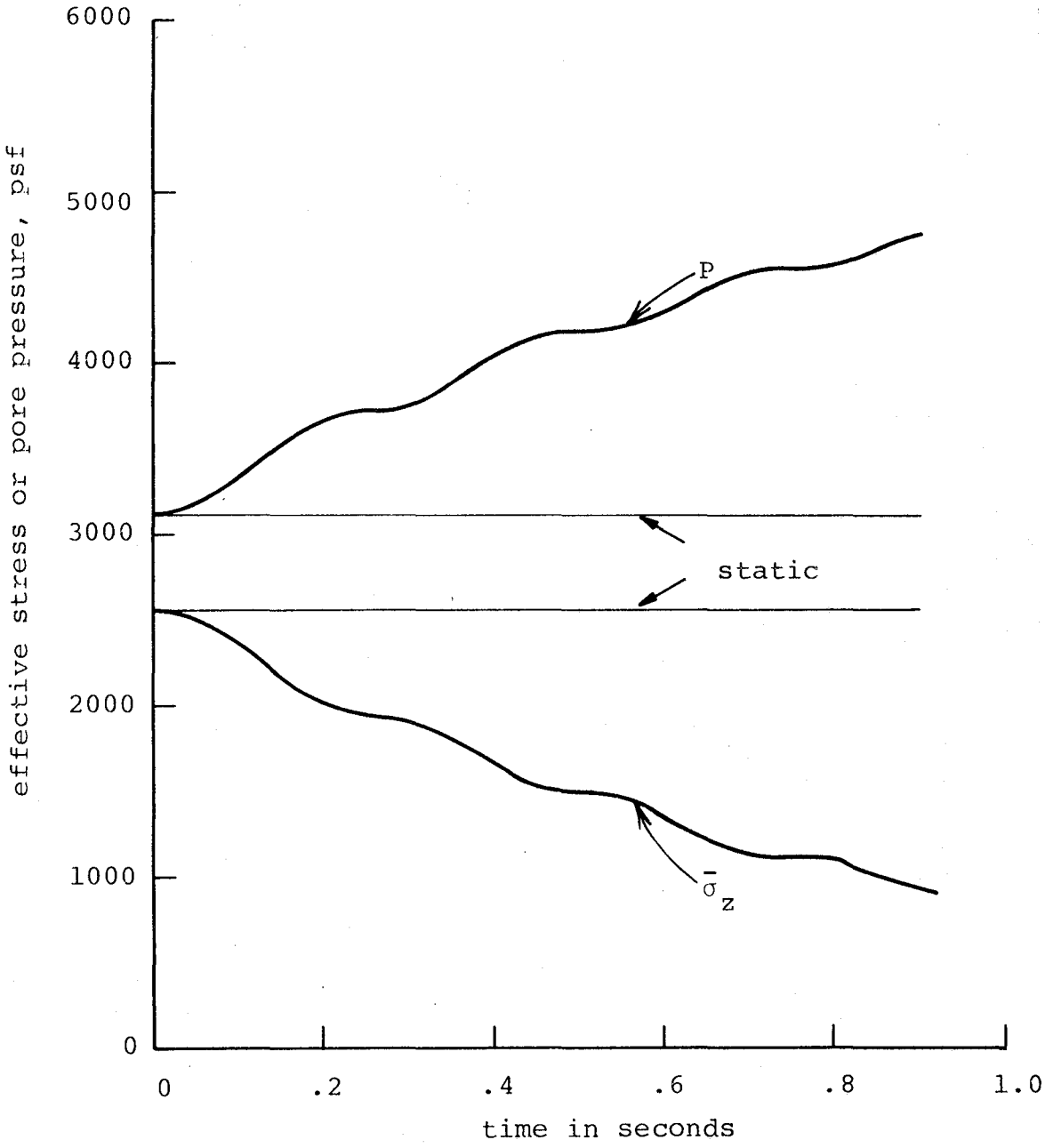

Figure 7-6 Transient pore water pressure and effective stress at the bottom of the deposit

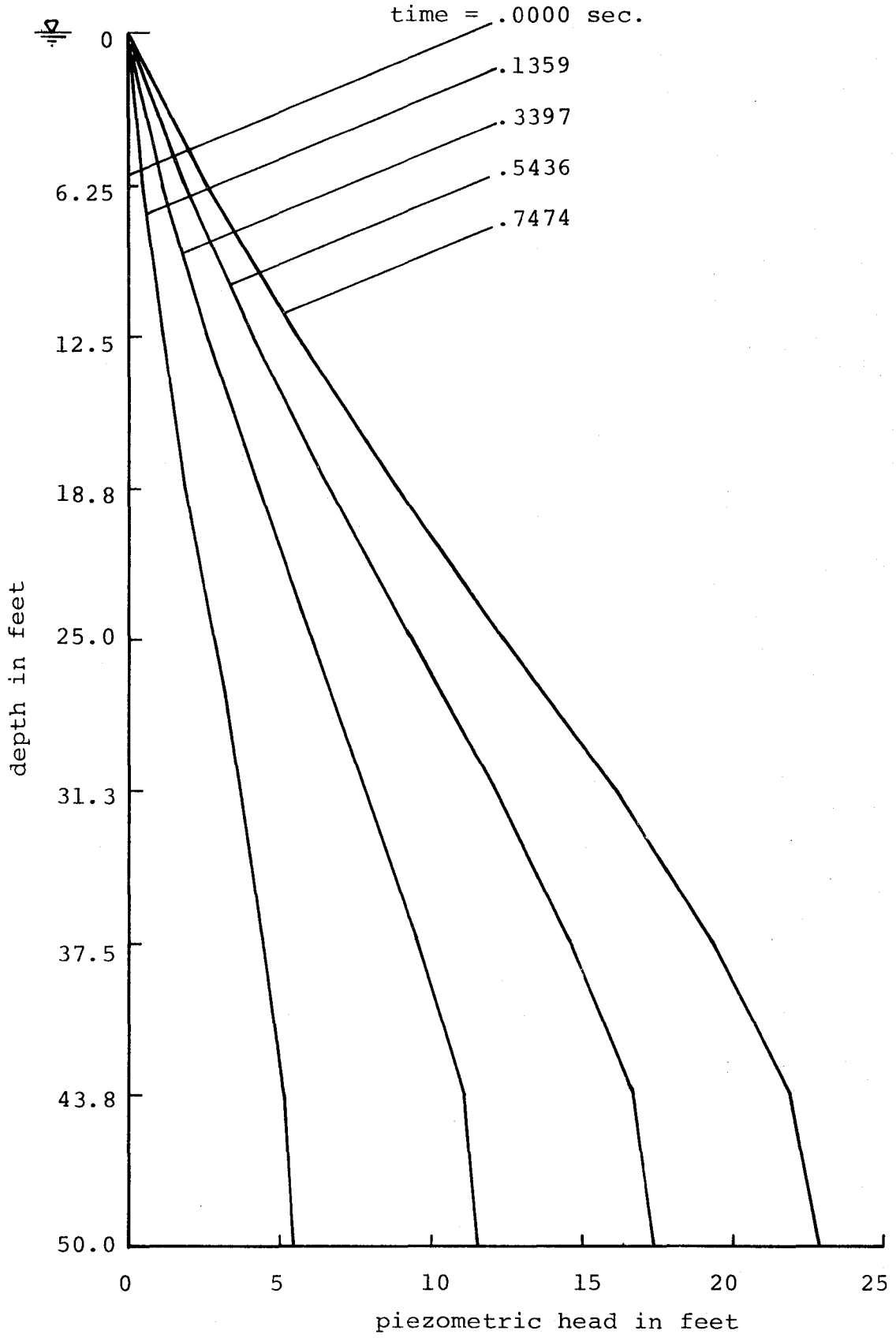

Figure 7-7 Profiles of excess pore pressure at selected instants

seeped out of the deposit. The flow of pore water was more rapid at the later stages when the negative gradient became larger. Figure 7-8 shows the accompanying transient effective stress profiles.

Downward displacement of the skeleton occurred throughout the deposit, as shown in Figure 7-9. It is noted that the maximum downward displacement occurred at approximately 18.75 feet, instead of at the ground surface. As a result, the porosity of the top three intervals increased as time progressed. This trend was consistent with the piezometric head profiles. In Figure 7-7, it can be seen that the maximum negative gradient occurred approximately at the middle of the deposit. According to Darcy's law and the principle of mass conservation, the amount of water contained in the top three intervals must increase as time went on, hence the increase of the porosity in the top three intervals. The porosity of the lower portion of the deposit decreased because of the upward drainage and the volume reduction in pore water itself.

The above example together with the example in Section 7-1 demonstrates that the pressure wave submodel is able to describe quantitavely the anticipated accumulated increase in pore water pressure and the corresponding reduction in effective stress when the constrained modulus of a saturated deposit is reduced.

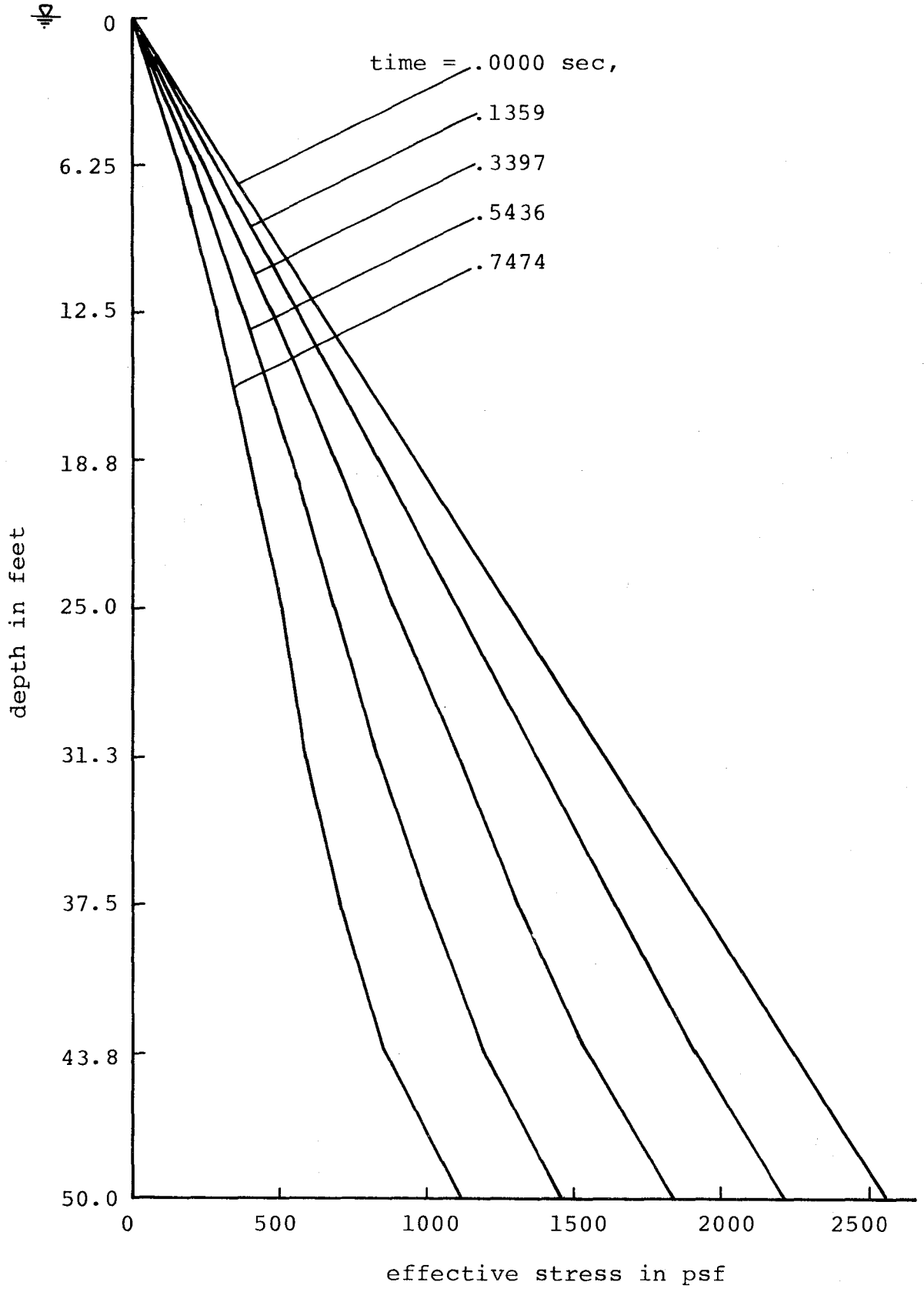

Figure 7-8 Profiles of effective stress at selected instants

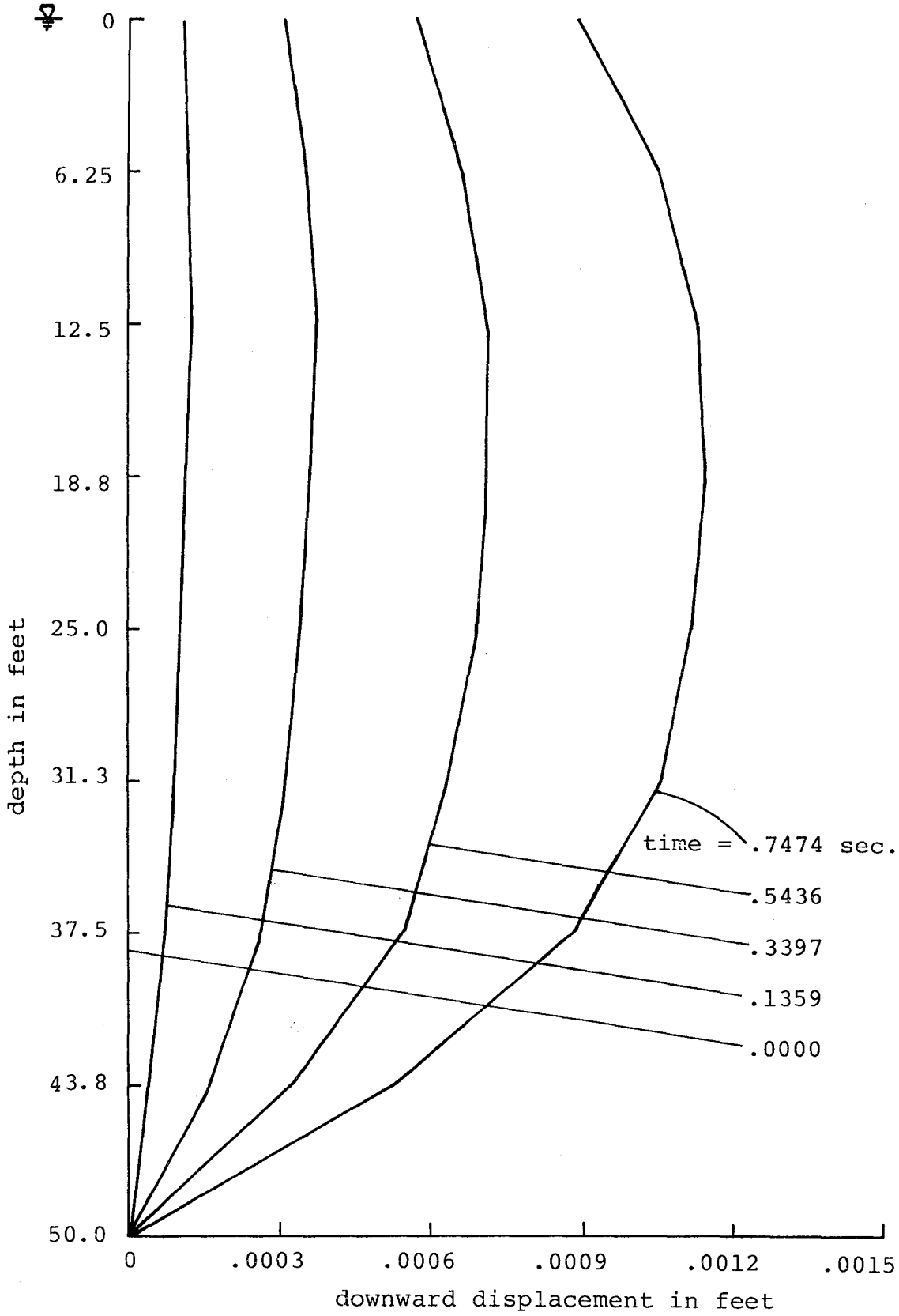

Figure 7-9 Profiles of downward displacement at selected instants

CHAPTER 8
THE LIQUEFACTION MODEL

The pressure wave submodel was presented in Chapter 7, where the time history of the shear modulus was specified in advance. A more realistic situation, in which the motion in the vertical direction is caused by repeated shearing, is developed in this chapter. A coupling between the propagation of plane shear waves and the vertical motion of the soil due to changes in its constrained compressibility is developed. The coupled motions constitute the model for liquefaction.

The liquefaction model is presented with the help of a flow diagram. The modeling of transient effective stress and changes in pore water pressure in horizontal deposits is demonstrated by examples. The use of the model to predict the onset of mass earth movement of slightly inclined deposits due to liquefaction is also presented.

8-1. Modified Ramberg-Osgood shearing stress-shearing strain relationships

The Ramberg-Osgood relationships, outlined in Chapter 3, have been used successfully to describe the shearing stress-shearing strain relationships for unsaturated soils deformed in the strain softening range. Since the effective stress at the depth under consideration is constant during shearing, the initial small motion shear modulus, G_0, and the shear strength, τ_m, are independent of time. When a

saturated soil is sheared rapidly, the effective stress at the depth under consideration is affected by the development of excess pore water pressure at that depth. Therefore the deformation characteristics of the skeleton vary with time.

The shearing stress-strain relationships used in the liquefaction model are

for initial loading,

$$\gamma = \frac{\tau}{G_0(\bar{\sigma}_z)} \left(1 + \alpha \left|\frac{\tau}{C_1 \tau_m(\bar{\sigma}_z)}\right|^{R-1}\right) , \qquad (8\text{-}1)$$

for unloading and reloading,

$$\gamma - \gamma_1 = \frac{\tau - \tau_1}{G_0(\bar{\sigma}_z)} \left(1 + \alpha \left|\frac{\tau - \tau_1}{2C_1 \tau_m(\bar{\sigma}_z)}\right|^{R-1}\right) \qquad (8\text{-}2)$$

in which $\bar{\sigma}_z$ denotes vertical effective stress. The meaning of the remaining variables are the same as those defined in Chapter 3.

Since at the depth under consideration, G_0 and τ_m are functions of the transient effective stress, the stress-strain curves represented by Equations (8-1) and (8-2) are no longer Ramberg-Osgood curves. For the rest of the study, Equations (8-1) and (8-2) are called the modified Ramberg-Osgood relationships. The dependence of G_0 on $\bar{\sigma}_z$ can be expressed by

$$G_0(\bar{\sigma}_z) = \eta \left(\frac{1 + 2K_0}{3} \bar{\sigma}_z\right)^{0.5} \qquad (8\text{-}3)$$

in which K_0 is the coefficient of earth pressure at rest. It is treated as constant throughout the depth and does not

change during shearing. η is a coefficient, its value at depth z depends upon the initial shearing rigidity of the soil at that depth. Equation (8-3) is similar to Equations (6-10) and (6-11), except that the effect of the void ratio is neglected. The relationship between τ_m and $\bar{\sigma}_z$ is

$$\tau_m = \{(\frac{1 + K_0}{2} \bar{\sigma}_z \sin \phi)^2 - (\frac{1 - K_0}{2} \bar{\sigma}_z)^2\}^{0.5} \qquad (8\text{-}4)$$

in which ϕ is the effective internal angle of friction.

An example was used to illustrate the effects of reduction in G_0 and τ_m upon the shearing behavior of soils. Assume that, as a result of shearing, the effective stress in a saturated soil element changed with the shearing stress. The assumed relation between the effective stress and the shearing stress is shown in Figure 8-1. Other parameters used in the example were $\alpha = 1$, $R = 3$, $C_1 = 0.8$, $\eta = 5000$, $K_0 = 0.5$ and $\phi = 35$ degrees. The modified Ramberg-Osgood curves for one cycle of shearing are shown in Figure 8-2. The original Ramberg-Osgood curves based on constant and maximum G_0 and τ_m are also shown in the same figure. It is seen that, for a given shearing stress amplitude, the modified Ramberg-Osgood relationships gave a larger strain amplitude than that given by the original Ramberg-Osgood relationships. The general shape of the modified curves depends upon how the effective stress is changed during shearing. The modified curves may not necessarily be similar to the original Ramberg-Osgood curves.

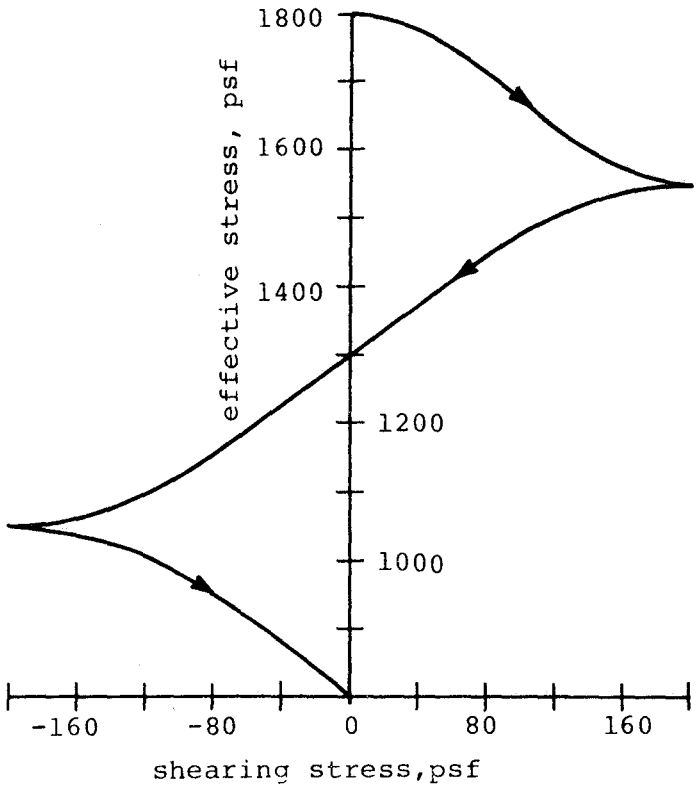

Figure 8—1 Assumed effective stress caused by shearing

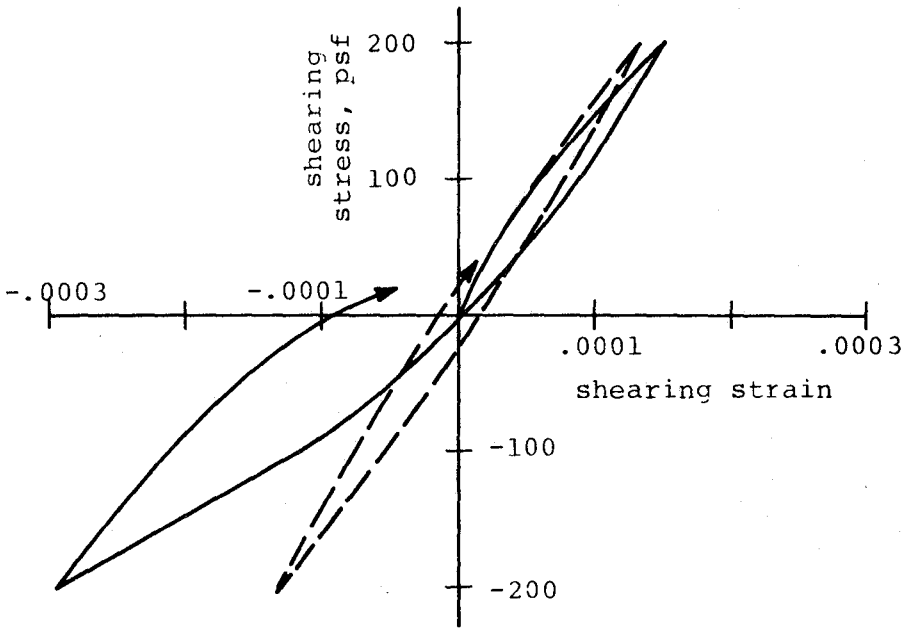

Figure 8-2 Ramberg-Osgood and Modified Ramberg-Osgood curves

8-2. The liquefaction model.

The deposit below the water table is divided into a number of equal distance intervals. Within each interval, the properties of the soil are considered to be uniform. Both the shear wave submodel and the pressure wave submodel are applied to the same intervals of soils so discretized. For each interval, the bulk compressibility, C_b, and the small motion shear modulus are related by

$$\frac{1}{C_b} = \mu G_0 , \qquad (8\text{-}5)$$

in which μ is a coefficient. Equation (8-5) is used to estimate C_b when only G_0 is known. When this is the case, the value of μ can be estimated from Poisson's ratio of the soil under consideration. When both C_b and G_0 can be estimated from laboratory or field data, then Equation (8-5) is not needed. C_b of each interval is assumed to be constant during shearing. Thus any change in the constrained compressibility in each interval is attributed to the change in the secant shear modulus in that interval.

For both submodels the Courant condition only needs to be checked once based on the initial speeds of shear wave and first pressure wave. Since a fixed z-t grid and a specified time step are used, and since these speeds are the maxima during the entire period of shaking, this check on the Courant condition insures the stability of the numerical procedure as time progresses.

The coupling between the two submodels is described in

terms of the sequence of events occurring during repeated shearing. Suppose that at time t the state of stresses and velocities throughout the deposit are known, and that the boundary conditions are given. One can use the shear wave submodel to calculate the shearing stress, the shearing strain, and the secant shear modulus at time $t + \overline{\Delta t}$. The time rate of change of the constrained compressibility, caused by the secant shear modulus changes over the time step $\overline{\Delta t}$, can then be calculated. This quantity represents the weakening of the skeleton to sustain confined compression. It is used in the pressure wave submodel which computes the resulting transient effective stress and pore water pressure, and the velocities of soil skeleton and pore water during $\overline{\Delta t}$. Because the first pressure wave speed is much higher than the shear wave speed, these computations are carried out for several smaller time steps, Δt. Δt is determined by the initial highest first pressure wave speed in the discretized deposit and the length of distance interval used. This allows the time in the pressure wave submodel to catch up with the time in the shear wave submodel. In other words, for every time step $\overline{\Delta t}$, the computation of pressure wave motion is carried out N times such that N Δt equals $\overline{\Delta t}$. During the N steps in the pressure wave submodel, the constrained compressibility in each interval is updated at the end of every time step Δt. This adjustment is in accordance with $\partial C_c/\partial t$ computed from the shear wave submodel between time t and time $t + \overline{\Delta t}$. When the time in the

pressure wave submodel catches up with the time in the shear wave submodel, Equations (8-3) and (8-4) are used to compute a new G_0 and τ_m from current effective stresses at the ends of every distance interval. The new G_0 and τ_m so computed for each interval represent the shearing characteristics of that interval at the new state of effective stress. Thus far, one cycle of the computation is completed. The next cycle of computation starts out with the shear wave submodel and the newly defined shearing characteristics of the soil. Figure 8-3 illustrates the sequence of events described above.

At the moment of shearing strain reversal, there is a sudden increase in the secant shear modulus. Through the use of Equation (4-40), the constrained compressibility of the interval in which strain reversal just took place is computed according to the newly increased secant shear modulus. In the meantime, $\partial C_c/\partial t$ in this interval is set to zero over the time step $\overline{\Delta t}$ which immediately follows the strain reversal. With the newly defined soil properties, the pressure wave submodel is then used to compute the effective stress, the pore water pressure, and the velocities of the skeleton and pore water over the time step $\overline{\Delta t}$. Chart 8-1 outlines the liquefaction model by a flow diagram.

8-3. Examples.

Example 8-1. Consider a horizontal deposit having a depth of 50 feet. The deposit was composed of round-grained sand[54]. The soil properties were: $n = 0.4, \phi = 34$ degrees,

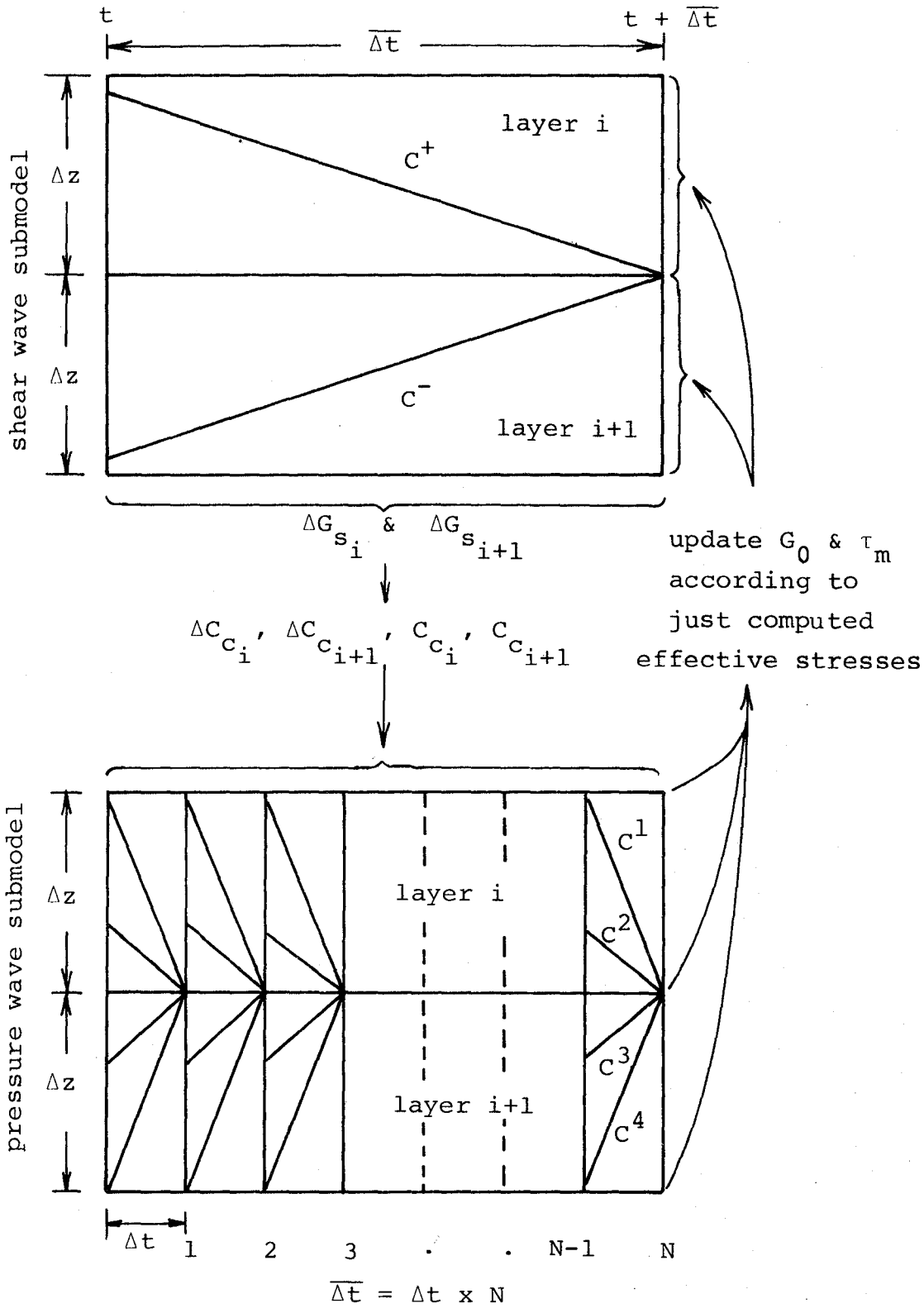

Figure 8-3 Coupling between the shear wave submodel and the pressure wave submodel

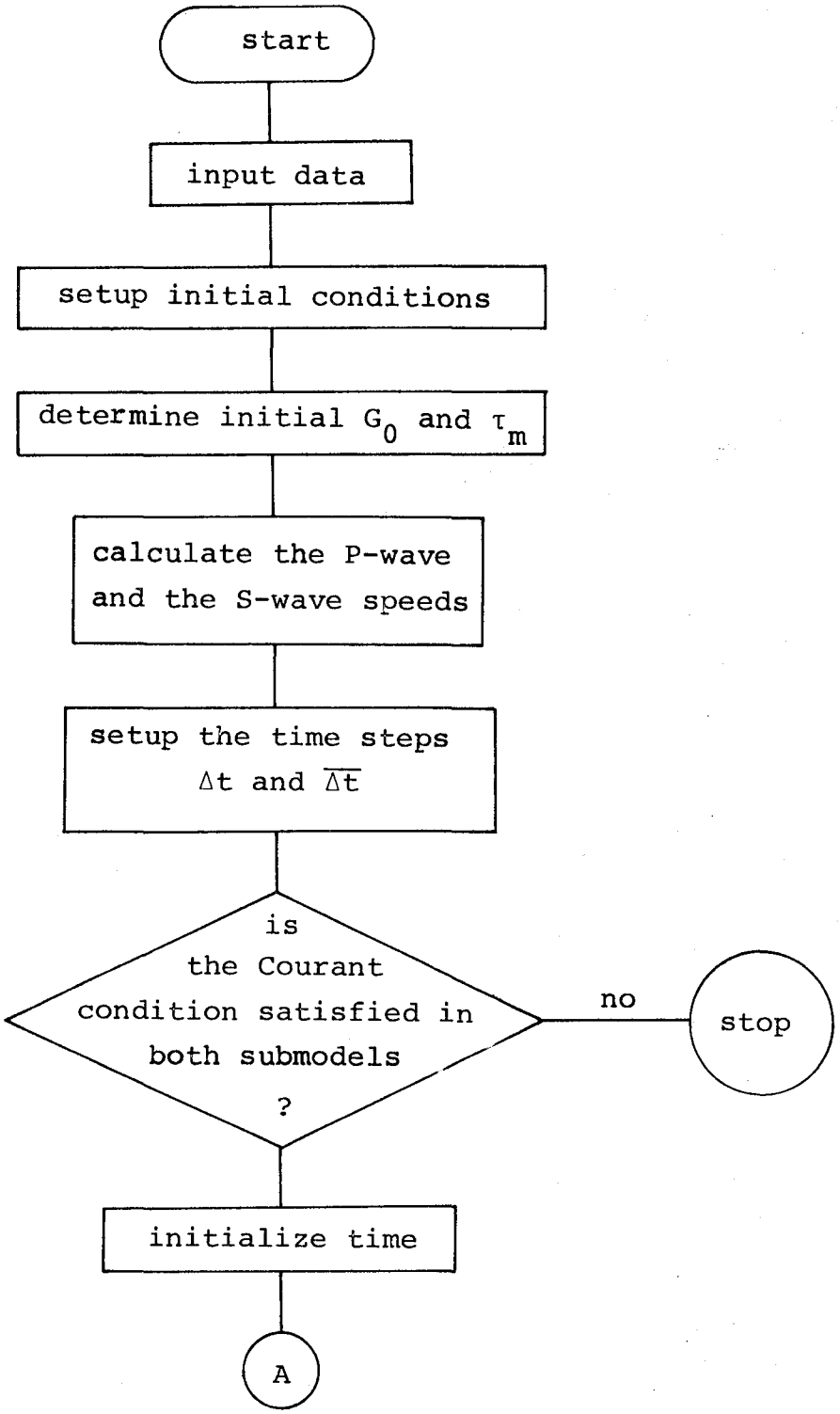

Chart 8-1 The flow diagram of the liquefaction model

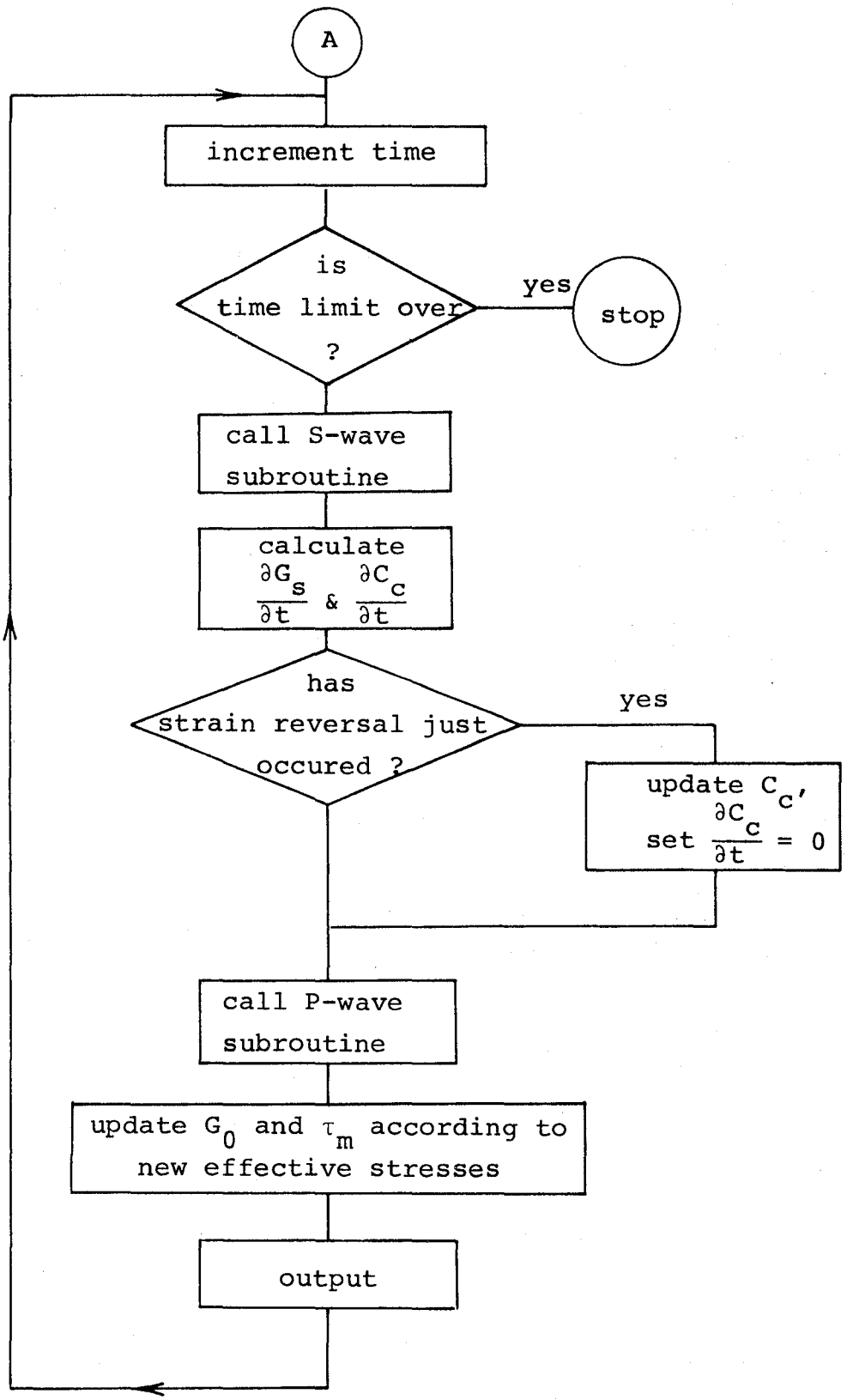

(flow diagram continued)

$K_0 = 1 - \sin \phi = 0.4354$, $\rho_s = 5.13$ lb-sec^2/ft, $\mu = 1.2$, $\alpha = 1$, $R = 3$, and $C_1 = 0.8$. The small motion shear modulus throughout the deposit was computed from Equation (6-10). The shear strength throughout the deposit was computed from Equation (8-4). Other relevant properties were $\rho_w = 1.94$ lb-sec^2/ft, $C_w = 2.348 \times 10^{-8}$ ft^2/lb, and $k = 0.00328$ fps.

The deposit was divided into 8 equal distance intervals. The initial discretized G_0 and τ_m are listed in Table 8-1.

TABLE 8-1

SMALL MOTION SHEAR MODULUS AND SHEAR STRENGTH

Layer	G_0, psf	τ_m, psf
1	0.469×10^6	56
2	0.812×10^6	168
3	1.049×10^6	280
4	1.241×10^6	393
5	1.407×10^6	504
6	1.556×10^6	616
7	1.691×10^6	728
8	1.816×10^6	840

The bedrock underlying the deposit was assumed to be rigid and to move back and forth sinusoidally with a frequency of 4 Hertz. For the purpose of comparison, two single amplitudes of the bedrock velocity were used. They were 0.05 fps and 0.10 fps. The dynamic response of the deposit to these bedrock motions is shown in Figures 8-4 through 8-11.

Figure 8-4c represents the sinusoidal horizontal velocities of the bedrock, or the velocities at the base of the deposit. Figure 8-4a and Figure 8-4b illustrate the time variations of the shearing stress and shearing strain in the 6th interval counted from the ground surface. For the case of small bedrock motion and except the initial transient, the soil oscillated around its static position. A gradual decrease in the amplitude of shearing stress trace after the initial transient can be seen in Figure 8-4a. A corresponding increase in the amplitude of the shearing strain trace can be seen in Figure 8-4b. Hence the shearing rigidity of the soil was reduced by the repeated shearing. This process is more explicitly illustrated by Figure 8-5 where the shearing stress is plotted against the shearing strain. The gradual leveling of the longitudinal axes of the hysteresis loops indicates that the soil was softened by the repeated shearing. For the case of large bedrock motion, similar but more pronounced results were obtained. Due to the high shearing stress developed and the rapid loss of shearing rigidity, neither the shearing stress nor the shearing strain oscillated around their static value. The dynamic shearing stress-shearing strain relation for the large excitation is shown in Figure 8-6. For the last few cycles of shearing, very little stress was needed to develop a large strain. Hence the soil was softened considerably. Compared with Figure 8-5, the area of the loops is larger, indicating that more energy was dissipated in the soil.

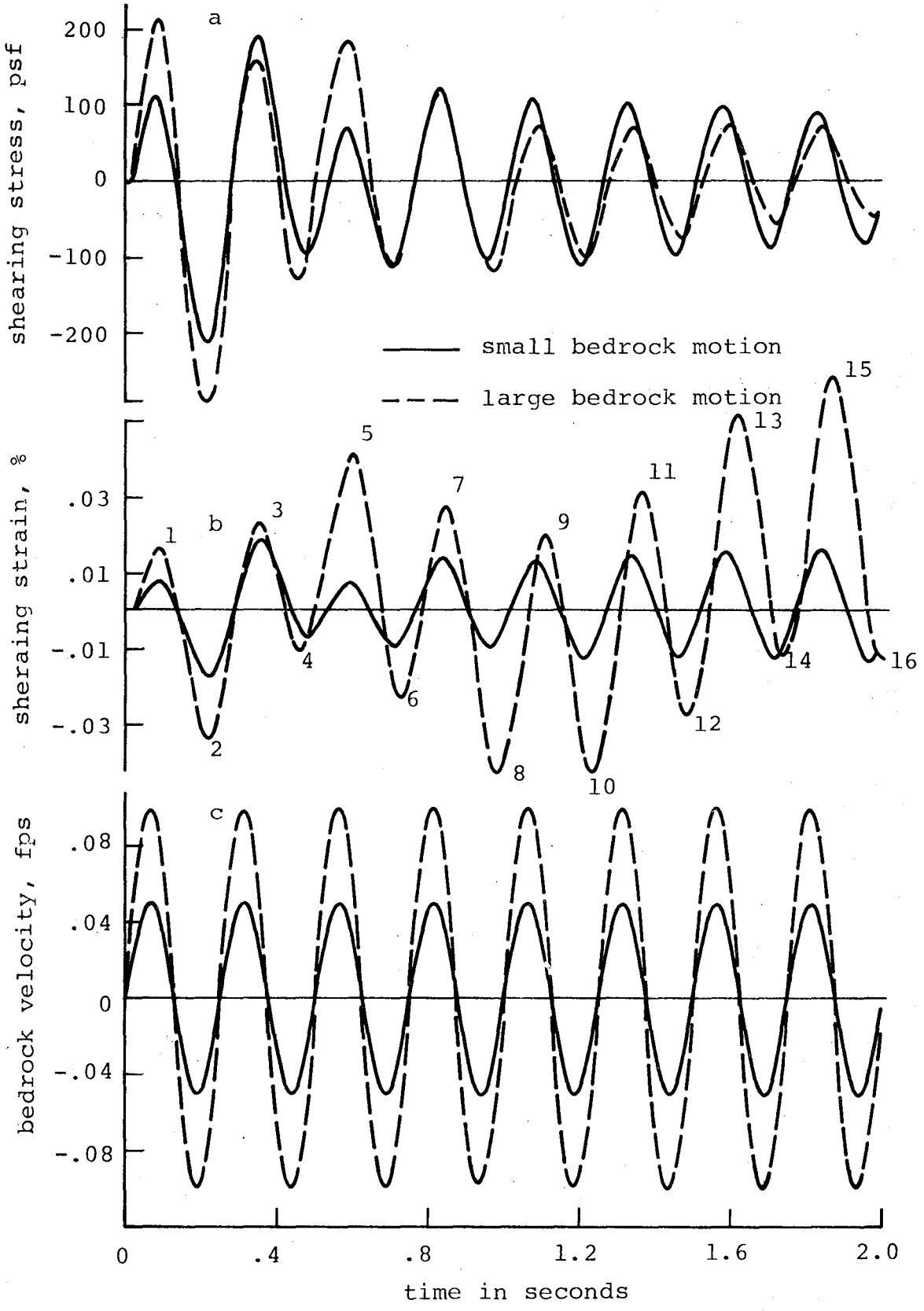

Figure 8-4 Example 8-1, time variation of bedrock velocity, shearing stress and shearing strain

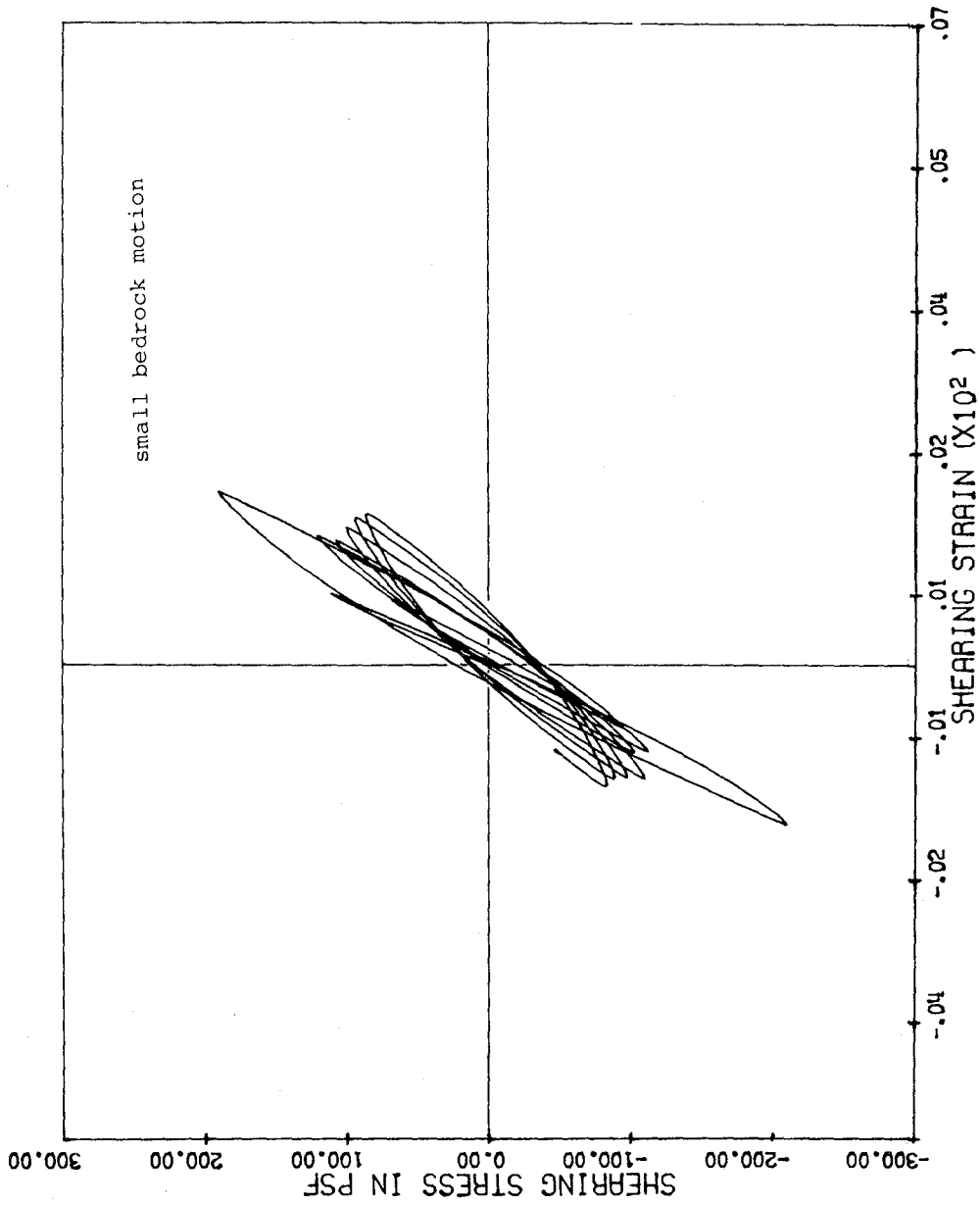

Figure 8-5 Example 8-1, shearing stress-strain relationships in layer 6; small excitation

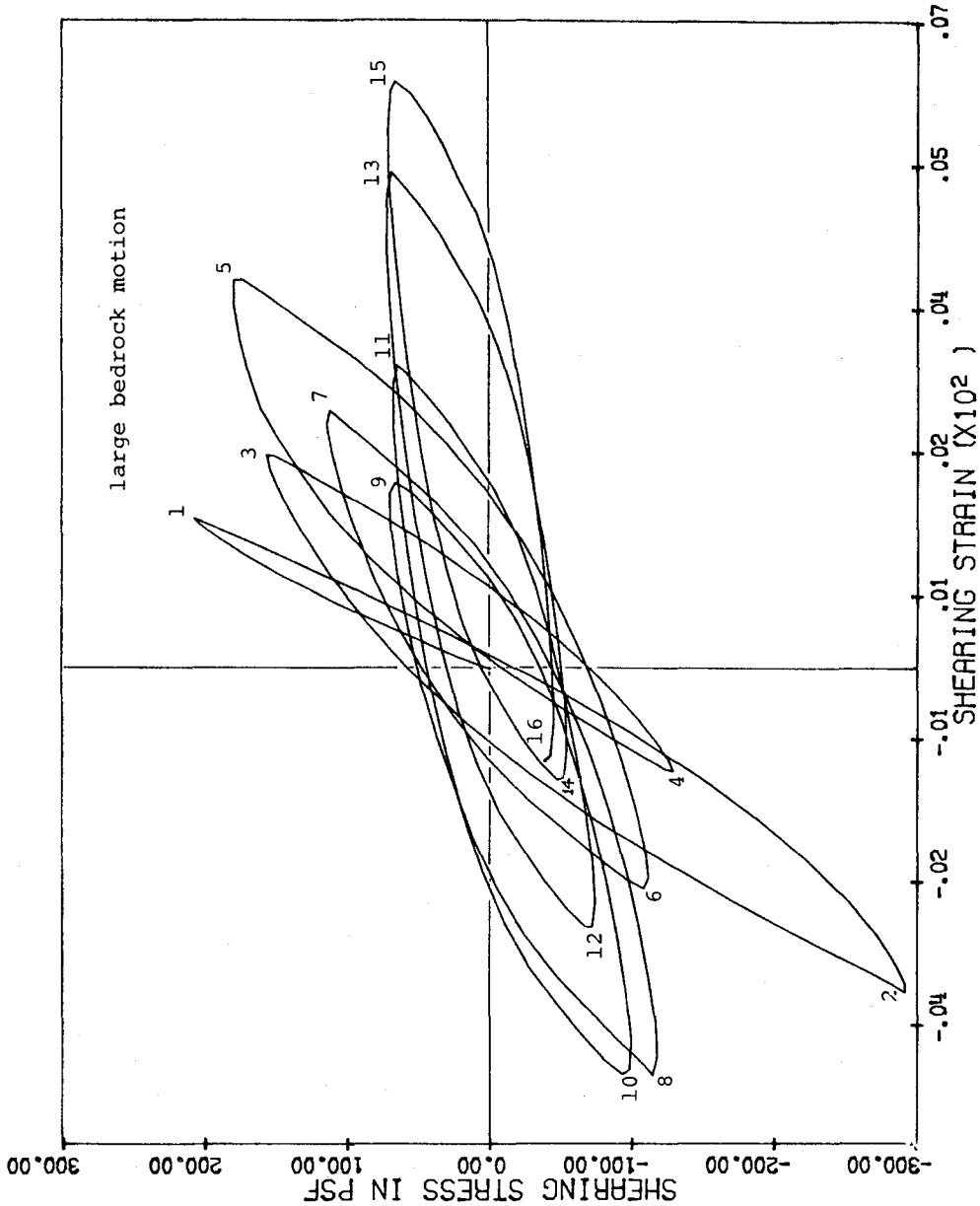

Figure 8-6 Example 8-1, Shearing stress-strain relationship in layer 6; large excitation

Figure 8-7 illustrates the accumulative increase in the pore water pressure and the corresponding reduction of effective stress at a depth of 31.25 feet. It is seen that the sum of the pore water pressure and the effective stress at any instant was approximately equal to the total static stress at that depth. The time rate of increase in the pore water pressure decreased as the soil became softer. The effective stress curves for both cases indicate that, generally, for a deposit with a uniform permeability where the re-distribution of pore water pressure is not inhibited, the effective stress approaches zero asymptotically.

Figure 8-8 shows the gradually reduced shearing strength of layer 6 together with the shearing stress actually developed in the same layer. For the case of large bedrock motion, the shearing strength was not enough for some brief moments. Since the deposit was horizontal, there was no driving force to cause large strain to develop during these brief moments. The occurrence of shearing stress which exceeded the shearing strength could have been eliminated by allowing inelastic slip[56] to occur.

Figure 8-9 shows the downward surface displacement of the deposit for the two cases. The volume decrease in the deposit associated with the settlement could be decomposed into two parts. The first part was due to the volume reduction of pore water by the excess pore water pressure, and was proportional to the excess pore pressure level. The second part was attributed to the volume of water that was expelled out of the deposit from the ground surface. This

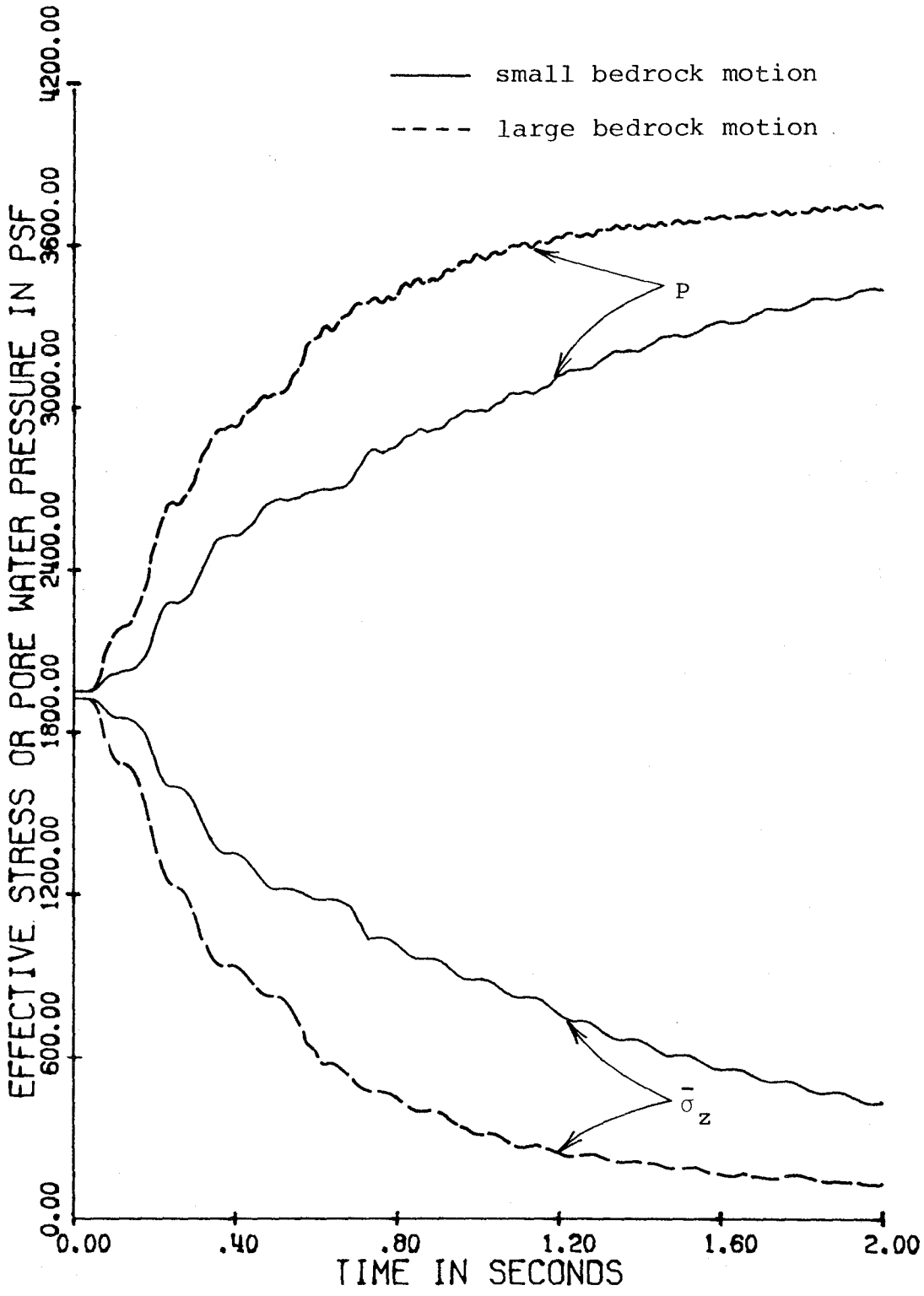

Figure 8-7 Example 8-1, time variation of effective stress and pore water pressure

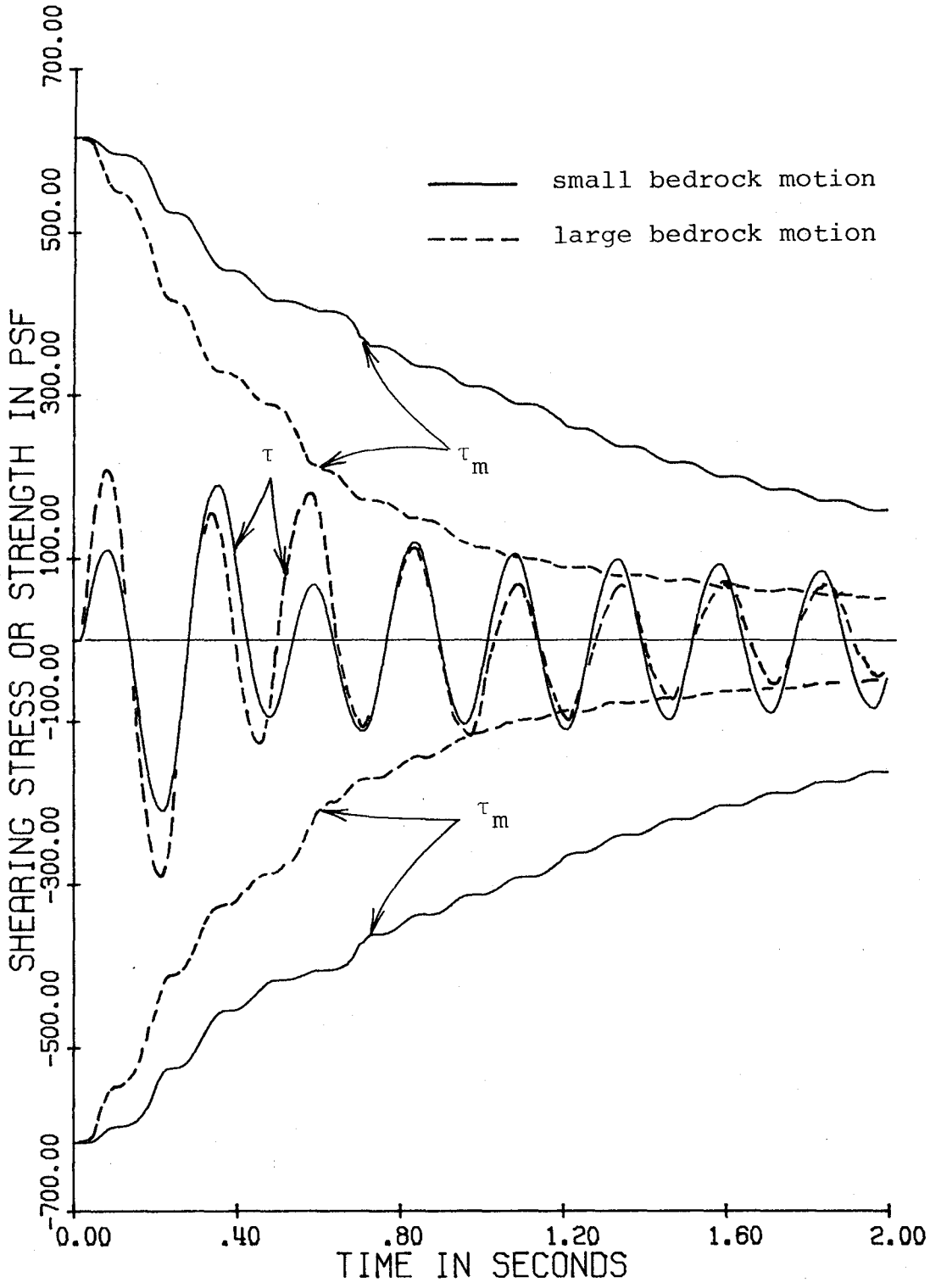

Figure 8-8 Example 8-1, time variation of shearing strength and shearing stress

volume was proportional to the gradient of excess pore water pressure in the deposit. The pore water pressure at the ground surface was zero and the excess pore pressure gradient was nearly uniform between 0 and 31.25 feet, as shown in Figure 8-11. Hence the volume decrease due to drainage was also proportional to the excess pore water pressure level. One can compare Figure 8-7 and Figure 8-9 to see that this indeed was the case. If the motion of the bedrock was stopped at 2 seconds, the settlement would continue until the pore water pressure distribution becomes hydrostatic again.

Figure 8-10 shows the lateral displacement of the ground surface relative to that of the bedrock as functions of time. The fundamental frequency of the deposit before shaking was 2.678 Hertz. At 2 seconds, the fundamental frequency was 1.343 Hertz for the small excitation case and 0.584 Hertz for the large excitation case. Since the exciting frequency was 4 Hertz, higher than the fundamental frequency of the deposit throughout the 8 cycles of shearing, the relative displacements shown did not indicate the overall shearing strain of the deposit.

Figure 8-11 demonstrates the spatial distribution of the effective stress, drop in the effective stress, and the excess pore water pressure at 2 seconds. For both cases, the excess pore water pressure was very close to the drop in the effective stress. Note that the bedrock was impervious and hence there was no excess pore water pressure gradient at the bottom of the deposit.

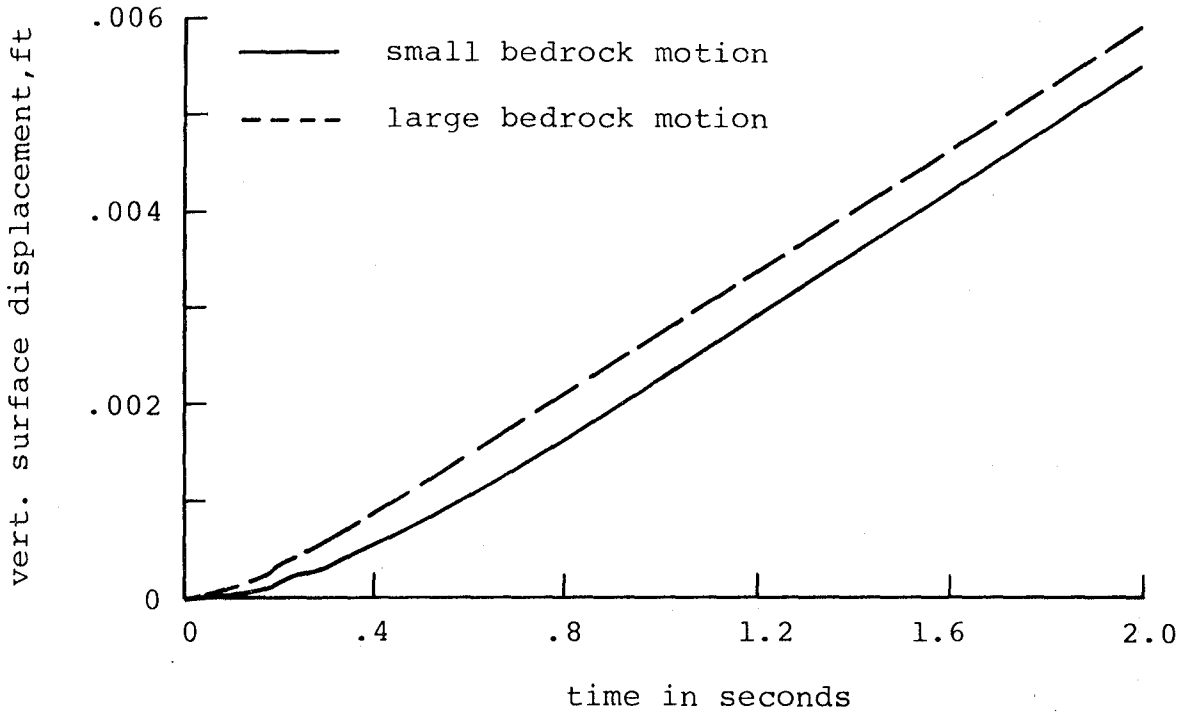

Figure 8-9 Example 8-1, time variation of downward surface displacements

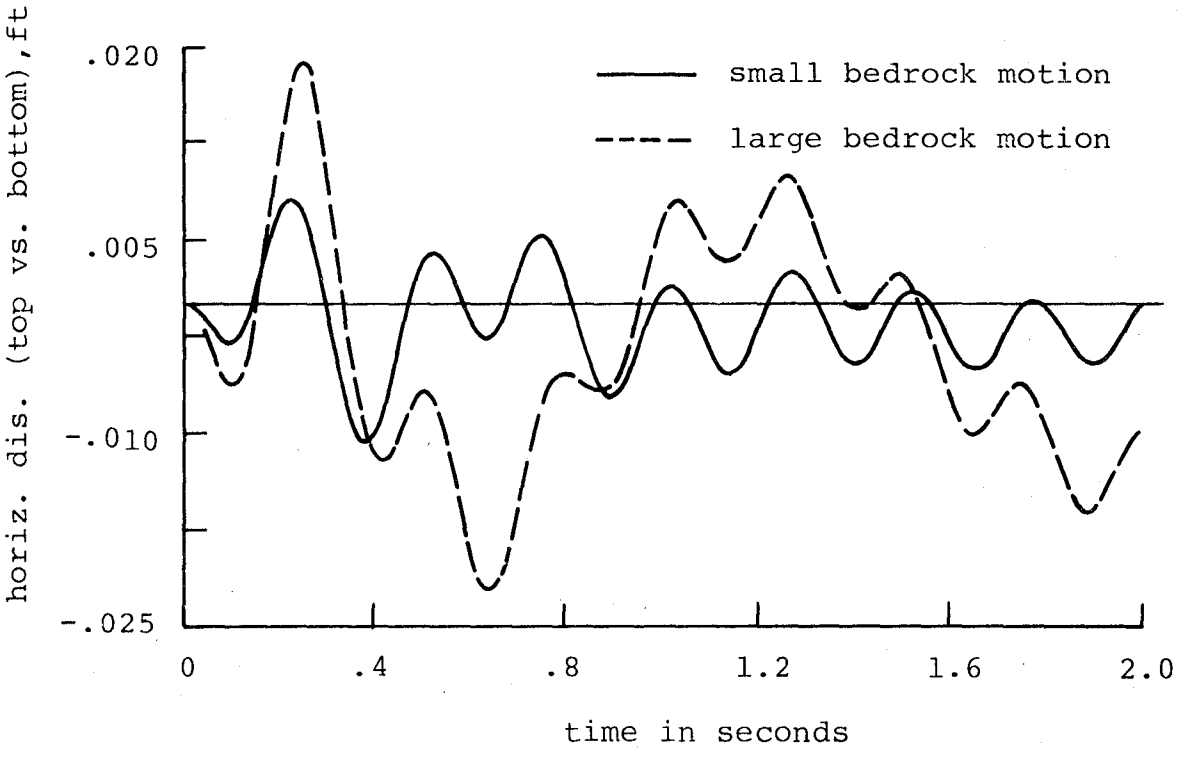

Figure 8-10 Example 8-1. time variation of horizontal displacements

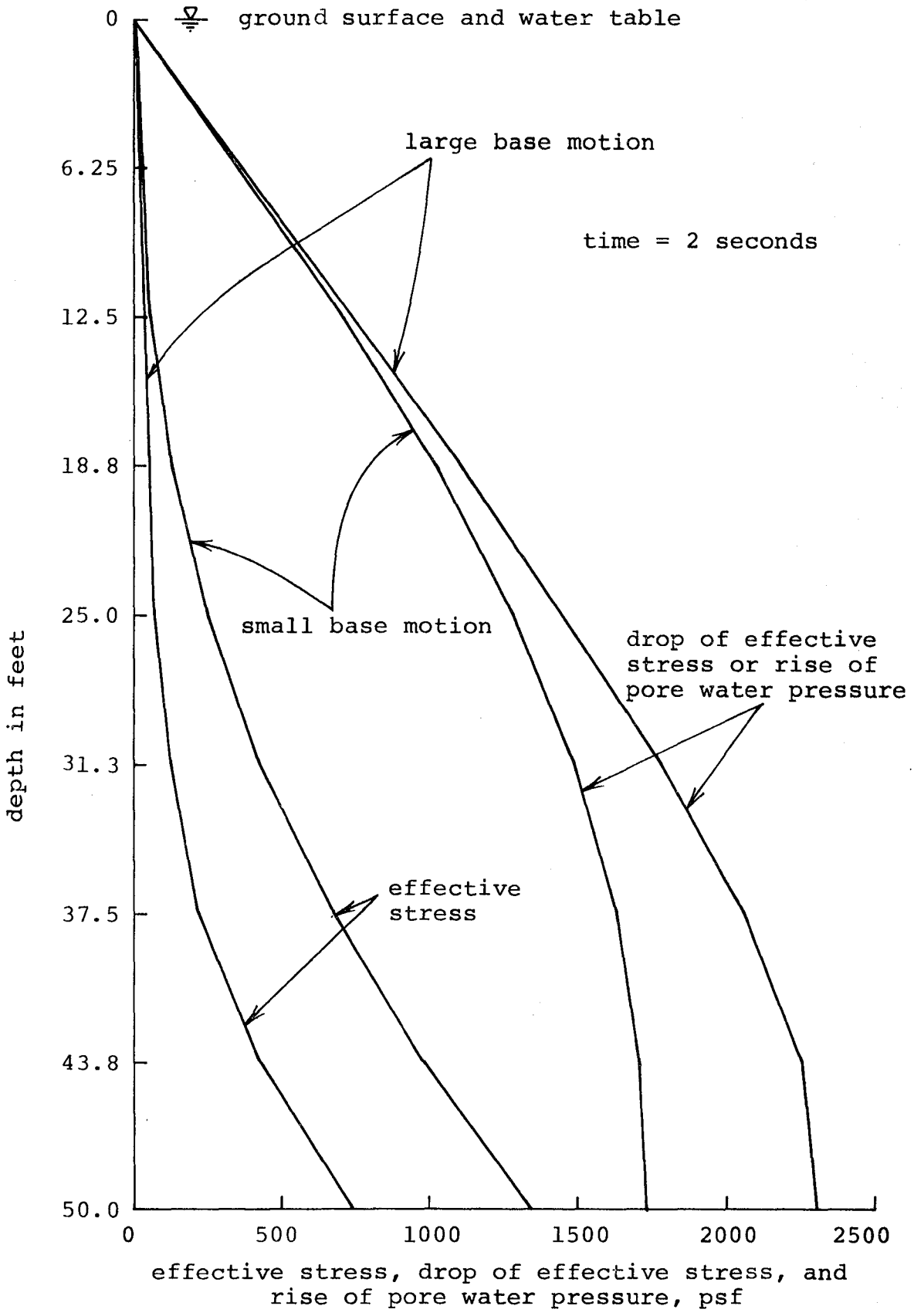

Figure 8-11 Example 8-1, spatial variation of effective stress, effective stress drop, and pore water pressure rise

Example 8-2. Frequently the water table may lie below the ground surface. This may either be a natural state or a fill has been placed to bring the surface level above water. In either cases, its effect is to increase the shearing strength of the deposit. It was seen in the previous example that for the large bedrock motion, the deposit did not have sufficient strength to sustain the 8 cycles of shearing. The response of the same deposit with the same bedrock motion is studied in this example when a 12.5 foot layer of soil was placed as overburden.

The fill was composed of a soil with a moist unit weight of 103 lb/ft^3. G_0 and τ_m were computed from Equation (6-10) and Equation (8-4) respectively. The deposit below the water table was divided into 8 equal intervals. The discretized G_0 and τ_m are shown in Table 8-2.

TABLE 8-2

SMALL MOTION SHEAR MODULUS AND SHEAR STRENGTH

Layer	G_0, psf	τ_m, psf
1	1.279×10^6	416
2	1.440×10^6	529
3	1.586×10^6	640
4	1.719×10^6	753
5	1.842×10^6	864
6	1.958×10^6	976
7	2.067×10^6	1088
8	2.171×10^6	1200

The response of the deposit is shown in Figures 8-12 through 8-18. Figures 8-12a and 8-12b indicate that in layer 6 the shearing stress was larger, while the shearing strain was smaller than that when the fill was absent. The dynamic shearing stress-shearing strain curves in Figure 8-13 show that the shearing stress developed was not large enough to cause rapid weakening, such as those shown in Figure 8-6, although the softening trend was evident.

The time variations of pore water pressure and effective stress at a depth of 31.25 feet below the water table are shown in Figure 8-14. At the end of 2 seconds, the pore water pressure was still increasing at a high rate. This indicates that the soil still had a big margin of safety at the end of 2 seconds.

The strengthening effect of the fill upon the deposit is more clearly shown in Figure 8-15. Compared with Figure 8-8, it is seen that for the same number of shearing cycles the deposit with fill had a greater margin between the time varying shearing strength and the actual dynamic shearing stress.

The downward displacement of the surface, shown in Figure 8-16, was larger than that shown in Figure 8-9. This was caused by the higher excess pore water pressure, which was, in turn, caused by the larger changes in the secant shear modulus during shaking.

In Figure 8-18, the distribution of the effective stress across the deposit at five selected instants are plotted.

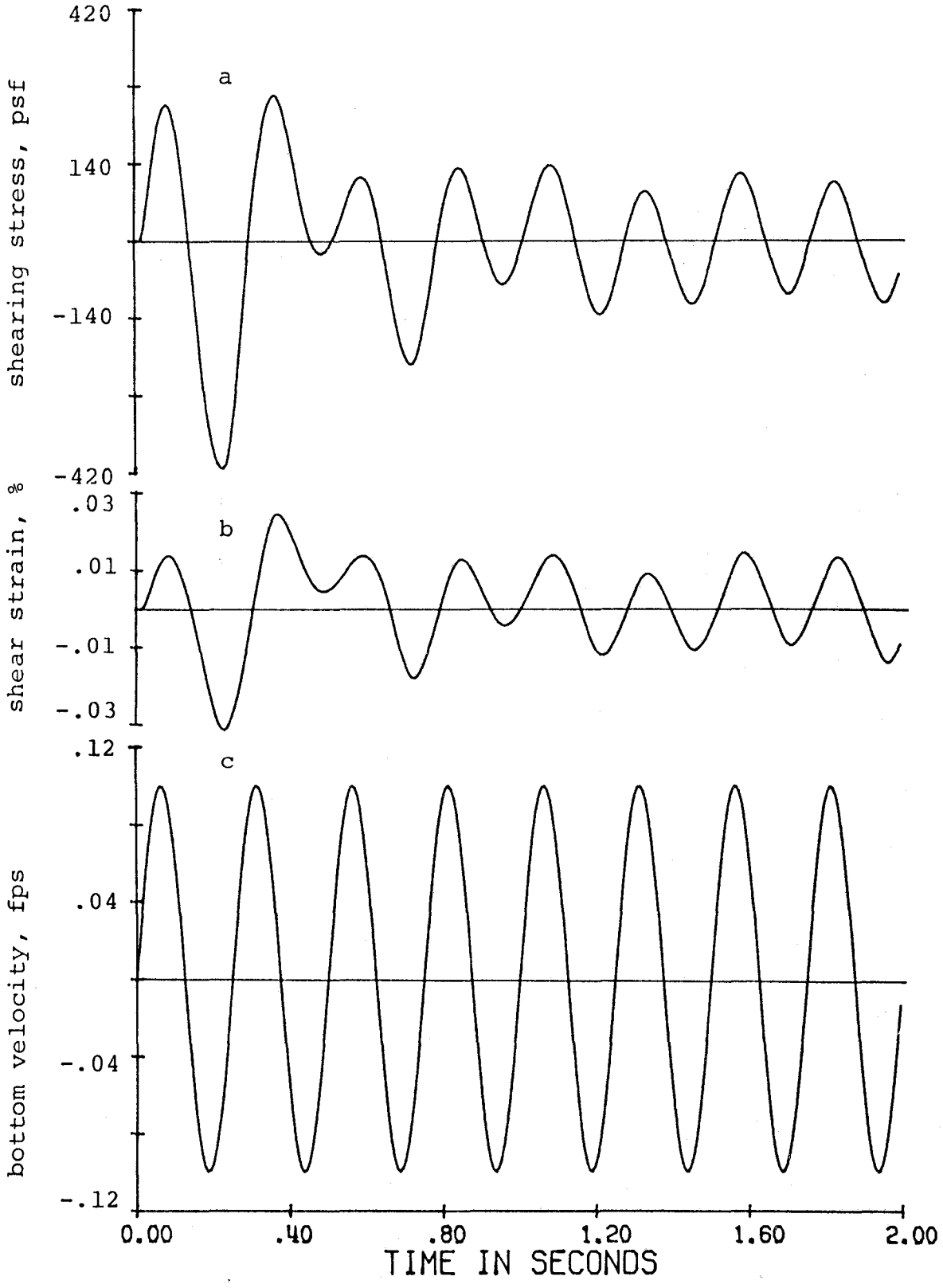

Figure 8-12 Example 8-2, time variation of base velocity, shearing stress, and shearing strain

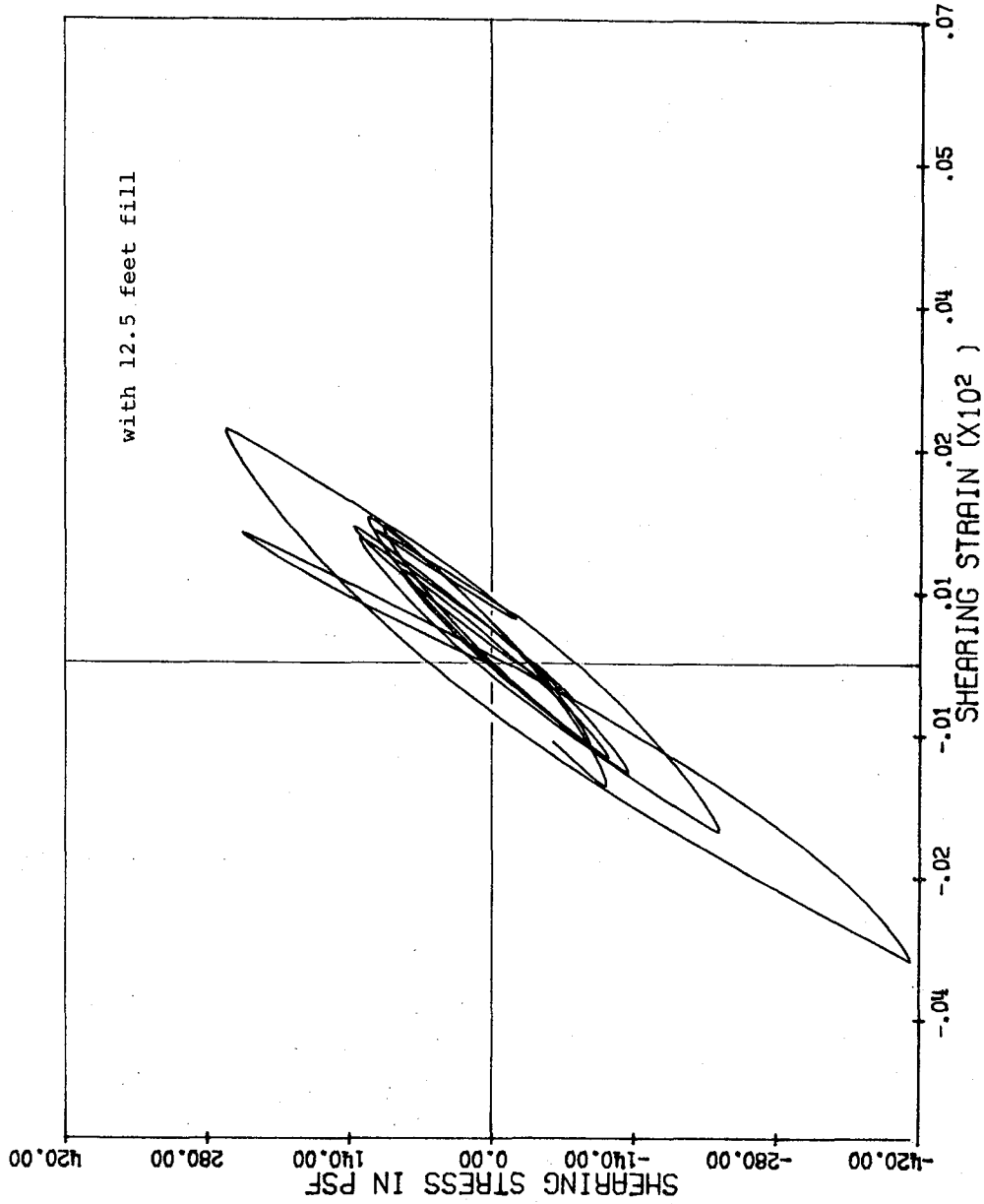

Figure 8-13 Example 8-2, shearing stress-strain relationship in layer 6

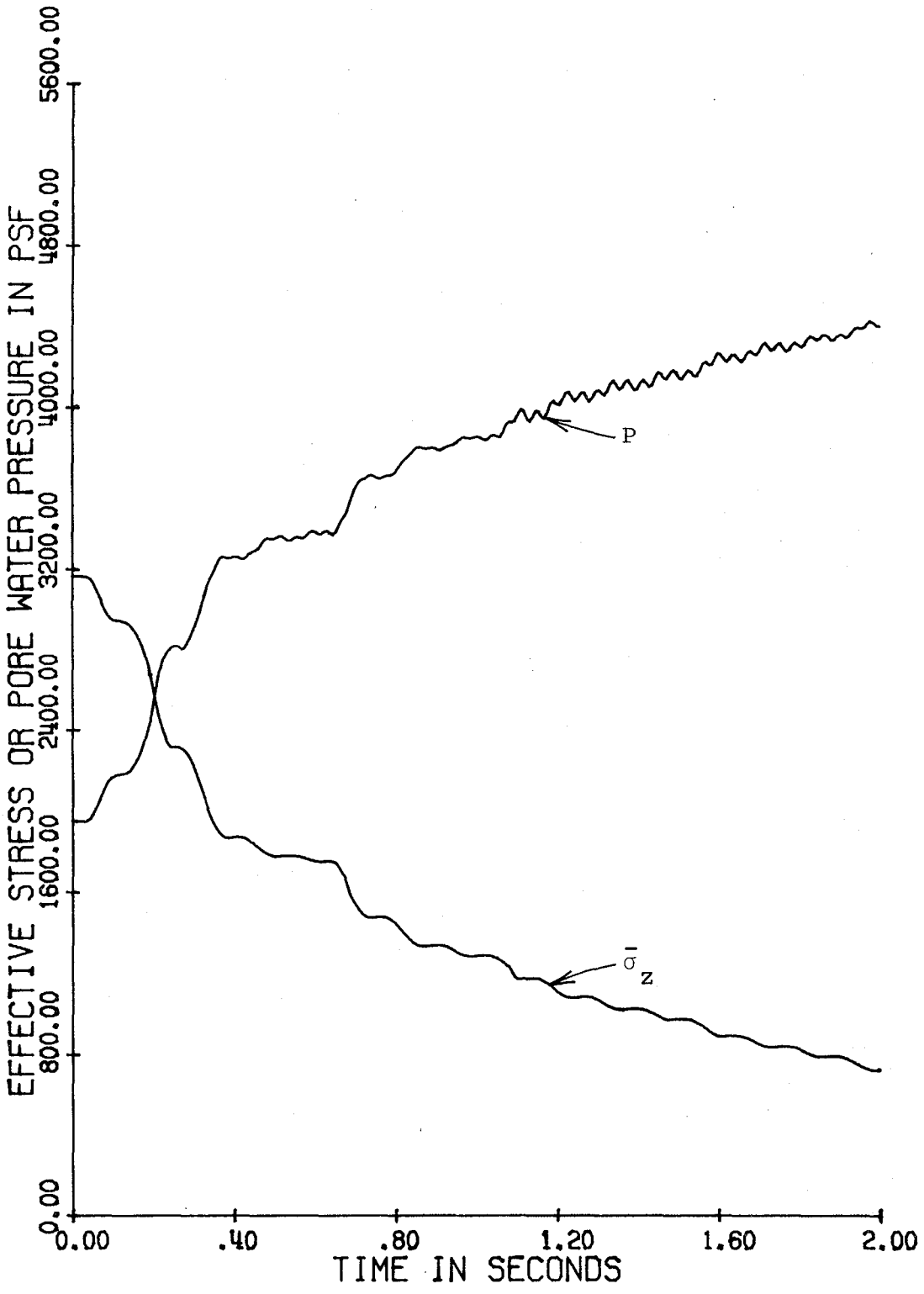

Figure 8-14 Example 8-2, time variation of effective stress and pore water pressure

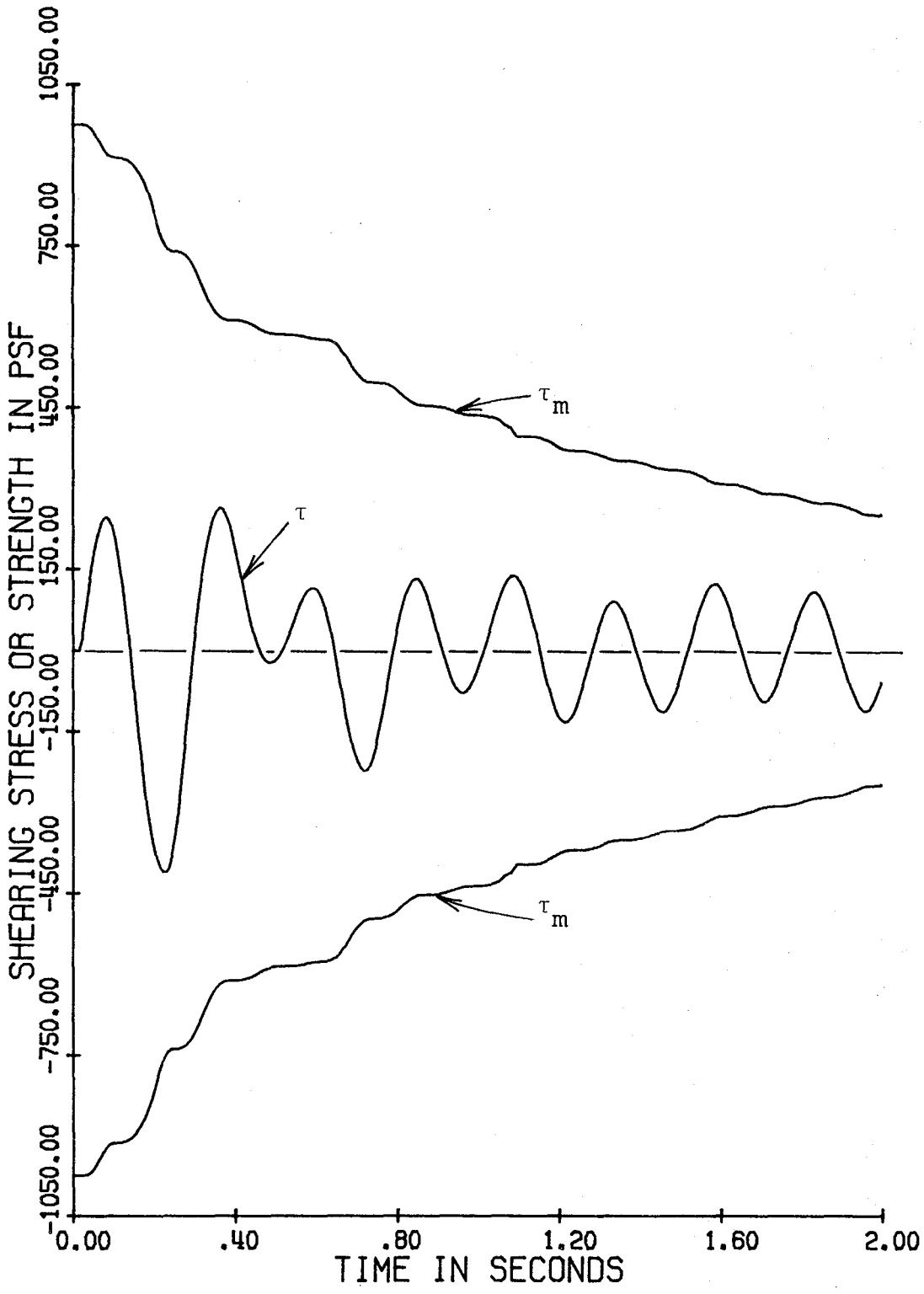

Figure 8-15 Example 8-2, time variation of shearing strength and shearing stress

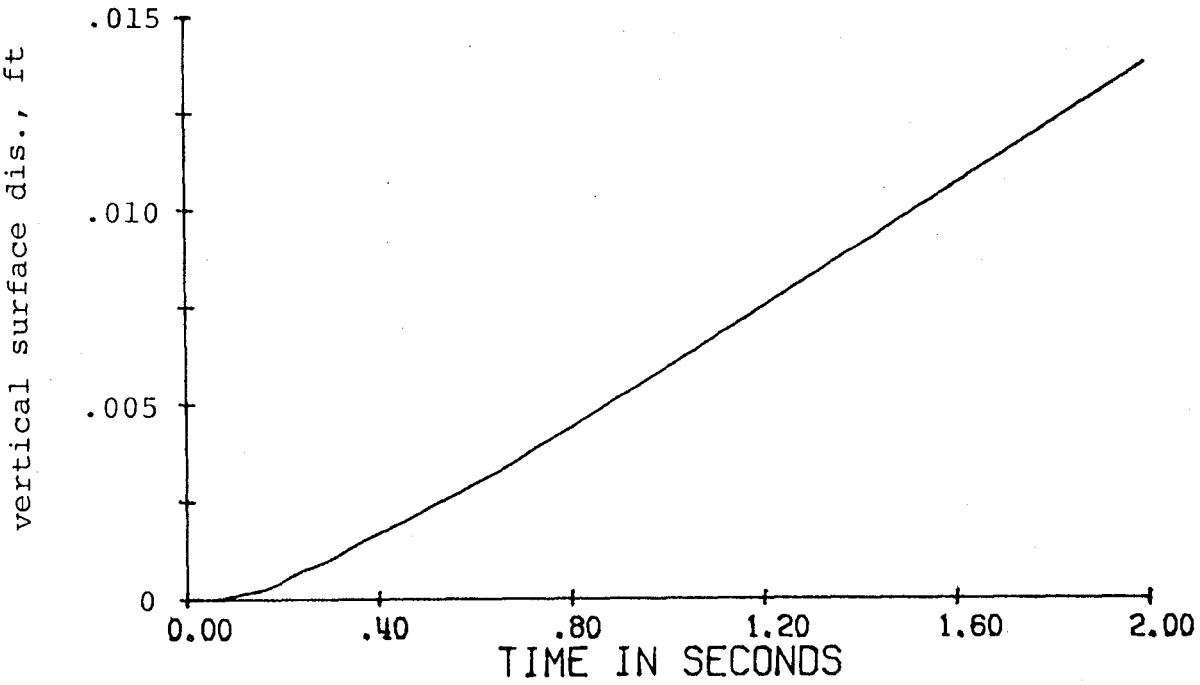

Figure 8-16 Example 8-2, time variation of downward surface displacement

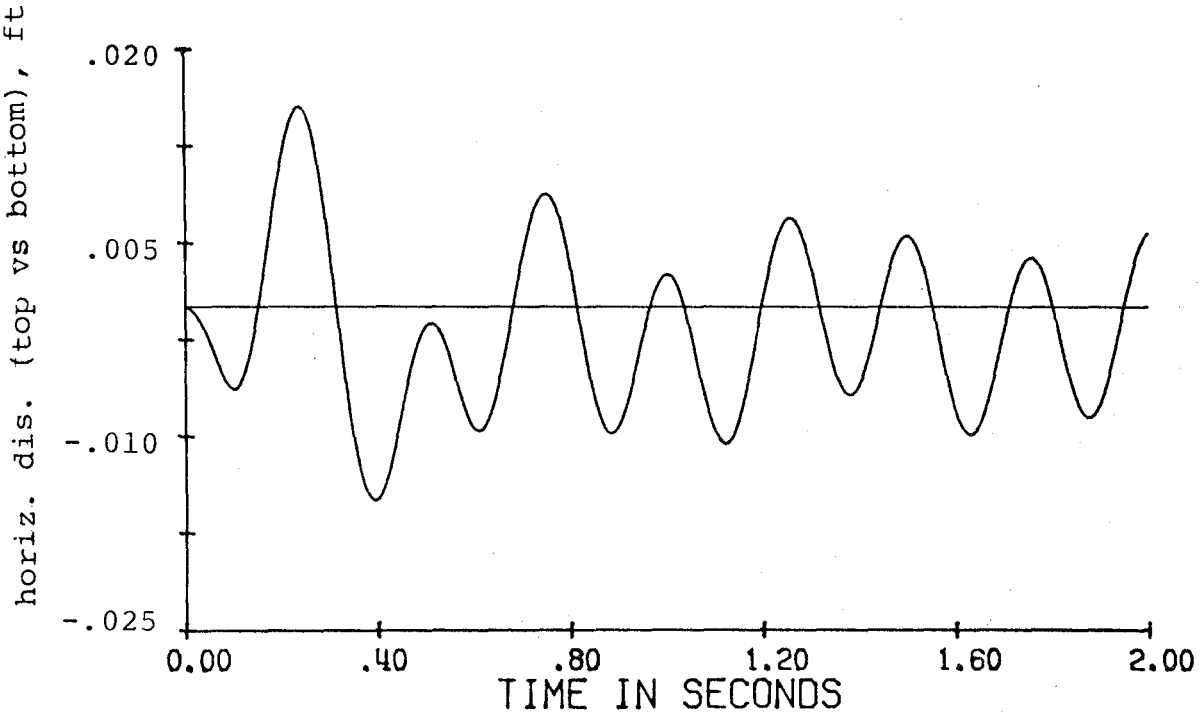

Figure 8-17 Example 8-2, time variation of horizontal relative displacement

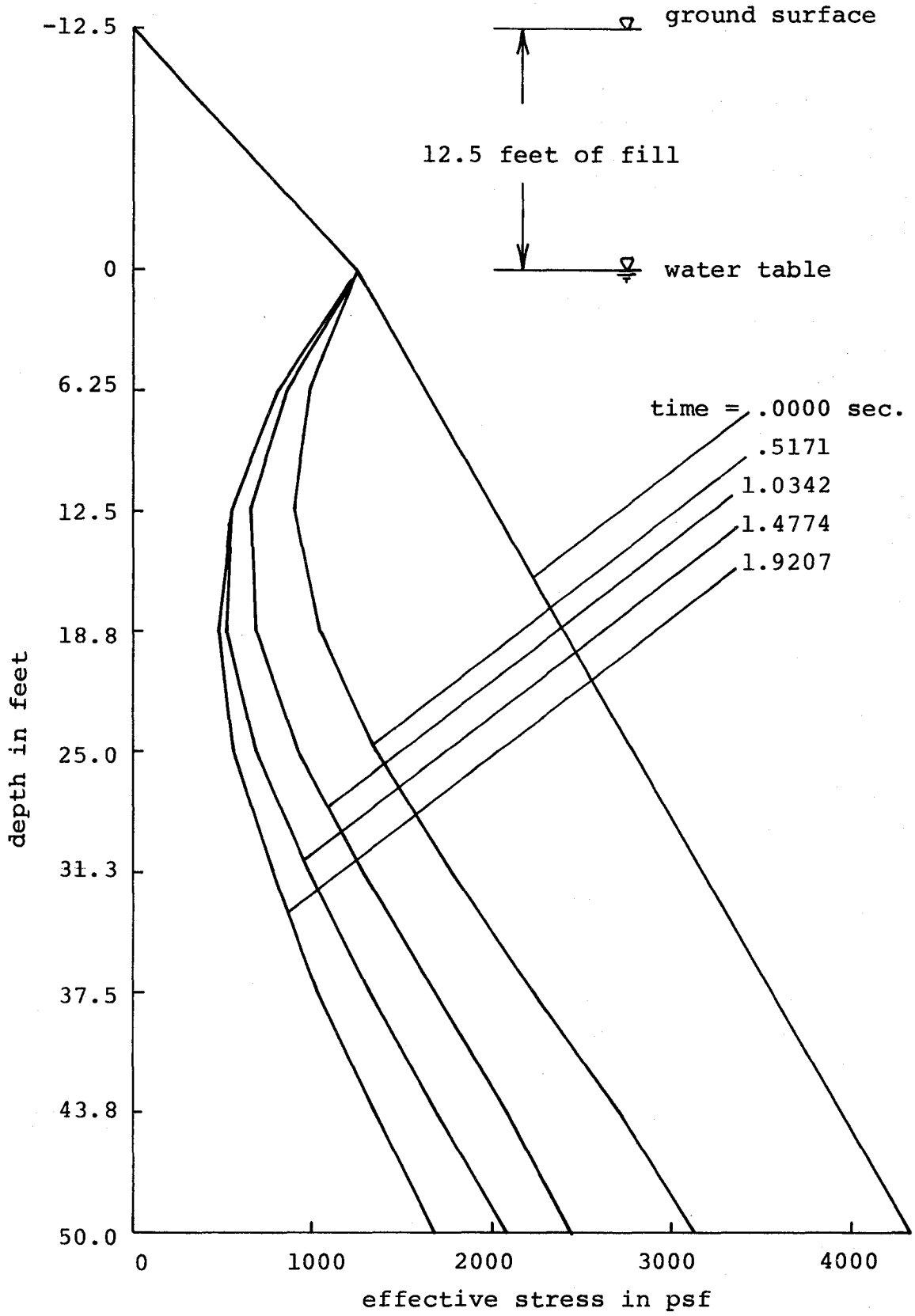

Figure 8-18 Example 8-2, profiles of effective stress at selected instants

The effective stress at the original ground surface was set to be the weight of the fill per unit surface area. As a result, the minimum effective stress occured at a greater depth. Since the initial effective stress was larger at a greater depth, the severity of liquefaction throughout the whole deposit was lessened.

Example 8-3. Consider a 50 foot deep round-grained sand deposit. It was composed of 8 layers of sand having equal thickness. Layers 4 and 5 had a smaller porosity and were much less premeable than the remaining layers. The soil properties were: for all layers, ρ_s = 5.13 lb-sec^2/ft, α = 1, R = 3, c_1 = 0.8, μ = 1.2, for layers 1,2,3, and 6,7,8, n = 0.4, ϕ = 34 degrees, K_0 = 0.4354, k = 0.00328 fps, for layers 4 and 5, n = 0.35, ϕ = 40 degrees, K_0 = 0.3558, and k = 0.0000328 fps. The relevant pore water properties were: $C_w = 2.34 \times 10^{-8}$ ft^2/lb, and ρ_w = 1.94 lb-sec^2/ft. The shearing strength and the small motion shear modulus throughout the the deposit were computed from Equations (8-4) and (6-10). The discretized G_0 and τ_m are listed in Table 8-3.

The lateral velocity of the bedrock, shown in Figure 8-19c, was sinusoidal with a frequency of 4 Hertz and a single amplitude of 0.06 fps. The deposit was inclined by 1 degree and the water table was at the ground surface.

Because of the gravity, the initial shearing stress was proportional to the depth. The dynamic shearing stress and shearing strain in layers 5 and 6 are shown in Figures 8-19a and 8-19b. In both layers, the dynamic shearing stress and

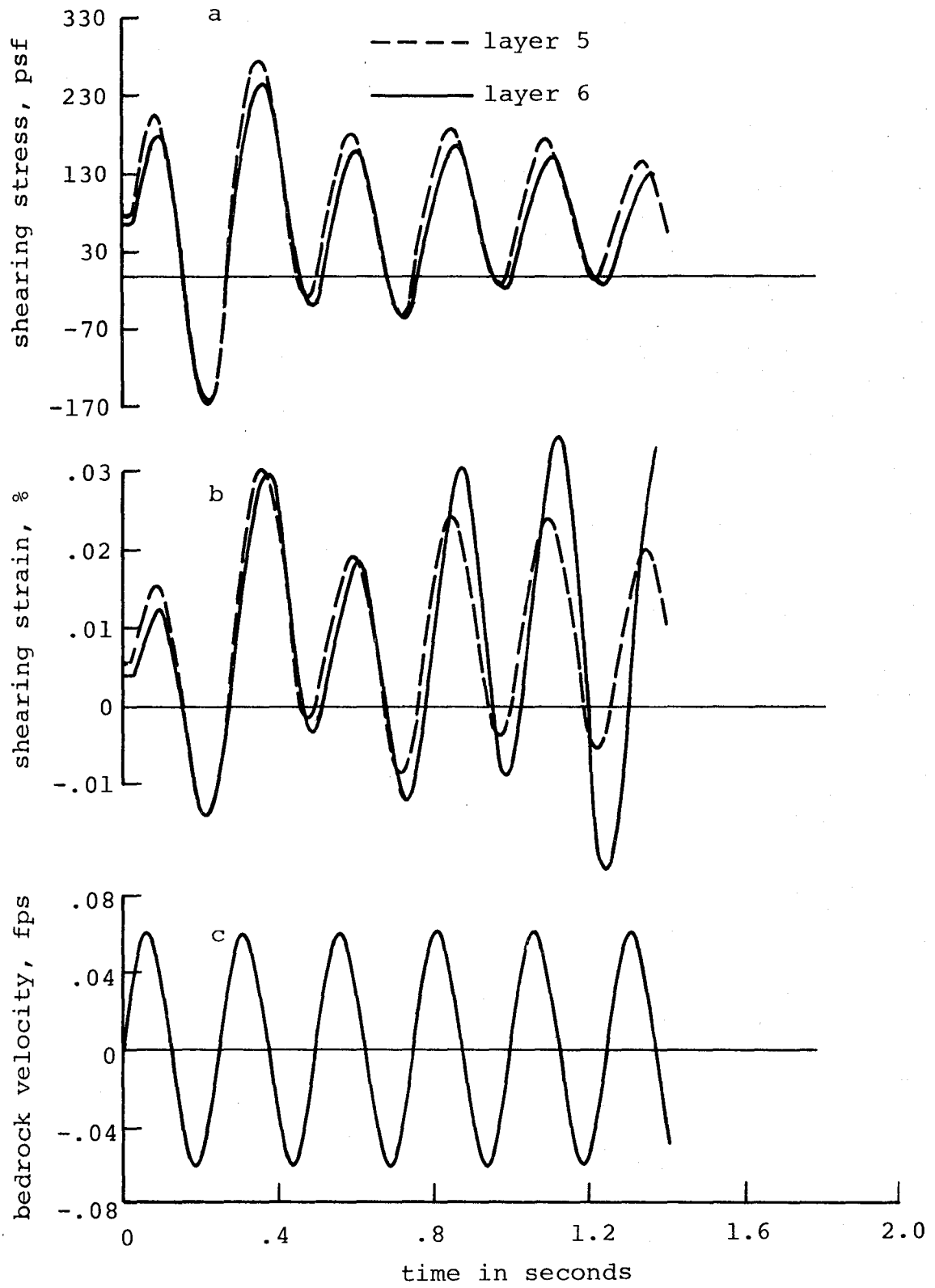

Figure 8-19 Example 8-3, time variation of bedrock velocity, shearing stress, and shearing strain

TABLE 8-3

SMALL MOTION SHEAR MODULUS AND SHEAR STRENGTH

Layer	G_0, psf	τ_m, psf
1	0.469×10^6	61
2	0.812×10^6	168
3	1.049×10^6	280
4	1.523×10^6	403
5	1.741×10^6	525
6	1.579×10^6	635
7	1.713×10^6	746
8	1.837×10^6	859

shearing strain oscillated around their initial values after the initial transients disappeared. The shearing strains were skewed with respect to the initial shearing strains, indicating that permanent shearing strains occurred. After about 0.8 seconds, the shearing strain in layer 5 was considerably larger than that in layer 6, although the shearing stresses in these two layers were close. This is explained later.

The shearing stress-shearing strain relationships are shown in Figure 8-20 and Figure 8-21. Due to the initial shearing stress and shearing strain, the loops are not centered approximately around the origin. The soil was strained into a more nonlinear region in one direction than the other. It is also seen that after 3 cycles of shearing, layer 5 became considerably softer than layer 6.

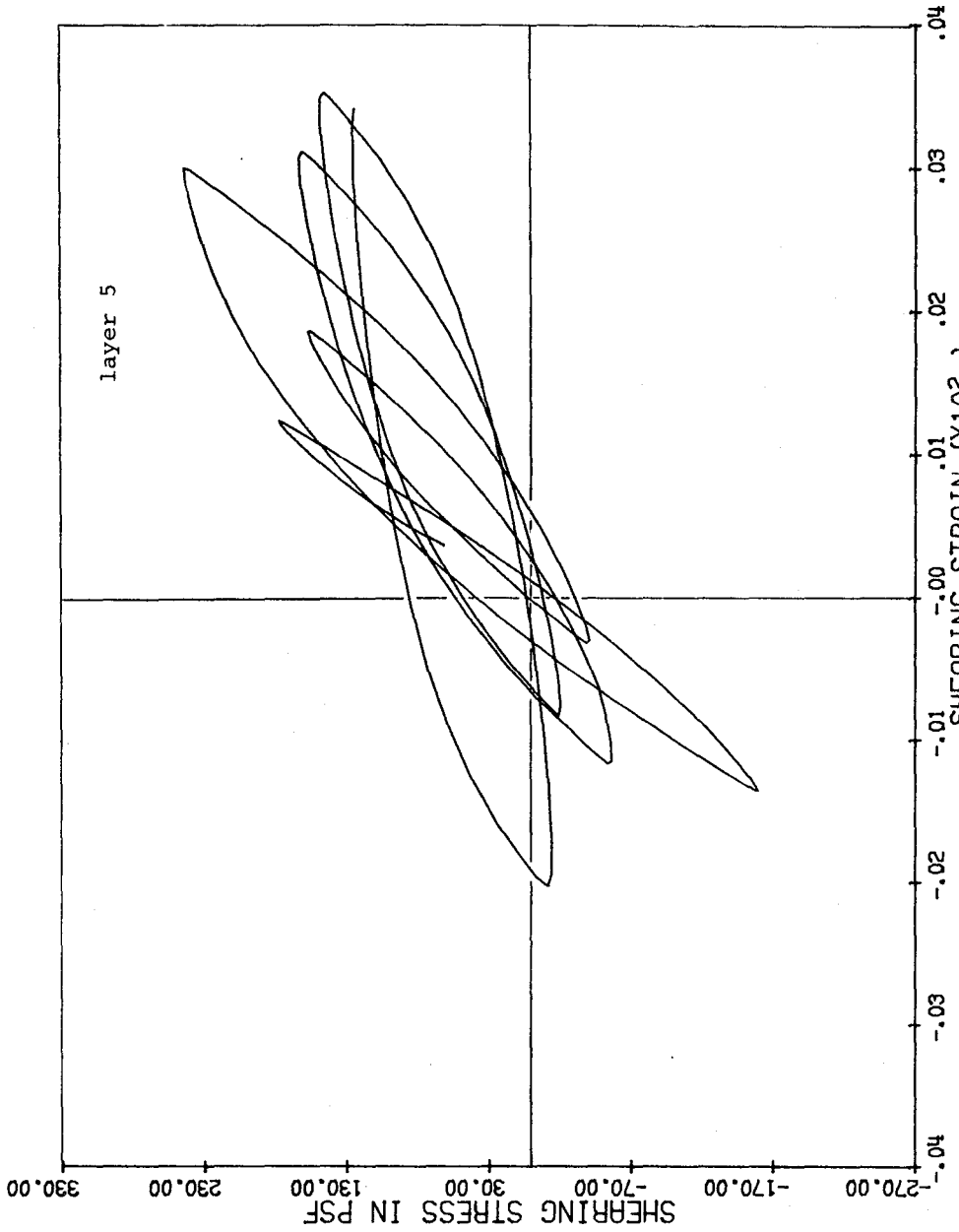

Figure 8-20 Example 8-3, shearing stress-strain relationship in layer 5

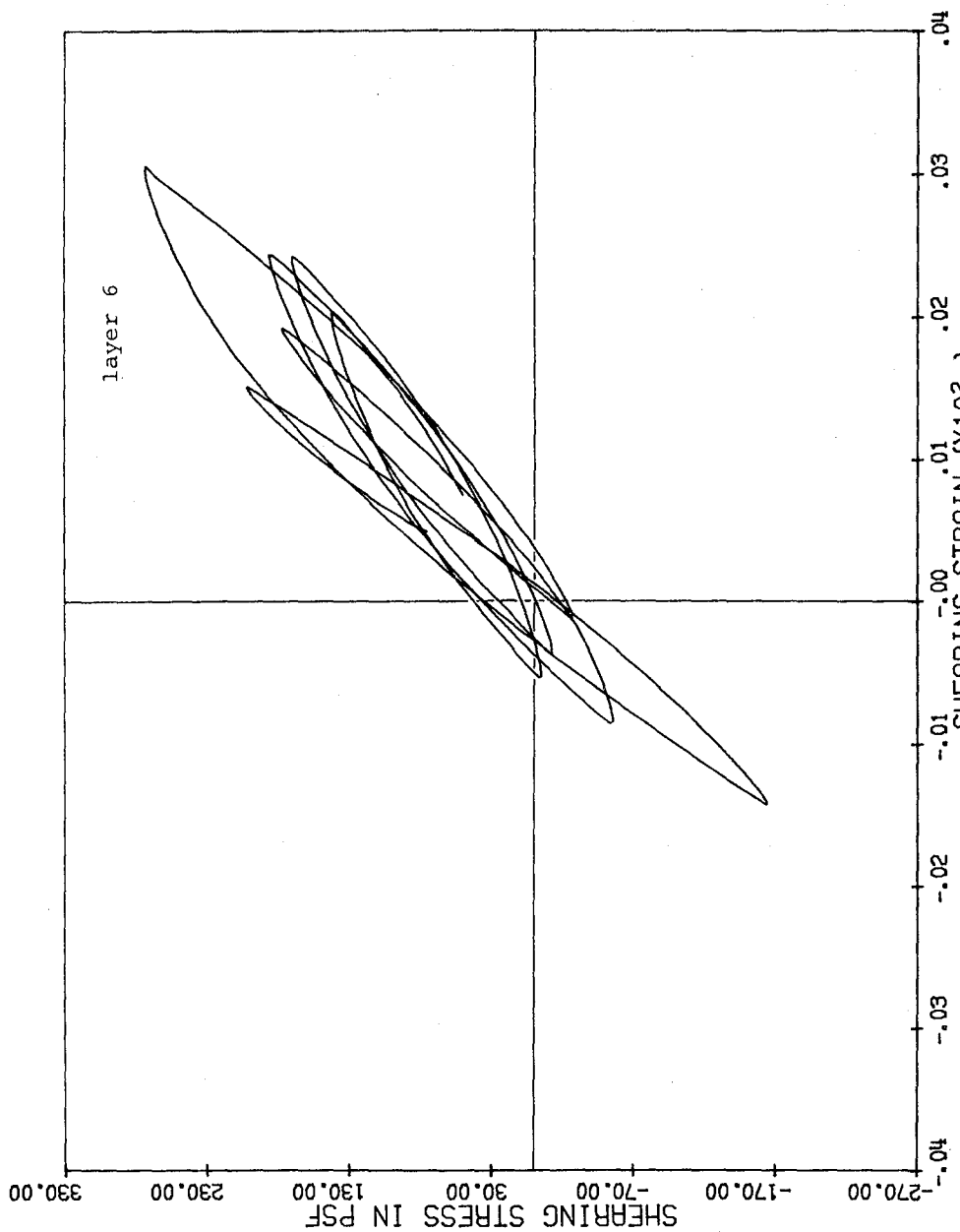

Figure 8-21 Example 8-3, shearing stress-strain relationship in layer 6

Figure 8-22 illustrates the time variations of pore water pressure and effective stress at 25 feet and at 31.25 feet from the surface. These two sets of curves are similar except for the static values of pore water pressure and effective stress.

Figure 8-23 shows the dynamic shearing stress and the shearing strength in layers 5 and 6. In layer 5 the peak shearing stress exceeded the shearing strength after about 0.8 seconds for some brief moments. This was not considered to be a failure, since the lack of strength was only temporary. However, relatively large shearing strains resulted from this temporary shearing strength deficiency. This can be readily seen in Figure 8-19b, in which the peaks of shearing strain in layer 5 deviated remarkably from those in layer 6 temporarily after about 0.8 seconds.

Failure of an inclined deposit is considered to occur when the shearing strength of any layer of the deposit becomes less than or equal to the average static shearing stress in that layer. In the present example, failure occurred when the shearing strength of layer 5 dropped below its static shearing stress at 1.4 seconds. The computation was terminated when failure occurred. After the failure large lateral or downhill movement would occur. The modeling of mass earth movement itself is beyond the scope of the study.

Figures 8-26 and 8-27 illustrate the spatial variations of the piezometric head and the effective stress at five selected instants. The soil below the less permeable layers was sheared nearly in an undrained condition. As a result,

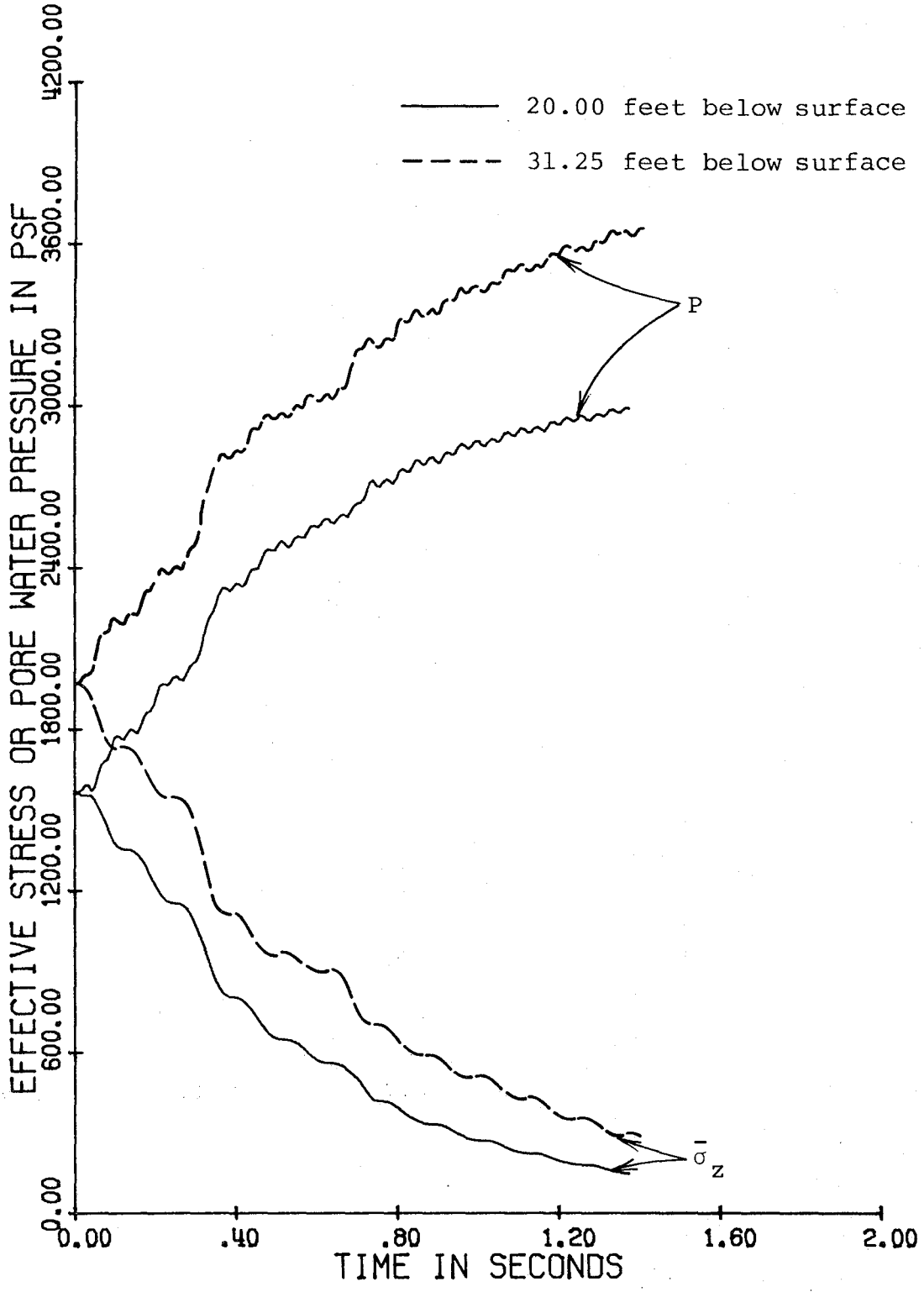

Figure 8-22 Example 8-3, time variation of effective stress and pore water pressure

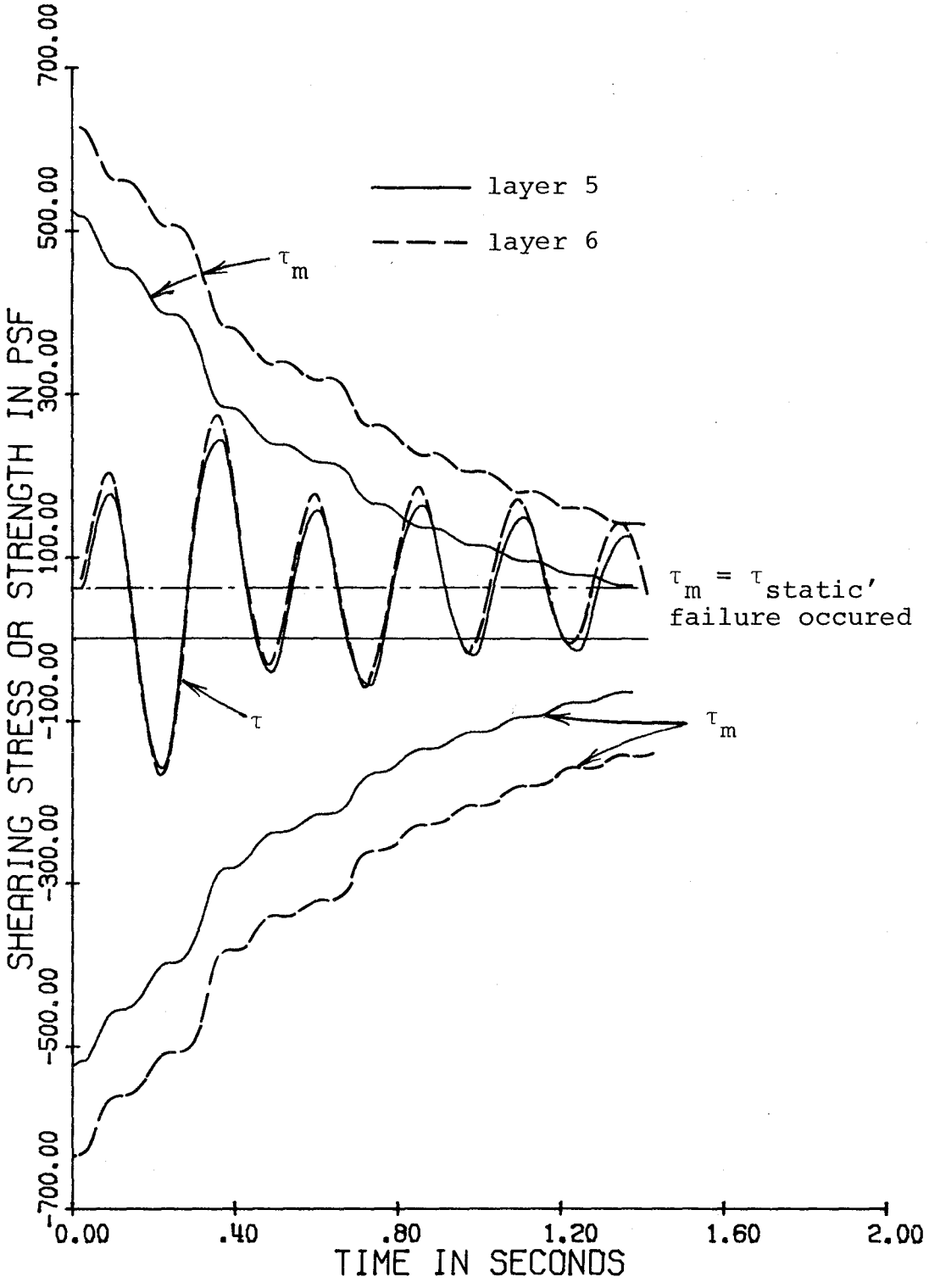

Figure 8-23 Example 8-3, time variation of shearing strength and shearing stress

the effective stress reduction and the piezometric head were nearly uniform in this portion of the deposit. The condition of the soil that lies above the less permeable layers was very similar to that shown in Figure 8-11. Water squeezed out of the upper portion of the less permeable zone was drained upwards more easily than that in the lower portion. This is evidenced by the difference in the gradient of the piezometric head in the less permeable layers. Minimum average effective stress occurred in the lower portion of the less permeable zone during the late stages of shearing. It was this portion of the deposit that failed first.

The response of the same deposit resting on a horizontal rock surface was also obtained. The dynamic shearing stress and shearing strain were similar to those in the inclined deposit, except that the strain was smaller. The initial rise in pore water pressure and the corresponding drop in effective stress were less rapid in the horizontal deposit than those in the inclined deposit. This could be explained by the larger changes in the secant shear modulus in the inclined deposit in which the initial shearing stress was present. The shearing strength of the horizontal deposit was slightly larger than that in the inclined deposit during the 8 cycles of shearing. The downward displacements of the ground surface were almost identical for the two cases. This displacement for the inclined deposit is shown in Figure 8-24. The lateral relative displacement between the surface and the bedrock of the inclined deposit, shown in Figure 8-25,

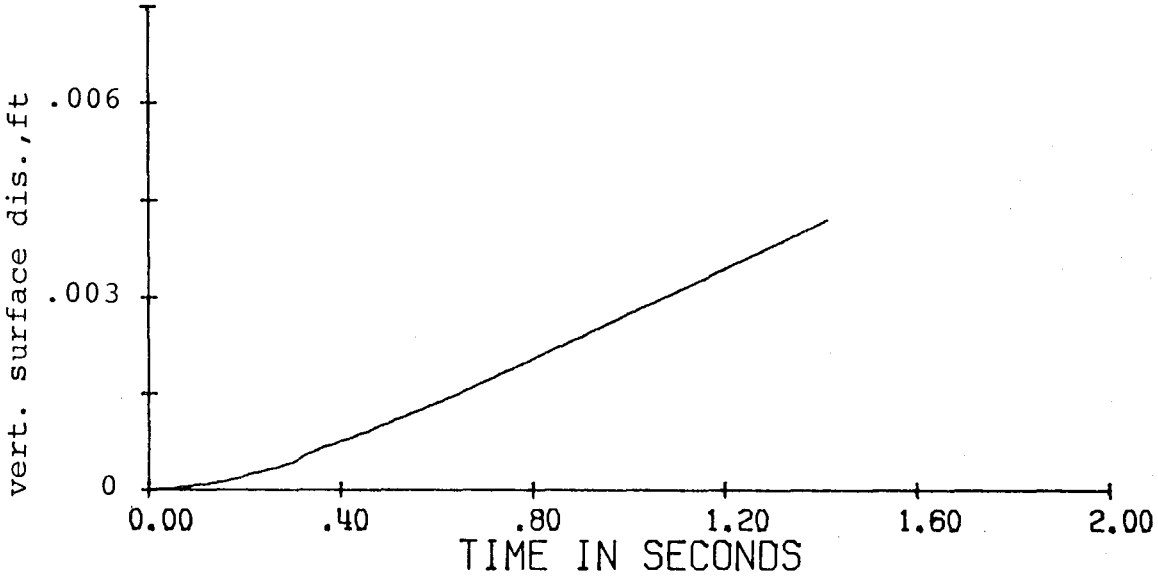

Figure 8-24 Example 8-3, time variation of downward surface displacement

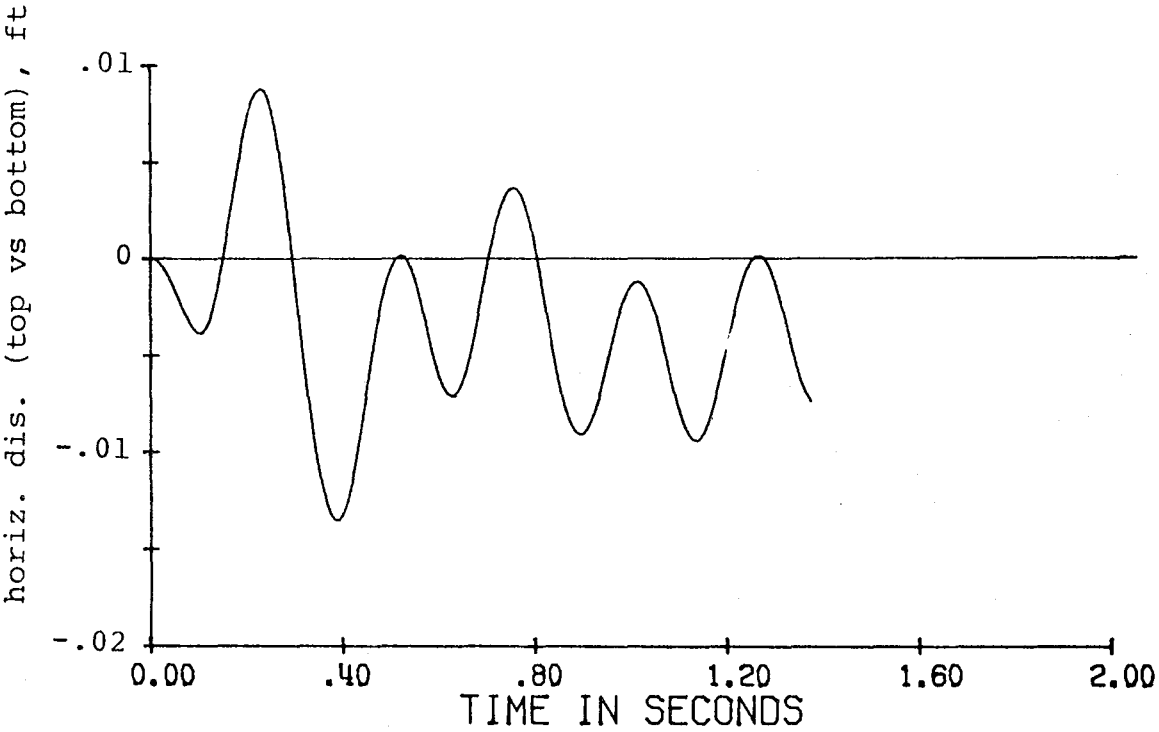

Figure 8-25 Example 8-3, time variation of horizontal relative displacement

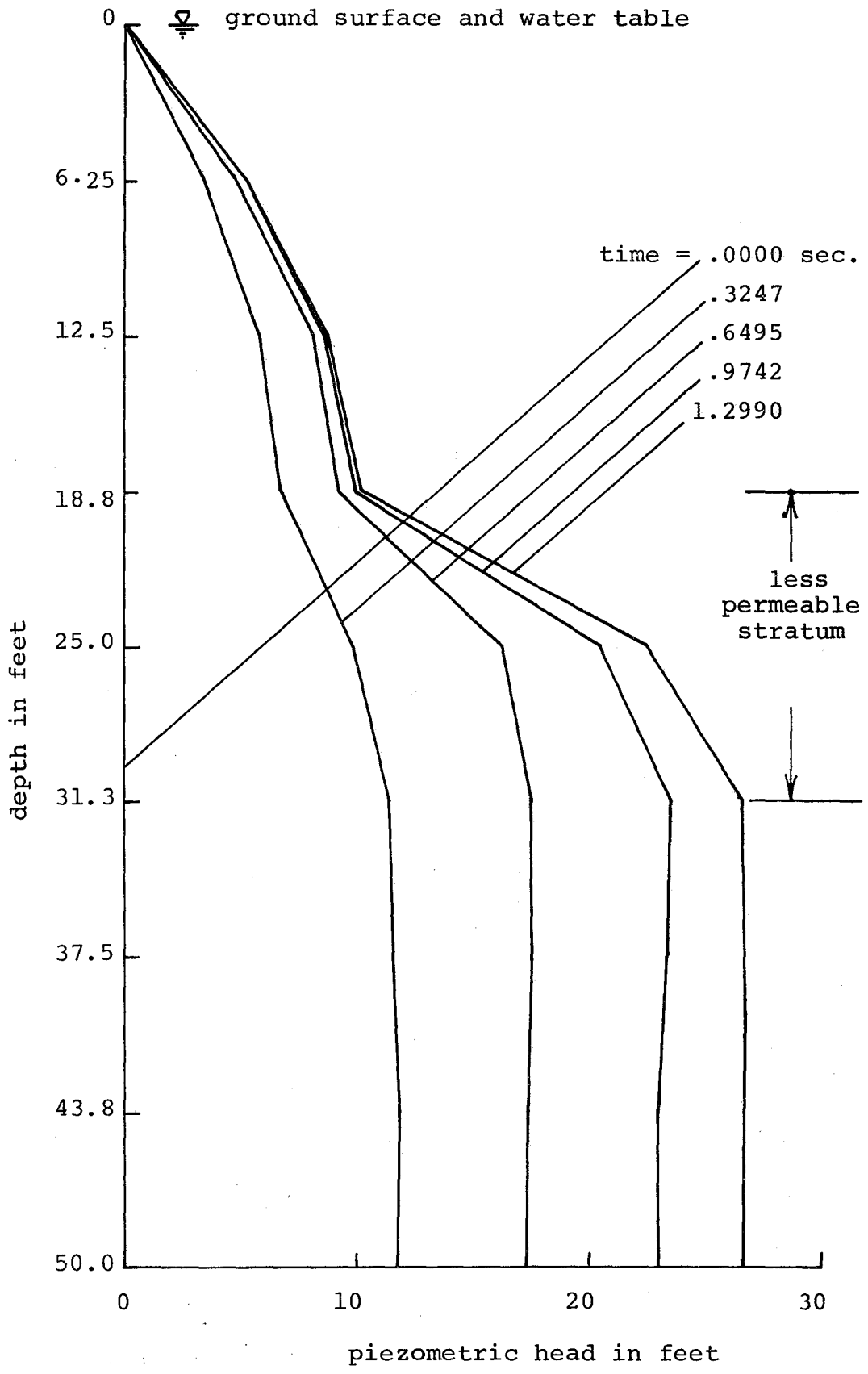

Figure 8-26 Example 8-3, profiles of piezometric head at selected instants

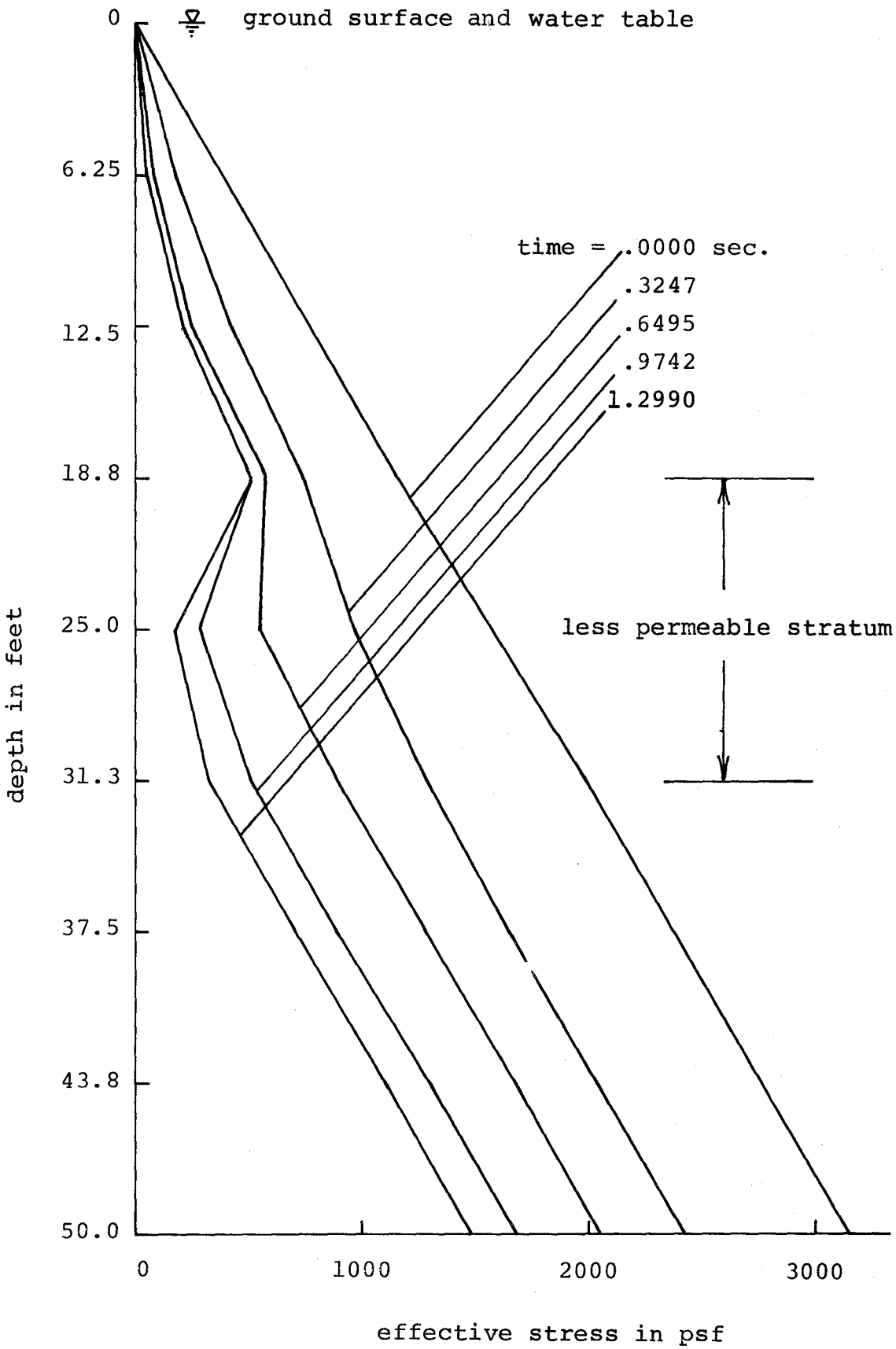

Figure 8-2 7 Example 8-3, profiles of effective stress at selected instants

was larger than that of the horizontal deposit. This difference was due to the gravitational force.

The response of the same horizontal deposit subjected to a slightly larger excitation was obtained as well. A single amplitude of 0.07 fps, instead of 0.06 fps, was used for the bedrock velocity. In this case, liquefaction was completed beneath the less permeable layers at approximately 1.82 seconds or after 7 cycles of shearing. Due to the absence of any driving force, no large deformation was developed, although the soil at a depth of 31.25 feet was in a liquid state.

CHAPTER 9

LIQUEFACTION CASE STUDIES

During the earthquake of June 16, 1964 in Niigata, Japan, 340 out of the 1530 reinforced concrete buildings in the city were damaged by the earthquake. From the distribution of buildings that tilted more than 2.5 degrees, Ohsaki[48] defined three zones of severity of damage in Niigata. The map showing the zones of damage is shown in Figure 9-1a.

The soil strata of Niigata City is composed of sand layers. It was observed that in zone C, the heavily damaged zone, light structures buried in the ground, such as a reinforced concrete box for purifying sewage floated up, while heavy buildings sank down.[48] Numerous sand craters were also observed. These facts indicate that liquefaction was completed at some locations during the earthquake. There is a section in zone C on which a 9 foot fill had been placed. This section showed no evidence of failure due to liquefaction while the surrounding areas without fill were damaged.[62] It was also observed that ground failure due to liquefaction did not occur in zone A or zone B. The different severity of liquefaction in the same city during the earthquake was attributed to differences in soil conditions.[48,62] Thus the soil behavior of Niigata provides an opportunity to judge the applicability of the proposed model for liquefaction.

The responses of the deposit in zone B, zone C, and the

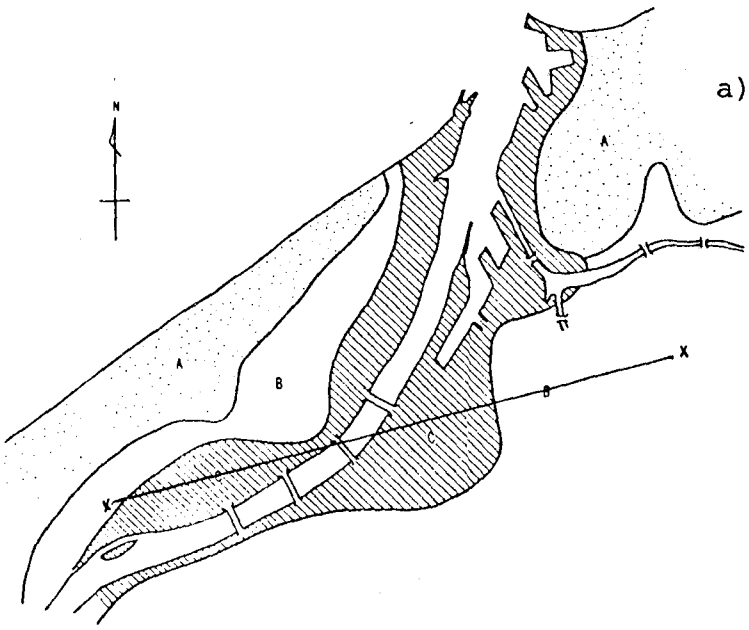

a) zoning of damage

b) soil profiles

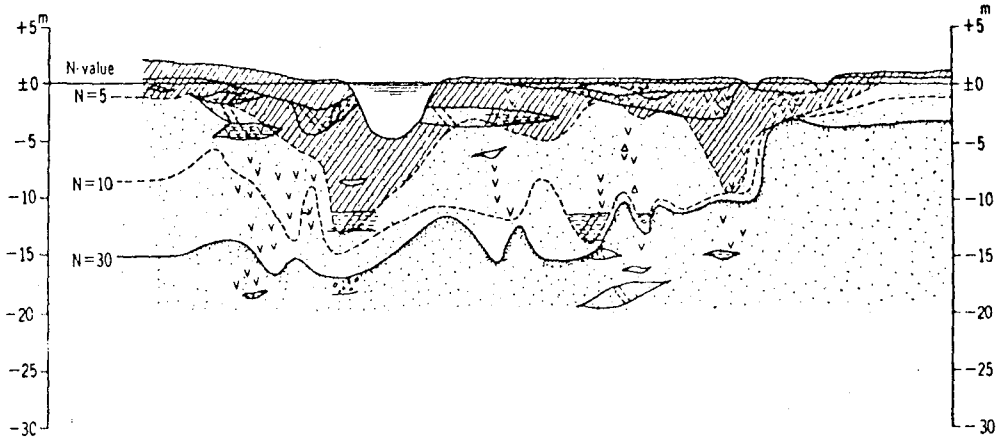

Figure 9-1 Zoning of damage and soil profile of Niigata(86)

filled section in zone C to an earthquake were studied. In zone A, the water table was about 10 feet below the ground surface, and the soil conditions were assumed to be similar to those of the section with fill. Thus no study was conducted for zone A. In the following sections the soil conditions, the earthquake used, the response of the ground in the 3 areas of interest and a discussion on the computed results are presented.

9-1. Reported and estimated soil conditions.

Sand layers underlie the city of Niigata. A cross section of the strata together with three lines indicating the blow counts, N, of the standard penetration test are shown in Figure 9-1b. Very loose sand with N-values less than 5 lie near the ground surface. Loose and medium sand with N-values between 10 and 30 lie, in general, at depth from 30 to 45 feet below the ground surface. Sand with N values greater than 30, in general, lie at a depth greater than 45 feet. The distance between the ground surface and firm base material is about 200 feet.[62] Lens-like layers of silty sand are scattered about in the sand layers.[48] This local non-uniformity was not considered in the study. Since soil usually does not fail in shear at large effective confining pressure, only the top 50 feet of the deposit was used in the case studies. The depth of saturated deposit was 47 feet. This depth was divided into 7 equal layers. Soil properties varied with depth, but in each layer, they are considered to be uniform. The water table in both zone B and zone C was 3 feet below the ground surface.

The specific gravity of the solid material in Niigata sand is 2.66.[75] The unit weight of the sand above the water table was estimated as 110 lb/ft^3 and the submerged unit weight was estimated as 50 lb/ft^3.[62] Based on this submerged weight and the unit weight of water, a porosity of 0.52 was calculated. Niigata sand is poorly graded, with a coefficient of uniformity less than 5.[48] The permeability was estimated as 0.00024 ft/sec. All the properties described above were considered common to all zones.

The differences in soil conditions between zone B and zone C were characterized by the blow counts, N, from the standard penetration test. The variations of the blow count with depth for these two zones has been reported by Seed[62] and is reproduced in Figure 9-2. It is seen that at a depth of 15 feet from the ground surface or deeper, the penetration resistance of zone C was considerably less than that of zone B. This infers the shearing strength of zone C was lower than that of zone B. The friction angle, ϕ, for the 7 layers in both zones could be obtained from the blow counts by using the correlation established by Peck, Hanson and Thornborn.[80] The blow counts and ϕ values in degrees are listed in Table 9-1.

The coefficient of earth pressure at rest, K_0, was estimated as 0.46 for zone B and 0.48 for zone C, and was considered to be uniform in both zones. Due to the high void ratio, which was assumed to be common for all zones, Equation (6-11) was used to calculate G_0 for the three areas.

TABLE 9-1

BLOW COUNTS AND FRICTION ANGLES IN ZONE B AND ZONE C

	Zone B		Zone C	
Layer No.	Blow Count	ϕ	Blow Count	ϕ
1	7	29	6	28
2	8	29	7	29
3	13	31	8	29
4	19	33	10	30
5	26	35	17	32
6	34	37	24	34
7	39	38	30	36

A comparison was made between the Niigata sand and that at the Eglin Field, Florida. The Eglin marine sand[81] is a medium, poorly graded sand with a void ratio of approximately 0.7. The specific gravity of the solid material of Eglin sand is 2.66 and its moist unit weight is 110 lb/ft^3. The envelope of the grain size distribution curves of the Niigata sand, reported by Ohsaki[48], and that of the Eglin marine sand, reported by Heller[82], are shown in Figure 9-3. Based on these data, it was assumed that Niigata sand is similar, but has a lower density than Eglin marine sand. Figure 9-4 shows the comparison between the estimated small motion shear modulus of the deposit in Niigata city and the same quantity in the Eglin Field Site. The latter was determined in situ by vibration and steady state tests. The tests only extended to a depth of 12 feet. It can be seen that the estimated small motion shear moduli throughout the deposit were realistic. The small motion shear moduli so estimated were used for both zone B and zone C.

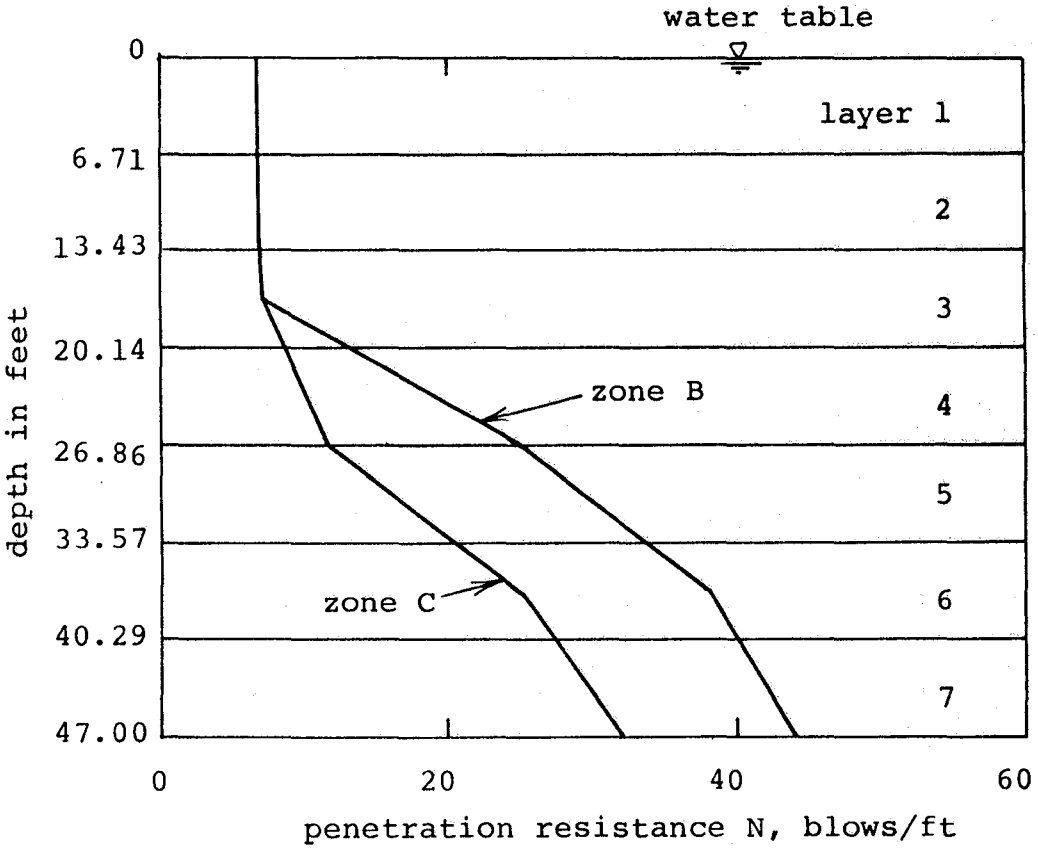

Figure 9-2 Penetration resistance of zones B and C

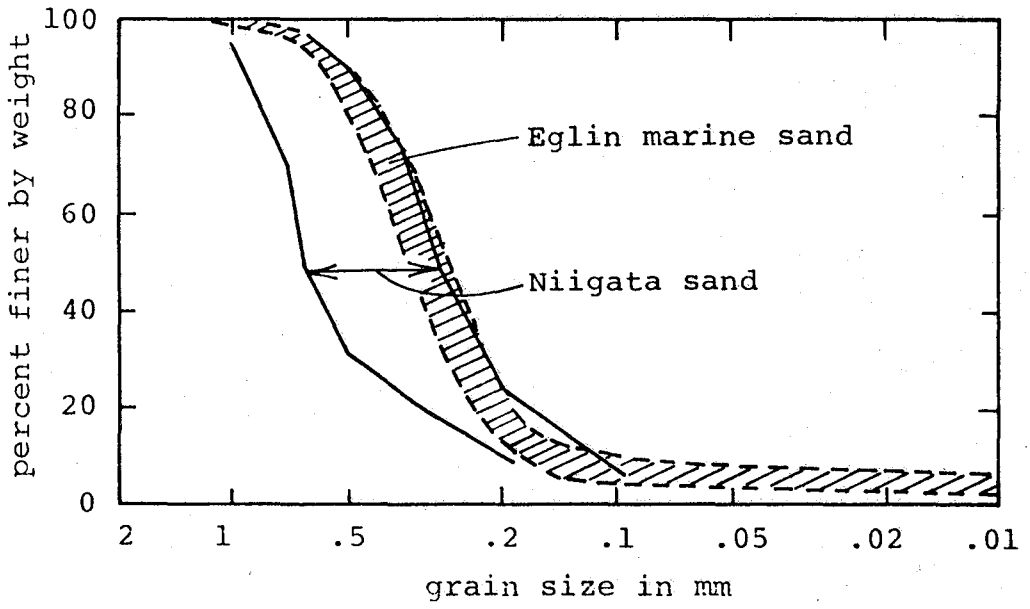

Figure 9-3 Grain size distributions of Niigata sand and Eglin marine sand

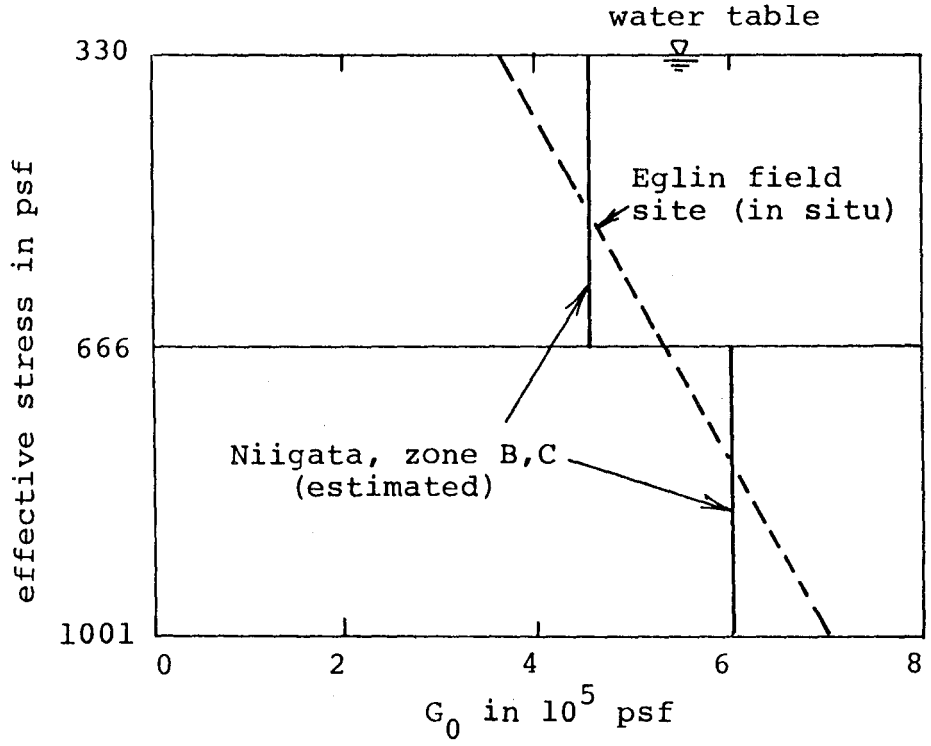

Figure 9-4 Comparison of estimated G_0 in Niigata and the G_0 of Eglin field site tested in situ

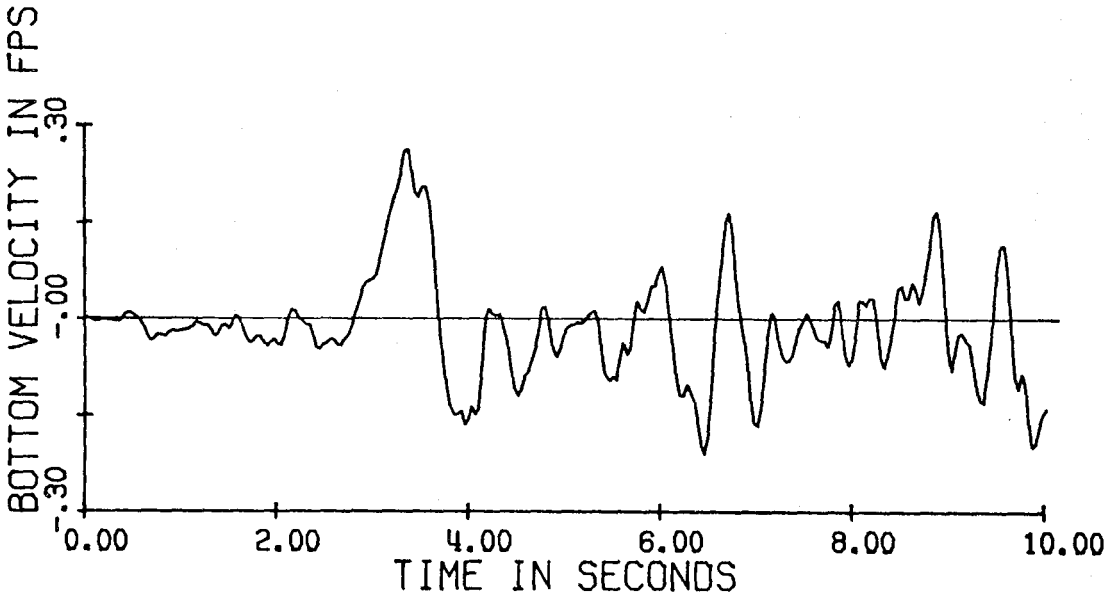

Figure 9-5 Specified horizontal velocity at a depth of 50 feet below the ground surface

Before estimating the bulk moduli, the following observations were made. Al-Hussaini[83] conducted plane strain and triaxial compression tests on saturated Chattahoochee river sand to demonstrate the effect of relative density and strain conditions on the strength and stress-strain characteristics of sand. He concluded that the bulk modulus of sand tested increased with increasing relative density. On the other hand, Richart, Hall and Woods[54] demonstrated that, besides its influence via void ratio, relative density has a negligible influence on low strain level shear modulus. Pyke[52] also observed that variations of low strain level shear modulus with respect to relative density were not very great. Thus it is reasonable to anticipate that, in general, the ratio of bulk modulus, B, to the small motion shear modulus, G_0, increases with increasing relative density. Based on Figures 4 and 8 of Al-Hussaini's paper, the following tabulation of variation of B/G_0 versus relative density was obtained. The effective confining pressure corresponding to the derived data in Table 9-2 is 70

TABLE 9-2

VARIATION OF B/G_0 W.R.T. RELATIVE DENSITY

relative density	36	42	63	77	88	95
B/G_0	.633	.717	1.22	1.43	1.67	2.34

psi. The bulk moduli B were secant moduli, calculated from Figure 4 mentioned above. In the course of obtaining G_0 from Figure 8 of Al-Hussaini's, a Poisson's ratio of 1/3

was assumed. Table 9-2 supports the stated trend that B/G_0 increases with increasing relative density. This trend was assumed to hold for Niigata sand.

The moduli B and G_0 can be regarded as properties of the soil skeleton at small deformations. For small deformations, the soil skeleton can be treated as a linear elastic material. Therefore, the ratio B/G_0 can be expressed in terms of Poisson's ratio, ν, as[60]

$$\frac{B}{G_0} = \frac{2(1 + \nu)}{3(1 - 2\nu)} \tag{9-1}$$

The Poisson's ratio of each zone in Niigata City was not reported and hence had to be estimated. It would be helpful if the Poisson's ratio of a similar sand were known. This information was again provided by the test data of Eglin marine sand. The shear wave speed and the pressure wave speed of the unsaturated soil were obtained in situ at the Eglin Field Site by vibratory and steady state methods.[81] The motion of soil during these field tests was small, thus elasticity theory applied. The Poisson's ratio calculated from these two wave speeds lie between 0.36 and 0.46. Based on this information and noting that Eglin marine sand is denser than Niigata sand, the Poisson's ratio of zone B in Niigata was estimated as 0.4 and that of zone C in Niigata was estimated as 0.3. From the estimated Poisson's ratio and from Equation (9-1), B/G_0 was calculated as 4.67 for zone B and 2.17 for zone C.

Because of the fill, the effective confining pressure

was larger in the filled area than that surrounding it. The moist unit weight of the fill was estimated as 110 lb/ft^3. The depth of the fill was 9 feet[62], and the water table was 12 feet below the ground surface. Except for the properties that were affected by the effective confining pressure, the soil was considered to be the same as that in zone C. The initial small motion shear modulus and the initial shear strength for the three areas are summarized in Tables 9-3, 9-4 and 9-5.

TABLE 9-3

INITIAL G_0 AND τ_m IN ZONE B

Layer No.	G_0, psf	τ_m, psf
1	0.457×10^6	114
2	0.591×10^6	191
3	0.700×10^6	306
4	0.794×10^6	439
5	0.878×10^6	589
6	0.955×10^6	754
7	1.026×10^6	902

For all zones, the soil below the water table was assumed to be fully saturated. A bulk modulus of 4.26×10^7 psf and a mass density of 1.94 $lb\text{-}sec^2/ft$ were used for the pore water. In the modified Ramberg-Osgood relationship, $\alpha = 1$, $R = 3.0$ and $C_1 = 0.8$ were used for all the case studies.

TABLE 9-4

INITIAL G_0 AND τ_m IN ZONE C

Layer No.	G_0, psf	τ_m, psf
1	0.426×10^6	115
2	0.597×10^6	206
3	0.707×10^6	289
4	0.802×10^6	396
5	0.887×10^6	540
6	0.965×10^6	701
7	1.037×10^6	875

TABLE 9-5

INITIAL G_0 AND τ_m IN THE FILLED SECTION OF ZONE C

Layer No.	G_0, psf	τ_m, psf
1	0.773×10^6	322
2	0.861×10^6	428
3	0.941×10^6	511
4	1.014×10^6	633
5	1.083×10^6	805
6	1.147×10^6	990
7	1.208×10^6	1190

9-2. The excitation used in the case studies.

The maximum ground acceleration recorded at the basement of an apartment building during the earthquake was recorded as 0.16g.[62] The bedrock is located at about 200

feet below ground surface and its motion was unknown. Seed and Idriss scaled down the accelerogram of the Taft earthquake of July 21, 1952 by a factor of 0.72, and then used it in the analysis of liquefaction in Niigata.[62]

Since only the top 50 feet of the deposit was used in the present study, it was necessary to specify the motion of the sand at a depth of 50 feet, instead of at the bedrock. The velocity obtained by integrating the accelerogram of the Taft earthquake was multiplied by 0.55 and was used as the horizontal velocity of the sand at a depth of 50 feet. The corresponding maximum acceleration at the ground surface, computed through the use of CHARSOIL[84] was 0.16g. This specified velocity, or the "base velocity" is shown in Figure 9-5.

9-3. Results and interpretations of the computed response.

Shown in Figure 9-6 are the time histories of shearing stress in layer 4 of zone B, zone C, and the filled section of zone C. During the first 3 seconds, the dynamic shearing stresses in zone B and zone C were similar. This is reasonable since the "base velocity" variation was small during this period and both zone B and zone C were strong enough to be responsive to the excitation. The shearing stress in layer 4 of the filled area of zone C was different from that in the remainder of zone C. This was attributed to the 9 foot fill which strengthened the soil and changed the natural frequencies of the deposit. The shearing stress variation of the filled section was larger than those in

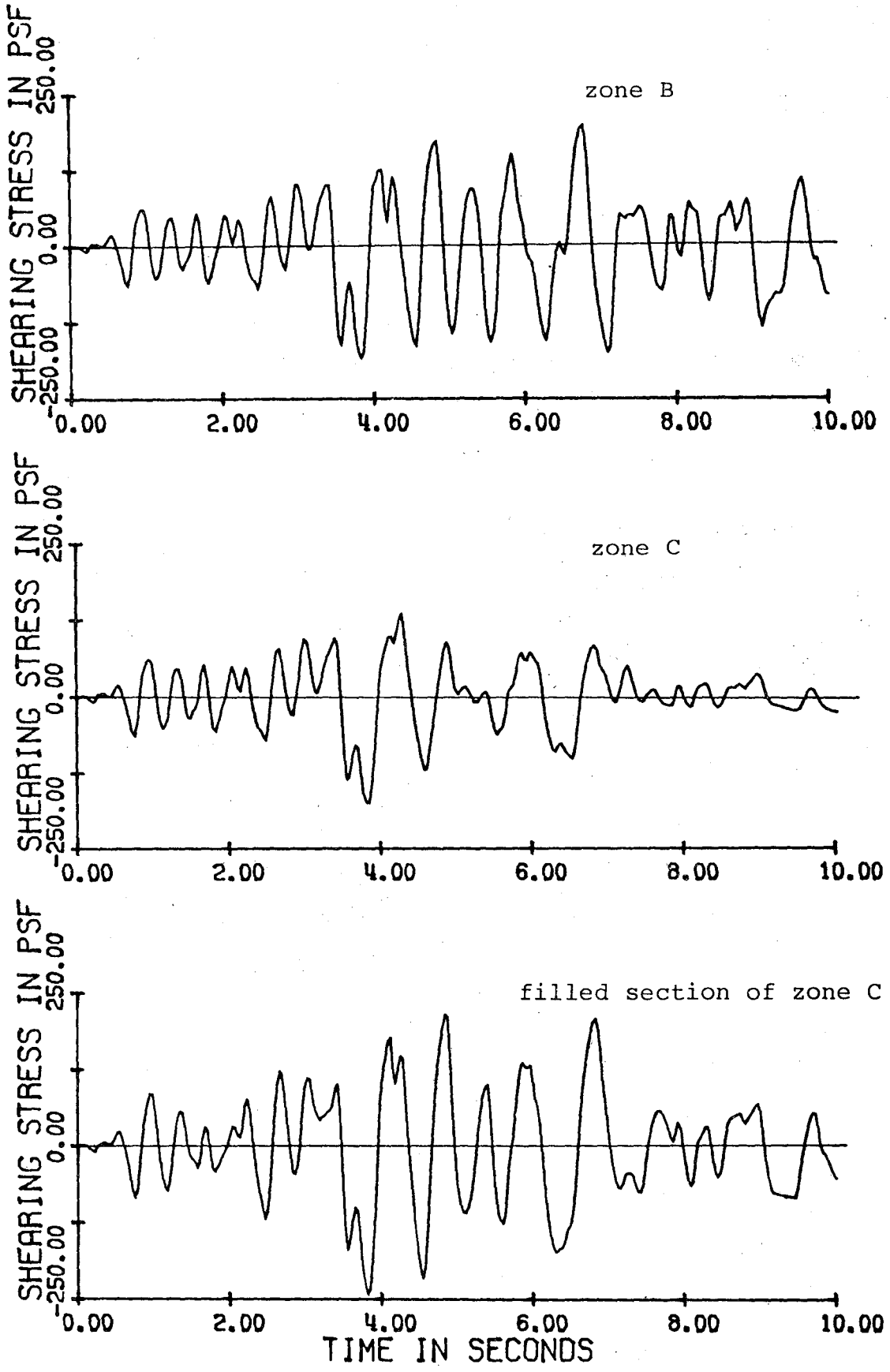

Figure 9-6 Time history of shearing stresses

zones B and C. After 3 seconds the variation of "base velocity" became more violent. The shearing stress trace in zone B began to deviate from that in zone C, with zone B being more responsive to the shaking. The shearing stress in zone C became smaller after 7 seconds of shaking, indicating that the deposit was softened considerably. The improvement of performance attributed to the fill was reflected by the higher shearing stress, compared with that of zone C, during the same time interval. Figure 9-7 shows the strain history of the three cases. After 6 seconds, the strain difference between zone B and zone C was more pronounced. The strain in the filled section of zone C was smaller than that surrounding it, although the shearing stress developed in the latter was smaller.

Figures 9-8, 9-9 and 9-10 show the hysteresis loops of layer 4 of zone B, zone C, and the filled section of zone C. It is seen that near the end of the shaking, the incremental strain associated with a given incremental stress was much larger in zone C, than those in zone B and the filled section. This sharp contrast suggests that at the end of 10 seconds, zone C failed while zone B and the filled section did not. However, the rigidity of zone B and the filled section had been reduced as well.

Figures 9-11, 9-12 and 9-13 show the rising pore water pressure and the corresponding effective stress reductions at a depth of 20.14 feet. It is seen that liquefaction was almost completed in zone C at this depth. In the filled section the drop in effective stress was the largest among

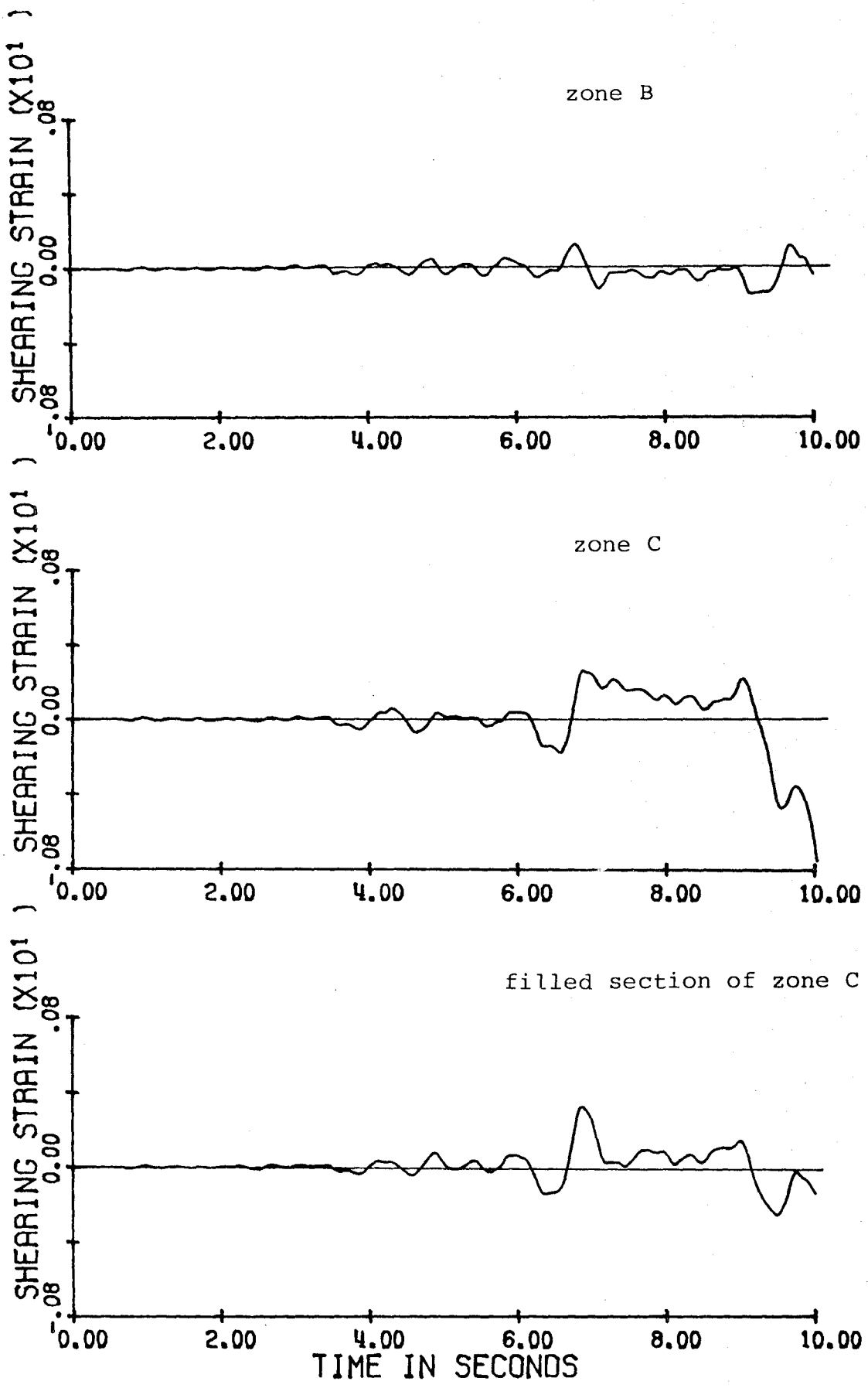

Figure 9-7 Time history of shearing strains

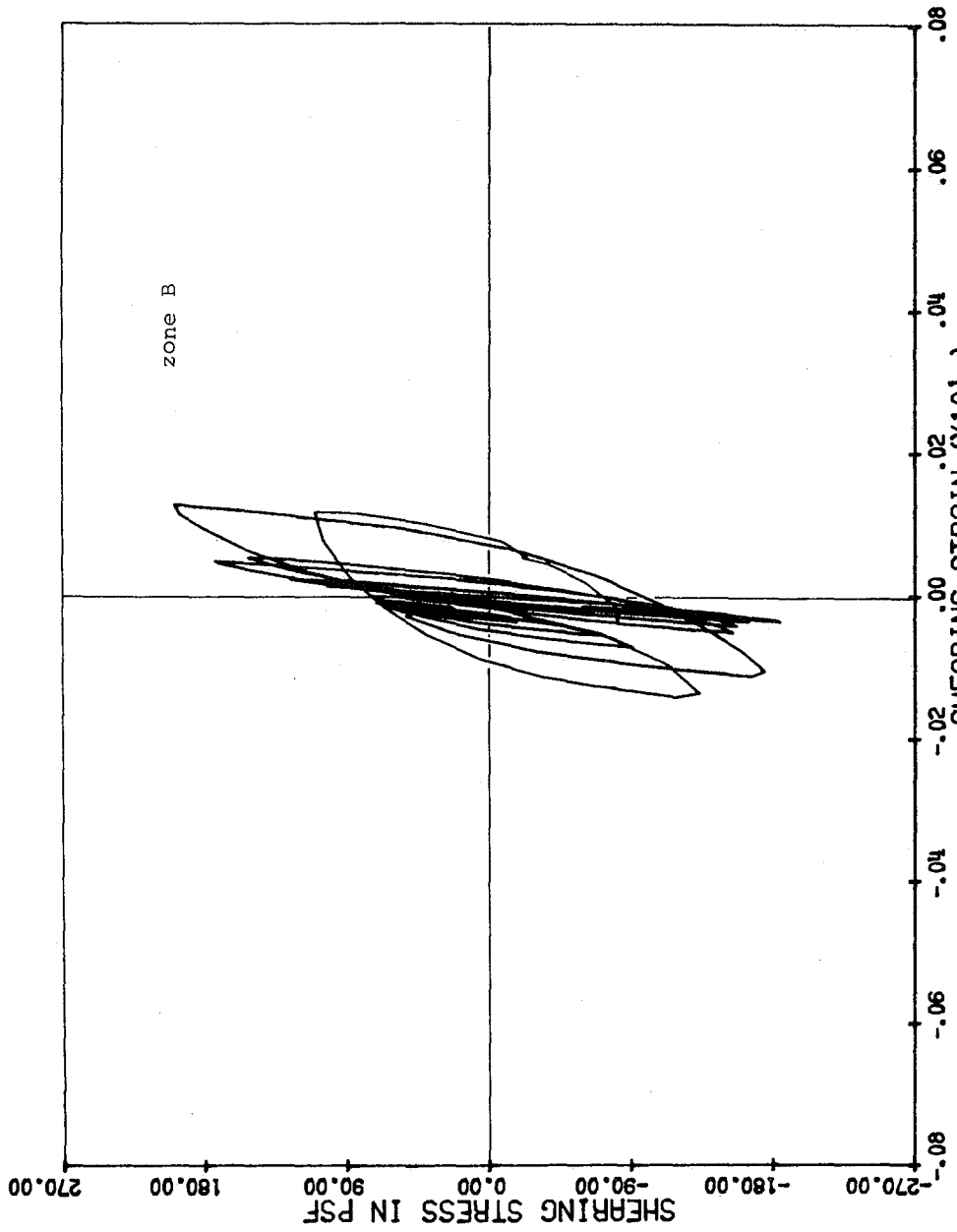

Figure 9-8 Hysteresis loops in the 4th layer of zone B

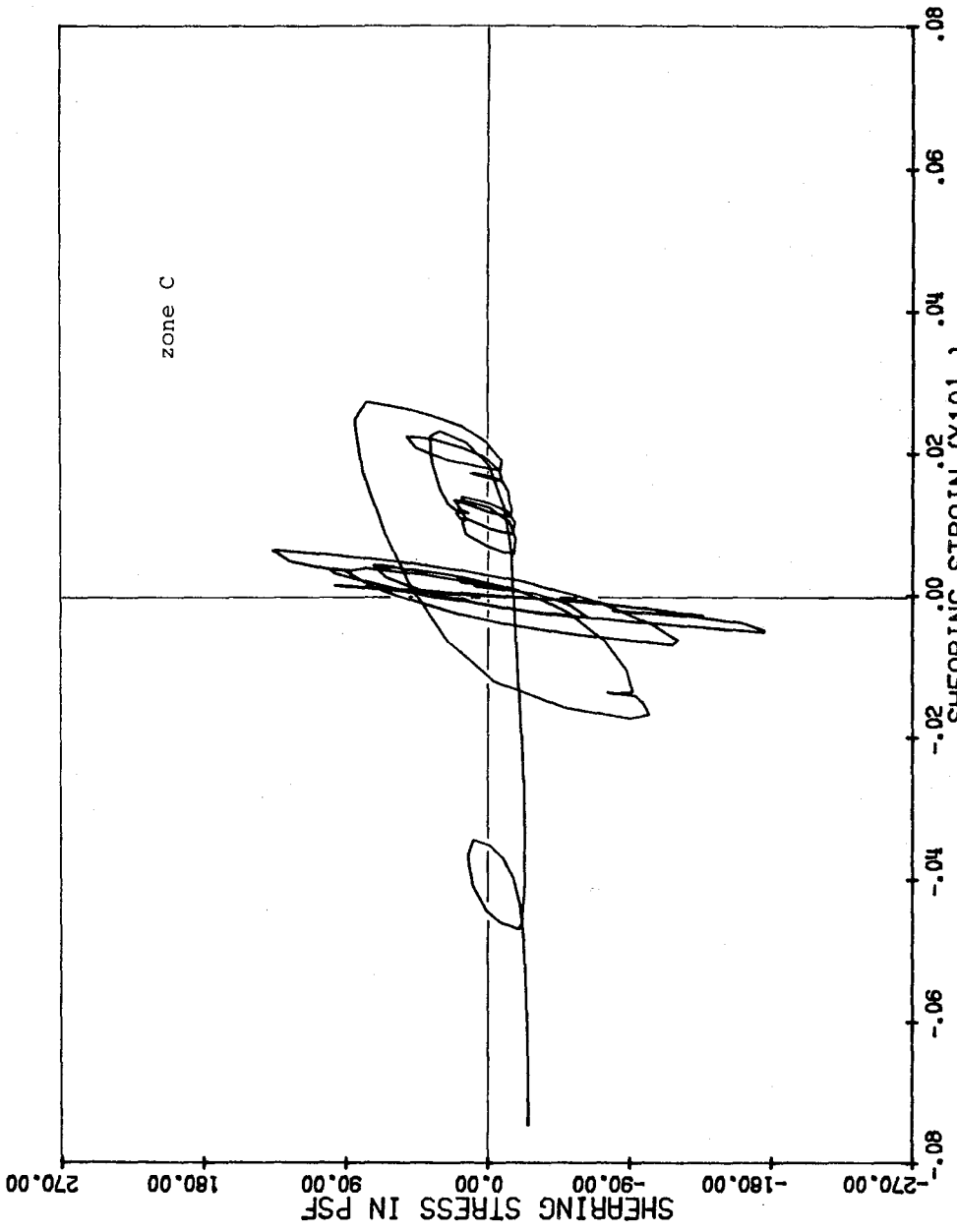

Figure 9-9 Hysteresis loops in the 4th layer of zone C

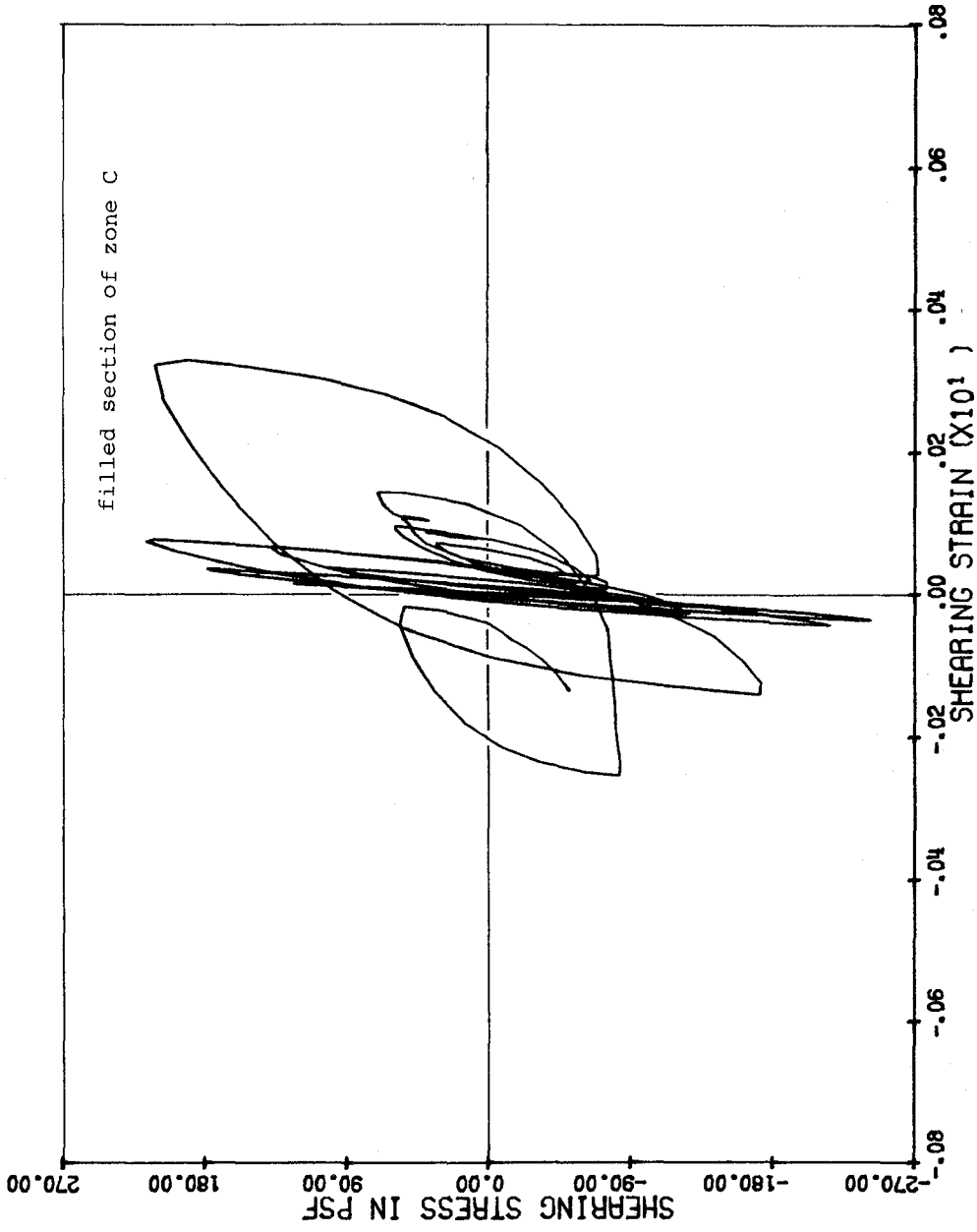

Figure 9-10 Hysteresis loops in the 4th layer of the filled section of zone C

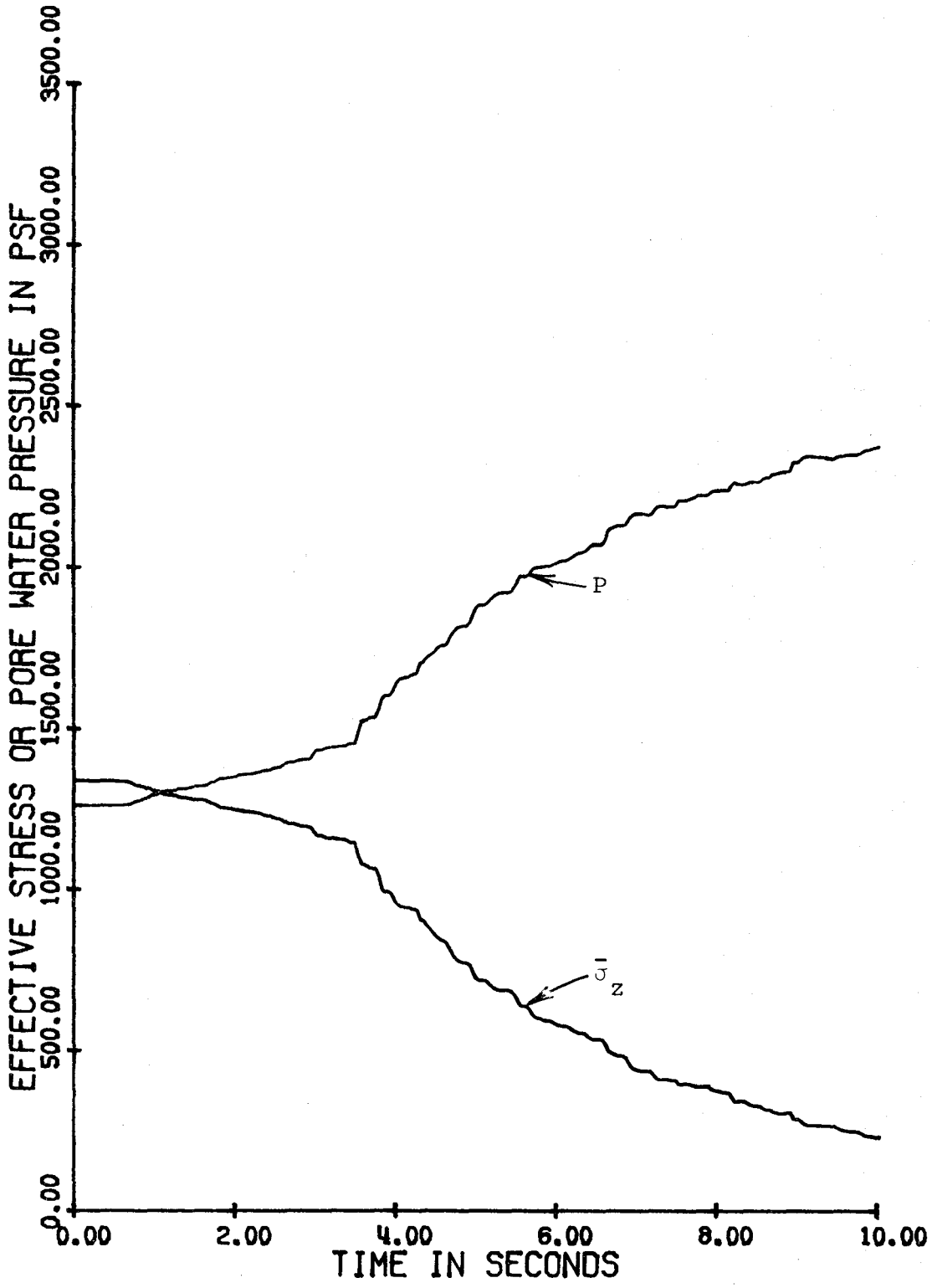

Figure 9-11 Time history of effective stress and pore water pressure in zone B

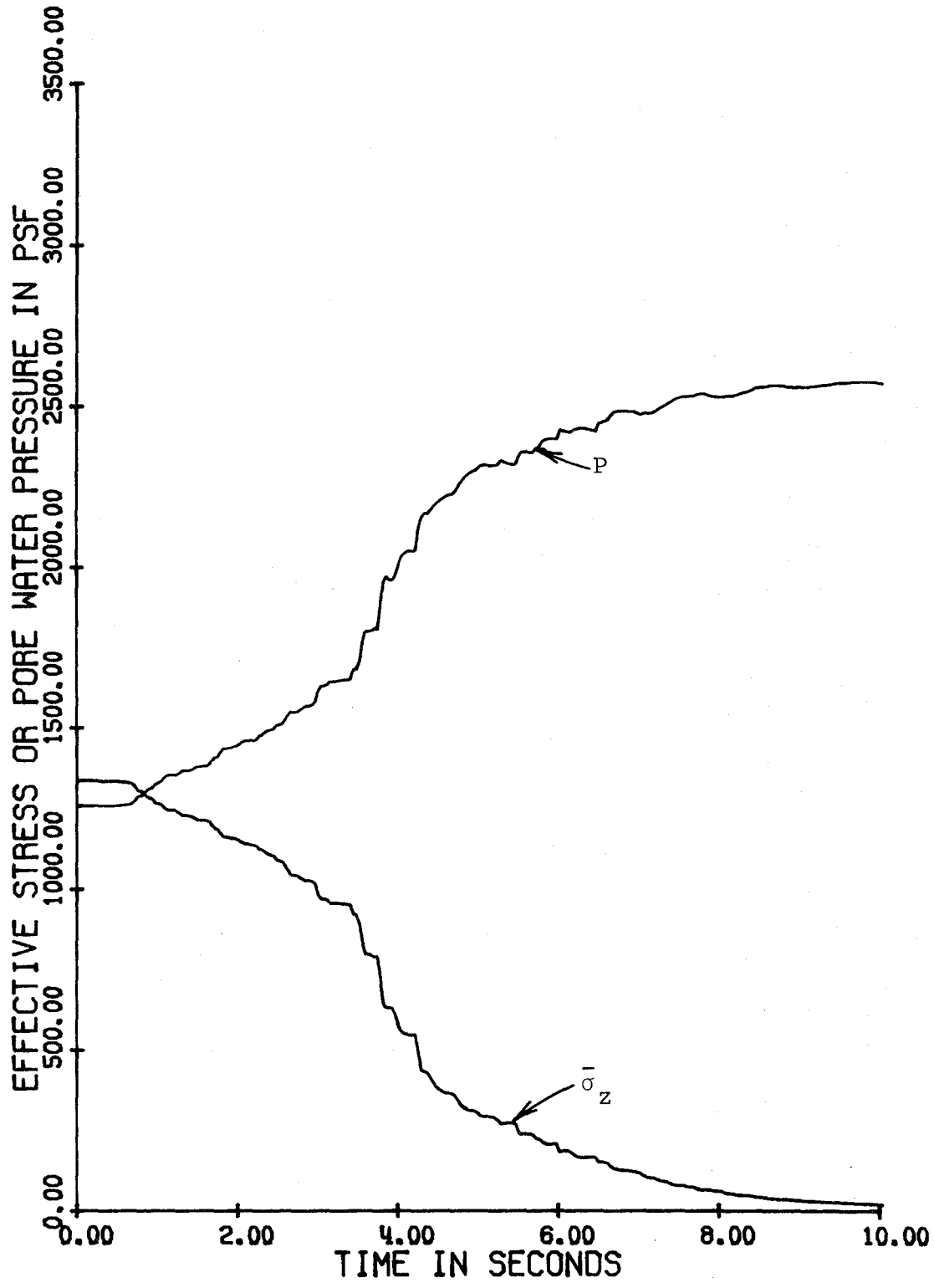

Figure 9-12 Time history of effective stress and pore water pressure in zone C

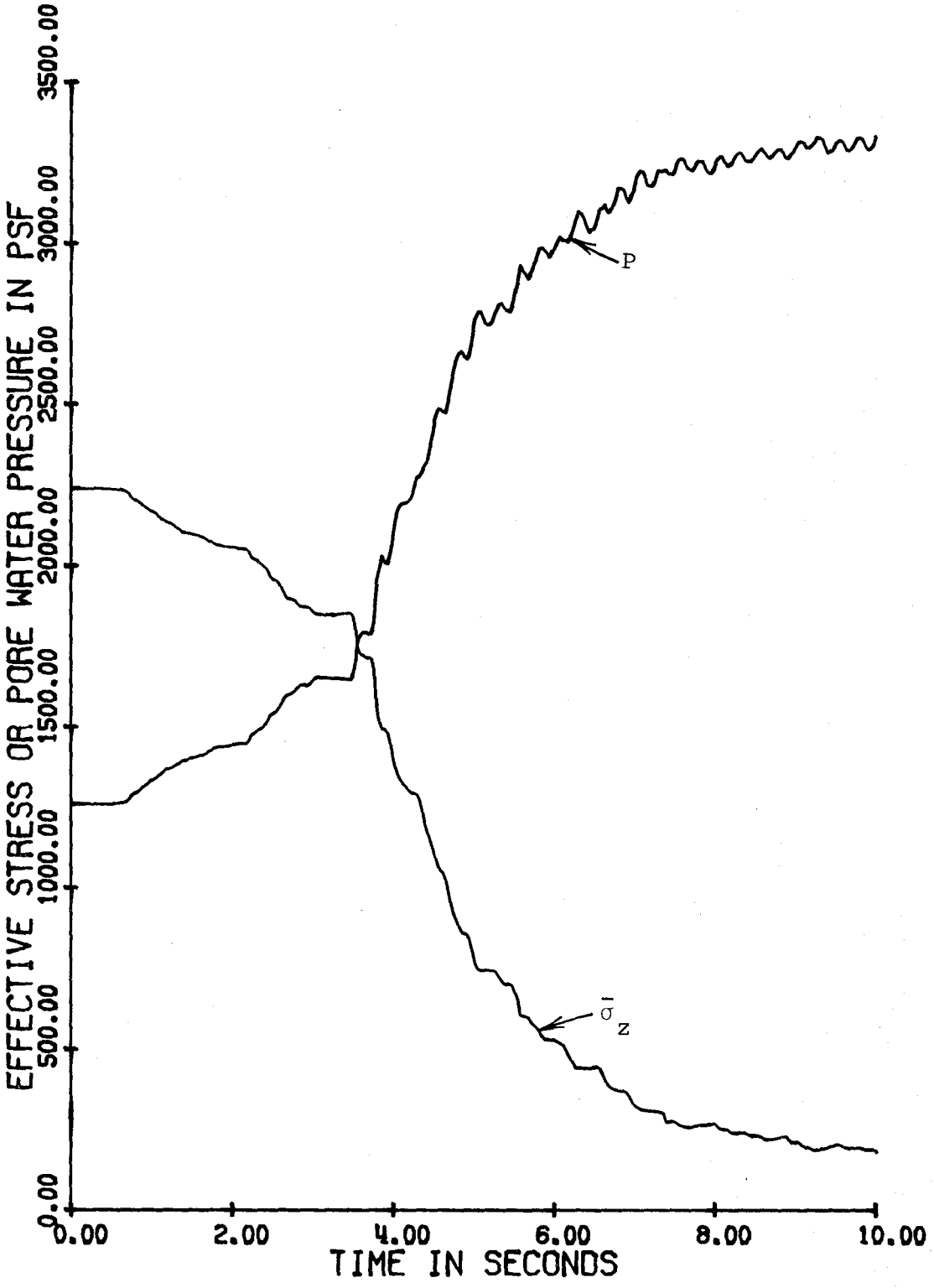

Figure 9-13 Time history of effective stress and pore water pressure in the filled section of zone C

these three areas. The level of effective stress in the filled zone remained higher than that in zone C during the transients, because the initial effective stress in the filled zone was larger. Figures 9-12 and 9-13 reveal that after 3 seconds, the time rate of effective stress reduction in the filled section was greater than that in zone C. This corresponds to the more violent motion of the "base". At about 7 seconds the difference in the rate of decrease of effective stress started to diminish. After 9 seconds the difference was almost non-existent. Meanwhile, the "base" was still moving violently. Hence the results suggest that for a given period of shaking, there was a net gain in effective stress, and hence in shearing strength, when a fill had been placed.

Figures 9-14, 9-15 and 9-16 show the shearing strength and the shearing stress in layer 4 of the three areas. Since the friction angle of layer 4 of zone C was 3 degrees less than that of layer 4 of zone B, the initial shearing strength of the former was less than that of the latter. The high initial shearing strength of the filled section was caused by the higher initial effective confining pressure in the deposit. In all three areas, the dynamic shearing stress exceeded the shearing strength for several brief moments after 6 seconds. At 10 seconds the shearing strength in zone C was only 7.9 psf as compared to 83.3 psf in zone B and 41.7 psf in the filled section of zone C.

Figures 9-17 and 9-18 show the time variation of the relative displacement between the "top" and the "base" of

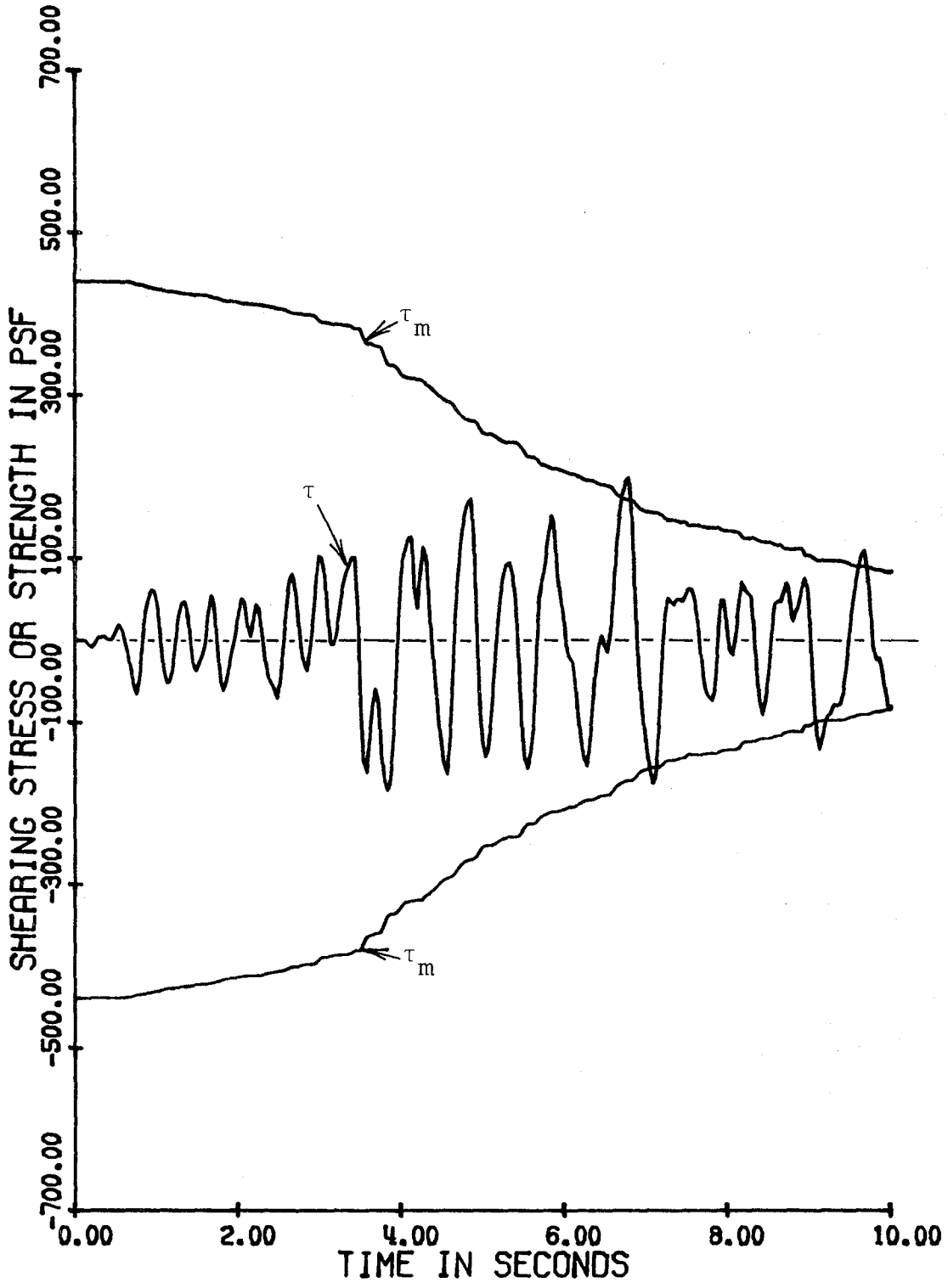

Figure 9-14 Time history of shearing strength and shearing stress in zone B

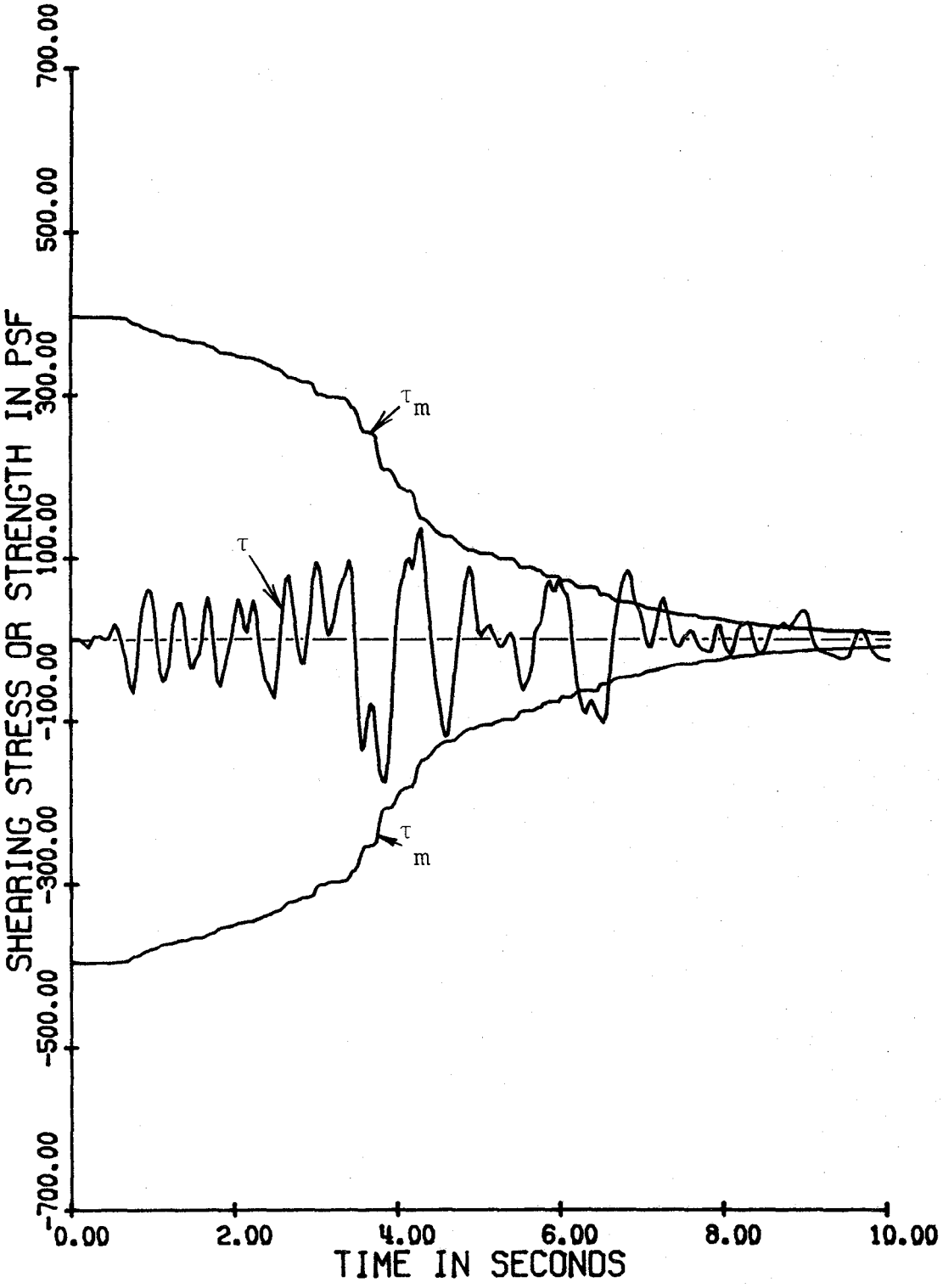

Figure 9-15 Time history of shearing strength and shearing stress in zone C

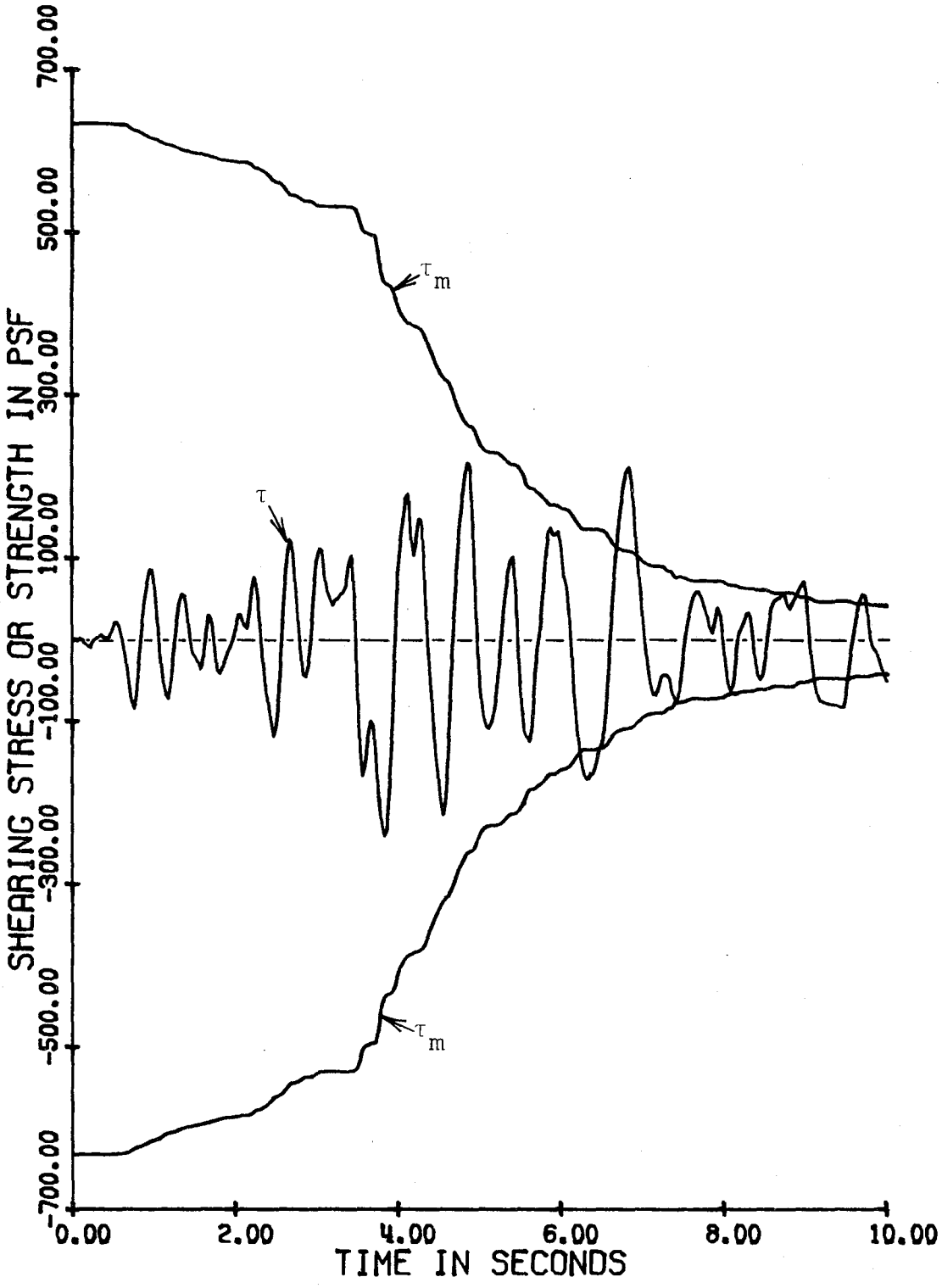

Figure 9-16 Time history of shearing strength and shearing stress in the filled section of zone C

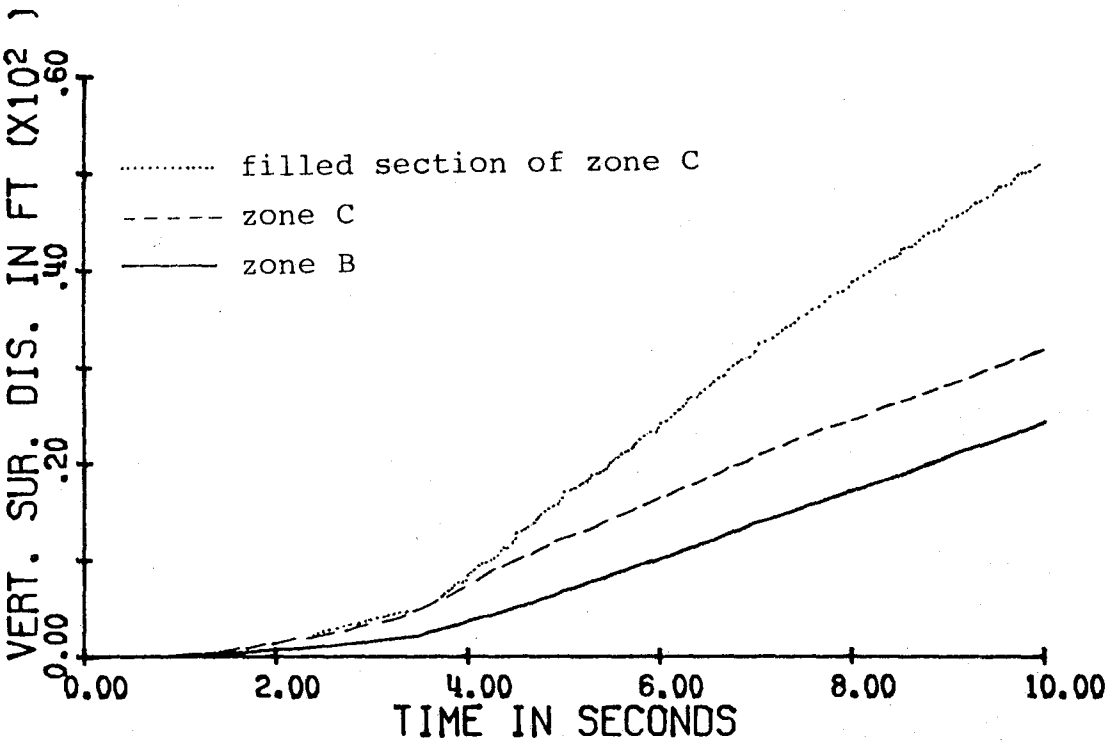

Figure 9-17 Time history of surface downward displacement

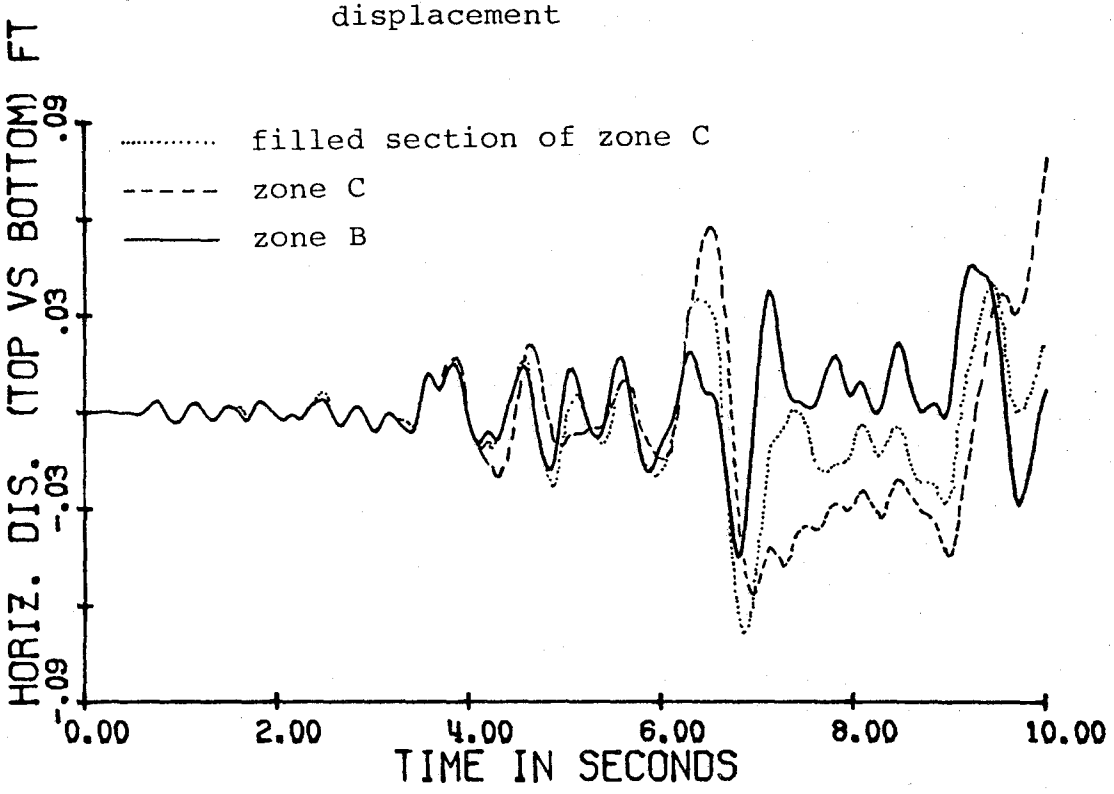

Figure 9-18 Time history of horizontal displacement (surface relative to bottom)

the deposit. The magnitude of the settlements were consistent with the pore water pressures. All were very small. The horizontal relative displacement traces were similar to the strain traces shown in Figure 9-7 except that the difference among the three displacement curves was not as large. This is reasonable since the strain traces shown are associated with the weakest layer.

The spatial variation of effective stress in zone B and zone C at several selected moments are shown in Figure 9-19. In zone C, liquefaction was almost completed after 9 seconds of shaking. In both zones, loss of effective stress increased with depth. However, at a greater depth, the soil had more effective stress that could be lost potentially. The soil at a shallower depth lost its effective stress almost completely before the same situation developed at a greater depth. On the other hand, the fill maintained the effective stress near the water table at an approximately constant level. Therefore the critical depth, the depth at which liquefaction was first completed, was some intermediate depth.

9-4. Discussion of the computed results.

It is believed that the estimated soil properties are reasonably representative of those in situ at Niigata. However, the imposed velocity at a depth of 50 feet was only a crude estimate of the actual event. There was no specific reason for using the Taft earthquake accelerogram, except that Seed and Idriss[62] used it in a similar study. A

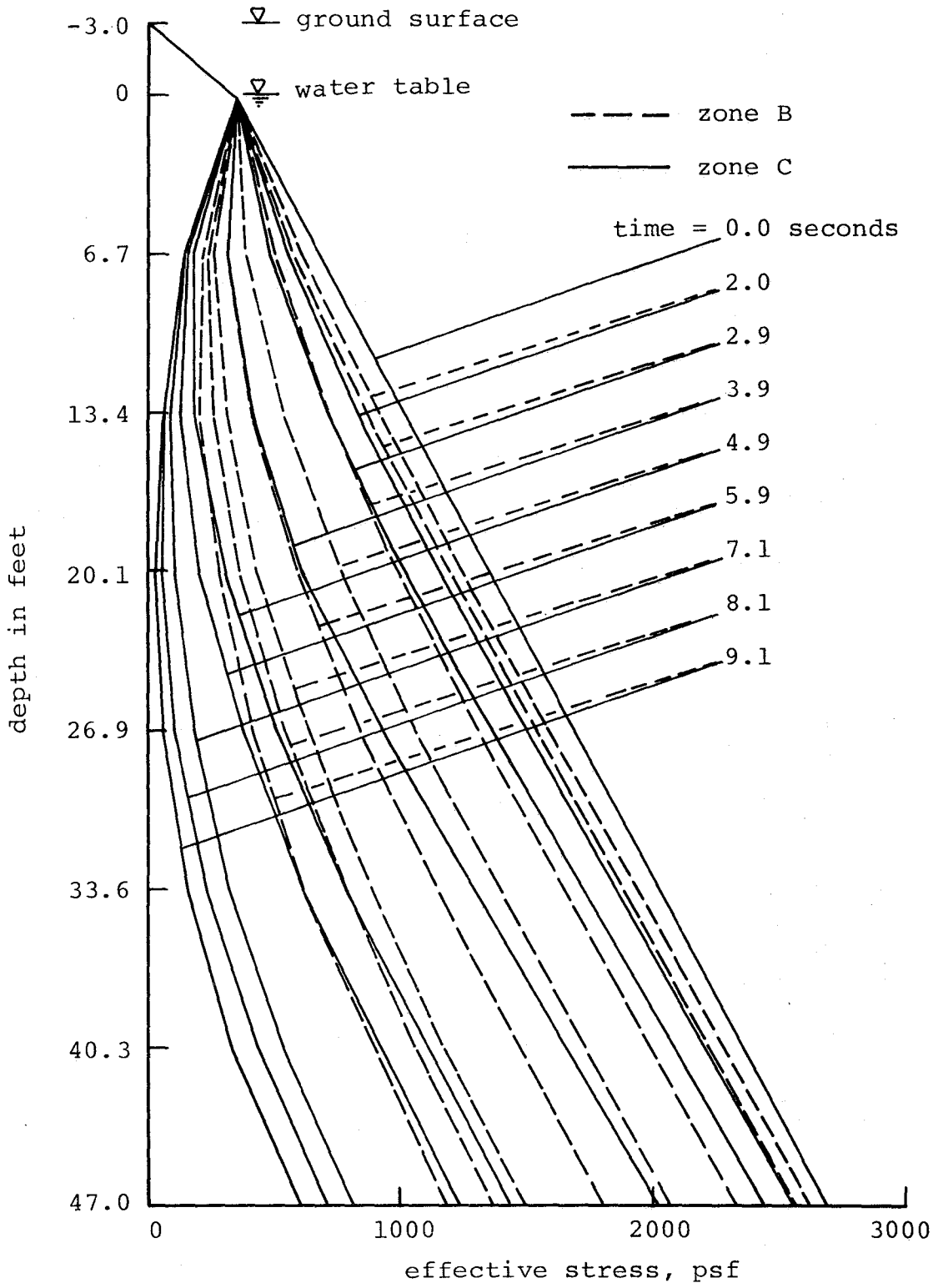

Figure 9-19 Spatial variation of vertical effective stress in zone B and zone C at selected moments

factor that scaled down the velocity, obtained from the Taft accelerogram, was used. Its magnitude was determined by the criterion that the maximum ground acceleration, computed from CHARSOIL, matched with that actually recorded, i.e., 0.16g. It is noted that in this computation the loss of effective stress of the deposit was not considered. When the loss of effective stress was taken into consideration, the resulting maximum ground acceleration was smaller than 0.16g. Table 9-6 is a summary of the maximum accelerations computed for the three different areas. By examining the

TABLE 9-6

COMPUTED MAXIMUM GROUND ACCELERATIONS

CONDITIONS	MAXIMUM GROUND ACCELERATION	TIME TO MAX. ACC., SECONDS
from CHARSOIL, zone C	0.16g	7.26
zone B	0.09g	6.83
filled section in zone C	0.07g	4.58
zone C	0.07g	3.37

time to the maximum ground acceleration and the "base" velocity shown in Figure 9-5, it is seen that when the loss of effective stress was considered, the deposit became rather soft before it could experience the large excitation occurring during the late stages of shaking.

The maximum acceleration alone is not an adequate description of an earthquake excitation but the frequency content of the earthquake needs to be considered as well. A comparison between the Taft accelerogram[62] and the

Niigata accelerogram[86] revealed that the Taft earthquake contains more high frequency components than does the Niigata earthquake. Thus more shearing cycles were involved when the Taft accelerogram was used. This fact may somewhat offset the discrepancy of the smaller calculated acceleration at the ground surface.

Figures 9-14 and 9-15 indicate that there was a difference of 43 psf in the initial shearing strength between zone B and zone C. Although helpful, this difference was not the only factor which differentiated the response of these two zones. In this study, the bulk moduli were estimated from the small motion shear moduli and Poisson's ratios. The bulk moduli thus estimated were kept constant, while the shear moduli were allowed to change according to the effective stress. The larger Poisson's ratio of zone B implied a smaller percentage of its constrained moduli that could be reduced by shaking. This percentage was an important factor that differentiated the response of zone B from that of zone C.

In order to describe the severity of liquefaction, an index called "relative fluidity", is defined as follows

$$\text{relative fluidity} = \frac{\text{initial constrained modulus} - \text{current constrained modulus}}{\text{initial constrained modulus} - \text{bulk modulus}}$$

Before shaking starts, the relative fluidity is zero. When the rigidity is completely lost by shaking, there is no difference between the constrained modulus and the bulk modulus, then the relative fluidity equals 1. The changes

in conditions existing in the three areas are shown in Table 9-7. At 10 seconds, the relative fluidity in the 4th layer of the deposit in zone C was almost 1, indicating its shearing rigidity was almost non-existent.

TABLE 9-7

INITIAL AND FINAL CONDITIONS IN THE THREE ZONES

	Zone B	Zone C	Filled Section of Zone C
initial C_c, psf	4.768×10^6	2.811×10^6	3.554×10^6
C_c at 10 sec, psf	3.863×10^6	1.743×10^6	2.301×10^6
B, psf	3.709×10^6	1.741×10^6	2.201×10^6
relative fluidity	0.8546	0.9981	0.9261

During the 10 second period, the first pressure wave speed almost remained constant while the shear wave speed dropped considerably. The tangential shear modulus of layer 4 in zone C and in the filled section of zone C dropped to less than 1/6 of its original static value for a large portion of the last 2 seconds of shaking. Since the accuracy of the shear wave submodel has not been investigated for the large interpolations associated with low tangential shear moduli, these portions of the results were only qualitative.

The significantly different computed response obtained for each region is in agreement with the actual performance observed at Niigata. In addition, Figure 9-19 shows that in zone C, after about 9 seconds of shaking, a zone of low

effective stress, ranging approximately from 13 feet to 27 feet below the water table, was established. In Figure 19 of the work by Seed and Idriss[62], the "zone of liquefaction after 10 seconds of ground motion" ranged from 15 feet to 27 feet below the water table. These two results compare favorably although the term "liquefaction" used by Seed and Idriss means zero effective stress or excessive shearing strain, instead of just low effective stress. In the same study, Seed and Idriss reported a greater margin of safety in the filled section of zone C than that of zone B. While in the present case studies, liquefaction was more severe in the filled section of zone C than that in zone B.

All the computations were performed on the Amdahl 470V/6 computer at the Computing center of The University of Michigan. The time steps used in the computation for zone C was 0.01225 seconds in the shear wave submodel and 0.001225 seconds in the pressure wave submodel. For the 10 seconds of shaking the CPU time used was 28 seconds. The program for the liquefaction model is listed in Appendix 3.

CHAPTER 10

SUMMARY AND CONCLUSIONS

A numerical model was developed for liquefaction in a horizontal or nearly horizontal deposit subjected to ground shaking. The deposit was considered to be one dimensional, composed of layers of soils with different properties, and the water table could lie at or below the ground surface. The model was composed of two interactive parts, i.e., the shear wave submodel and the pressure wave submodel. The modeling of plane shear wave propagation in a soil deposit was reviewed. The development of the pressure wave submodel and a coupling between the two submodels was presented in detail.

The soil was idealized as a two-phase medium composed of water and a structural skeleton. The shearing behavior of the skeleton was strain-softening. In the vertical direction, the soil deformation was considered to be constrained compression. Stress-strain relationships for the two phases, with the skeleton under constrained compression, was developed. For the structural skeleton, a secant constrained modulus, its inverse being the constrained compressibility, was used. It was assumed that the bulk modulus of the skeleton remained constant during shearing, but that the shear modulus decreased with shearing strain amplitude. Therefore, according to Equation (4-40), the secant constrained modulus was reduced by shearing strain. This was the fundamental hypothesis of the liquefaction model.

The governing equations for pressure wave propagation in saturated deposits were then formulated. An analytical solution for a uniform linear elastic deposit undergoing steady oscillatory motion in the vertical direction was obtained. This solution was employed to study the influence of permeability and porosity upon the response of saturated deposits.

The set of governing equations for the pressure wave propagation was demonstrated to be hyperbolic for a wide range of soils, and a numerical procedure based on the method of characteristics was developed. Excellent comparisons between the numerical solution and the analytical solution for a deposit in steady oscillatory motion were obtained. With the variation of constrained compressibility included, the numerical procedure was used to calculate changes in effective stress and pore water pressure, settlement of the skeleton, and upward flow of pore water in nonlinear deposits when the stiffness of the skeleton was weakened rapidly. Satisfactory results were obtained.

A coupling between the propagation of shear waves and the vertical motion of the soil due to changes in its constrained compressibility was developed. The two submodels, when coupled together, constituted the model for liquefaction. Several examples were used to demonstrate the features of the model and the results were in agreement with known behavior of saturated deposits during shaking. In addition, the model showed that when the movement of pore

water was not inhibited the effective stress in a deposit approached zero asymptotically as shaking continued. The effective stress could be reduced to zero rather quickly if the movement of pore water was inhibited by a less permeable layer. The use of the model to predict the onset of lateral spreading of a slightly inclined deposit due to liquefaction was also demonstrated.

Case studies in relation to the Niigata earthquake of 1964 were presented. Three areas of Niigata city were involved and a significantly different computed response was obtained for each region. This was in agreement with the actual performance observed at Niigata. These case studies demonstrated the potential applicability of the model to liquefaction.

In this study, liquefaction was considered as a process, instead of a state. Hence, in saturated deposits with strain-softening shearing behavior, liquefaction always took place no matter how slight the shaking. A measure of severity of liquefaction was given by the "relative fluidity", an index defined in Chapter 9.

Further studies related to the present model should include verifications of Equations (4-40) and (4-42) by experiments or by available data. The shearing stress-shearing strain relationship used for saturated soil undergoing rapid shearing is also needed to be substantiated experimentally.

APPENDIX 1

By using Darcy's law, it can be shown that the viscous force generated by flows in a rigid porous material can be regarded as a body force. This is shown in the following.

Darcy's law for vertically downward flow can be written as

$$n \bar{W} = k \frac{d}{dz} \left(\frac{P}{\rho_w g} - z\right) ,$$

or

$$\frac{dP}{dz} = \frac{n\rho_w g}{k} \bar{W} + \rho_w g \ . \qquad \text{(A-1)}$$

Let Z be a body force per unit mass of water, positive in the z direction. For steady flow, balancing of forces on an elementary volume of water yields

$$\frac{dP}{dz} = \rho_w Z + \rho_w g \qquad \text{(A-2)}$$

From Equations (A-1) and (A-2), one obtains

$$Z = \frac{n g}{k} \bar{W} \qquad \text{(A-3)}$$

This equation is used in deriving Equation (5-5).

APPENDIX 2

```
C   STEADY OSCILLATORY MOTION OF LEVEL UNIFORM ELASTIC
C   SATURATED DEPOSITS
C   F: POROSITY
C   KZ: PERMIBILITY IN FPS
C   RHOF: MASS DENSITY OF THE FLUID IN SLUGS PER CUBIC FOOT
C   RHOS: MASS DENSITY OF THE SOLID IN SLUGS PER CUBIC FOOT
C   D: DEPTH OF THE DEPOSIT IN FOOT
C   CC: CONSTRAINED COMPRESSIBILITY OF SKELETON IN FT**2/LB
C   CW: COMPRESSIBILITY OF WATER IN FT**2/LB
C   AMP: AMPLITUDE OF SKELETAL VELOCITY AT BASE IN FT/SEC
C   OM: ANGULAR FREQUENCY OF THE MOTION IN RAD/SEC
C   NEXP: AN INTEGER USED TO AVOID TOO LARGE AN ARGUMENT IN THE
C   EXPONTIATION, SET NEXP TO A LARGE VALUE, SAY, 10. WHEN
C   D IS TOO LARGE OR KZ IS TOO SMALL
C
C
      IMPLICIT COMPLEX*16 (A-H,L,O-Z)
      REAL*8 CDABS,DIMAG,DREAL,DATAN2,F,RHOF,RHOS,CC,CW,KZ,D,
     1TSTART,TEND,ZZ,TF,AMP,OM
      DIMENSION LM(4),A(4),B(4),C(4),S(4),CCC(4)
      NAMELIST/DIN/F,RHOF,RHOS,CC,CW,KZ,AMP,OM,N,NPT,TSTART
     1,D,NEXP,TEND
   10 READ(5,DIN,END=99)
      WRITE(6,DIN)
      A11=1./CC+1./(F*CW)
      A22=F/CW
      AA=1./CW
      Z=DCMPLX(0.D0,1.D0)
      RHO=F*RHOF+(1.-F)*RHOS
      AL1=A11/RHO
      AL2=AA/RHO
      AL3=OM*OM
      AL4=F*RHOF*OM*OM/RHO
      AL5=AA/(F*RHOF)
      AL6=A22/(F*RHOF)
      AL7=AL3
      AL8=OM*(OM-Z*F*32.2/KZ)
      GA1=AL1*AL6-AL2*AL5
      GA2=AL1*AL8-AL4*AL5-AL2*AL7+AL3*AL6
      GA3=AL3*AL8-AL4*AL7
      CCCC=CDSQRT(GA2*GA2-4.D0*GA1*GA3)
      LM(1)=CDSQRT(.5D0/GA1*(-GA2+CCCC))
      LM(2)=CDSQRT(.5D0/GA1*(-GA2-CCCC))
      LM(3)=-LM(2)
      LM(4)=-LM(1)
      DO 1 I=1,4
      A(I)=-LM(I)*(AL2*LM(I)*LM(I)+AL4)/(AL1*LM(I)*LM(I)+AL3)
```

```
      B(I)=LM(I)
    1 C(I)=-(AL2*LM(I)*LM(I)+AL4)/(AL1*LM(I)*LM(I)+AL3)
      C2=1.
      DO 11 I=1,NEXP
   11 C2=C2*CDEXP((LM(2)-LM(1))*D/NEXP)
      AAA=C(2)/C(1)*C2-A(2)/A(1)
      BBB=C2-A(2)/A(1)
      P1=(B(3)/B(1)-A(3)/A(1))/(B(2)/B(1)-A(2)/A(1))
      P2=(B(4)/B(1)-A(4)/A(1))/(B(2)/B(1)-A(2)/A(1))
      C3=1.
      DO 12 I=1,NEXP
   12 C3=C3*CDEXP((LM(3)-LM(1))*D/NEXP)
      P3=(C3-A(3)/A(1))/BBB
      C4=1.
      DO 13 I=1,NEXP
   13 C4=C4*CDEXP((LM(4)-LM(1))*D/NEXP)
      P4=(C4-A(4)/A(1))/BBB
      P5=(C(3)/C(1)*C3-A(3)/A(1))/AAA
      P6=(C(4)/C(1)*C4-A(4)/A(1))/AAA
      C1=1.
      DO 14 I=1,NEXP
   14 C1=C1*CDEXP(LM(1)*D/NEXP)
      P7=AMP/(C(1)*C1*AAA)
      S(3)=P7/((P6-P2)*((P5-P1)/(P6-P2)-(P3-P1)/(P4-P2)))
      S(4)=-(P3-P1)/(P4-P2)*S(3)
      S(2)=-S(3)*P1-S(4)*P2
      S(1)=-S(2)*A(2)/A(1)-S(3)*A(3)/A(1)-S(4)*A(4)/A(1)
      DZZ=D/N
      ZZ=-DZZ
      NP1=N+1
      DO 100 II=1,NP1
      ZZ=ZZ+DZZ
      WRITE(6,333)ZZ
  333 FORMAT(1HO,'  DEPTH FROM SURFACE IS ',F12.4,2X,'FT'/16X,
     1'TIME',8X,'UZ',10X,'WZ',10X,'S',11X,'T')
      DO 2 I=1,4
      CCC(I)=1.
      DO 2 J=1,NEXP
    2 CCC(I)=CCC(I)*CDEXP(LM(I)*ZZ/NEXP)
      P=S(1)*A(1)*CCC(1)+S(2)*A(2)*CCC(2)+S(3)*A(3)*CCC(3)+
     1S(4)*A(4)*CCC(4)
      Q=S(1)*B(1)*CCC(1)+S(2)*B(2)*CCC(2)+S(3)*B(3)*CCC(3)+
     1S(4)*B(4)*CCC(4)
      H=S(1)*C(1)*CCC(1)+S(2)*C(2)*CCC(2)+S(3)*C(3)*CCC(3)+
     1S(4)*C(4)*CCC(4)
      G=S(1)*CCC(1)+S(2)*CCC(2)+S(3)*CCC(3)+S(4)*CCC(4)
      SS=(AA*P+A22*Q)/(DM*Z)
      TT=(A11*P+AA*Q)/(DM*Z)
      $AMPH=CDABS(H)
      $AMPG=CDABS(G)
      $AMPSS=CDABS(SS)
      $AMPTT=CDABS(TT)
      $ANGH=DATAN2(DIMAG(H),DREAL(H))
      $ANGG=DATAN2(DIMAG(G),DREAL(G))
```

```
      $ANGSS=DATAN2(DIMAG(SS),DREAL(SS))
      $ANGTT=DATAN2(DIMAG(TT),DREAL(TT))
      WRITE(6,222)$AMPH,$AMPG,$AMPSS,$AMPTT
      WRITE(6,222)$ANGH,$ANGG,$ANGSS,$ANGTT
  222 FORMAT(10X,10F12.5)
      DTF=(TEND-TSTART)/(NPT-1)
      TF=TSTART-DTF
      DO 4 I=1,NPT
      TF=TF+DTF
      ZZZ=OM*TF-1.5707963
      $UZ=$AMPH*CDEXP(Z*(ZZZ+$ANGH))
      $WZ=$AMPG*CDEXP(Z*(ZZZ+$ANGG))
      $SSS=$AMPSS*CDEXP(Z*(ZZZ+$ANGSS))
      $T=$AMPTT*CDEXP(Z*(ZZZ+$ANGTT))
    4 WRITE(6,222)TF,$UZ,$WZ,$SSS,$T
  100 CONTINUE
      GO TO 10
   99 STOP
      END
C
C  SAMPLE DATA
C
 &DIN F=.4,RHOF=1.94,RHOS=5.13,CC=2.4D-7,CW=2.3D-8,KZ=.001,
 AMP=.2,OM=32.406,N=10,NPT=2,TSTART=0.,TEND=1.,D=400.,
 NEXP=5,  &END
```

APPENDIX 3

```
C   FILE NIIGATA 1/7/76
C   NONLINEAR TRANSIENTS OF LAYERED SATURATED DEPOSIT
C   SUBJECTED TO GROUND SHAKING
C   RAMBERG-OSGOOD REVERSAL BASED ON SHEARING STRAIN
C   TANGENT G IN SWAVE, SCENT G IN PWAVE
C   HORIZONTAL QUAKE INPUT IS FEED THROUGH DEVICE 7
C   THE SOIL DEPOSIT MAY BE INCLINED.
C   UNIFORM SECTIONING ON BOTH P-WAVE AND S-WAVE SUBROUTINES
C   2ND. ORDER INTERPOLATION AT POINTS 2 AND 3
C   $R OBNI 5=ONII 6=-X 7=QUAKEVEL 8=OUTFILE  T=30
C
C   NAMES FOR INPUT
C
C   A,B,C:  CONSTANTS IN EQS. (6-10) AND (6-11)
C   ALP:  PARAMETER IN RAMBERG-OSGOOD RELATIONS
C   KO:  COEFFICIENT OF EARTH PRESSURE AT REST
C   D:  DEPTH OF THE DEPOSIT(SATURATED PART), FT
C   F:  POROSITY
C   RHOF:  MASS DENSITY OF WATER, SLUGS/FT**3
C   RHOS:  MASS DENSITY OF SOLID, SLUGS/FT**3
C   N:  NUMBER OF EQUAL DISTANCE INTERVALS
C   TMAX:  TAME SPAN OF COMPUTATIONS, SEC
C   CW:  COMPRESSIBILITY OF WATER, FT**2/LB
C   SIGMIN:  MINIMUM EFFECTIVE STRESS,PSF
C   THETA:  FRICTION ANGLE, RADIANS
C   AMP:  AMPLITUDE OF BEDROCK VELOCITY, FPS
C   OM:  FREQUENCY OF BEDROCK VELOCITY, RADIANS/SEC
C   R:  PAPAMETER IN THE RAMBERG-OSGOOD RELATIONS
C   KZ:  PERMEABILITY, FPS
C   JPR,JPRSIG:  PRINTING PARAMETERS
C   CBEAC:  RATIO OF BULK MODULUS TO STATIC SHEAR MODULUS
C   ISIM:  ISIM=1 IMPLY EARTHQUAKE EXCITATION
C   FAC:  A FACTOR APPLIED TO EARTHQUAKE VELOCITY INPUT
C   N4:  NUMBER OF EARTHQUAKE VELOCITY DATA POINTS
C   III:  DETAILED OUTPUT IS PRINTED OUT FOR THE IIITH LAYER
C   SLB1,SLB2:  CONSTANTS USED FOR BEDROCK EXCITATION
C   TSTOP:  TIME THAT EXCITATION IS SUSPENDED
C   TPMIN,TPMAX:  TIME INTERVAL FOR DETAILED P-WAVE OUTPUT
C   TPMAIN:  TIME AFTER WHICH OUTPUT STARTS
C   SLOPE:  SLOPE OF DEPOSIT, RADIANS
C   M,MMM:  TOP AND BOTTOM LAYERS OF A LESS PERMEABLE ZONE
C   TOC:  TOC=SHEAR STRENGTH/YIELD SHEAR STRESS
C   W:  OVERBURDON, PSF
C
C   NAME FOR OUTPUT
C
C   SIGB:  EFFECTIVE STRESS, PSF
C   PPOR:  PORE WATER PRESSURE, PSF
C   DISZ1:  DOWNWARD SURFACE DISPLACEMENT, FT
C   TTAU:  SHEARING STRESS IN LAYER III, PSF
C   SSTN:  SHEARING STRAIN IN LAYER III
```

```
C   G:  TANGENTIAL SHEAR MODULUS OF LAYER III, PSF
C   RED:  RELATIVE DISPLACEMENT(LATERAL) BETWEEN
C         SURFACE AND BOTTOM OF DEPOSIT, FT
C   TAUM:  SHEARING STRENGTH OF LAYER III, PSF
C   TAU(1),TAU(N),TAU(N1):  SHEARING STRESSES, PSF
C   PPORN1:  PORE WATER PRESSURE AT THE BOTTOM, PSF
C   GS:  SECANT SHEAR MODULUS OF LAYER III, PSF
C   IC:  INDEX THAT TRACES THE RAMBERG-OSGOOD CURVES
C
C
C
      IMPLICIT REAL*8(A-H,K,L,O-Z)
      COMMON /PPP/SIGB(10),UZ(10),WZU(10),SU(10),T(10),
     1DISZ1,DELTG(10),CC(10),CB(10),AAL1(10),BT1(10),D58,
     1WZD(10),SD(10),D5,D46(10),D458(10),D4625(10),D2(10),
     1KZ(10),CW,DELTGO(10),OLDG(10),DTPG,D4(10),D6(10),D8,
     1QUA1,QUA2,QUA3,TPMIN,TPMAX,CCO(10),M,MMM,NN,IQUIT
      COMMON /SSS/TAUP(10),TAU(10),DT(10),ACC,PKACC,PKT,
     1DISX(10),SLB1,SLB2,TSTOP,CV(999),FAC,ISIM
      COMMON /RABOSG/GO(10),TY(10),R(10),G(10),GS(10),ALP
     1,UXO(10),UX(10),IREV(10),IC(20),IVC(10)
      COMMON DZP,RHOF,RHOS,TF,DT,DTP,AMP,OM,
     1F(10),RHO(10),W,SSLOPE,N,N1,JJJ
      DIMENSION TAUO(10),VS(10),VP(10),VP2(10),SSTNO(10)
     1,KO(10),THETA(10),PZH(10),PWPO(10),F(10),DELSIG(10)
      NAMELIST/DIN/A,B,C,ALP,KO,D,F,RHOF,RHOS,N,TMAX,CW,SIGMIN,
     1THETA,AMP,OM,R,KZ,JPR,JPRSIG,CBFAC,ISIM,FAC,N4,III
     1,SLB1,SLB2,TSTOP,TPMIN,TPMAX,TPMAIN,SLOPE,M,MMM,TOC,W
      TYELD(XX,XK,XT)=.5*XX*DSQRT(((1.+XK)*DSIN(XT))**2-(1.-XK)
     1**2)/TOC
      GOLD(XX,XK)=A*(B-EN)**2/(1.+EN)*((1.+2.*XK)/3.*XX)**C
  110 READ(5,DIN,END=99)
      WRITE(6,DIN)
      IF(ISIM.EQ.1)READ(7,112)(CV(I),I=1,N4)
  112 FORMAT(9F8.5)
      IQUIT=0
      N1=N+1
      DISZ1=0.
      DO 4 I=1,N
      RHO(I)=F(I)*RHOF+(1.-F(I))*RHOS
    4 F(I)=F(I)/(1.-F(I))
      EN=F(1)
      DELSIG(1)=0.
      JJJ=0
      JJJ1=0
      DZP=D/N
      PKACC=0.
      PKT=0.
C   INITIAL CONDITION
      ZZ=0.
      ZZZ=W
      DO 8 I=1,N1
      UZ(I)=0.
      WZU(I)=0.
```

```
      WZD(I)=0.
      PWPO(I)=ZZ
      T(I)=-ZZZ
      SIGB(I)=-ZZ-T(I)
      UX(I)=0.
      UXO(I)=0.
      TAU(I)=ZZZ*DSIN(SLOPE)
      IF(I.EQ.N1)GO TO 8
      ZZ=ZZ+RHOF*32.2*DZP
      ZZZ=ZZZ+RHO(I)*32.2*DZP
    8 DISX(I)=0.
      SU(1)=0.
      SD(1)=0.
      ZZ=0.
      DO 81 I=2,N1
      TAUO(I-1)=.5*(TAU(I-1)+TAU(I))
      ZZ=ZZ+RHOF*32.2*DZP
      SU(I)=-ZZ*F(I-1)
   81 SD(I)=-ZZ*F(I)
      VSMAX=0.
      DO 71 I=1,N
      I1=I+1
      DT(I)=.5*(TAU(I)+TAU(I1))
      FN=F(I)
      TY(I)=TYFLD(.5*(SIGB(I)+SIGB(I1)),KO(I),THETA(I))
      GO(I)=GOLD(.5*(SIGB(I)+SIGB(I1)),KO(I))
      CB(I)=1./(CBFAC*GO(I))
      VS(I)=DSQRT(GO(I)/RHO(I))
      IF(VS(I).GT.VSMAX)VSMAX=VS(I)
      SSTNO(I)=.5*(TAU(I)+TAU(I1))/GO(I)*(1.+
     1(.5*(TAU(I)+TAU(I1))/TY(I))**(R(I)-1.))
      IVC(I)=1
      IREV(I)=1
      DELTG(I)=0.
      OLDG(I)=GO(I)
   71 DELTG(I)=0.
      WRITE(6,2222)(GO(I),I=1,N)
      WRITE(6,2222)(VS(I),I=1,N)
      WRITE(6,2222)(TY(I),I=1,N)
 2222 FORMAT(10F12.2)
      VPMAX=0.
      DO 18 I=1,N
      CC(I)=1./(1.333333*OLDG(I)+1./CB(I))
      CCO(I)=CC(I)
      D1=1./(RHO(I)-F(I)*RHOF)
      D2(I)=-D1
      D3=-RHO(I)*D1/(F(I)*RHOF)
      D4(I)=D1
      D5=-1./CW
      D6(I)=-F(I)/CW
      D8=D5
      D7=-1./(F(I)*CW)-1./CC(I)
      AAL1(I)=D4(I)*D8+D3*D6(I)+D1*D5
      BT1(I)=D1*D4(I)-D2(I)*D3
```

```
      D58=D5*D8
      D46(I)=D4(I)*D6(I)
      D458(I)=D4(I)*D58
      D4625(I)=D4(I)*D6(I)+D2(I)*D5
      AL=AAL1(I)+D2(I)*D7
      BT=(D58-D6(I)*D7)*BT1(I)
      VP2(I)=DSQRT((AL-DSQRT(AL*AL-4.D0*BT))*.5D0)
      VP(I)=DSQRT((AL+DSQRT(AL*AL-4.D0*BT))*.5D0)
      IF(VP(I).GT.VPMAX)VPMAX=VP(I)
   18 CONTINUE
      WRITE(6,2222)(VP(I),I=1,N)
      WRITE(6,2222)(VP2(I),I=1,N)
      DTP=DZP/VPMAX
      NN=IDINT(VPMAX/VSMAX)
      DT=DTP*NN
      WRITE(6,2224)DTP,DT,NN,DZP
      DO 22 I=1,N
      IF(VS(I)*DT .GT.DZP)CALL EXIT
      IF(VP(I)*DTP .GT.DZP)CALL EXIT
   22 CONTINUE
      IF(VS(N)*DT .GT.DZP)CALL EXIT
 2224 FORMAT(1X,'DTP=',F12.5,' DT=',F12.5,' NN=',I2,' DZP=',
     1F12.5)
      DTPG=DTP*32.2
      SSLOPE=DT*32.2*DSIN(SLOPE)
      QUA1=DZP*(DZP+DZP)
      QUA2=-DZP*DZP
      QUA3=(DZP+DZP)*DZP
      TE=0.
      G(III)=G0(III)
      GS(III)=G0(III)
      IC(III)=0
      GO TO 23
   20 TE=TE+DT
      JJJ=JJJ+1
      IF(TE.GT.TMAX)GO TO 111
      CALL SWAVE
      DO 21 I=1,N
      DELTG0(I)=DELTG(I)
      DELTG(I)=(GS(I)-OLDG(I))/NN
      IF(IREV(I).EQ.0)DELTG(I)=0.
      IF(TE.GE.TSTOP)DELTG(I)=0.
   21 CONTINUE
      DO 25 I=2,N1
      DELSIG(I)=0.
      IF(SIGB(I).LE.SIGMIN)DELSIG(I)=SIGMIN
   25 CONTINUE
      DO 9 I=1,N
      I1=I+1
      IF(IREV(I).EQ.1)GO TO 9
      EN=E(I)/(1.-E(I))
      OLDG(I)=G0(I)
      CC(I)=1./(1.333333*OLDG(I)+1./CB(I))
    9 CONTINUE
```

```
      CALL PWAVE
      IF(IQUIT.EQ.1)GO TO 111
      DO 24 I=1,N
      I1=I+1
      EN=E(I)/(1.-E(I))
      OLDG(I)=GS(I)
      GO(I)=GOLD(.5*(SIGB(I)+DELSIG(I)+SIGB(I1)+DELSIG(I1)),KO(I))
      TAU(I)=TAUP(I)
      TY(I)=TYELD(.5*(SIGB(I)+DELSIG(I)+SIGB(I1)+DELSIG(I1))
     1,KO(I),THETA(I))
   24 IREV(I)=1
      TAU(N1)=TAUP(N1)
      DO 28 I=1,N
      IF(TAUO(I).GE.TOC*TY(I))GO TO 29
   28 CONTINUE
      GO TO 30
   29 WRITE(6,1115)I,TF
 1115 FORMAT(1X,'REACH NO. ',I2,' FAILED AT ',F12.4,' SECONDS.')
      CALL EXIT
30    IF(TF.LE.TPMAIN)GO TO 20
      IF(JJJ/JPRSIG*JPRSIG.NE.JJJ)GO TO 26
      WRITE(6,1113)TF,(SIGB(I),I=1,N1)
      DO 27 I=1,N1
   27 PZH(I)=(-SD(I)/E(I)-PWPO(I))/(32.2*RHOF)
      WRITE(6,1114)TF,(PZH(I),I=1,N1)
 1114 FORMAT(1X,'TF=',F10.4,'  PZH= ',10F10.3)
 1113 FORMAT(1X,'TF=',F10.4,' SIGB= ',10F10.2)
   26 IF(JJJ/JPR*JPR.EQ.JJJ)GO TO 23
      GO TO 20
   23 PPOR=-SD(III)/E(III)
      PPORN1=-SU(N1)/E(N)
      SSTN=SSTNO(III)+(DISX(III+1)-DISX(III))/DZP
      IF(DABS(SSTN).GT..05)CALL EXIT
      TTAU=.5*(TAU(III)+TAU(III+1))
      TAUM=TOC*TY(III)
      RED=DISX(1)-DISX(N1)
      JJJ1=JJJ1+1
      WRITE(8,113)PPOR,SIGB(III),DISZ1,TTAU,SSTN,G(III),RED,TAUM,
     1TAU(1),TAU(N),TAU(N1),PPORN1,GS(III),IC(III)
  113 FORMAT(2F8.2,F10.7,F8.2,F10.7,F8.0,F10.5,5F8.2,F8.0,I3)
      GO TO 20
  111 WRITE(6,114)(E(I),I=1,N)
  114 FORMAT(15F8.5)
      WRITE(6,116)PKACC,PKT
  116 FORMAT(1X,'MAX. GROUNT ACC. = ',F12.4,' OCCURED AT ',F12.4,
     1' SECONDS.')
      WRITE(8,115)DT,JPR,JJJ1
  115 FORMAT(F8.5,2I4)
   99 STOP
      END
C
      SUBROUTINE SWAVE
      IMPLICIT REAL*8(A-H,K,L,O-Z)
      COMMON /SSS/TAUP(10),TAU(10),DT(10),ACC,PKACC,PKT,
```

```
     1DISX(10),SLB1,SLB2,TSTOP,CV(999),FAC,ISIM
      COMMON /RABOSG/GO(10),TY(10),R(10),G(10),GS(10),ALP
     1,UXO(10),UX(10),IREV(10),IC(20),IVC(10)
      COMMON DZP,RHOE,RHOS,TF,DT,DTP,AMP,OM,
     1E(10),RHO(10),W,SSLOPE,N,N1,JJJ
      DIMENSION UXP(10),VS(10)
      DO 6 I=1,N
      TT=.5*(TAU(I)+TAU(I+1))
      CALL GG(TT,DT(I),I)
      DT(I)=TT
    6 VS(I)=DSQRT(G(I)/RHO(I))
      DO 9 I=2,N
      IP1=I+1
      IM1=I-1
      C1P=1./DSQRT(RHO(IM1)*G(IM1))
      C1M=1./DSQRT(RHO(I)*G(I))
      THAP=VS(IM1)*DT/DZP
      THAM=VS(I)*DT/DZP
      UXR=UX(I)+THAP*(UX(IM1)-UX(I))
      TAUR=TAU(I)+THAP*(TAU(IM1)-TAU(I))
      UXS=UX(I)+THAM*(UX(IP1)-UX(I))
      TAUS=TAU(I)+THAM*(TAU(IP1)-TAU(I))
      CP=C1P*TAUR-UXR+SSLOPE
      CM=-C1M*TAUS-UXS+SSLOPE
      TAUP(I)=(CP-CM)/(C1P+C1M)
      UXP(I)=TAUP(I)*C1P-CP
    9 DISX(I)=DISX(I)+.5*(UXP(I)+UX(I))*DT
C   UPPER B.C.
      C1M=1./DSQRT(RHO(1)*G(1))
      THAM=VS(1)*DT/DZP
      UXS=UX(1)+THAM*(UX(2)-UX(1))
      TAUS=TAU(1)+THAM*(TAU(2)-TAU(1))
      C1M=1./DSQRT(RHO(1)*G(1))
      CM=-C1M*TAUS-UXS+SSLOPE
      WGDT=W/(16.1*DT)
      TAUP(1)=(WGDT*SSLOPE-(TAU(1)+WGDT*(UX(1)+CM)))/(1.+
     1WGDT*C1M)
      UXP(1)=-(TAUP(1)*C1M+CM)
      ACC=(UXP(1)-UX(1))/DT
      IF(DABS(ACC).GT.PKACC)PKACC=DABS(ACC)
      IF(DABS(ACC).GE.PKACC)PKT=TF
      DISX(1)=DISX(1)+.5*(UXP(1)+UX(1))*DT
C   LOWER B.C.
      IF(ISIM.EQ.1)GO TO 8
      UXP(N1)=AMP*DSIN(OM*TF)*(1.-SLB1*DEXP(-SLB2*TF))
    8 IF(ISIM.EQ.1)UXP(N1)=CV(JJJ)*FAC
      IF(TF.GT.TSTOP)UXP(N1)=0.
      THAP=VS(N)*DT/DZP
      UXR=UX(N1)+THAP*(UX(N)-UX(N1))
      TAUR=TAU(N1)+THAP*(TAU(N)-TAU(N1))
      C1P=1./DSQRT(RHO(N)*G(N))
      CP=TAUR*C1P-UXR+SSLOPE
      TAUP(N1)=(CP+UXP(N1))/C1P
      UXP(N1)=C1P*TAUP(N1)-CP
```

```
      DISX(N1)=DISX(N1)+.5*(UXP(N1)+UX(N1))*DT
C  UPDATING VARIABLES
      DO 10 I=1,N1
      UXO(I)=UX(I)
   10 UX(I)=UXP(I)
      RETURN
      END
C
      SUBROUTINE GG(TT,DTT,I)
      IMPLICIT REAL*8(A-H,K,L,O-Z)
      COMMON /RABOSG/GO(10),TY(10),R(10),G(10),GS(10),ALP
     1,UXO(10),UX(10),IREV(10),IC(20),IVC(10)
      DIMENSION UP(20),YM(20,20)
      GV(DY,DR)=1./(1.+DR*ALP*DABS(DY)**(DR-1.))
      GSV(DY,DR)=1./(1.+ALP*DABS(DY)**(DR-1.))
      GRO(DY,DYO,DR)=1./(1.+DR*ALP*DABS((DY-DYO)/2.)**(DR-1.))
      GSRO(DY,DYO,DR)=1./(1.+ALP*DABS((DY-DYO)/2.)**(DR-1.))
      T=TT/TY(I)
      DT=DTT/TY(I)
      IF(IVC(I).EQ.0)GO TO 10
      IF((UXO(I)-UXO(I+1))*(UX(I)-UX(I+1)).LT.0.)GO TO 5
    9 G(I)=GO(I)*GV(T,R(I))
      GS(I)=GO(I)*GSV(T,R(I))
      IC(I)=0
      RETURN
    5 IVC(I)=0
      UP(I)=UX(I+1)-UX(I)
      IC(I)=2
      YM(1,I)=-DTT
      YM(2,I)=DTT
      IREV(I)=0
      G(I)=GO(I)*GRO(T,DT,R(I))
      GS(I)=GO(I)*GSRO(T,DT,R(I))
      RETURN
   10 IF(DABS(T).GE.DABS(YM(1,I)/TY(I)))GO TO 15
      IF((UXO(I)-UXO(I+1))*(UX(I)-UX(I+1)).GT.0.)GO TO 20
      UP(I)=UX(I+1)-UX(I)
      IC(I)=IC(I)+1
      IF(IC(I).GT.20)IC(I)=19
      IREV(I)=0
      IF(UP(I)*(T-YM(IC(I)-1,I)/TY(I)).GT.0.)GO TO 22
      YM(IC(I),I)=DTT
   11 G(I)=GO(I)*GRO(T,YM(IC(I),I)/TY(I),R(I))
      GS(I)=GO(I)*GSRO(T,YM(IC(I),I)/TY(I),R(I))
      RETURN
   15 IVC(I)=1
      GO TO 9
   20 IF(UP(I)*(T-YM(IC(I)-1,I)/TY(I)).LT.0.)GO TO 11
   22 IC(I)=IC(I)-2
      IF(IC(I).EQ.3)GO TO 11
      IF(IC(I).EQ.2)GO TO 11
      GO TO 20
      END
C
```

```
      SUBROUTINE PWAVE
      IMPLICIT REAL*8(A-H,K,L,O-Z)
      DIMENSION UZP(10),WZPU(10),SPU(10),TP(10),TR(4,4,10),
     1TSAVE(4,10),L(4,10),WZPD(10),SPD(10)
      COMMON /PPP/SIGB(10),UZ(10),WZU(10),SU(10),T(10),
     1DISZ1,DELTG(10),CC(10),CB(10),AAL1(10),BT1(10),D58,
     1WZD(10),SD(10),D5,D46(10),D458(10),D4625(10),D2(10),
     1KZ(10),CW,DELTGO(10),OLDG(10),DTPG,D4(10),D6(10),D8,
     1QUA1,QUA2,QUA3,TPMIN,TPMAX,CCO(10),M,MMM,NN,IQUIT
      COMMON DZP,RHOF,RHOS,TF,DT,DTP,AMP,OM,
     1F(10),RHO(10),W,SSLOPE,N,N1,JJJ
      WZPU(N1)=0.
      WZPD(N1)=0.
      SPU(1)=0.
      SPD(1)=0.
      UZP(N1)=0.
      TIME=TF-DT+DTP
  100 DO 1 I=1,N
      OLDG(I)=OLDG(I)+DELTG(I)
      CC(I)=1./(1.333333*OLDG(I)+1./CB(I))
      D7=-1./(F(I)*CW)-1./CCO(I)
      AL=AAL1(I)+D2(I)*D7
      BT=(D58-D6(I)*D7)*BT1(I)
      DDD=DSQRT(AL*AL-4.D0*BT)
      L(1,I)=DSQRT((AL+DDD)*.5)
      L(2,I)=DSQRT((AL-DDD)*.5)
      L(3,I)=-L(2,I)
      L(4,I)=-L(1,I)
      CONST1=-16.1*DTP*F(I)*D4(I)/KZ(I)
      CONST7=.666667*CC(I)*DELTG(I)/F(I)
      DO 1 J=1,4
      TR(J,1,I)=(L(J,I)*L(J,I)*D5+D46(I)*D7-D458(I))/(L(J,I)
     1*D4625(I))
      TR(J,2,I)=(L(J,I)-TR(J,1,I)*D2(I))/D4(I)
      TR(J,3,I)=(L(J,I)*TR(J,2,I)-D8)/D6(I)+CONST7
      TSAVE(J,I)=TR(J,2,I)-CONST1*(TR(J,1,I)*F(I)*RHOF-
     1TR(J,2,I)*RHO(I))
      TR(J,4,I)=1.-CONST7*F(I)
      TR(J,2,I)=2.*TR(J,2,I)-TSAVE(J,I)
    1 CONTINUE
C   SURFACE B.C.
      TH3=-L(3,1)*DTP
      TH4=-L(4,1)*DTP/DZP
      QUA4=(DZP+DZP-TH3)*(DZP-TH3)/QUA1
      QUA5=TH3*(TH3-DZP-DZP)/QUA2
      QUA6=TH3*(TH3-DZP)/QUA3
      S3=SD(1)*QUA4+SU(2)*QUA5+SU(3)*QUA6
      T3=T(1)*QUA4+T(2)*QUA5+T(3)*QUA6
      UZ4=UZ(1)+TH4*(UZ(2)-UZ(1))
      WZ4=WZD(1)+TH4*(WZU(2)-WZD(1))
      S4=SD(1)+TH4*(SU(2)-SD(1))
      T4=T(1)+TH4*(T(2)-T(1))
      UZ3=UZ(1)*QUA4+UZ(2)*QUA5+UZ(3)*QUA6
      WZ3=WZD(1)*QUA4+WZU(2)*QUA5+WZU(3)*QUA6
```

```
      CONST2=.66666667*CC(1)*DELTG(1)/F(1)
      CONST3=.66666667*CCO(1)*DELTGO(1)/F(1)
      C3=TR(3,1,1)*UZ3+TSAVF(3,1)*WZ3+(TR(3,3,1)-CONST2-
     1CONST3)*S3
     1+(1.+CONST3*F(1))*T3+TR(3,1,1)*DTPG+TR(3,4,1)*W
      C4=TR(4,1,1)*UZ4+TSAVF(4,1)*WZ4+(TR(4,3,1)-CONST2-
     1CONST3)*S4
     1+(1.+CONST3*F(1))*T4+TR(4,1,1)*DTPG+TR(4,4,1)*W
      WZPU(1)=(C3/TR(3,1,1)-C4/TR(4,1,1))/(TR(3,2,1)/
     1TR(3,1,1)-TR(4,2,1)/TR(4,1,1))
      WZPD(1)=WZPU(1)
      UZP(1)=C3/TR(3,1,1)-TR(3,2,1)/TR(3,1,1)*WZPU(1)
      TP(1)=-W
      SIGB(1)=SPD(1)/F(1)-TP(1)
      DISZ1=DISZ1+.5*DTP*(UZP(1)+UZ(1))
C  BOTTOM B.C.
      TH1=L(1,N)*DTP/DZP
      TH2=L(2,N)*DTP
      NM1=N-1
      QUA7=(TH2-DZP)*TH2/QUA1
      QUA8=(TH2-DZP-DZP)*TH2/QUA2
      QUA9=(DZP+DZP-TH2)*(DZP-TH2)/QUA3
      UZ1=UZ(N1)+TH1*(UZ(N)-UZ(N1))
      WZ1=WZU(N1)+TH1*(WZU(N)-WZU(N1))
      S1=SU(N1)+TH1*(SU(N)-SU(N1))
      T1=T(N1)+TH1*(T(N)-T(N1))
      S2=SD(NM1)*QUA7+SU(N)*QUA8+SU(N1)*QUA9
      T2=T(NM1)*QUA7+T(N)*QUA8+T(N1)*QUA9
      UZ2=UZ(NM1)*QUA7+UZ(N)*QUA8+UZ(N1)*QUA9
      WZ2=WZD(NM1)*QUA7+WZU(N)*QUA8+WZU(N1)*QUA9
      CONST2=.66666667*CC(N)*DELTG(N)/F(N)
      CONST3=.66666667*CCO(N)*DELTGO(N)/F(N)
      C1=TR(1,1,N)*UZ1+TSAVF(1,N)*WZ1+(TR(1,3,N)-CONST3-
     1CONST2)*S1
     1+(1.+CONST3*F(N))*T1+TR(1,1,N)*DTPG
      C2=TR(2,1,N)*UZ2+TSAVF(2,N)*WZ2+(TR(2,3,N)-CONST3-
     1CONST2)*S2
     1+(1.+CONST3*F(N))*T2+TR(2,1,N)*DTPG
      SPU(N1)=(C1-TR(1,1,N)*UZP(N1)-C2+TR(2,1,N)*UZP(N1))/
     1TR(1,3,N)-TR(2,3,N))
      SPD(N1)=SPU(N1)
      TP(N1)=(C2-TR(2,1,N)*UZP(N1)-TR(2,3,N)*SPU(N1))/TR(2,4,N)
      SIGB(N1)=SPU(N1)/F(N)-TP(N1)
      IF(SIGB(N1).LE.0.)GO TO 98
C  INTERIOR POINTS
      DO 399 I=2,N
      IM1=I-1
      IP1=I+1
      F11=F(IM1)/F(I)
      TH1=L(1,IM1)*DTP/DZP
      TH2=L(2,IM1)*DTP
      TH3=-L(3,I)*DTP
      TH4=-L(4,I)*DTP/DZP
      QUA7=TH2*(TH2+DZP)/QUA1
```

```
      OUA8=(TH2-DZP)*(TH2+DZP)/OUA2
      OUA9=(TH2-DZP)*TH2/OUA3
      OUA10=TH3*(TH3-DZP)/OUA1
      OUA11=(TH3-DZP)*(TH3+DZP)/OUA2
      OUA12=(DZP+TH3)*TH3/OUA3
      UZ1=UZ(I)+TH1*(UZ(IM1)-UZ(I))
      WZ1=WZU(I)+TH1*(WZD(IM1)-WZU(I))
      S1=SU(I)+TH1*(SD(IM1)-SU(I))
      T1=T(I)+TH1*(T(IM1)-T(I))
      UZ4=UZ(I)+TH4*(UZ(IP1)-UZ(I))
      WZ4=WZD(I)+TH4*(WZU(IP1)-WZD(I))
      S4=SD(I)+TH4*(SU(IP1)-SD(I))
      T4=T(I)+TH4*(T(IP1)-T(I))
      IF(I.EQ.M .OR. I.EQ.M+MMM)GO TO 330
      S2=SD(IM1)*OUA7+SU(I)*OUA8+SU(IP1)*OUA9
      T2=T(IM1)*OUA7+T(I)*OUA8+T(IP1)*OUA9
      S3=SD(IM1)*OUA10+SU(I)*OUA11+SU(IP1)*OUA12
      T3=T(IM1)*OUA10+T(I)*OUA11+T(IP1)*OUA12
      UZ2=UZ(IM1)*OUA7+UZ(I)*OUA8+UZ(IP1)*OUA9
      WZ2=WZD(IM1)*OUA7+WZU(I)*OUA8+WZU(IP1)*OUA9
      UZ3=UZ(IM1)*OUA10+UZ(I)*OUA11+UZ(IP1)*OUA12
      WZ3=WZD(IM1)*OUA10+WZU(I)*OUA11+WZU(IP1)*OUA12
      GO TO 331
  330 MM1=I-1
      MM2=I-2
      OUA7=(TH2-DZP)*TH2/OUA1
      OUA8=(TH2-DZP-DZP)*TH2/OUA2
      OUA9=(DZP+DZP-TH2)*(DZP-TH2)/OUA3
      S2=SD(MM2)*OUA7+SU(MM1)*OUA8+SU(I)*OUA9
      T2=T(MM2)*OUA7+T(MM1)*OUA8+T(I)*OUA9
      UZ2=UZ(MM2)*OUA7+UZ(MM1)*OUA8+UZ(I)*OUA9
      WZ2=WZD(MM2)*OUA7+WZU(MM1)*OUA8+WZU(I)*OUA9
      MP1=I+1
      MP2=I+2
      OUA4=(DZP+DZP-TH3)*(DZP-TH3)/OUA1
      OUA5=TH3*(TH3-DZP-DZP)/OUA2
      OUA6=TH3*(TH3-DZP)/OUA3
      S3=SD(I)*OUA4+SU(MP1)*OUA5+SU(MP2)*OUA6
      T3=T(I)*OUA4+T(MP1)*OUA5+T(MP2)*OUA6
      UZ3=UZ(I)*OUA4+UZ(MP1)*OUA5+UZ(MP2)*OUA6
      WZ3=WZD(I)*OUA4+WZU(MP1)*OUA5+WZU(MP2)*OUA6
  331 CONST2=.66666667*CC(IM1)*DELTG(IM1)/F(IM1)
      CONST4=.66666667*CCO(IM1)*DELTGO(IM1)/F(IM1)
      CD1=TR(1,1,IM1)*UZ1+TSAVF(1,IM1)*WZ1+(TR(1,3,IM1)-
     1CONST4-CONST2)
     1*S1+(1.+CONST4*F(IM1))*T1+TR(1,1,IM1)*DTPG
      CD2=TR(2,1,IM1)*UZ2+TSAVF(2,IM1)*WZ2+(TR(2,3,IM1)-
     1CONST4-CONST2)
     1*S2+(1.+CONST4*F(IM1))*T2+TR(2,1,IM1)*DTPG
      CONST3=.66666667*CC(I)*DELTG(I)/F(I)
      CONST5=.66666667*CCO(I)*DELTGO(I)/F(I)
      CD3=TR(3,1,I)*UZ3+TSAVF(3,I)*WZ3+(TR(3,3,I)-CONST5-
     1CONST3)*S3
     1+(1.+CONST5*F(I))*T3+TR(3,1,I)*DTPG
```

```
      CD4=TR(4,1,I)*UZ4+TSAVE(4,I)*WZ4+(TR(4,3,I)-CONST5-
     1CONST3)*S4
     1+(1.+CONST5*F(I))*T4+TR(4,1,I)*DTPG
      TR12=TR(1,1,IM1)-TR(2,1,IM1)
      TR34=TR(3,1,I)-TR(4,1,I)
      TR13=TR(1,1,IM1)/TR(1,4,IM1)-TR(3,1,I)/TR(3,4,I)
      AL1=(TR(1,2,IM1)-TR(2,2,IM1))/TR12
      AL2=(TR(1,3,IM1)-TR(2,3,IM1))/TR12
      AL3=(CD1-CD2)/TR12
      AL4=(TR(3,2,I)-TR(4,2,I))/TR34*F11
      AL5=(TR(3,3,I)-TR(4,3,I))/TR34/F11
      AL6=(CD3-CD4)/TR34
      AL7=(TR(1,2,IM1)/TR(1,4,IM1)-TR(3,2,I)*F11/TR(3,4,I))/TR13
      AL8=(TR(1,3,IM1)/TR(1,4,IM1)-TR(3,3,I)/F11/TR(3,4,I))/TR13
      AL9=(CD1/TR(1,4,IM1)-CD3/TR(3,4,I))/TR13
      SPU(I)=((AL9-AL3)/(AL7-AL1)-(AL9-AL6)/(AL7-AL4))/
     1((AL8-AL2)/(AL7-AL1)-(AL8-AL5)/(AL7-AL4))
      WZPU(I)=(AL9-AL3)/(AL7-AL1)-(AL8-AL2)/(AL7-AL1)*SPU(I)
      UZP(I)=AL3-AL1*WZPU(I)-AL2*SPU(I)
      TP(I)=(CD1-TR(1,1,IM1)*UZP(I)-TR(1,2,IM1)*WZPU(I)
     1-TR(1,3,IM1)*SPU(I))/TR(1,4,IM1)
      SPD(I)=SPU(I)/F11
      WZPD(I)=WZPU(I)*F11
      SIGB(I)=SPD(I)/F(I)-TP(I)
      IF(SIGB(I).LE.0.)GO TO 98
  399 CONTINUE
      DO 6 I=1,N
    6 F(I)=F(I)+(1.-F(I))*(UZP(I+1)+UZ(I+1)-UZP(I)-UZ(I))*
     1.5*DTP/DZP
C  UPDATING VARIABLES
      DO 4 I=1,N1
      UZ(I)=UZP(I)
      WZU(I)=WZPU(I)
      WZD(I)=WZPD(I)
      SU(I)=SPU(I)
      SD(I)=SPD(I)
    4 T(I)=TP(I)
      IF(TIME.LT.TPMIN .OR. TIME.GT.TPMAX)GO TO 96
      WRITE(6,2222)(SU(I),I=1,N1)
      WRITE(6,2222)(SD(I),I=1,N1)
      WRITE(6,2222)(T(I),I=1,N1)
      WRITE(6,2222)(UZ(I),I=1,N1)
      WRITE(6,2222)(WZU(I),I=1,N1)
      WRITE(6,2222)(WZD(I),I=1,N1)
      WRITE(6,2222)(CC(I),I=1,N)
      WRITE(6,2222)(DELTG(I),I=1,N)
 2222 FORMAT(1X,10F13.6)
   96 DO 7 I=1,N
    7 CC0(I)=CC(I)
      TIME=TIME+DTP
      IF(TIME.GT.TF)GO TO 99
      GO TO 100
   98 WRITE(6,3334)I,TIME
 3334 FORMAT(1X,'LIQUEFACTION IS COMPLETED AT SECTION ',I2,
```

```
     1' AT ',F8.5,' SECONDS.')
       IQUIT=1
   99 RETURN
      END
C
C  SAMPLE DATA
C
 &DIN A=14760.,B=2.97,C=.5,ALP=1.,K0=10*.5,D=47.,F=10*.5,
  RHOF=1.94,RHOS=5.13,N=7,TMAX=10.,CW=2.3D-8,SIGMIN=1.,
  THETA=10*.5,AMP=.2,OM=12.5,R=10*3.,KZ=10*.003,JPR=3,
  JPRSIG=20,CBFAC=2.67,ISIM=1,FAC=.5,N4=800,III=4,SLB1=0.,
  SLB2=1.,TSTOP=10.,TPMIN=9.98,TPMAX=10.,SLOPE=0.,
  M=10,MMM=10,TOC=1.25,W=300.,TPMAIN=0., &END
```

REFERENCES

1. Alba, P. D., Chan, C. K., and Seed, H. B., 1975, "Determination of Soil Liquefaction Characteristics by Large-Scale Laboratory Tests," Earthquake Engineering Research Center, Report No. EERC 75-14.

2. Ambraseys, N. N., and Sarma, S., 1969, "Liquefaction of Soils Induced by Earthquakes," Seismological Society of America Bulletin, Vol. 59, No. 2, pp. 651-664.

3. Bazant, Z. P., and Krizek, R. T., 1975, "Saturated Sand as an Inelastic Two-Phase Medium," Journal of the Engineering Mechanics Division, ASCE, Vol. 101, No. EM4, pp. 317-332.

4. Biot, M. A., 1940, "The Influence of Initial Stress on Elastic Waves," Journal of Applied Physics, Vol. 11, pp. 522-530.

5. Biot, M. A., 1941, "General Theory of Three-Dimensional Consolidation," Journal of Applied Physics, Vol. 12, pp. 155-164.

6. Biot, M. A., 1955, "Theory of Elasticity and Consolidation for a Porous Anisotropic Solid," Journal of Applied Physics, Vol. 26, No. 2, pp. 182-185.

7. Biot, M. A., 1956, "Theory of Propagation of Elastic Waves in a Fluid-Saturated Porous Solid, Part I, Low-Frequency Range," The Journal of the Acoustical Society of America, Vol. 28, No. 2, pp. 158-178.

8. Biot, M. A., and Willis, D. G., 1957, "The Elastic Coefficients of the Theory of Consolidation," Journal of Applied Mechanics, ASME, Paper No. 57-APM-44.

9. Biot, M. A., 1962, "Mechanics of Deformation and Acoustic Propagation in Porous Media," Journal of Applied Physics, Vol. 33, No. 4, pp. 1482-1498.

10. Biot, M. A., 1962, "Generalized Theory of Acoustic Propagation in Porous Dissipative Media," The Journal of the Acoustical Society of America, Vol. 34, No. 9, pp. 1254-1264.

11. Biot, M. A., 1963, "Theory of Stability and Consolidation of a Porous Media under Initial Stress," Journal of Mathematical Mechanics, Vol. 4, pp. 521-542.

12. Biot, M. A., 1965, Mechanics of Incremental Deformations, John Wiley & Sons Inc.

13. Biot, M. A., 1972, "Theory of Finite Deformations of Porous Solids," Indiana University Mathematics Journal, Vol. 21, No. 7, pp. 597-620.

14. Brandt, H., 1955, "A Study of the Speed of Sound in Porous Granular Media," Journal of Applied Mechanics, ASME, Paper No. 55-APM-37.

15. Burmister, D. M., 1962, "Physical Stress-Strain and Strength Response of Granular Soils," ASTM STP No. 322.

16. Casagrande, A., 1936, "Characteristics of Cohesionless Soils Affecting the Stability of Slopes and Earth Fills," Journal of Boston Society of Civil Engineers, January, 1936.

17. Castro, G., 1975, "Liquefaction and Cyclic Mobility of Saturated Sands," Journal of the Geotechnical Engineering Division, ASCE, Vol. 101, No. GT-6.

18. Crochet, M. J., and Naghdi, P. M., 1966, "On Constitutive Equations for Flow of Fluids Through an Elastic Solid," International Journal of Engineering Science, Vol. 4, pp. 383-401.

19. Dixon, S. J., and Burke, W. J., 1973 "Liquefaction Case History," Journal of the Soil Mechanics and Foundations Division, ASCE, Vol. 99, No. SM11, pp. 921-937.

20. Durham, G. N., and Townsend, F. C., 1973, "Effect of Relative Density on the Liquefaction Susceptibility of Fine Sand under Controlled-Stress Loading," Evaluation of Relative Density and its Role in Geotechnical Projects Involving Cohesionless Soils, ASTM STP-523, pp. 319-331.

21. Fatt, I., 1959, "The Biot-Willis Elastic Coefficients for a Sandstone," Journal of Applied Mechanics, Vol. 26, No. 3, Transactions, ASME, Vol. 81, Series E, pp. 296-297.

22. Finn, W. D. L., Pickering, D. J., and Bransby, P. L., 1971, "Sand Liquefaction in Triaxial and Simple Shear Tests," Journal of Soil Mechanics and Foundations Division, ASCE, Vol. 97, No. SM4, pp. 639-659.

23. Florin, V. A., and Ivanov, P. L., 1961, "Liquefaction of Saturated Sandy Soils," Proceedings, 5th International Conference on Soil Mechanics and Foundation Engineering, Paris, France.

24. Geertsma, J., 1957, "The Effect of Fluid Pressure Decline on Volumetric Changes of Porous Rocks," AIME Transactions, Vol. 210, pp. 331-340.

25. Ghaboussi, J., 1971, "Dynamic Shear Analysis of Porous Elastic Solids Saturated with Compressible Fluids," Earthquake Engineering Research Center, Report No. EERC-71-6.

26. Ghaboussi, J., and Wilson, E. L., 1972, "Variational Formulation of Dynamics of Fluid Saturated Porous Elastic Solids," Journal of the Engineering Mechanics Division, ASCE, Vol. 98, No. EM4, pp. 947-963.

27. Ghaboussi, J., and Wilson, E. L., 1973, "Seismic Analysis of Earthdam-Reservoir Systems," Journal of the Soil Mechanics and Foundations Division, ASCE, Vol. 99, No. SM10, pp. 849-862.

28. Ghaboussi, J., and Wilson, E. L., 1973, "Liquefaction Analysis of Saturated Granular Soils," Proceedings, Fifth World Conference on Earthquake Engineering, Rome, Vol. 1, pp. 380-389.

29. Goto, S., 1966, "An Experimental Study of Liquefaction of Saturated Sands," Soils and Foundations, Vol. 9, No. 1, pp. 53-65.

30. Gardner, W. S., 1966, "Stress-Strain Behavior of Granular Soils in One-Dimensional Compression," Conference Preprint 325, Structural Engineering Conference, Miami, Florida.

31. Green, P. A., and Ferguson, P. A. S., 1971, "On Liquefaction Phenomena, by Professor A. Casagrande: Report of Lecture," Geotechnique, Vol. 21, No. 3, pp. 197-202.

32. Green, A. E., and Naghdi, P. M., 1965, "A Dynamic Theory of Interacting Continua," International Journal of Engineering Science, Vol. 3, pp. 231-241.

33. Hall, J. R., Jr., 1962, "Effect of Amplitude on Damping and Wave Propagation in Granular Materials," Ph.D. Dissertation, University of Florida, Gainesville, Florida.

34. Hall, J. R., Jr., and Richart, F. E., Jr., 1963, "Dissipation of Elastic Wave Energy in Granular Soils," Journal of Soil Mechanics and Foundations Divison, ASCE, Vol. 89, No. SM6, pp. 27-56.

35. Hardin, B. O., and Richart, F. E., Jr., 1963, "Elastic Wave Velocities in Granular Soils," Journal of Soil Mechanics and Foundations Division, ASCE, Vol. 89, No. SM1, pp. 33-65.

36. Harr, M. E., 1962, Groundwater and Seepage, McGraw-Hill Book Company.

37. Hsieh, L., and Yew, C. H., 1973, "Wave Motion in a Fluid Saturated Porous Medium," Journal of Applied Mechanics, ASME, Paper No. 73-APMW-16.

38. Ishibashi, I., and Sherif, M. A., 1974, "Soil Liquefaction by Torsional Simple Shear Device," Journal of the Geotechnical Engineering Division, ASCE, No. GT8, Vol. 100, pp. 871-888.

39. Ishihara, K., 1968, "Propagation of Compressional Waves in a Saturated Soil," Proc. of the International Symposium of Wave Propagation and Dynamic Properties of Earth Materials, University of New Mexico Press, pp. 195-206.

40. Ishihara, K., 1970, "Approximate Forms of Wave Equations for Water-Saturated Porous Materials and Related Dynamic Modulus," Soils and Foundations, Vol. 10, No. 4, pp. 10-38.

41. Ishihara, K., and Yasuda, S., 1973, "Sand Liquefaction under Random Earthquake Loading Condition," Proceedings, Fifth World Conference on Earthquake Engineering, Rome, Vol. 1, pp. 329-338.

42. Kishida, H., 1969, "Characteristics of Liquified Sands During Mino-Owari, Tohnankai and Fukui Earthquakes," Soils and Foundations, Vol. 9, No. 1, pp. 75-91.

43. Kishida, H., 1970, "Characteristics of Liquefaction of Level Sandy Ground During Tokachioki Earthquake," Soils and Foundations, Vol. 10, No. 2, pp. 103-111.

44. Ko, H. Y., and Scott, R. F., 1967, "Deformation of Sand in Hydrostatic Compression," Journal of the Soil Mechanics and Foundations Division, ASCE, Vol. 93, No. SM3, pp. 137-156.

45. Lee, K. L., and Seed, H. B., 1967, "Cyclic Stress Conditions Causing Liquefaction of Sand," Journal of the Soil Mechanics and Foundations Division, ASCE, Vol. 93, No. SM1, pp. 47-70.

46. Lee, K. L., and Seed, H. B., 1967, "Dynamic Strength of Anisotropically Consolidated Sand," Journal of the Soil Mechanics and Foundations Division, ASCE, Vol. 93, No. SM5, pp. 169-190.

47. Martin, G. R., Finn W. D. Liam, and Seed, H. B., 1975, "Fundamentals of Liquefaction under Cyclic Loading," Journal of the Geotechnical Engineering Division, ASCE, Vol. 101, No. GT5, pp. 423-438.

48. Ohsaki, Y., 1966, "Niigata Earthquake, 1964, Building Damage and Soil Condition," Soils and Foundations, Vol. 5, No. 2, pp. 14-37.

49. Ohsaki, Y., 1970, "Effects of Sand Compaction on Liquefaction during the Tokachioki Earthquake," Soils and Foundations, Vol. 10, No. 2, pp. 112-128.

50. Papadakis, C. N., 1973, "Soil Transients by Characteristics Method," Ph.D. Dissertation, The University of Michigan, Ann Arbor, Michigan.

51. Peacock, W. H., and Seed, H. B., 1968, "Sand Liquefaction Under Cyclic Loading Simple Shear Conditions," Journal of the Soil Mechanics and Foundations Division, ASCE, Vol. 94, No. SM3, pp. 689-708.

52. Pyke, R. M., 1973, "Settlement and Liquefaction of Sands under Multi-Directional Loading," Ph.D. Dissertation, University of California, Berkeley, California.

53. Reynolds, O., 1885, "On the Dilatancy of Media Composed of Rigid Particles in Contact," Philosophical Magazine, Vol. 20.

54. Richart, F. E., Jr., Hall, J. R., Jr., and Woods, R. D., 1970, Vibrations of Soils and Foundations, Prentice-Hall Inc.

55. Richart, F. E., Jr., 1971, discussion on "Approximate Forms of Wave Equations for Water-Saturated Porous Materials and Related Dynamic Modulus," Soils and Foundations, Vol. 11, No. 4, pp. 69-71.

56. Richart, F. E., Jr., 1975, "Some Effects of Dynamic Soil Properties on Soil-Structure Interaction," Journal of the Geotechnical Engineering Division, ASCE, Vol. 101, No. GT12, Proc. Paper 11764, Dec., pp. 1193-1240.

57. Roberts, J. E., and Souza, J. M. DE., 1958, "The Compressibility of Sands," Proceedings, ASTM, Vol. 50, pp. 1269-1277.

58. Roscoe, K. H., Schofield, A. N., and Worth, C. P., 1958, "On the Yielding of Soils," Geotechnique, Vol. 8, No. 22, pp. 22-53.

59. Sawabini, C. T., 1974, "Compressibility of Unconsolidated Arkosic Oil Sands," Society of Petroleum Engineers Journal, pp. 132-138.

60. Scott, R. F., 1963, Principles of Soil Mechanics, Addison-Wesley, Inc.

61. Seed, H. B., and Lee, K. L., 1966, "Liquefaction of Saturated Sands During Cyclic Loading," Journal of the Soil Mechanics and Foundations Division, ASCE, No. SM6, pp. 105-134.

62. Seed, H. B., and Idriss, I. M., 1967, "Analysis of Soil Liquefaction: Niigata Earthquake," Journal of the Soil Mechanics and Foundations Division, ASCE, Vol. 93, No. SM3, pp. 83-108.

63. Seed, H. B., 1968, "Landslides During Earthquakes Due to Soil Liquefaction," Journal of the Soil Mechanics and Foundations Division, ASCE, Vol. 94, No. SM5, pp. 1053-1122.

64. Seed, H. B., and Peacock, W. H., 1971, "Test Procedures for Measuring Soil Liquefaction Characteristics," Journal of Soil Mechanics and Foundations Division, ASCE, Vol. 97, No. SM8, pp. 1099-1119.

65. Seed, H. B., and Idriss, M. I., 1971, "Simplified Procedure for Evaluating Soil Liquefaction Potential," Journal of Soil Mechanics and Foundations Division, ASCE, Vol. 97, No. SM9, pp. 1249-1273.

66. Skempton, A. W., 1954, "The Pore Pressure Coefficients A and B," Geotechnique, Vol. 4, No. 4, pp. 143-147.

67. Skempton, A. W., 1960, "Effective Stress in Soils, Concrete, and Rocks," Pore Pressure and Suction in Soils, Conference of Institution of Civil Engineers (U.K.) Butterworth and Company Ltd., London.

68. Streeter, V. L., Wylie, E. B., and Richart, F. E., Jr., 1973, "Soil Motion Computations by Characteristics Method," Journal of the Geotechnical Engineering Division, ASCE, Vol. 100, No. GT3, pp. 247-263.

69. Wylie, E. B., and Streeter, V. L., 1976, "Characteristic Method for Liquefaction of Soils," Second International Conference on Numerical Methods in Geomechanics, June 20-25, Virginia Polytechnic Institute, Blacksburg, Virginia 24061.

70. Terzaghi, K., 1925, "Principle of Soil Mechanics," Engineering News Record.

71. Terzaghi, K., 1943, Theoretical Soil Mechanics, John Wiley and Sons, Inc.

72. Truesdell, C., and Toupin, R., 1960, "Principles of Classical Mechanics and Field Theory," Handbuch der Physik, Vol. III/1, Berlin-Cottingern-Heidelberg, Springer-Verlag.

73. Verruijt, A., 1969, "Elastic Storage of Aquifers," Flow Through Porous Media, Edited by R. J. M. De Wiest, Academic Press.

74. Whitman, R. V., 1971, "Resistance of Soil to Liquefaction," Soils and Foundations, Vol. 11, No. 4, pp. 59-68.

75. Yoshimi, Y., 1967, "An Experimental Study of Liquefaction of Saturated Sands," Soils and Foundations, Vol. 9, No. 1, pp. 53-65.

76. Yoshimi, Y., and Oh-oka, H., 1975, "Influence of Degree of Shear Stress Reversal on the Liquefaction Potential of Saturated Sand," Soils and Foundations, Vol. 15, No. 3, pp. 27-40.

77. Youd, T. L., 1973, "Liquefaction, Flow, and Associated Ground Failure," Geological Survey Circular 688, Geological Survey, United States Department of the Interior.

78. Youd, T. L., 1972, "Compaction of Sands by Repeated Shear Straining," Journal of the Soil Mechanics and Foundations Division, ASCE, Vol. 98, No. SM7, pp. 709-725.

79. Zwikker, C., and Kosten, C. W., 1949, "Sound Absorbing Materials," Elsevier Publishing Co., Inc. New York.

80. Peck, R. B., Hanson, W. E., and Thornborn, T. H., 1953, Foundation Engineering, John Wiley and Sons, New York.

81. Fry, Z. B., 1963, "Development and Evaluation of Soil Bearing Capacity, Foundations of Structures," Waterway Experiment Station, Tech. Rep. No. 3-632, Rep. No. 1, July.

82. Heller, L. W., 1971, "The Partical Motion Field Generated by the Torsional Vibration of a Circular Footing on Sand," Ph.D. Dissertation, The University of Fla.

83. Al-Hussaini, M. M., 1973, "Influence of Relative Density on the Strength and Deformation of Sand under Plane Strain Conditions," ASTM Special Technical Publication 523, pp. 332-347.

84. Streeter, V. L., Wylie, E. B., and Richart, F. E. Jr., 1974, CHARSOIL, available through NISEE, University of California, Berkeley, California 94720.

85. Wylie, E. B., Streeter, V. L., 1976, "One-Dimensional Soil Transients by Characteristics," Second International Conference on Numerical Methods in Geomechanics, June 20-25, Virginia Polytechnic Institute, Blacksburg, Virginia 24061.

86. Kawasumi,H., Editor-in-Chief, 1968, General Report on the Niigata Earthquake of 1964, Tokyo Electrical Engineering College Press, Tokyo, Japan.

87. Becker, R. B., 1975, "Application of Mixture Theory to Soil Mechanics," Ph.D. Dissertation, The University of Michigan, Ann Arbor, Michigan.